Inverse models for ice-induced propeller moments on a polar vessel

by

Brendon Mark Nickerson

Dissertation presented for the degree of Doctor of Philosophy
in the Faculty of Engineering at Stellenbosch University

Supervisor: Prof. Anriëtte Bekker

March 2021

Stellenbosch University https://scholar.sun.ac.za

Declaration

By submitting this dissertation electronically, I declare that the entirety of the work contained therein is my own, original work, that I am the sole author thereof (save to the extent explicitly otherwise stated), that reproduction and publication thereof by Stellenbosch University will not infringe any third party rights and that I have not previously in its entirety or in part submitted it for obtaining any qualification.

Date: 01/02/2021

Copyright © 2021 Stellenbosch University
All rights reserved.

Stellenbosch University https://scholar.sun.ac.za

Abstract

Inverse models for ice-induced propeller moments on a polar vessel

B. M. Nickerson
Department of Mechanical and Mechatronic Engineering,
University of Stellenbosch,
Private Bag X1, Matieland 7602, South Africa.

Dissertation: PhD
March 2021

It is necessary to quantify the loads experienced by the propellers of ice-going vessels. Knowledge of these loads will serve to improve propulsion design specifications and maintenance strategies for polar class ships. Recent developments include the inverse solutions of the external ice-induced propeller moments from indirect measurements on the propulsion shaft. These inverse solutions are performed using models that account for the dynamic influence of the shaft. Although torsional vibration calculations are required by design rules there is little information on the methodology to calculate external propeller moments as their use, in this context, is still relatively new. Full-scale propulsion shaft measurements were conducted on board the S.A. Agulhas II, in which the torque and angular velocity were captured, to be transformed into external propeller moments. Two inverse models of the propulsion shaft were investigated. The first is an existing model which represents the shaft as a combination of lumped masses. The inverse problem in this case is ill-posed and requires regularization. It was found that the assumptions made in the derivation of this model, that both the hydrodynamic and motor torques were constant, and its computational expense made it ill-suited for use in the inverse estimation of propeller moments. The second inverse model is newly developed and based on the superposition of the shaft modes, resulting in a well-posed problem. This model accounts for the modal inertia in the flexible modes of the shaft, as full-scale data indicated that this was important, and has increased accuracy and efficiency. To the author's knowledge, this is the first model that has been efficiently applied to determine the inverse propeller moments from full-scale measurements for a complete voyage. The derivation of the corresponding estimated propeller load profiles is presented. The new model is suitable for the real-time monitoring of propeller loads, which can assist in ship operation.

Stellenbosch University https://scholar.sun.ac.za

Uittreksel

Inverse modelle vir ys-geïnduseerde propellermomente op a poolskip

("Inverse models for ice-induced propeller moments on a polar vessel")

B. M. Nickerson
Departement Meganiese en Megatroniese Ingenieurswese,
Universiteit van Stellenbosch,
Privaatsak X1, Matieland 7602, Suid Afrika.

Proefskrif: PhD
Maart 2021

Dit is nodig om die laste te kwantifiseer waaraan die skroewe van skepe onderhewig is tydens ysvaart. Kennis van hierdie laste dien om die spesifikasies en instandhoudingstrategieë van aandrywingstelsels van ys-klas skepe toe te lig. Onlangse verwikkelinge sluit inverse oplossings van die eksterne in ys-geënduseerde skroefmomente in deur gebruik te maak van indirekte metings op die dryfas. Hierdie inverse oplossings word uitgevoer met behulp van modelle wat die dinamiese invloed van die as in ag neem. Hoewel torsionele vibrasieberekening deur ontwerpsreëls vereis word, is daar min inligting oor metodologie om inverse skroefmomente te bepaal, aangesien werk in die konteks nog relatief nuut is. Volskaalse dryfasmetings van wringkrag en hoeksnelheid is op die S.A. Agulhas II uitgevoer met die doel om skroefmomente van hier af te bereken. Twee inverse modelle van die SA Aghulhas II dryfas is ondersoek. Die eerste model is 'n bestaande model, wat die skag voorstel as 'n kombinasie van gekonsentreerde massas. Die inverse probleem in hierdie geval is swak gestel en vereis regularisering. Verder word daar aangeneem dat beide die hidrodinamiese- en die motorwringkrag konstant is. Die berekeningsvereistes maak dit ongeskik vir gebruik in die inverse beraming van skroefmomente. 'n Tweede inverse model is nuut ontwikkel en gebaseer op die superposisie van die modusse van die dryfas. Dit is meer akkuraat en doeltreffend en lei tot 'n volledig gestelde probleem. Dit sluit die modale traagheid van die as in, aangesien volskaalse data aandui dat dit belangrik is. Volgens die outeur is hierdie die eerste inverse model wat effektief aangewend is om invers-berekende skroefmomente vanaf volskaal meetings te beraam vir 'n volledige vaart. Die afleiding van geskatte skroef lasprofiele word aangebied. Die nuwe model is geskik vir intydse monitering van operasionele skroeflaste.

Stellenbosch University https://scholar.sun.ac.za

To my family and friends, and to my loving wife Karina.

Stellenbosch University https://scholar.sun.ac.za

Acknowledgements

I would like to express my sincere gratitude to the following people and organisations:

- Prof. Annie Bekker for her guidance and contribution throughout this research.
- Captain Gavin Syndercombe and Captain Knowledge Bengu, and their crews aboard the S.A. Agulhas II for their assistance during the installation of measurement equipment and during the 2018/19 Annual Relief and 2019 SCALE Spring voyages.
- The South African National Antarctic Programme and the South African Department of Environment, Forestry, and Fisheries for accommodating this research on board the S.A. Agulhas II.
- The Department of Mechanical and Mechatronic Engineering at Stellenbosch University for funding and the equipment and resources necessary for the completion of this research.

The financial assistance of the South African National Research Foundation through the South African National Antarctic Programme (Ref.: SNA170420228015, Grant No.: 110737) is gratefully acknowledged.

Stellenbosch University https://scholar.sun.ac.za

Table of Contents

Stellenbosch University https://scholar.sun.ac.za

Stellenbosch University https://scholar.sun.ac.za

Stellenbosch University https://scholar.sun.ac.za

List of Figures

Stellenbosch University https://scholar.sun.ac.za

Stellenbosch University https://scholar.sun.ac.za

Stellenbosch University https://scholar.sun.ac.za

Stellenbosch University https://scholar.sun.ac.za

Stellenbosch University https://scholar.sun.ac.za

List of Tables

Stellenbosch University https://scholar.sun.ac.za

Acronyms

CPP	Controllable pitch propeller
CMU	Central measurement unit
DGSVD	Damped generalised singular value decomposition
DNV	Det Norske Veritas
DSVD	Damped singular value decomposition
FE	Finite element
FPP	Fixed pitch propeller
HBM	Hottinger Baldwin Messtechnik
IACS	International Association of Classification Societies
IAS	Instantaneous angular speed
ICP	Integrated circuit piezoelectric
PSRV	Polar supply and research vessel
MCR	Maximum continuous rating
MISO	Multiple-input single-output
MTSVD	Modified truncated singular value decomposition
RAM	Random access memory
SAA II	S.A. Agulhas II
SANAE	South African National Antarctic Expedition
SANAP	South African National Antarctic Programme
SCALE	Southern ocean seasonal experiment
SISO	Single-input single-output
SVRG	Sound and Vibration Research Group
TRD	Transmissibility of displacement
TRF	Transmissibility of force
(T)GSVD	(Truncated) generalised singular value decomposition
(T)SVD	(Truncated) singular value decomposition

Stellenbosch University https://scholar.sun.ac.za

Nomenclature

Constants

β	Constant used in Newmark-β time integration scheme
γ	Constant used in Newmark-β time integration scheme
ρ_∞	Constant used in JWH-α time integration scheme

Variables

A	Propulsion shaft cross sectional area	[m^2]
C_p	Propeller hydrodynamic damping	[N · m · s/rad]
c	Wave speed	[m/s]
c_{1-12}	Torsional damping element for discrete model	[N · m · s/rad]
D	Propeller diameter	[m]
d_i	Propulsion shaft inner diameter	[m]
d_o	Propulsion shaft outer diameter	[m]
E	Young's modulus	[GPa]
EAR	Expanded blade area ratio	[ ]
F	Force	[N]
f	Natural frequency	[Hz]
G	Shear modulus	[GPa]
H	Impulse response function	[ ]
J	Polar moment of inertia	[m^4]
J_0	Mass moment of inertia per unit length	[kg · m]
J_{1-13}	Inertial components for discrete model	[kg · m^2]
J_{motor}	Motor mass moment of inertia	[kg · m^2]
J_p	Propeller mass moment of inertia	[kg · m^2]
k	Gauge factor	[ ]
k_{1-12}	Torsional stiffness element for discrete model	[N/m]
L	Length	[m]
M	Applied torsional moment or torque	[Nm]
N	Number of mode shapes	[ ]

Stellenbosch University https://scholar.sun.ac.za

n	nominal rotational speed (at MCR) for open propeller	[Hz]
P	Propeller pitch	[m]
$P_{0.7}$	Propeller pitch at 0.7 of propeller radius	[m]
Q	Torque or torsional moment	[Nm]
Q_1	Fore measured torque on SAA II propulsion shaft	[Nm]
Q_2	Aft measured torque on SAA II propulsion shaft	[Nm]
Q_{ice}	Ice induced propeller moment	[Nm]
Q_{motor}	Motor torque	[Nm]
Q_{prop}	Propeller torque or moment	[Nm]
Q_{shaft}	Propulsion shaft torque	[Nm]
q	Generalized modal coordinate	[ ]
R	Electrical resistance	[Ω]
t	Time	[s]
U_E	Excitation voltage	[V]
U_A	Output voltage	[V]
x	Distance	[m]
Z	No. of propeller blades	[ ]

γ_s	Shear or angular strain	[ ]
ϵ	Normal strain	[mm/mm]
θ	Angular displacement	[rad]
$\dot{\theta}$	Angular velocity	[rad/s]
$\ddot{\theta}$	Angular acceleration	[rad/s^2]
λ	Regularization parameter	[ ]
ρ	Density	[kg/m^3]
τ	Torsional stress	[Pa]
ϕ	Mode shape	[ ]
ω	Natural frequency	[rad/s]

Vectors and Matrices

$\mathbf{C}$	Damping matrix
$\mathbf{H}$	Impulse response function
$\mathbf{J}$	Mass moment of inertia matrix
$\mathbf{K}$	Stiffness matrix
$\mathbf{L}$	Regularization matrix
$\mathbf{Q}$	Load vector
$\mathbf{Q}_{ice}$	Ice induced propeller moment vector

Stellenbosch University https://scholar.sun.ac.za

$\mathbf{Q}_{shaft}$	Propulsion shaft torque vector
$\mathbf{q}$	Generalized modal coordinate vector

Subscripts

i	Numbering 1,2,3,...
j	Numbering 1,2,3,...
max	Maximum
min	Minimum
n	Numbering 1,2,3,...

Chapter 1

Introduction

There is an increasing need for safety and efficiency with regards to shipping in Arctic regions. This is due to the fact that maritime transport in ice-covered seas is expected to increase in future decades (Ikonen *et al.*, 2014). The propulsion systems of vessels passing through icy waters are exposed to ice-related loading in addition to the hydrodynamic loading usually experienced. According to Polić *et al.* (2014) this effects the safety and efficiency of vessel operation.

Structural failure of the propeller blades or shaft-line could occur due to either a loading condition that exceeds the ultimate strength of the component, or a cyclic loading condition leading to fatigue failure. These loading conditions are exacerbated during propeller-ice interaction (Huisman *et al.*, 2014). This is due to the fact that ice impacts increase the maximum loading on the propellers as well as introduce transient torsional vibration into the propulsion system (Batrak *et al.*, 2014).

This research focuses on the propeller of the shaft-line systems of polar vessels during operation. It follows on from research completed by De Waal (2017) in which a method for external ice-induced moment estimation for the propeller of the S.A. Agulhas II (SAA II) was investigated. This was done due to the general difficulty in measuring the loading conditions directly at the propeller as the sensors suffer in the harsh operating conditions.

Thus the loads are usually measured at some point on the shaft between the propeller and the motor (Polić *et al.*, 2014), and the loading condition at the propeller must be determined from these measurements. This leads to an inverse problem, where the outputs are known variables and the input propeller moments become the unknown variables.

The research presented here expands upon previous research (De Waal, 2017), and produces a new method for the estimation of external propeller moments. The new method, based on the modal superposition of a continuous shaft model, is significantly more efficient and robust to measurement errors.

The propeller moment estimates provided by the model can then be used to:

Stellenbosch University https://scholar.sun.ac.za

- provide the crew with information, such as maximum loading conditions, during the vessel's operation. This information can be used to assess the safe operation of the vessel.
- monitor the propeller loads over the course of multiple voyages. Along with other models, this can be used to monitor the fatigue of the vessel's propulsion line.
- monitor the propeller loads during a voyage, to assist in the operation of a vessel.
- predict expected load profiles from recorded voyages, which can be used for comparisons to other vessels, or as an indication of what voyages a particular vessel can safely undertake
- provide information in the design and testing of new vessels.

This project forms part of the ongoing research being conducted on the SAA II by the Sound and Vibration Research Group (SVRG) at the Department of Mechanical and Mechatronic Engineering of Stellenbosch University.

1.1 Objectives

The aim of this research was to investigate the estimation of propeller moments of ice going vessels. Furthermore, the research set out to add novel contributions to the literature currently available. The objectives set forth to achieve this were:

1. to conduct a review of the current literature available for the inverse estimation of propeller moments.
2. to perform full-scale measurements on the SAA II, for use in estimating propeller moments.
3. to investigate the model used by De Waal (2017); De Waal *et al.* (2018*b*).
    a) Specifically, this model needed to be improved in terms of its regularization parameter selection.
    b) The accuracy of the model needed to be investigated to assess its suitability for inverse propeller moment estimates.
4. to develop a new model for the inverse estimation of propeller moments.
    a) This model needed to be more efficient than the regularization based inverse methods. Ideally, it should be able to provide propeller moment estimates in real-time, or sufficiently close to real-time, so as to be useful in the monitoring of operational propeller loads.

Stellenbosch University https://scholar.sun.ac.za

   b) The accuracy of the model needed to be investigated to assess its suitability for inverse propeller moment estimates.

5. to apply the models to measured data to verify its use during vessel operation, or in the analysis of the voyages thereafter.

1.2 Original contributions

The main contributions from this research to the literature are:

1. Full-scale propulsion shaft measurements, including both shaft torque and angular velocity, from the SAA II during voyages in the Southern Ocean and Antarctica (Chapter 3 and Appendix C). The measurements include navigation through open water and ice and add to the sparsely available data of full-scale ice impacts.

2. Further development of the discrete lumped mass model of the propulsion shaft developed and used by Ikonen *et al.* (2014) and De Waal *et al.* (2018*b*) was conducted. It was found that the optimised regularization parameters employed by these authors were not generally optimal and led to over- or under-regularization in other cases. Automated optimization of the regularization parameter was developed and employed on a case-by-case basis, and this was found to lead to well regularized results (Chapter 4).

3. Despite the increase in the quality of regularized results, after evaluation it was found that the discrete lumped mass model is ill-suited to the inverse estimations of propeller moments (Chapter 4).

4. A new continuous propulsion shaft model based on modal superposition, and using a better suited numerical time integration scheme, was developed and evaluated. It was found that the model was more accurate and efficient than the discrete lumped mass model, and offers advantages over the state of the art (Polić *et al.*, 2019) in literature (Chapter 5).

5. The new continuous model was applied to the full dataset of a voyage of the SAA II. It was found to efficiently perform the inverse solution for this large set of data, and can be used to monitor the propeller loads in close to real-time during a voyage (Chapters 5 and 6).

Figure 1.1 provides a breakdown of the presented research, and shows where these contributions arise.

Stellenbosch University https://scholar.sun.ac.za

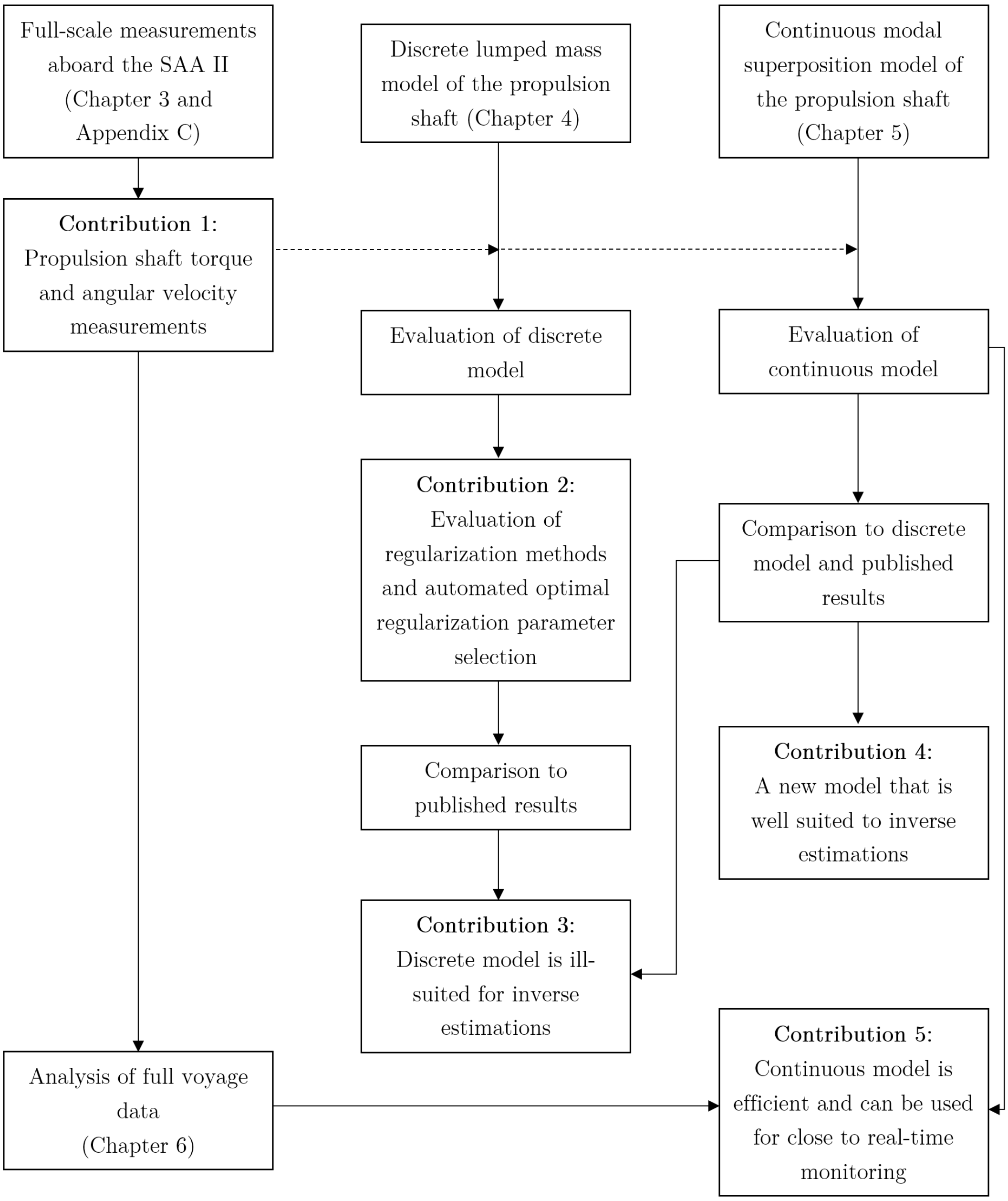

Figure 1.1: Breakdown of the presented research and contributions

Chapter 2

Literature review

This review includes the explanations for vessel propulsion systems, torsional vibrations, operational loads and the conduction of full-scale measurements. Furthermore there is a discussion of the current state of the art in models for inverse propeller moment estimation.

2.1 Vessel propulsion systems

The propulsion system of a seafaring vessel enables its motion through water. In the case of ice-faring vessels, the propulsion system needs to operate within both open water and ice. The main components of such a system include a diesel engine, electric motor or a combination of both, a transmission line, and a propeller. The SAA II makes use of diesel engines powering electric motors, which in turn drive the shaft-line and propeller. An example of a propulsion system for an ice-faring vessel is depicted in Figure 2.1.

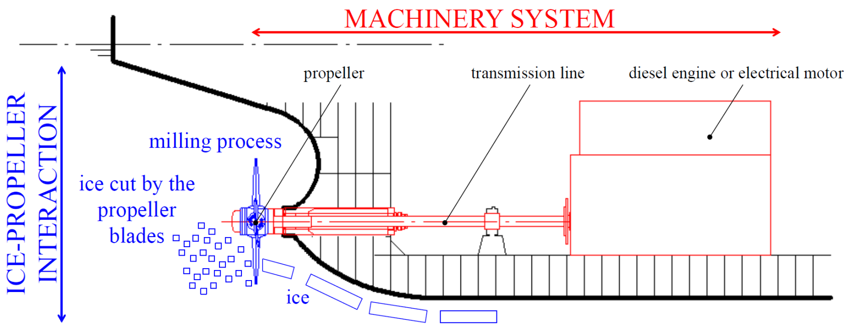

Figure 2.1: Ice-faring vessel propulsion system (Polić *et al.*, 2014)

The propeller is the component that creates directional thrust from machine power through rotation, inducing a pressure difference between its suction and pressure surfaces (Polić *et al.*, 2014). During vessel operation in ice the

Stellenbosch University https://scholar.sun.ac.za

propeller will make contact with the ice and transfer loads through to the other components of the propulsion system.

During the propeller design process, the impact strength of the blade edge must be considered. This is due to the fact that blade contact with multi-year hard blue ice could result in local pressures between 30 to 40 MPa (Det Norske Veritas, 2011). Propeller blades must therefore be strengthened to prevent localised indentations under these contact pressures (Det Norske Veritas, 2011).

Furthermore, the propeller blade is designed as the weakest point in the shaft-line system. This is to ensure that the bending or failure of a propeller blade should not cause further damage to any other propulsion system components (Det Norske Veritas, 2011).

According to Araujo *et al.* (2013), there are two main types of propeller designs. These are fixed pitch propellers (FPP) and variable- or controllable-pitch propellers (CPP). The SAA II makes use of CPPs and this is therefore discussed in further detail below.

As CPPs operate at a higher power to volume ratio, they need to be actuated via a hydraulic oil power system which typically consists of a piston in a cylinder (Martelli *et al.*, 2013). CPPs operate at constant shaft speed, with varying thrust achieved by controlling the pitch of the propeller blades. This has a number of benefits such as improved efficiency for diesel and gas turbines, as well as reducing the weight required as reverse gears are no longer necessary (Araujo *et al.*, 2013). However, CPPs are more expensive then FPPs due to the specialised parts (shafting, hydraulics, bridge controls, etc.) that are required (Araujo *et al.*, 2013). Figure 2.2 depicts the internal components of a CPP.

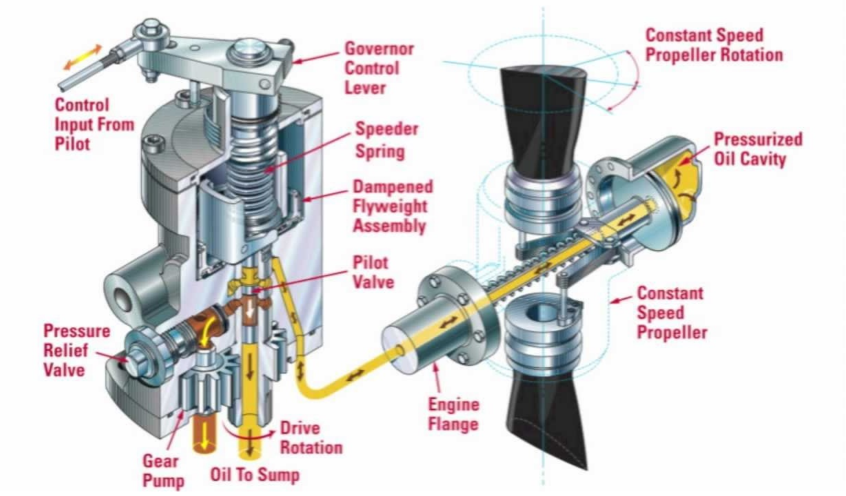

Figure 2.2: Internal view of a CPP system (Valeri, 2015)

Stellenbosch University https://scholar.sun.ac.za

According to Martelli *et al.* (2013), the main components of a CPP include the tank, pumps, valves, filters, pipelines, oil distribution box, cooler, double-effect cylinder and sensors. The process of altering the propeller blade pitch is described by Martelli *et al.* (2013) as follows:

- Oil flows through a directional valve on the tank to the oil distribution box.
- The oil flows through a twin pipe situated within the propulsion shaft to a piston in the propeller hub.
- A double-effect hydraulic cylinder within the hub is actuated by the oil pressure.
- The piston is connected to the blades through a pin which converts its stroke to angular rotation of the blades.
- It is noted that two actuating cylinder chambers are necessary in order to achieve rotation in both positive and negative directions.

2.2 Torsional vibration

Torsional vibration of a shaft can be defined as a vibration that occurs in the angular direction around the centre axis of a shaft in a plane perpendicular to the cross section of the shaft (Inman, 2014). This vibration may also be superimposed upon the rotational motion of the shaft.

The measurement of torsional vibration in rotating machinery is important to the assessment of possible damage or premature fatigue failure of machine components (Kushwaha, 2012). Furthermore, Kushwaha (2012) states that there is the possibility for a significant increase in vibration amplitudes if the system operates at or near to its natural frequencies.

The natural frequency of a system is defined as the frequency at which a system will oscillate when it is disturbed from rest and not subjected to any external driving or damping forces. A system excited at this frequency will experience constructive interference with regards to vibration and the amplitude thus increases significantly. This is referred to as resonance (Inman, 2014). For an undamped system, the amplitude would increase indefinitely, while a damped system with external loads will reach some maximum value. This would result in higher stress levels and could lead to failure.

A system has as many natural frequencies as degrees of freedom. For example an ideal spring-mass system, consisting of rigid masses or lumps connected by springs, will have one natural frequency for each lump in the system. In the case of a non-rigid or flexible body, where the mass and stiffness are distributed throughout the body, there will be infinite number of natural frequencies (Inman, 2014). Each of these natural frequencies has an associated mode shape,

Stellenbosch University https://scholar.sun.ac.za

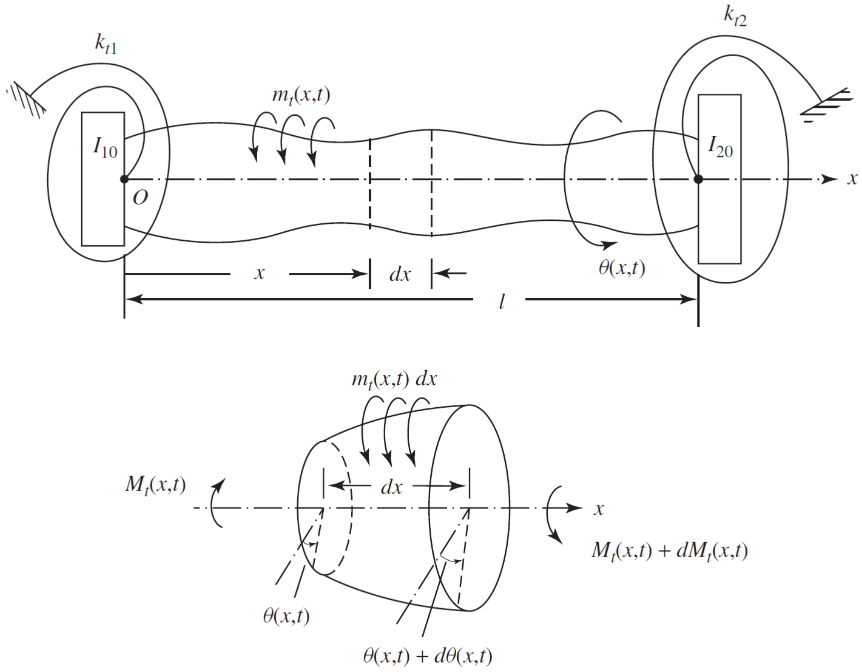

Figure 2.3: Torsional vibration of a shaft (Rao, 2007)

which describes the shape of a system's vibration should it be excited at that particular natural frequency (Inman, 2014). In general, the word mode is used to refer to both a natural frequency and its associated mode shape (Inman, 2014).

According to Barro and Lee (2011), the main source of torsional vibration excitation for polar class propulsion systems is the interaction between the propeller and the ice. For the forced torsional vibration of propulsion lines, the first torsional mode is dominant (Senjanović *et al.*, 2019).

The characteristic equation for the torsional vibration of a shaft can be obtained through the use of equilibrium (Rao, 2007). Considering a differential element of a shaft, such as in Figure 2.3, in equilibrium results in Equation 2.1.

$$\left(M_t(x,t) + \frac{\partial M_t(x,t)}{\partial x}dx\right) - M_t(x,t) + m_t(x,t)dx = J_0\frac{\partial^2\theta(x,t)}{\partial t^2}dx \tag{2.1}$$

where $M_t(x,t)$ is the internal torque, $\theta(x,t)$ the angular displacement, $m_t(x,t)$ the applied loads, $J(x)$ the shaft cross section polar moment of inertia, and J_0 is the mass moment of inertia of the shaft per unit length (Rao, 2007).

From solid mechanics the relationship between the torque in the shaft at x and the torsional deflection at x is (Shames and Pitarresi, 2000):

$$M_t(x,t) = GJ(x)\frac{\partial\theta(x,t)}{\partial x} \tag{2.2}$$

Stellenbosch University https://scholar.sun.ac.za

Substituting Equation 2.2 into Equation 2.1 gives the characteristic equation for the shaft (Rao, 2007):

$$\frac{\partial}{\partial x}\left(GJ(x)\frac{\partial\theta(x,t)}{\partial x}\right)+m_t(x,t)=J_0\frac{\partial^2\theta(x,t)}{\partial t^2} \tag{2.3}$$

Assuming a constant circular cross-sectional area, Equation 2.3 becomes:

$$GJ\frac{\partial^2\theta(x,t)}{\partial x^2}+m_t(x,t)=\rho J\frac{\partial^2\theta(x,t)}{\partial t^2} \tag{2.4}$$

where ρ is the density of the shaft.

Before solving a forced vibration problem, the free vibration case without any applied loads is considered. For the free vibration case $m_t(x,t) = 0$. This reduces Equation 2.4 to:

$$c^2\frac{\partial^2\theta(x,t)}{\partial x^2}=\frac{\partial^2\theta(x,t)}{\partial t^2} \tag{2.5}$$

where

$$c=\sqrt{\frac{G}{\rho}} \tag{2.6}$$

The term c is the wave speed and has dimensions of linear velocity, units of length per units of time (Rao, 2007).

The solution of Equation 2.5 can be obtained through separation of variables. This assumes the solution takes the form of the product of two separate functions, one a function of only x and the other depending only on t (Inman, 2014):

$$\theta(x,t)=X(x)T(t) \tag{2.7}$$

Substitution into Equation 2.5 gives:

$$c^2X''(x)T(t)=\ddot{T}(t) \tag{2.8}$$

where the primes on $X''(x)$ denotes the second derivative with respect to x and the overdots on $\ddot{T}(t)$ represents the second derivative with respect to t. Rearranging Equation 2.8, and noting that each side of the equation must be constant, gives:

$$\frac{X''(x)}{X(x)}=\frac{\ddot{T}(t)}{c^2T(t)}=-\sigma^2 \tag{2.9}$$

Stellenbosch University https://scholar.sun.ac.za

with σ some constant value.

This leads to two separate equations for x and t, Equations 2.10 and 2.11 respectively.

$$X''(x) + \sigma^2 X(x) = 0 \tag{2.10}$$

$$\ddot{T}(t) + c^2\sigma^2 T(t) = 0 \tag{2.11}$$

From Inman (2014) σ is shown to be equal to ω/c, where ω is the natural frequency.

$$X''(x) + \left(\frac{\omega}{c}\right)^2 X(x) = 0 \tag{2.12}$$

$$\ddot{T}(t) + \omega^2 T(t) = 0 \tag{2.13}$$

Since there are infinite natural frequencies for a continuous system there are also infinite solutions to Equations 2.12 and 2.13, one for each value of ω (Rao, 2007):

$$X_n(x) = A_n \cos\left(\frac{\omega_n x}{c}\right) + B_n \sin\left(\frac{\omega_n x}{c}\right) \tag{2.14}$$

$$T_n(t) = C_n \cos(\omega_n t) + D_n \sin(\omega_n t) \tag{2.15}$$

where Equation 2.14 is the spatial solution representing the mode shape corresponding to ω_n, Equation 2.15 is the temporal solution, and A_n, B_n, C_n, and D_n are constants. A_n and B_n are solved using the boundary conditions, while C_n and D_n are solved using the initial conditions.

In the case of a ship propulsion shaft, the boundary conditions would be free on either end to allow the shaft to rotate around its axis. Since the internal torque $M_t(x,t)$ at a free end is zero (Rao, 2007), from Equation 2.2 the boundary conditions are given by:

$$\frac{\partial\theta(0,t)}{\partial x} = \frac{dX(0)}{dx} = 0 \tag{2.16}$$

$$\frac{\partial\theta(l,t)}{\partial x} = \frac{dX(l)}{dx} = 0 \tag{2.17}$$

Substitution of Equation 2.16 into Equation 2.14 gives:

Stellenbosch University https://scholar.sun.ac.za

$$\frac{dX(0)}{dx} = -\frac{A_n \omega_n}{c} \sin\left(\frac{\omega_n x}{c}\right) + \frac{B_n \omega_n}{c} \cos\left(\frac{\omega_n x}{c}\right) = 0 \tag{2.18}$$

Since $\sin(0) = 0$ it follows that

$$B_n = 0 \tag{2.19}$$

Meaning that the nth spatial solution, or mode shape, becomes

$$X_n(x) = A_n \cos\left(\frac{\omega_n x}{c}\right) \tag{2.20}$$

Substitution of Equations 2.17 and 2.19 into Equation 2.14 gives:

$$\frac{dX(l)}{dx} = -\frac{A\omega_n}{c} \sin\left(\frac{\omega_n l}{c}\right) = 0 \tag{2.21}$$

Since $\sin(n\pi) = 0$ it follows that:

$$\omega_n = \frac{n\pi c}{l} \tag{2.22}$$

Substituting Equation 2.22 into Equation 2.20 the nth spatial solution, or mode shape, becomes:

$$X_n(x) = A_n \cos\left(\frac{n\pi x}{l}\right) \tag{2.23}$$

The general solution of the free vibration case is the summation of the products of the spatial and temporal solutions:

$$\theta(x,t) = \sum_{n=1}^{\infty} X(x)T(t) = \sum_{n=1}^{\infty} \cos\left(\frac{n\pi x}{l}\right) \left(C_n \cos(\omega_n t) + D_n \sin(\omega_n t)\right) \tag{2.24}$$

where the constants A_n have been absorbed into the constants C_n and D_n.

The solution can be estimated by using a finite number of mode shapes in Equation 2.24. This is referred to as modal superposition (see Appendix A for more information).

Stellenbosch University https://scholar.sun.ac.za

2.3 Polar class vessel rules

There are a number of classification rules that have been developed for polar class vessels intended for Arctic navigation. Rules have been set by various organisations such as the International Association of Classification Societies (IACS) (International Association of Classification Societies, 2016) and classification societies which include the Korean Register (Korean Register, 2015), the American Bureau of Shipping (American Bureau of Shipping, 2006), Det Norske Veritas (DNV) (Det Norske Veritas, 2016), Lloyd's Register (Germanishcer Lloyd, 2007) and Finnish-Swedish Ice Class Rules' Guidelines (Finnish Maritime Administration and Swedish Maritime Administration, 2006)..

The SAA II has been classified according to the DNV Ice Class Rules, which define requirements for many types of vessels which are intended for navigation in ice. Different ratings exist for differing levels of ice that the vessel is expected to experience.

These classifications contain rules and methods for the design of polar class vessels, including the design of their propulsion systems.

2.4 Operational loads for ice-faring propulsion systems

During vessel operation in ice, the propeller is exposed to varying loads. These loads can be classified as either non-contact or contact loads (Barro and Lee, 2011).

Non-contact loads refer to the hydrodynamic loading of the water on the blade. This load is due to the water resistance and will result in a constant torque. The load is dependent on the velocity (viscous damping due to interaction with water) and acceleration (added inertia from the mass of entrained water) of the propeller. These influences are referred to as the hydrodynamic damping and hydrodynamic mass respectively (Bertram, 2012).

Schwanecke (1963) developed an unsteady lifting-line method for determining the hydrodynamic damping and mass matrices for a propeller. The method considers the propeller as a rigid body with six degrees of freedom, three translational and three rotational, and the damping and mass are approximated as functions of the water and propeller properties. The method is described in detail by Bertram (2012).

Contact loads refer to ice impacts and milling. Barro and Lee (2011) define milling as a process in which ice becomes trapped between the hull and the blade. Milling can also be used to refer to the interaction of the propeller blades with generally large pieces of ice. The ice is crushed or milled by the propellers and this generates high loads, with the ice causing successive impacts as the multiple propeller blades make contact. The smaller pieces of ice result in ice

Stellenbosch University https://scholar.sun.ac.za

impacts which are reported to cause more moderate loads (Barro and Lee, 2011).

Figure 2.4, adapted from Ikonen *et al.* (2014), depicts an example of a torsional vibration measured on the shaft-line of a vessel during propeller-ice interaction. The hydrodynamic loading can clearly be seen as the mean of the vibration response, represented by the red dashed line. Numbers 1 and 2 on the figure indicate ice impacts, as can be seen by the increase in torque on the shaft. The area on the figure marked by number 3 shows an exponential decay in the vibration due to the viscous damping supplied by the water.

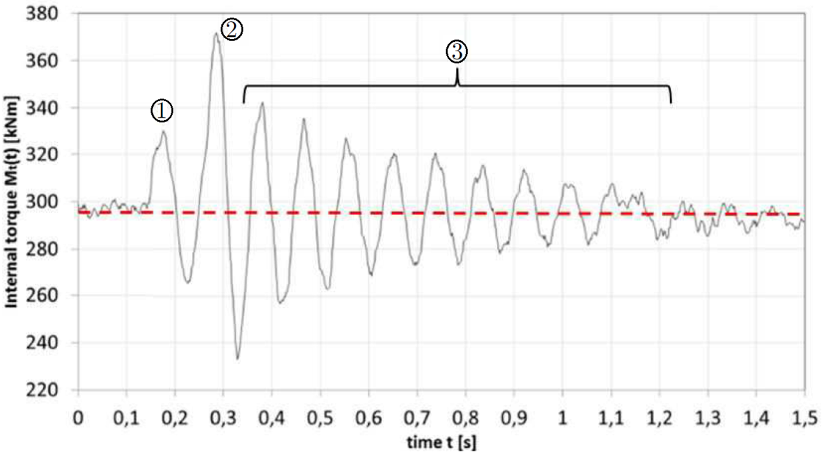

Figure 2.4: Example of a shaft-line torsional vibration due to ice impacts. Adapted from Ikonen *et al.* (2014)

Another form of loading that could be experienced by the propeller is attributed to cavitation (Casciani-Wood, 2015). This happens when the flow pattern of water over the blades degenerates, and causes vapour bubbles within the flow. The degeneration of the flow pattern depends on a complex relationship between the propeller type, the flow in which it works and its mean depth relative to its diameter (Casciani-Wood, 2015). Once the flow breaks down it leads to severe loss of thrust and possible damage to the propeller blades. Cavitation can be compared to boiling with the former taking place at constant ambient temperature and the latter at constant ambient pressure (Casciani-Wood, 2015). The collapsing of vapour bubbles not only has the potential to cause damage to the propeller blades, but also to impart vibrations to the shaft-line system.

Walker (1996) has shown that cavitation does not occur solely in open water, but for vessel passage in ice as well. According to Walker (1996), stable sheet and vortex cavitation occur when the propeller blade passes behind a piece of ice, with cloud cavitation forming as the wake of the ice flow develops.

Stellenbosch University https://scholar.sun.ac.za

2.5 Full-scale measurements

Ideally, the loads on the propeller blades could be determined through direct measurements made on the blades (Ikonen *et al.*, 2014). This has been demonstrated in research conducted by Dashnaw and Reed (1971) and Brewer (1972), where a full fixed pitch propeller assembly was removed, instrumented, and reinstalled onto the SS Michigan. Strain gauges were fixed to one of the blades and the wiring was carefully insulated and passed through a specially machined hollow tail shaft through a waterproof bulkhead.

Full-scale direct measurements of ice-induced propeller loads have also successfully been conducted, and documented in literature. Jussila and Koskinen (1989*a*,*b*) measured normal and shear stresses on a single propeller blade of an ice going ferry, such that bending moments and torque could be determined. Williams and Spencer (1992) conducted full-scale direct measurements of propeller loads and ice conditions for a Canadian R-class icebreaker.

However, under the harsh operating conditions experience in icy waters, this is not always feasible as the sensors will likely be damaged (Al-Bedoor *et al.*, 2006). Studies such as those conducted by Kaufman and Kershisnik (1984), Scalzo *et al.* (1986), Fan *et al.* (1994), and Srinivasan and Cuts (1995) have demonstrated the practical limitations with regards to sensor survival under such harsh operating conditions. Installation of such sensors can also be difficult and expensive as this requires cables to be installed through the shaft-line to the propeller blades (Ikonen *et al.*, 2014).

Full-scale measurements can therefore be conducted through sensors applied to the shaft-line at points between the propeller and the engine. The torque and thrust loads experienced by the shaft-line of the propulsion system is then used to determine the propeller loading through an inverse problem.

Full-scale measurements have been conducted on board the SAA II (Bekker *et al.*, 2019), in which measurements of the propulsion shaft torque and thrust were made. Case studies of the propulsion shaft torque and thrust loads for use with inverse models are provided by De Waal *et al.* (2018*a*).

One of the major challenges of determining propeller ice-related loading based on shaft measurements, is that these measurements also include the dynamic response of the propulsion system components (Ikonen *et al.*, 2014). Thus the models and estimation methods, that are used to obtain the loading conditions, need to be able to take the dynamic responses of the propulsion system into account.

2.6 Propeller moment estimation with inverse models

As mentioned in Section 2.5, it is challenging and expensive to directly measure loading on the propeller blades. The loading condition at the propeller

Stellenbosch University https://scholar.sun.ac.za

therefore needs to be estimated from measurements made on the shaft-line. This is referred to as the indirect force estimation approach (Jacquelin *et al.*, 2003). The models used to transform these shaft measurements to propeller loads are referred to as inverse models.

Inverse models have been investigated in the literature from both a frequency perspective, such as the study conducted by Doyle (1987), and a time perspective as done by Ikonen *et al.* (2014). According to Batrak *et al.* (2014), impact loading of the propulsion system with transient torsional vibrations, such as those experienced during vessel operation in ice, require the time domain approach. The frequency domain approach is better suited for vessel operation in open water.

The earliest inverse model that was found in literature was by Browne *et al.* (1998). The model estimated the propeller loads by inverting the shaft measurements using a deconvolution technique. Impulse response functions were determined from shaft responses, with a knowledge of the propulsion system masses, inertias, stiffnesses, and damping.

2.6.1 Discrete models

Discrete models of structures often make use of lumped masses or inertias, connected with springs or dampers. Thus, various components of a system are represented as lumped masses, when dealing with translational vibration, or mass moments of inertia, when dealing with torsional vibration. In the case of a vessel propulsion system, the various components are modelled as mass moments of inertia while the connecting shafts are modelled as torsional springs. These discrete models then result in a system of equations of motion that can be solved to determine the dynamic response of the shaft-line:

$$\mathbf{J}\ddot{\theta}(t) + \mathbf{C}\dot{\theta}(t) + \mathbf{K}\theta(t) = \mathbf{Q}_{ice}(t) \tag{2.25}$$

These models can then be used to determine transfer functions between the different components of a system. He and Du (2010), Tang and Brennan (2013), Ikonen *et al.* (2014), Batrak *et al.* (2014), Persson (2015) and De Waal *et al.* (2018*b*) have used lumped mass models to approximate the structural transmissibility of the shaft-lines of vessels, with Ikonen *et al.* (2014), Batrak *et al.* (2014), Persson (2015), and De Waal *et al.* (2018*b*) looking specifically at ice faring propulsion systems. Of these, Ikonen *et al.* (2014) and De Waal *et al.* (2018*b*) investigated the inverse determination of ice induced propeller moments with a lumped mass model. The model used by Tang and Brennan (2013) is shown in Figure 2.5, where it can be seen how the complicated shaft-line arrangement can be represented by a simpler lumped model.

The lumped mass model by Rolls-Royce AB (2010*a*), and adapted and used by Ikonen *et al.* (2014) and De Waal *et al.* (2018*b*), for the propulsion system

Stellenbosch University https://scholar.sun.ac.za

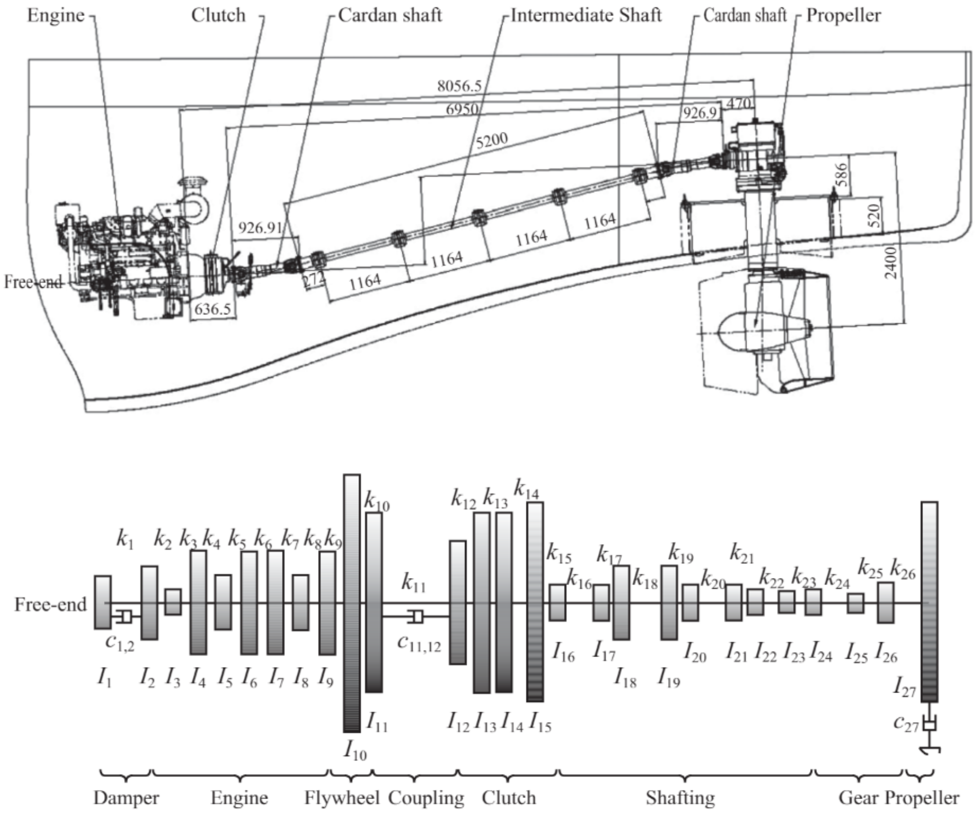

Figure 2.5: Discrete lumped model for a shaft-line (adapted from Tang and Brennan (2013))

of the SAA II is provided in Figure 2.6. The ice induced moment (Q_{ice}) can be seen on the left followed by the propeller inertia (J_1), the mid-propeller shaft (J_3), the sleeve coupling (J_5), the flange at the oil distribution box (J_7), the thrust shaft collar (J_9), the motor flange (J_{11}), and the electric motor (J_{13}). The damping due to the water is denoted c_1 while the remaining elements represent the stiffness and damping of the shaft-line.

The inverse solution of these models relies on the discrete sampling of the convolution integral (Equation 2.26) resulting in a system of linear equations (Equation 2.27) (Jacquelin *et al.*, 2003).

$$Q_{shaft}(t) = \int_0^t H(t-\tau)Q_{ice}(\tau)d\tau \tag{2.26}$$

$$\mathbf{Q}_{shaft}(t) = \mathbf{H}(t)\mathbf{Q}_{ice}(t) \tag{2.27}$$

where H is the impulse response function, Q_{shaft} is the simulated or measured shaft torque, and Q_{ice} the ice-induced propeller moment.

Stellenbosch University https://scholar.sun.ac.za

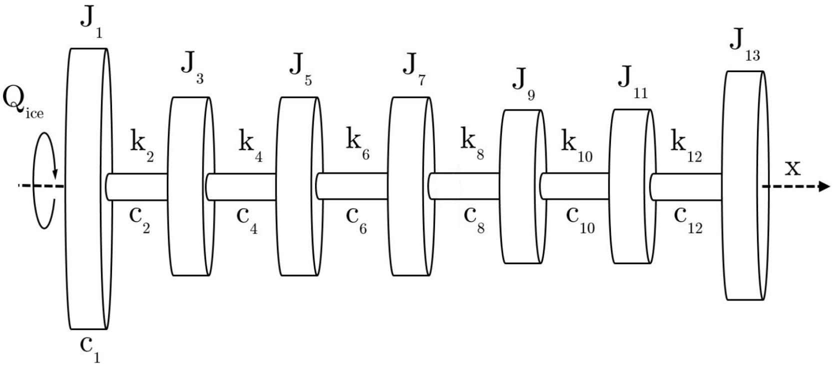

Figure 2.6: Simplified lumped mass model for the SA Agulhas II propulsion system. Adapted from De Waal (2017)

The inverse solution is then performed as:

$$\mathbf{Q}_{ice}(t) = \mathbf{H}^{-1}(t)\mathbf{Q}_{shaft}(t) \tag{2.28}$$

In both cases, Ikonen *et al.* (2014) and De Waal *et al.* (2018*b*) assumed that motor torque and the hydrodynamic load on the propeller were constant during an ice impact. As such, the impulse response function used in these models only represents the transmissibility between the propeller moment and the measured torque.

This assumption may not hold during ice-impacts, as the loading would cause a reduction in the rotational speed of the shaft. When the speed drops so will the hydrodynamic load as it depends partially on the angular velocity of the propeller. In addition, the motor torque would increase in response to the lost speed based on its control system.

The models made use of full-scale measured data from the shaft-line of the SAA II polar supply and research vessel (PSRV). Only a single measurement location was considered for the inverse estimations.

A common issue in the use of discrete models for indirect force estimation, is that the problem becomes ill-conditioned or ill-posed (Golub *et al.*, 1999). This is due to the coefficient matrix in the problem having a number of singular values that are small or close to zero, thus leading to an underdetermined problem (Hansen, 2008).

For a linear system of equations:

$$\mathbf{A}\mathbf{x} = \mathbf{b} \tag{2.29}$$

the problem can be said to be ill-posed if (Hansen, 2008):

- the singular values of **A** slowly decay to zero.

Stellenbosch University https://scholar.sun.ac.za

- the condition number of **A**, that is the ratio between the largest and smallest singular values, is large.

Inverse solutions of these ill-posed problems are usually unreliable. This is due to the tendency for any errors, or noise, on **b** to be significantly amplified on the solution for **x** (Jacquelin *et al.*, 2003). As these discrete models are used with a measured response **b** on the shaft-line, it can be expected that there will be unknown measurement errors that will be amplified.

The ill-conditioning of these discrete problems mean that standard numerical linear algebra cannot be used to compute a meaningful approximate solution (Hansen, 2008). Instead, more complicated methods, referred to as regularization methods, are necessary.

The purpose of regularization is to provide further information to the essentially underdetermined problem, in order to make the problem stable and provide a single solution. The most popular approach is to require that the solution norm $\|\mathbf{x}\|_2$, or semi-norm $\|\mathbf{Lx}\|_2$, be minimized (Hansen, 2008). The regularization matrix **L** is usually the identity matrix or a $p \times n$ discrete approximation of the $(n-p)^{th}$ derivative operator (Hansen, 2008).

The original problem is then replaced with one where the solution is as a result of the balance between the minimization of both the solution and residual norms:

$$\min \|\mathbf{Lx}\|_2 \quad \text{subject to} \quad \min \|\mathbf{Ax} - \mathbf{b}\|_2 \tag{2.30}$$

The basis for this regularized solution is that, with small solution and residual norms, it approximates the exact solution fairly well (Hansen, 2008).

As an example, a common regularization method is the Tikhonov method, where the weighted sum of the residual and solution norms are minimized (Hansen, 2008)

$$\min \left(\|\mathbf{Ax} - \mathbf{b}\|_2^2 + \lambda \|\mathbf{Lx}\|_2^2 \right) \tag{2.31}$$

Here, λ is referred to as the regularisation parameter. It can be seen from Equation 2.31 that large λ results in a small solution norm at the expense of the residual norm, leading to over-regularization. Conversely, small λ results in a small residual norm at the expense of the solution norm, leading to under-regularization. For these methods it therefore becomes important to select the regularization parameter in such a way as to balance the minimization of both norms.

A number of methods for the selection of regularization parameters exist. These include the discrepancy principle (Morozov, 1984), the quasi-optimality criterion (Morozov, 1984), generalised cross validation (Wahba, 1990), and the L-curve criterion (Hansen and O'Leary, 1993).

Stellenbosch University https://scholar.sun.ac.za

Ikonen *et al.* (2014) made use of three regularization methods:

- truncated singular value decomposition,
- truncated generalized singular value decomposition,
- and Tikhonov regularization.

De Waal *et al.* (2018*b*) made use of the same methods, but made use of the compact versions of the decompositions. In both cases, Ikonen *et al.* (2014) and De Waal *et al.* (2018*b*) used an optimised regularization parameter for each method. The parameter was optimised according to a known linear moment impulse using the L-curve method.

A disadvantage of the inverse models discussed until now is that the additional information required by these regularization methods is often derived from arbitrarily assumed outputs (Polić *et al.*, 2019).

Furthermore, these regularizations can be computationally expensive.

2.6.2 Bond graph models

An inverse model based on the bond graph method was developed by Polić *et al.* (2014). The method graphically represents physical systems, showing the flow of energy between their various elements (Paynter, 1998).

As an example of a bond graph system, consider the simple spring-mass-damper system in Figure 2.7(a). The system can be represented using bond graph elements, Figure 2.7(b), with the energy flow described by the half-arrow bonds. The force acting on the system becomes a source of effort (Se), the mass is an inertial element (I), the spring is a compliance element (C), and the damping is a resistance element (R). The elements are joined at junctions which can either be 0-junctions (net flow (f) is zero, effort (e) is constant) or 1-junctions (net effort (e) is zero, flow (f) is constant). In the case of the spring-mass-damper system, a 1-junction is used which results in the net force, or effort, in the system being zero, thereby enforcing dynamic equilibrium.

Once the bond graph has been developed, a state space equation can be derived of the form:

$$\dot{\mathbf{x}}(t) = \mathbf{A}\mathbf{x}(t) + \mathbf{B}\mathbf{u}(t) \tag{2.32}$$

Each source of effort will supply an input that is collected into the $u(t)$ vector, while the state vector will contain the generalized momentums (p) for I elements and generalized displacements (q) for C elements. For the example system in Figure 2.7, the state variables are p_3 and q_4, and the equations of motion for the system are:

Stellenbosch University https://scholar.sun.ac.za

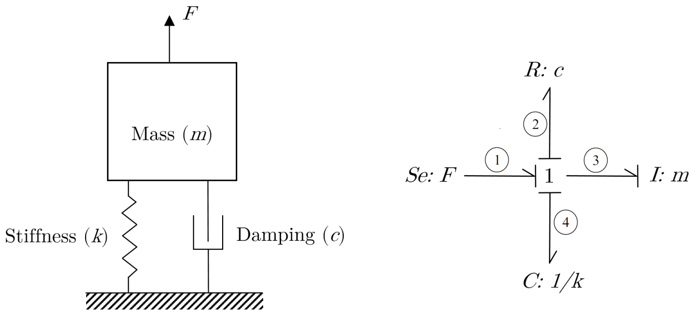

(a) System (b) Bond graph representation

Figure 2.7: Bond graph of a simple spring-mass-damper system

$$\dot{p}_3 = e_3 \tag{2.33}$$

$$\dot{q}_4 = f_4 \tag{2.34}$$

Using equations for bond graph elements from Mashadi and Crolla (2012), the equations for elements in this example are:

$$e_1 = F \tag{2.35}$$

$$e_2 = cf_2 \tag{2.36}$$

$$e_4 = kq_4 \tag{2.37}$$

$$f_2 = f_3 = f_4 = \frac{p_3}{m} \tag{2.38}$$

$$e_3 = e_1 - e_2 - e_4 = F - c\frac{p_3}{m} - kq_4 \tag{2.39}$$

Which gives the final forms of the equations of motion:

$$\dot{p}_3 = F - c\frac{p_3}{m} - kq_4 \tag{2.40}$$

$$\dot{q}_4 = \frac{p_3}{m} \tag{2.41}$$

And the state space equation:

$$\begin{Bmatrix} \dot{p}_3 \\ \dot{q}_4 \end{Bmatrix} = \begin{bmatrix} -\frac{c}{m} & -k \\ -\frac{1}{m} & 0 \end{bmatrix} \begin{Bmatrix} p_3 \\ q_4 \end{Bmatrix} + \begin{Bmatrix} 1 \\ 0 \end{Bmatrix} F(t) \tag{2.42}$$

Stellenbosch University https://scholar.sun.ac.za

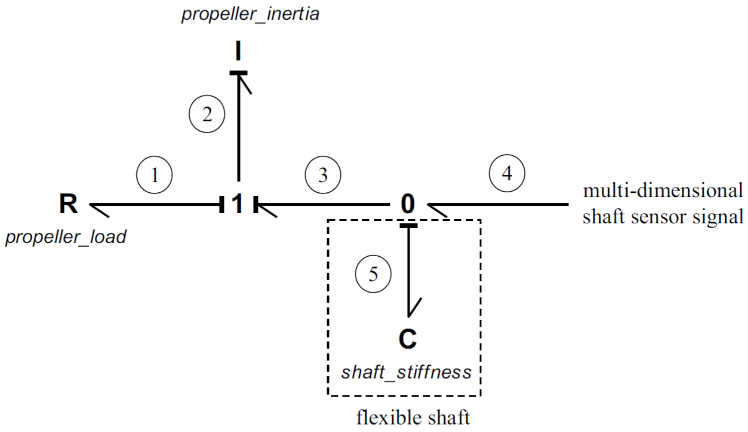

Figure 2.8: Bond graph inverse model (Polić *et al.*, 2014)

The inverse model by Polić *et al.* (2014) represents the propulsion shaft and propeller using the bond graph method as shown in Figure 2.8. In this model, the propeller parameters are connected to the 1-junction on the left and the shaft parameters to the 0-junction on the right. The shaft was considered to be either flexible or rigid. In the rigid case, the compliance element representing the shaft stiffness was removed.

A simulated shaft line measurement signal was provided as input, and the propeller load was determined based on the relationships between the bond graph elements.

It was found that further research was necessary to determine the relationship between the system properties (propeller loading, engine load, and shaft parameters) and the sampling frequency used in the model.

Further research into the modelling of the propulsion shaft, using the bond graph method, has been conducted by Polić *et al.* (2016). However, only the forward problem was considered and the bond-graph inverse model has not been developed further in the literature. It was recommended that a correlation between the propeller load and the shaft torque be determined, as a function of the propulsion system parameters. The correlation could then be used to develop an inverse model.

Further research into this correlation was conducted by Polić *et al.* (2017), in terms of the energy transfer in the propulsion shaft system. It was found that the differences between internal shaft torque and propeller loads were dependent on propeller kinetic energy (relating to the propeller inertia), followed by the kinetic energy stored in the rigid mode (relating to the inertia of the shaft), and the potential energy stored in the uneven flexible modes of the shaft (relating to the stiffness of the shaft). The energy in the even flexible modes were found to be negligible. This finding was dependent on the assumption of small frequency ratios, discussed in Section 2.6.3. The findings of Polić *et al.* (2017) lead to the development of the inverse model from Polić *et al.* (2019)

Stellenbosch University https://scholar.sun.ac.za

in Section 2.6.3

2.6.3 Continuous models

A continuous model of a structure can be created from a differential development of the equations of motion, as opposed to the discrete equations of motion used in the lumped models.

Senjanović *et al.* (2019) explored using a combination of discrete and continuous models for the analysis of shaft-line torsional vibrations. These models were only used for the solution of the forward problem, with known input propeller moments, instead of indirectly determining the propeller moments.

The only inverse model based on this concept that was found in literature has been developed by (Polić *et al.*, 2019). It simplifies the equations of motion into a solvable system of equations that do not require regularization. This is done by representing the shaft as a combination, or superposition, of modes as opposed to a combination of lumps or elements. Here, the equation of motion:

$$\mathbf{J}\ddot{\theta}(x,t) + \mathbf{C}\dot{\theta}(x,t) + \mathbf{K}\theta(x,t) = \mathbf{Q}_{prop}(t) + \mathbf{Q}_{motor}(t) \tag{2.43}$$

is developed into a system of differential equations (Equation 2.44) by using modal superposition (Equation 2.45):

$$\mathbf{J}\ddot{\mathbf{q}}(t) + \mathbf{C}\ddot{\mathbf{q}}(t) + \mathbf{K}\mathbf{q}(t) = \mathbf{Q}_{prop}(t) + \mathbf{Q}_{motor}(t) \tag{2.44}$$

$$\theta(x,t) = \sum_{n=0}^{N} \phi_n(x) q_n(t) \tag{2.45}$$

where $\phi_n(x)$ are the spatial mode shape functions and $q_n(t)$ the time based modal coordinates. Modal superposition is elaborated on in Appendix A.

In order to simplify the equations of motion, the contribution of the inertial terms ($J_n\ddot{q}_n$) were assumed to be negligible for flexible modes ($n > 0$). Since $J_n\ddot{q}_n \approx 0$ it follows that $\ddot{q}_n \approx 0$. This was based on the assumption of small frequency ratios, meaning that the transmissibility of force (TRF) is much smaller than the transmissibility of displacement (TRD) as shown in Figure 2.9. Here the frequencies of the external torque excitations (propeller and motor torques) are considered to be less than 20 % of the natural frequency of the shaft.

This simplification leads to two simultaneous equations, Equations 2.46 and 2.47, that can be solved to estimate the propeller moments. These equations require two measured inputs, the angular deformation or strain and the angular velocity.

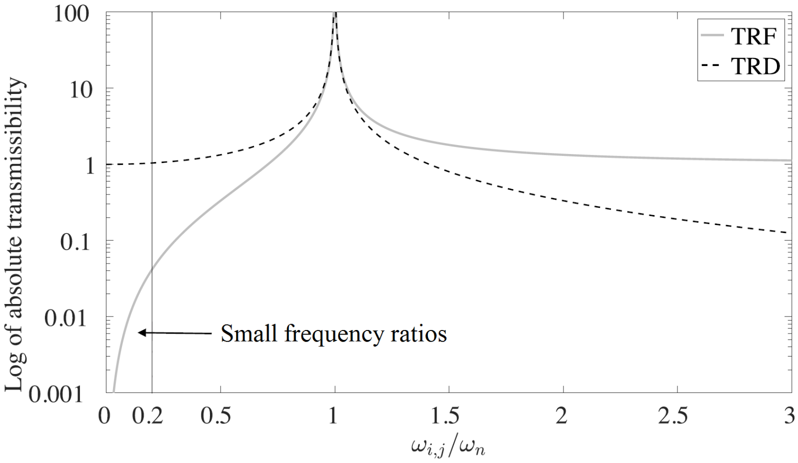

Figure 2.9: Comparison between TRF and TRD (Polić *et al.*, 2019)

$$\gamma_s(x_m,t) \approx -Q(0,t)\frac{D_{shaft}}{2}\sum_{n=1}^{N}\frac{\phi_n'(x_m)\phi_n(0)}{GJ\frac{(n\pi)^2}{2L}} + Q(L,t)\frac{D_{shaft}}{2}\sum_{n=1}^{N}\frac{\phi_n'(x_m)\phi_n(L)}{GJ\frac{(n\pi)^2}{2L}} \tag{2.46}$$

$$\frac{\partial\dot{\theta}(x_m,t)}{\partial t} \approx \phi_0(x_m)\left(\frac{-Q(0,t)\phi_0(0)+Q(L,t)\phi_0(L)}{\rho JL}\right) \tag{2.47}$$

where $Q(0,t)$ is the torque at $x = 0$ (the propeller end of the shaft), $\gamma_s(x_m,t)$ is the measured shaft angular deformation at $x = x_m$, and $\dot{\theta}(x_m,t)$ is the measured shaft angular velocity at $x = x_m$.

The torque at the propeller end of the shaft is then converted to the propeller moment by accounting for the mass moment of inertia for the propeller J_p:

$$Q_{prop}(t) = Q(0,t) - J_p\frac{\partial\dot{\theta}(x_m,t)}{\partial t} \tag{2.48}$$

The model used simulated measured data, with additional noise, from multiple locations in the inverse estimations. This data was simulated using a forward model based on the bond graph method (Polić *et al.*, 2016). It was found that the inverse model had limited success in the indirect calculation of the propeller load, when noise is present (Polić *et al.*, 2019). It was also found that increased accuracy could be achieved if both the measured torque and angular velocity were considered.

Stellenbosch University https://scholar.sun.ac.za

The simplification of $J_n\ddot{q}_n \approx 0$ for $n > 0$ assumes that the structure is excited far from resonance. In the case of an impulsive excitation, such as an ice-induced impact, a broad range of frequencies is excited (Inman, 2014) including any natural frequencies or resonances. At resonance, with the frequency ratio equal to 1, both the TRF and TRD would be at a maximum. Furthermore, if milling were to occur at a frequency close to a natural frequency, this assumption would not hold.

It should also be noted that continuous models based on modal superposition have been used in the numerical analysis of other structures. For example, in the analysis of railway vehicle and perway interaction, the rail is often modelled, using modal superposition, as a continuous beam while the remaining components are modelled using lumped masses (Zhai *et al.*, 2001; Sun and Dhanasekar, 2002). Though these models are not used for indirect force estimation, the techniques used to derive the continuous model are still relevant.

2.6.4 Summary

Based on the review of models for inverse propeller moment estimation, the following observations are made.

1. There is sparse literature available on inverse models for the estimation of propeller moments from indirect propulsion shaft measurements. Only four inverse models could be identified.
   a) The first (Browne *et al.*, 1998), made use of a deconvolution with the impulse response functions to estimate propeller loads from measured shaft responses.
   b) The discrete models from Ikonen *et al.* (2014) and De Waal (2017) similarly made use of the impulse response function, and derived a system of equations that can be solved with the help of regularization. These models are essentially the same, with slight differences in their inertial values and the implementation of the regularization.
   c) The third model was based on the bond graph method, and attempted to find the propeller loads by looking at the transfer of energy through the propulsion system. Further research into the inverse problem has been recommended.
   d) Finally, is the continuous model presented by Polić *et al.* (2019). This model used modal superposition to derive the equations of motion, and developed simplified equations for the propeller moment which could be solved directly.

Stellenbosch University https://scholar.sun.ac.za

2. The most recent contributions are the discrete model (De Waal *et al.*, 2018*b*) and the continuous model (Polić *et al.*, 2019). These are selected as the focus for further study.

3. For the discrete models presented by Ikonen *et al.* (2014) and De Waal *et al.* (2018*b*):

    a) only three regularization methods were considered. As the regularization can be computationally expensive, it may be worthwhile investigating and comparing additional regularization methods to find one that is the most efficient for this application.

    b) the methods were only tested against a small number of cases (three for Ikonen *et al.* (2014) and five for De Waal *et al.* (2018*b*)) and therefore does not provide much data for comparison.

    c) it is possible that the optimal regularization parameters that were determined may not be optimal for every case.

    d) the motor torque and hydrodynamic loading were both assumed to be constant. The influence of this assumption should be investigated, as these would likely not remain constant during ice-propeller interaction.

    e) the model only took measured input data from a single location. Comparing the results from multiple input locations could help to validate the model. This was also a recommendation from De Waal (2017).

4. For the continuous model presented by Polić *et al.* (2019):

    a) a key assumption of the model was that the modal inertias were negligible for flexible modes. This assumption would not hold for loading at a frequency close to resonance. A new model that accounts for the modal inertias could be developed to evaluate this assumption.

    b) Another model that achieves similar results would help validate and could be validated against Polić *et al.* (2019).

    c) the model has not been used with full-scale measured data.

    d) the model only considers the influence of the propeller inertia. This could be expanded to include the inertia of other components.

    e) it was shown that the inclusion of measured angular velocity as an input to the inverse model helped improve its accuracy.

5. There are no direct comparisons between the different inverse models.

Stellenbosch University https://scholar.sun.ac.za

Chapter 3

Full-scale measurements

Full-scale measurements were conducted on the SAA II PSRV shaft-line on multiple voyages. This was done in an effort to capture data to use for the indirect estimation of propeller loads.

The full measurement system consists of strain gauge bridges, accelerometers, and a tachometer installed on the port side shaft-line. Furthermore, navigation and machine control data were recorded by the Central Measurement Unit (CMU) installed aboard the ship. The measured parameters most important to this study were the shaft-line torque and angular velocity.

Section 3.1 describes the SAA II on which the full-scale measurements were conducted. Section 3.2 describes the voyages during which full-scale measurements were conducted. Section 3.3 describes the full-scale measurements that were conducted, with the propulsion shaft torque and angular velocity measurements covered by Sections 3.3.1 and 3.3.2 respectively.

3.1 Vessel, the S.A. Agulhas II

The SAA II, shown in Figure 3.1, was built by STX Finland in Rauma shipyard in 2012 (Ikonen *et al.*, 2014). Her hull was designed and strengthened according to DNV ICE-10 requirements and she was classified as Polar Ice Class PC-5 (Kujala *et al.*, 2014). According to the International Association of Classification Societies (2016), this rating allows the SAA II to conduct year-round operations in medium first year ice that may contain old ice inclusions. She is owned by the South African Department of Environment, Forestry, and Fisheries.

The SAA II is powered by four six-cylinder diesel engines, each generating 3 MW. These provide power to the propulsion system, as well as to the rest of the ship. The propulsion system consists of diesel-electric powertrains each with a 4.5 MW electric motor driving four-bladed controllable pitch propeller (CPP) (STX Finland Oy, 2012*b*). Table 3.1 provides specifications for the SAA II.

Stellenbosch University https://scholar.sun.ac.za

Figure 3.1: The S.A. Agulhas II

Table 3.1: Specifications for the S.A. Agulhas II (STX Finland Oy, 2012*b*; De Waal, 2017)

Gross tonnage	12 897 tons
Overall length	134.2 m
Length between perpendiculars	121.2 m
Breadth	22 m
Classification	DNV
Class notation	1A1 PC-5 / ICE-10
Built by	STX Finland
Location built	Rauma, Finland
Year built	2012
Diesel engine type	Wärtsilä 6L32
Electric motor type	Converteam N3 HXC 1120 LL8
MCR speed	140 rpm
MCR power	4.5 MW
MCR torque	307 kNm
Propeller manufacturer	Rolls-Royce
No. of propeller blades	4
Propeller diameter	4.3 m
Shaft characteristics	Direct drive
No. of motors / propellers	2 / 2

Stellenbosch University https://scholar.sun.ac.za

3.2 Voyages

The data used in this study come from two separate voyages:

- The 2018/19 Antarctic voyage, which took place from December 2018 to March 2019. This voyage included logistics operations for the SANAE IV Antarctic base as well as a research voyage into the Weddell Sea. Measurements taken aboard this voyage include the shaft-line torque at two separate locations, and recorded data from the CMU. Measurements from this voyage are used to validate and expand upon the lumped mass model used to estimate the propeller loading (Ikonen *et al.*, 2014; De Waal, 2017; De Waal *et al.*, 2018*b*).

- The 2019 SCALE Spring Cruise, which took place during October and November of 2019. This was a research voyage to the marginal ice zone. Measurements taken aboard this voyage include the shaft-line torque, shaft-line angular speed, and recorded data from the CMU. Measurements from this voyage were used in the development of the new method for estimating propeller loads, based on the use of a modal model. They are also used to compare the lumped mass and modal models.

3.3 Instrumentation and measurements

The measurement system on the SAA II shaft-line includes strain gauge bridges placed to record the thrust and torque, accelerometers placed at shaft-line bearings, and a tachometer and zebra tape for the measurement of shaft-line rotational speed. All measurements are conducted on the port side shaft-line. Only the data from the torque strain gauge bridges, the tachometer, and supporting data from the CMU are considered in this study. The measurement data for the voyages considered were saved every 5 minutes continuously over the course of the voyage.

For voyages prior to 2018, the torque on the shaft was measured at a single location (Q_1 in Figure 3.2). From the 2018-19 Annual Relief Voyage the shaft-line was instrumented with a second torque measurement location (Q_2 in Figure 3.2).

The tachometer was installed for the 2019 SCALE Spring Cruise and is also located at the measurement location Q_1.

Stellenbosch University https://scholar.sun.ac.za

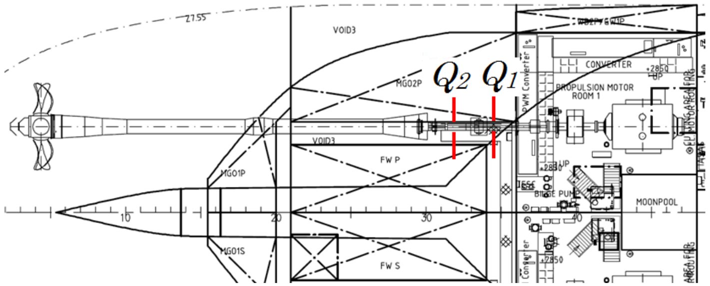

(a) Top down view of port side shaft-line on deck two (Adapted from STX Finland Oy (2012*a*))

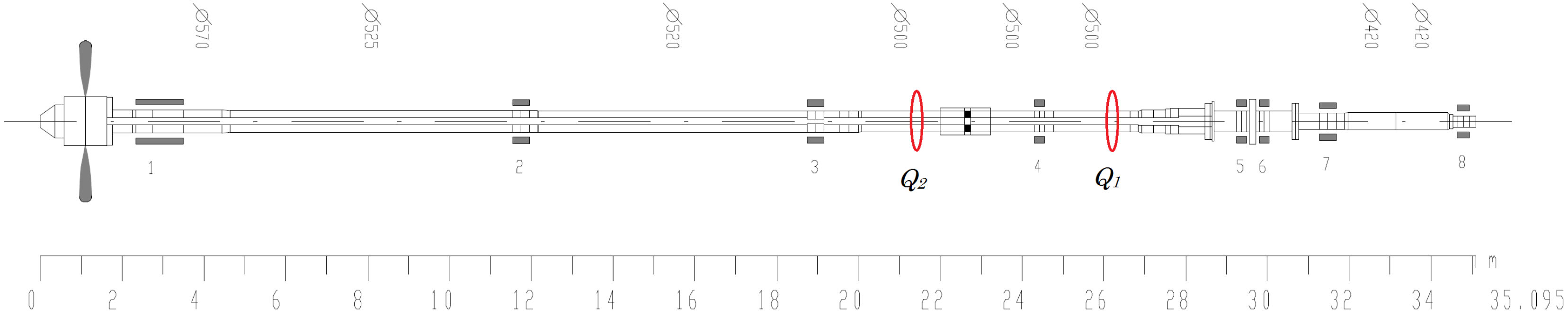

(b) Detail view of shaft-line (Adapted from Rolls-Royce AB (2010*c*))

Figure 3.2: Propulsion shaft measurement locations

Stellenbosch University https://scholar.sun.ac.za

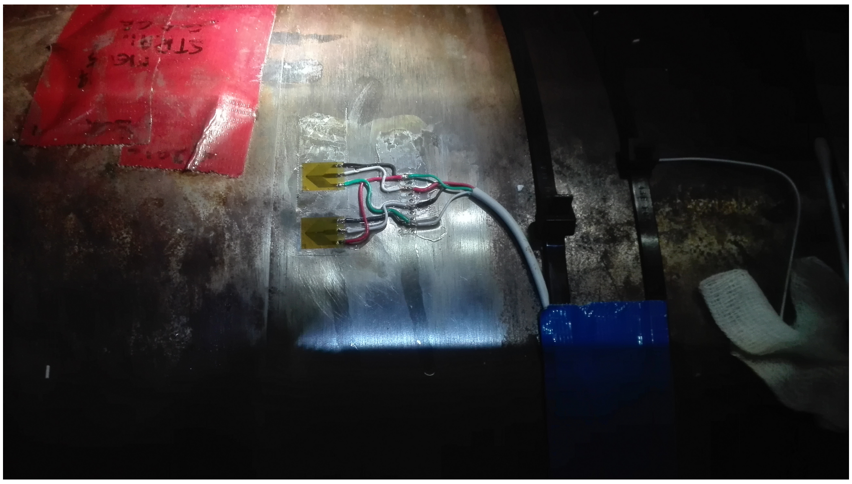

Figure 3.3: Strain gauge Wheatstone bridge at second measurement location

3.3.1 Torque measurements

The inverse models discussed in Chapter 2 require known responses from the vessel's propulsion line. As such, the shear strain on the propulsion shaft was measured and converted to an internal torque.

Strain gauges were installed on the port side shaft line to measure torque. At each measurement location, two 45° half-bridge T-rosettes were connected to form a full-bridge Wheatstone circuit. The strain gauges were arranged in a full-bridge circuit to reject axial and bending strain, and to compensate for strains caused by temperature variations. Figure 3.3 presents a photograph of the Wheatstone bridge installation for the second torque measurement point.

The diagram for a Wheatstone bridge is presented in Figure 3.4. From Hoffmann (2001), the equation describing a full-bridge Wheatstone circuit is

$$\frac{U_A}{U_E} = \frac{1}{4}\left(\frac{\Delta R_1}{R_1} - \frac{\Delta R_2}{R_2} + \frac{\Delta R_3}{R_3} - \frac{\Delta R_4}{R_4}\right) = \frac{k}{4}\left(\epsilon_1 - \epsilon_2 + \epsilon_3 - \epsilon_4\right) \tag{3.1}$$

When a torque is applied to the shaft, strain gauges two and four will measure strain equal in magnitude and opposite in direction to gauges one and three (Hoffmann, 2001). Equation 3.1 therefore becomes:

$$\frac{U_A}{U_E} = k\epsilon \tag{3.2}$$

The shear strain is obtained through the measured strain and the following equation (Hibbeler, 2011):

$$\frac{\gamma_{s,max}}{2} = \sqrt{\left(\frac{\epsilon_x - \epsilon_y}{2}\right)^2 + \left(\frac{\gamma_{xy}}{2}\right)^2} \tag{3.3}$$

Stellenbosch University https://scholar.sun.ac.za

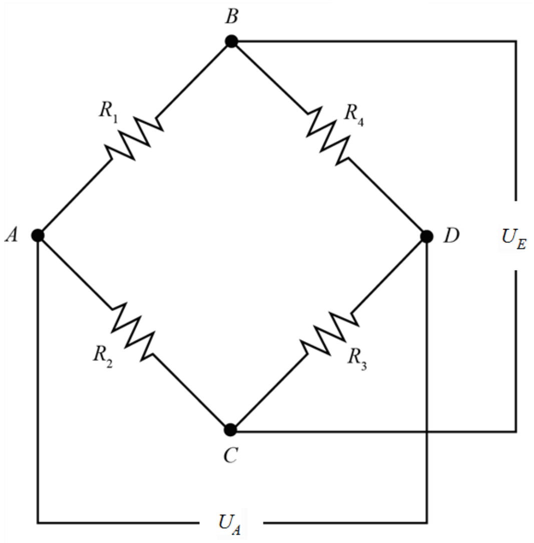

Figure 3.4: Wheatstone bridge circuit. Adapted from Figliola and Beasley (2011)

where ϵ_x and ϵ_y are the normal strains parallel and perpendicular to the shaft axis respectively, and γ_{xy} is the relative shear strain. Aligning the strain gauges at 45° to the shaft axis leads to a case of principal strain. This results in γ_{xy} being equal to zero and the normal strains are equal in magnitude and opposite direction. Thus, Equation 3.3 becomes:

$$\frac{\gamma_{s,max}}{2} = \epsilon \tag{3.4}$$

The shear strain can be related to the internal torque in the shaft-line using expressions provided by Hibbeler (2011).

$$\tau = G\gamma_s = \frac{Q_{shaft} d_o}{2S_p} \tag{3.5}$$

$$G = \frac{E}{2\,(1+\nu)} \tag{3.6}$$

$$S_p = \frac{\pi\,(d_o^4 - d_i^4)}{32} \tag{3.7}$$

Combining Equations 3.2 and 3.4 to 3.7 leads to an expression that can be used to relate the shaft-line torque directly to the measured strain. This expression is provided in Equation 3.8. Since this internal torque is directly related to the measurements on the shaft, it is henceforth referred to as measured torque.

Stellenbosch University https://scholar.sun.ac.za

$$Q_{shaft} = \epsilon \left(\frac{\pi E \left(d_o^4 - d_i^4 \right)}{16 d_o \left(1 + \nu \right)} \right) \tag{3.8}$$

The values for the parameters used in Equation 3.8 are provided in Table 3.2.

Table 3.2: Parameters used in torque calculations (Rolls-Royce AB, 2010*c*; STX Finland Oy, 2012*b*)

Parameter	Symbol	Value
Young's Modulus	E	210 GPa
Shear Modulus	G	81 GPa
Poisson's ratio	ν	0.29
Inner shaft diameter	d_i	0.175 m
Outer shaft diameter	d_o	0.5 m

The measurement is conducted through wireless sensor nodes that transmit the data to a nearby laptop for recording. The wireless system consists of V-Links (LORD MicroStrain sensing systems, 2016), attached to the shaft, that measure the voltage outputs from the strain gauge bridges. This measurement is then passed through an analogue-to-digital converter and transmitted wirelessly to a WSDA-Base station through Wi-Fi. The base station is controlled through the SensorConnect software, and sends data to an HBM QuantumX data acquisition unit for recording. The digital signal is converted to strain using calibration constants determined during the calibration of the strain gauge bridges through SensorConnect. The sample rate for the torque measurements was 600 Hz.

Ice impacts were identified from the measured data for indirect propeller moment estimations. An impact upon a structure results in a broadband frequency excitation (Inman, 2014). Thus the spectra of the measured torque were analysed to search for points in time where broadband frequency excitations were present. The internal torque corresponding to this broadband excitation could then be extracted for analysis. Figure 3.5(a) provides an example of a spectrum determined for the 30 October 2019 for an hour long extract of the measured torque at location Q_1. A number of ice impacts are visible, corresponding to the vertical lines on the spectrum representing broadband frequency excitations. The internal torque due to an ice impact at 20:06:23 is highlighted in Figure 3.5(a), and shown in Figure 3.5(b)

As is characteristic of measured signals, the torque measurements contained noise. Since the frequencies of interest in the torque signals are low, a low-pass filter could be applied to remove noise while keeping the signal intact.

However, there were instances of packet loss on the wireless measurements. This was due to the V-Link wireless nodes momentarily losing connection with

Stellenbosch University https://scholar.sun.ac.za

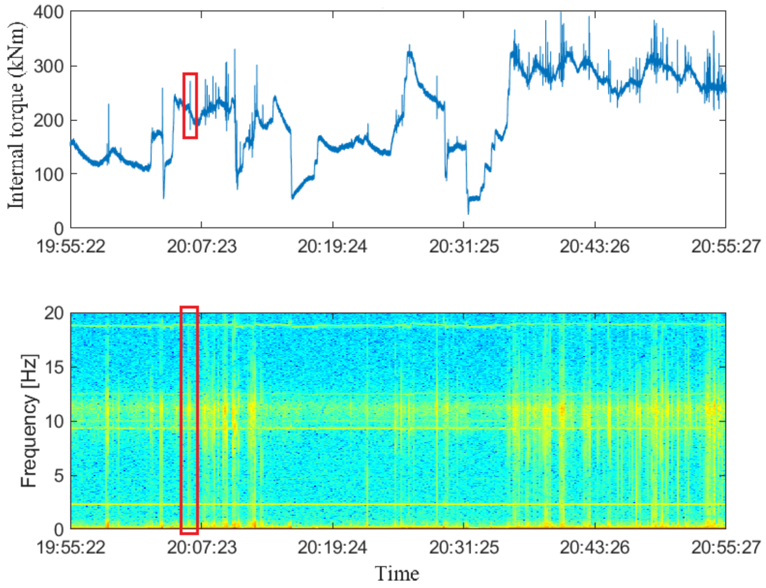

(a) Torque measurement and spectrum for 19:55:22 to 20:55:27 (UTC) on 30 October 2019

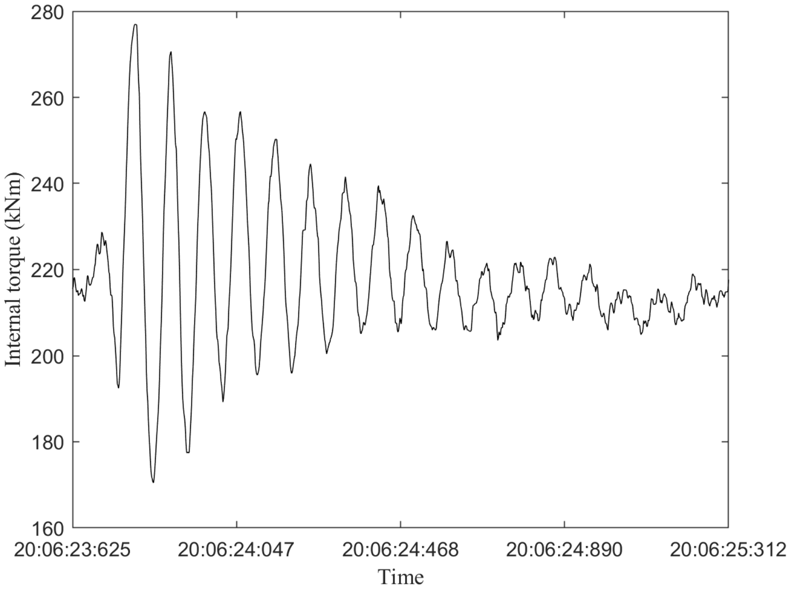

(b) Internal torque at 20:06:23 (UTC) on 30 October 2019 due to ice impact

Figure 3.5: Identification of propeller ice impacts

Stellenbosch University https://scholar.sun.ac.za

the WSDA-Base station. As a result, small discontinuities were introduced into the measured signal. Low pass filtering was not able to fully remove these errors.

Instead, a smoothing algorithm was employed to remove the noise and the discontinuities. The smoothing algorithm developed by Garcia (2010, 2020) was selected for its capability to efficiently and robustly smooth signals with missing values.

3.3.2 Angular velocity measurements

The rotational speed of the motor and propulsion shaft are recorded by the CMU on board the SAA II during voyages. However, these recordings are sampled at a low frequency (1 to 2 Hz) and are therefore not useful for any transient analysis of the shaft response.

Based on the recommendations of De Waal (2017) and the research by Polić *et al.* (2019), the measurement system was upgraded to include a higher frequency measurement of the rotational speed of the propulsion shaft. This could then be used along with the measured torque in the assessment and development of the inverse models.

Figure 3.6 shows the tachometer and zebra tape used to measure the rotational speed of the shaft-line. The tachometer works by emitting a laser that is reflected back by the reflective bars of the zebra tape. The tachometer then senses each time the light is reflected and emits a pulse, measured as a voltage signal that alternates between zero and five volts. The voltage pulses are recorded and saved using the same HBM QuantumX data acquisition unit that records the strain data. The pulses were sampled at 4800 Hz.

Each time a pulse is measured, a bar of the zebra tape has passed by the sensor. By knowing the circumference of the shaft and how many bars long the zebra tape is, the instantaneous angular speed (IAS) can be calculated as (Diamond *et al.*, 2016)

$$\dot{\theta} = \frac{d\theta}{dt} \approx \frac{\Delta\theta}{\Delta t} \tag{3.9}$$

where $\Delta\theta$ is the angular displacement and Δt is the time delay, both between subsequent zebra tape bars or pulses. For this study, the IAS of the shaft is calculated from the measured pulses using MATLAB's *tachorpm* function.

It is also important to note that the joint where the zebra tape ends meet causes errors on the calculated IAS. This is due to the joint not conforming in bar thickness with the rest of the tape. The calculated IAS at this section thus varies significantly, and can be seen as a large drop in the IAS. This can be seen in Figure 3.7, showing an extract of the measured IAS corresponding to the ice impact shown in Figure 3.5(b). This was corrected for by using the robust version of the smoothing function developed by Garcia (2010, 2020), which

Stellenbosch University https://scholar.sun.ac.za

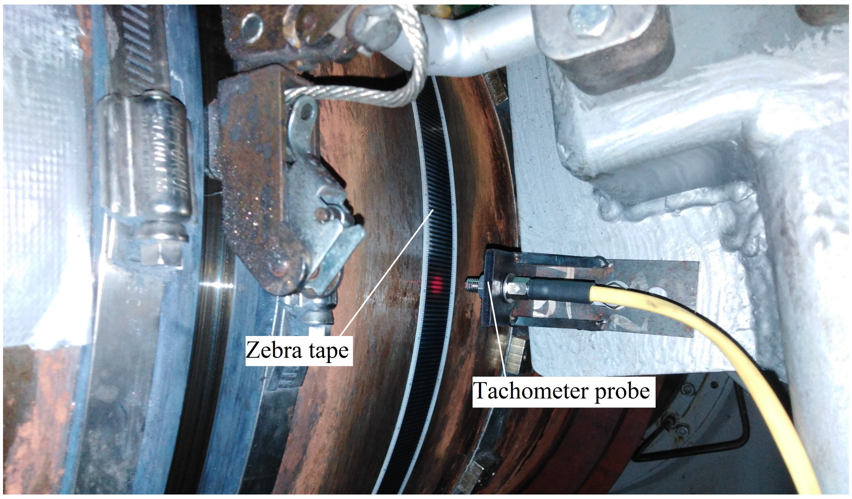

Figure 3.6: Tachometer and zebra tape

removes these outliers. This corrected measurement is shown in Figure 3.7. In addition, this smoothing was used to remove noise from the measured angular velocity.

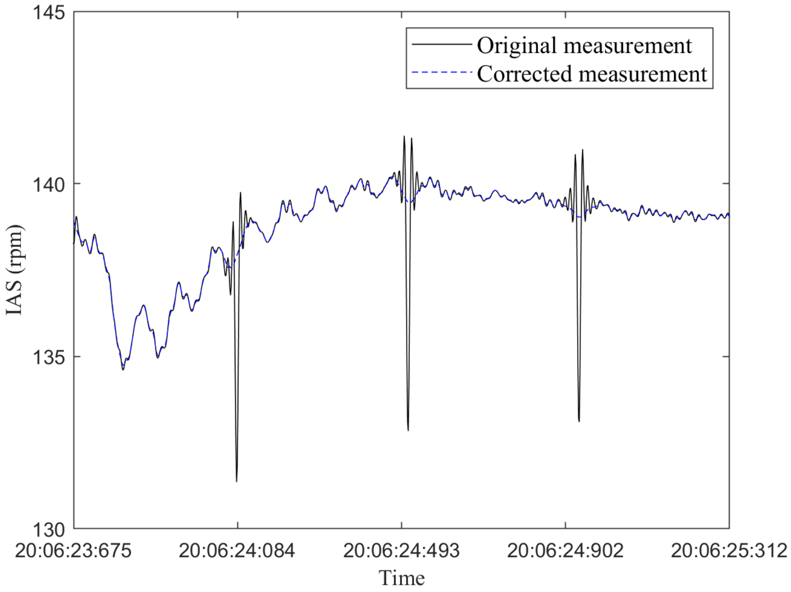

Figure 3.7: Extract of the shaft-line instantaneous angular speed for 30 October 2019 at 20:06:24 (UTC)

Stellenbosch University https://scholar.sun.ac.za

3.3.3 Dry-dock measurements

The SAA II was in dry dock in March of 2017. This was a scheduled maintenance event to be undertaken during the fifth year of the ship's operations. This allowed for the replacement of components not easily maintained while the ship was afloat, for example the anodes preventing the rusting of the hull. The hull was also sandblasted and repainted, and the propeller blades inspected and maintained.

During these operations, an effort was made to conduct vibration measurements on the port side shaft-line in order to perform a modal analysis of the system. The data acquisition software used was LMS Test.Lab from Siemens (Siemens PLM Software, 2014), and the hardware consisted of two LMS SCADAS Mobile data acquisition units connected in a master-slave configuration, thirteen ICP accelerometers (PCB Piezotronics, 2009) and one impedance sensor PCB Piezotronics (2017) from PCB Piezotronics, and a modal hammer (PCB Piezotronics, 2015) and sledgehammer to provide excitation to the system. A limitation of this test was that a modal sledgehammer was not available.

The shaft-line was instrumented with ICP accelerometers at three locations, each measuring the axial, perpendicular, and rotational vibrations. The first two measurement locations correspond with the strain gauge measurement locations. The last location is toward the stern of ship as close as possible to the point where the shaft line exits the stern. Figure 3.8 shows the instrumentation setup at measurement location Q_1, with similar setups used at Q_2 and the stern exit. A single propeller blade was also instrumented with four ICP accelerometers; at the blade root, at the centre of the blade, and one each on the leading and trailing edges respectively. An impedance sensor was installed on the blade tip, in an attempt to measure the input force from the hammer excitation in addition to acceleration. This installation is shown in Figure 3.9.

The tests were conducted by exciting the shaft-line system externally with a sledgehammer at various locations, including the blade tip, trailing edge, and propeller hub, in both axial and torsional directions to obtain vibration data. The vibration data could then be used to extract the frequency response of the shaft-line.

Due to the input excitation being too small to adequately excite the structure, it was not possible to perform modal analysis on the shaft line. It was, however, possible to extract the first two natural frequencies of the shaft-line. They are presented in Table 3.3 and compared to full-scale measurements conducted by Peltokorpi *et al.* (2014). The difference between the measurements is due to the different boundary conditions during dry-dock testing, when compared to operational measurements. The dry-dock testing took place on a stationary shaft, locked in place, with the propeller in air instead of water. Despite the differences, the frequencies are still close.

Stellenbosch University https://scholar.sun.ac.za

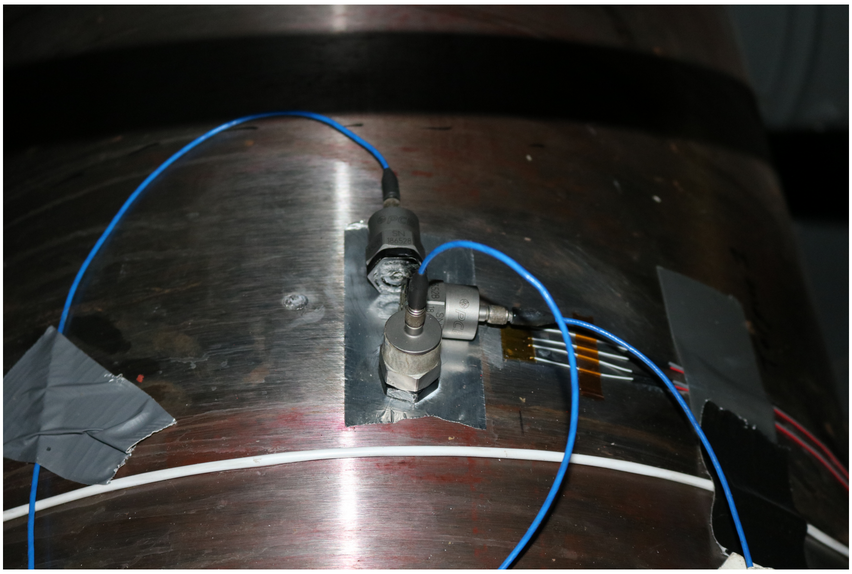

Figure 3.8: Accelerometers at first strain gauge location

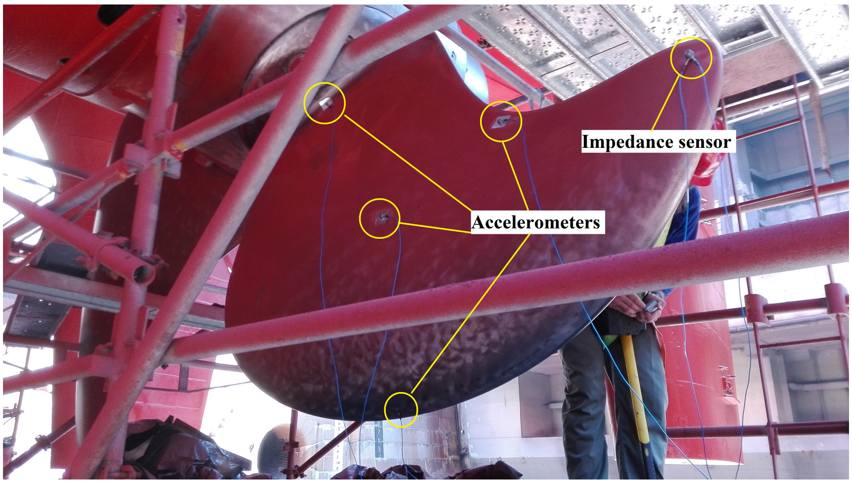

Figure 3.9: Accelerometers on blade

Table 3.3: Comparison of natural frequencies determined by Peltokorpi *et al.* (2014) and from dry-dock measurements

	Peltokorpi *et al.* (2014)	Dry-dock Measurements
f_1	11.2 Hz	10.1 Hz
f_2	46.3 Hz	49.6 Hz
Δf_1		9.82 %
Δf_2		7.13 %

Stellenbosch University https://scholar.sun.ac.za

Chapter 4

Propeller moment estimation using a discrete model of the propulsion shaft

A discrete lumped mass model was first used by Ikonen *et al.* (2014), and then by De Waal (2017); De Waal *et al.* (2018*b*) to estimate ice-induced propeller moments for the SAA II.

The lumped mass model is a discrete representation of the propulsion shaftline. Thus the angular displacement, velocity, and acceleration can only be computed for locations on the shaft that match the model discretization.

The propeller moment is estimated indirectly from the torque measurements taken on the propulsion shaft. This estimation is obtained by first subjecting the model to a forward problem to determine a transfer function from the propeller load to the propulsion shaft torque at the measurement point. This is then followed by an inverse problem using the propulsion shaft measurements as input.

For brevity, this model is henceforth referred to as the discrete model.

Section 4.1 provides the description and mathematical derivation of the discrete model.

The forward solution of the discrete model is covered in Section 4.2.

Section 4.3 describes the inverse solution of the discrete model, including explanations of the various regularization methods and the selections of regularization parameters.

Section 4.4 focuses on the evaluation of the discrete model. The different regularization methods are evaluated in Section 4.4.1 in terms of their robustness and efficiency. A comparison of the results between the inverse solutions from the two measurement locations on the propulsion shaft is provided in Section 4.4.2. Results from the inverse solution are compared to results provided by Rolls-Royce AB (2010*a*) in Section 4.4.3.

Finally, the limitations of the discrete model and a discussion of the results are provided in Sections 4.5 and 4.6 respectively.

Stellenbosch University https://scholar.sun.ac.za

Figure 4.1 provides a breakdown of the research presented in this chapter, and shows where the contributions to literature arise.

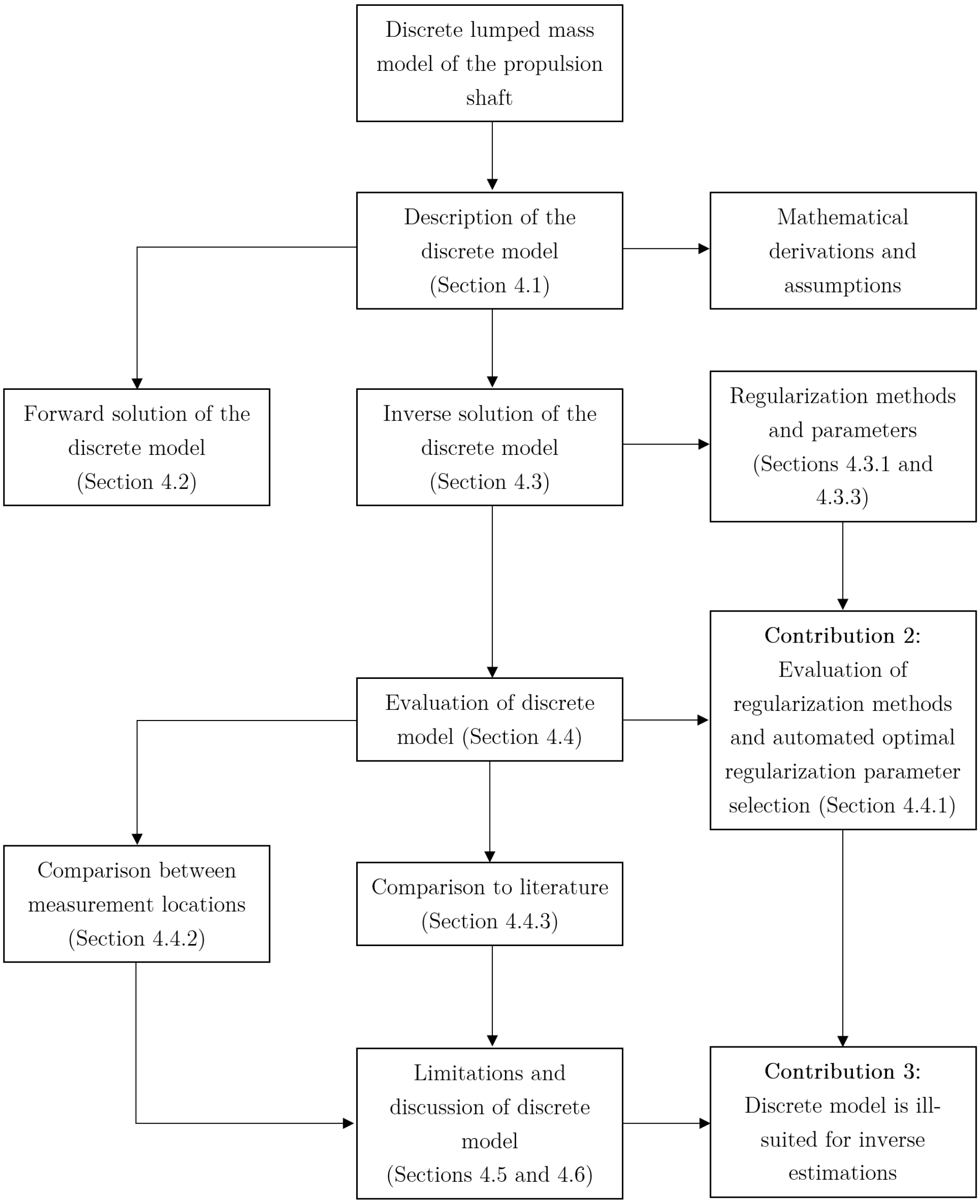

Figure 4.1: Breakdown for Chapter 4 research and contributions

Stellenbosch University https://scholar.sun.ac.za

4.1 Description of the discrete model

The discrete model used to model the SAA II shaft-line is based on a model by Rolls-Royce AB (2010*a*) for the forward solution of ice-impact simulations. The model and its associated algorithms were developed by De Waal (2017), based on the work done by Ikonen *et al.* (2014), and has been further developed during this study. The model is shown in Figure 4.2.

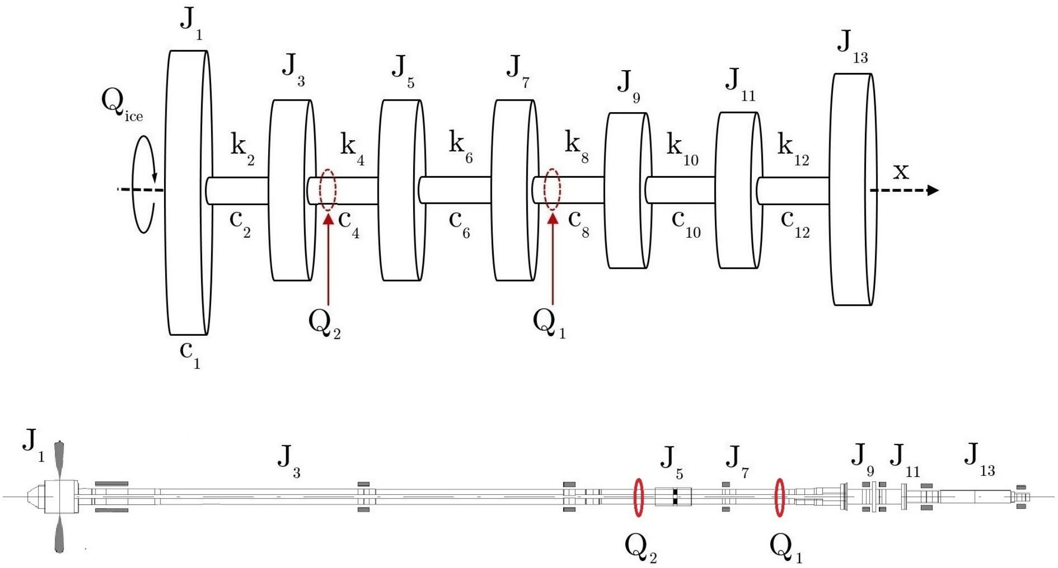

Figure 4.2: Discrete lumped mass model of the SAA II shaft-line (Adapted from De Waal (2017) and Rolls-Royce AB (2010*c*)). J_1 is the controllable pitch propeller, J_3 is the mid-propeller shaft, J_5 is the sleeve coupling, J_7 is the oil distribution box flange, J_9 is the thrust shaft collar, J_{11} is the electric motor flange, and J_{13} is the electric motor.

The model consists of thirteen elements, alternating between inertial and damping/stiffness elements, representing the various elements of the shaft-line assembly.

The damping c_1 represents the hydrodynamic damping on the propeller. The propeller inertia includes the hydrodynamic mass of the water it interacts with, and both the hydrodynamic mass and hydrodynamic damping were determined by Rolls-Royce AB (2010*b*) using the method developed by Schwanecke (1963). The values used for these parameters can be found in Table C.1 in Appendix C.

The model only considers rotational degrees of freedom about the shaft axis (x-axis in Figure 4.2). Each element has a node on either side as shown

Stellenbosch University https://scholar.sun.ac.za

in Figure 4.3. At each node, the internal torque and angular displacement are considered.

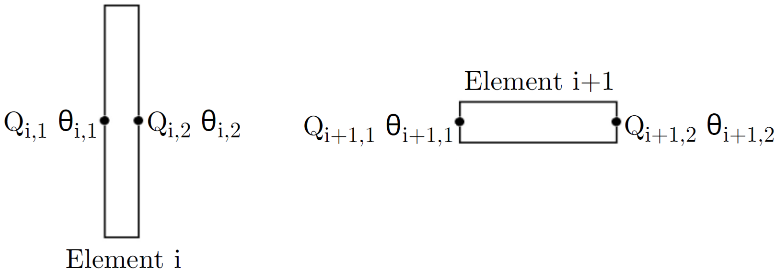

Figure 4.3: Lumped mass model elements (De Waal, 2017)

For the inertial elements, the angular displacement is constant across nodes ($\theta_{i,1} = \theta_{i,2}$). For the damping/stiffness elements, the internal torque is constant across nodes ($Q_{i,1} = Q_{i,2}$)

The equations for the torsional vibration of inertial elements (odd values of i) and damping/stiffness elements (even values of i) are provided in Equations 4.1 and 4.2 respectively (De Waal, 2017).

$$J_i\ddot{\theta}_{i,1} + c_i\dot{\theta}_{i,1} = -Q_{i,1} + Q_{i,2} + Q_{ice} \tag{4.1}$$

$$c_i\left(\dot{\theta}_{i,2} - \dot{\theta}_{i,1}\right) + k_i\left(\theta_{i,2} - \theta_{i,1}\right) = Q_{i,1} \tag{4.2}$$

Note that the Q_{ice} term in Equation 4.1 only applies to the propeller element, that is when $i = 1$. For all other inertial elements, $Q_{ice} = 0$.

The Newmark-β numerical time integration scheme (Appendix B.1) is employed to solve the dynamic system. This is done by combining incremental forms of the Newmark-β equations for the angular velocity and acceleration (Equations 4.3 and 4.4), with incremental forms of the equations for torsional vibration (Ikonen *et al.*, 2014). Here n is a counter representing the current time step.

$$\Delta\dot{\theta}_n = \dot{\theta}_{n+1} - \dot{\theta}_n = \frac{\gamma}{\beta\Delta t}\Delta\theta_n - \frac{\gamma}{\beta}\dot{\theta}_n - \left(\frac{\gamma}{2\beta} - 1\right)\ddot{\theta}_n\Delta t \tag{4.3}$$

$$\Delta\ddot{\theta}_n = \ddot{\theta}_{n+1} - \ddot{\theta}_n = \frac{1}{\beta\Delta t^2}\Delta\theta_n - \frac{1}{\beta\Delta t}\dot{\theta}_n - \frac{1}{2\beta}\ddot{\theta}_n \tag{4.4}$$

Rewriting the torsional vibration Equations 4.1 and 4.2 in incremental form and substituting in Equations 4.3 and 4.4 gives the following equations (Ikonen *et al.*, 2014):

Stellenbosch University https://scholar.sun.ac.za

$$\Delta Q_{i,1}(t) + A_i \Delta\theta_{i,1}(t) - \Delta Q_{i,2}(t) = B_i \tag{4.5}$$

$$\Delta Q_{i,1}(t) + A_i \Delta\theta_{i,1}(t) - A_i \Delta\theta_{i,2}(t) = B_i \tag{4.6}$$

where the variables A_i and B_i are described by Equations 4.7 and 4.8 for inertial elements (odd values of i), and Equations 4.9 and 4.10 damping/stiffness elements (even values of i).

$$A_i = \frac{J_i}{\beta \Delta t^2} + \frac{c_i \gamma}{\beta \Delta t} \tag{4.7}$$

$$\begin{aligned} B_i = J_i \left(\frac{1}{\beta \Delta t} \dot{\theta}_i(t) + \frac{1}{2\beta} \ddot{\theta}_i(t) \right) \\ + c_i \left(\frac{\gamma}{\beta} \dot{\theta}_i(t) + \left(\frac{\gamma}{2\beta} - 1 \right) \ddot{\theta}_i(t) \Delta t \right) + \Delta Q_{ice}(t) \end{aligned} \tag{4.8}$$

$$A_i = k_i + \frac{c_i \gamma}{\beta \Delta t} \tag{4.9}$$

$$\begin{aligned} B_i = c_i \left(\frac{\gamma}{\beta} \left(\dot{\theta}_i(t - \Delta t) - \dot{\theta}_i(t) \right) \right. \\ \left. + \left(\frac{\gamma}{2\beta} - 1 \right) \Delta t \left(\ddot{\theta}_i(t - \Delta t) - \ddot{\theta}_i(t) \right) \right) \end{aligned} \tag{4.10}$$

Equations 4.7 and 4.8 are written in matrix form to facilitate the solution of multiple element systems. Equation 4.11 is the matrix equation for inertial elements, while Equation 4.12 is the matrix equation for damping/stiffness elements:

$$\begin{bmatrix} 1 & A_i & -1 & 0 \\ 0 & 1 & 0 & -1 \end{bmatrix} \begin{Bmatrix} \Delta Q_{i,1} \\ \Delta\theta_{i,1} \\ \Delta Q_{i,2} \\ \Delta\theta_{i,2} \end{Bmatrix} = \begin{Bmatrix} B_i \\ 0 \end{Bmatrix} \tag{4.11}$$

$$\begin{bmatrix} 1 & A_i & 0 & -A_i \\ 1 & 0 & -1 & 0 \end{bmatrix} \begin{Bmatrix} \Delta Q_{i,1} \\ \Delta\theta_{i,1} \\ \Delta Q_{i,2} \\ \Delta\theta_{i,2} \end{Bmatrix} = \begin{Bmatrix} B_i \\ 0 \end{Bmatrix} \tag{4.12}$$

Stellenbosch University https://scholar.sun.ac.za

where the second row in Equations 4.11 and 4.12 satisfy the conditions $\theta_{i,1} = \theta_{i,2}$ for inertial elements and $Q_{i,1} = Q_{i,2}$ for damping/stiffness elements respectively.

Equations 4.11 and 4.12 are combined for each element in the discrete model, to form a single equation for the system (De Waal, 2017):

$$\mathbf{W}\begin{Bmatrix} \Delta Q_1 \\ \Delta\theta_1 \\ \Delta Q_2 \\ \Delta\theta_2 \\ \vdots \\ \Delta Q_{13} \\ \Delta\theta_{13} \\ \Delta Q_{14} \\ \Delta\theta_{14} \end{Bmatrix} = \begin{Bmatrix} 0 \\ B_1 \\ 0 \\ B_2 \\ \vdots \\ 0 \\ B_{13} \\ 0 \\ 0 \end{Bmatrix} \tag{4.13}$$

In Equation 4.13, ΔQ_1 to ΔQ_{14} and $\Delta\theta_1$ to $\Delta\theta_{14}$ refer to the internal torques and angular displacements at the element interfaces. The matrix $\mathbf{W}$ is defined as:

$$\mathbf{W} = \left[\begin{array}{ccccccccccccc}
1 & 0 & 0 & 0 & 0 & 0 & \cdots & 0 & 0 & 0 & 0 & 0 & 0 \\ \hdashline
1 & A_1 & -1 & 0 & 0 & 0 & \cdots & 0 & 0 & 0 & 0 & 0 & 0 \\
0 & 1 & 0 & -1 & 0 & 0 & \cdots & 0 & 0 & 0 & 0 & 0 & 0 \\
0 & 0 & 1 & A_2 & 0 & -A_2 & \cdots & 0 & 0 & 0 & 0 & 0 & 0 \\
0 & 0 & 1 & 0 & -1 & 0 & \cdots & 0 & 0 & 0 & 0 & 0 & 0 \\
\vdots & \vdots & \vdots & \ddots & \ddots & \ddots & \ddots & \ddots & \ddots & \ddots & \vdots & \vdots & \vdots \\
0 & 0 & 0 & 0 & 0 & 0 & \cdots & 1 & A_{12} & 0 & -A_{12} & 0 & 0 \\
0 & 0 & 0 & 0 & 0 & 0 & \cdots & 1 & 0 & -1 & 0 & 0 & 0 \\
0 & 0 & 0 & 0 & 0 & 0 & \cdots & 0 & 0 & 1 & A_{13} & -1 & 0 \\
0 & 0 & 0 & 0 & 0 & 0 & \cdots & 0 & 0 & 0 & 1 & 0 & -1 \\ \hdashline
0 & 0 & 0 & 0 & 0 & 0 & \cdots & 0 & 0 & 0 & 0 & 1 & 0
\end{array}\right] \tag{4.14}$$

The first and last rows of matrix $\mathbf{W}$ enforce the boundary conditions of zero internal torque at the end points, while allowing for free rotation around the x-axis.

It should be noted that this derivation of the model only considers changes in the external ice-induced propeller moment, and assumes that the motor torque is constant.

4.2 Forward solution of the discrete model

During the forward solution of the model, the changes in internal torques (ΔQ_i) and angular displacements ($\Delta\theta_i$) for each time step are obtained by solving Equation 4.15, from Equation 4.13.

Stellenbosch University https://scholar.sun.ac.za

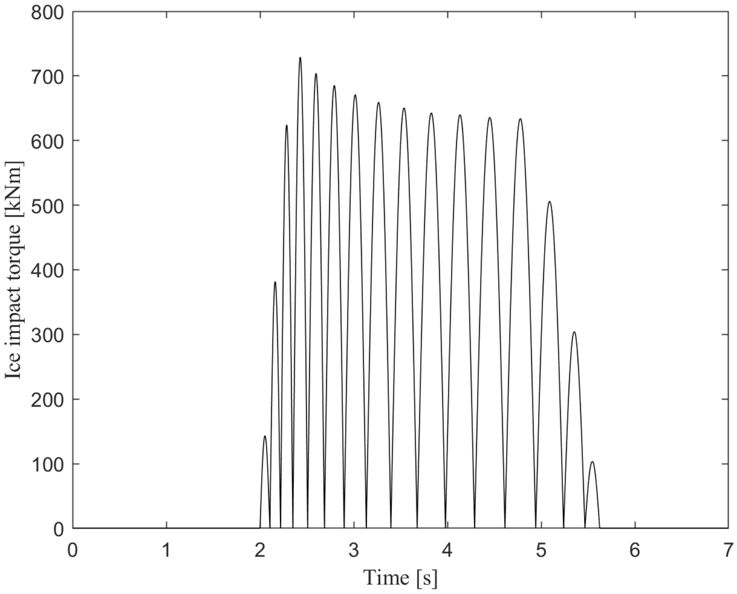

Figure 4.4: IACS case 1 ice impact simulation with 90° single blade impacts, as used by Rolls-Royce AB (2010*a*)

$$\begin{Bmatrix} \Delta Q_1 \\ \Delta\theta_1 \\ \Delta Q_2 \\ \Delta\theta_2 \\ \vdots \\ \Delta Q_{13} \\ \Delta\theta_{13} \\ \Delta Q_{14} \\ \Delta\theta_{14} \end{Bmatrix} = \mathbf{W}^{-1} \begin{Bmatrix} 0 \\ B_1 \\ 0 \\ B_2 \\ \vdots \\ 0 \\ B_{13} \\ 0 \\ 0 \end{Bmatrix} \tag{4.15}$$

The changes in angular velocity ($\Delta\dot{\theta}_i$) and acceleration ($\Delta\ddot{\theta}_i$) are determined using Equations 4.3 and 4.4. From these changes, the values for the next time step can be determined and used to update the variables B_i. This procedure is continued until the desired time step.

The model is evaluated using the IACS case 1 for 4 bladed propellers during 90° single-blade impact sequence, as used by Rolls-Royce in their ice impact simulation of the SAA II shaft line (Rolls-Royce AB, 2010*a*), as shown in Figure 4.4. The reason for the use of this IACS case is so that the results from the forward solution can be directly compared to the results from (Rolls-Royce AB, 2010*a*). The results of the solution for the internal torque, from this model and from Rolls-Royce AB (2010*a*), for the motor shaft in the model (between J_{11} and J_{13} in Figure 4.2) are presented in Figure 4.5.

Stellenbosch University https://scholar.sun.ac.za

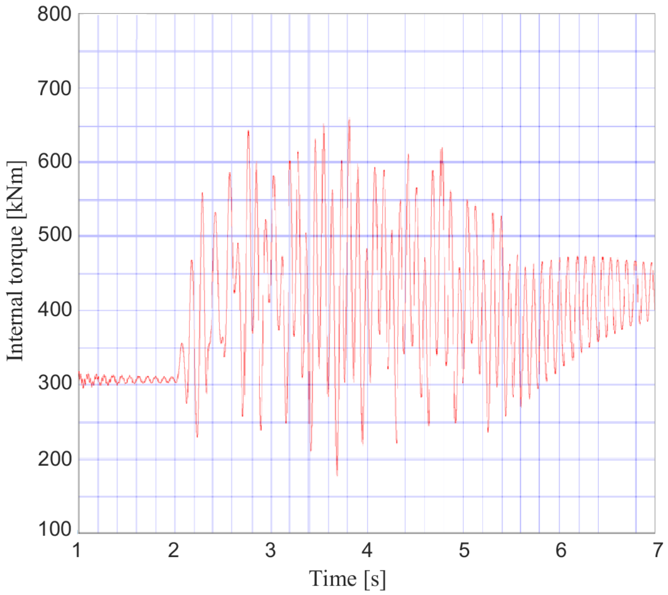

(a) Motor shaft internal torque adapted from Rolls-Royce AB (2010*a*)

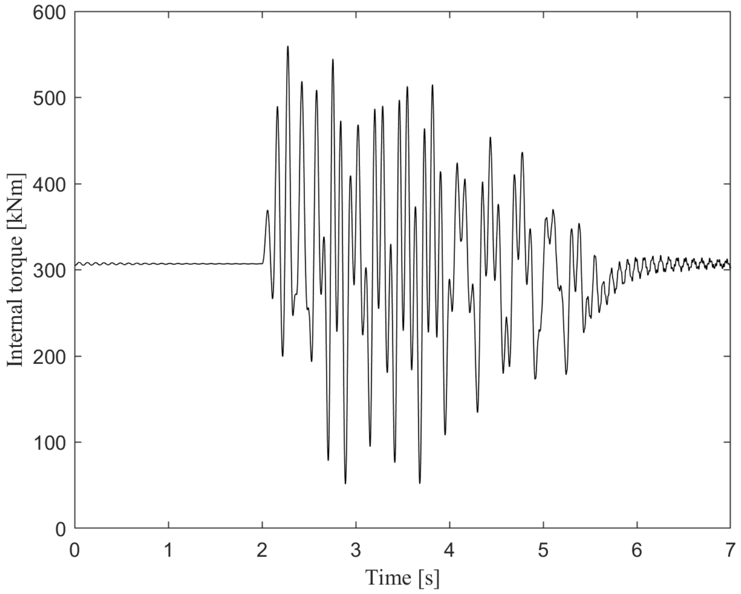

(b) Motor shaft internal torque from discrete model

Figure 4.5: Comparison of discrete model and Rolls-Royce AB (2010*a*) internal torques in motor shaft for forward solution

Stellenbosch University https://scholar.sun.ac.za

It can be seen that the two models produce different results, though they follow a similar pattern.

The differences can largely be attributed to the derivation of the discrete model which assumes a constant motor torque while the model used by Rolls-Royce AB (2010*a*) allows for the motor torque to change over time. This results in different angular velocities during the solutions of the models, and leads to the different internal torques. Specifically, it can be seen in Figure 4.5(a) that the torque calculated by Rolls-Royce AB (2010*a*) starts settling around a higher value than its initial starting point, after the influence of the ice impacts. This is due to an increase in motor torque and thus an increase in the angular velocity. The constant motor torque assumed for the discrete model results in the internal torque returning to its initial value, seen in Figure 4.5(b), at the same initial angular velocity.

The assumption of constant motor torque is not entirely accurate, and the actual motor torque would change when the shaft-line is subjected to external ice impacts as the propulsion system attempts to compensate for the unexpected loading.

4.3 Inverse solution of the discrete model

The inverse solution of the discrete model is performed using the impulse response function (H) between the propeller and measurement location.

The principle of superposition can be applied to systems that respond linearly, or are assumed to respond linearly (Inman, 2014). This linearity allows the use of the convolution integral to solve systems of linear equations. The convolution integral for this model is provided in Equation 4.16 (Inman, 2014).

$$Q_{shaft}(t) = \int_0^t H(t-\tau)Q_{ice}(\tau)d\tau \tag{4.16}$$

Equation 4.16 can be solved by sampling it at n discrete time intervals, leading to a system of linear equations (Jacquelin *et al.*, 2003):

$$\mathbf{Q}_{shaft}(t) = \mathbf{H}(t)\mathbf{Q}_{ice}(t) \tag{4.17}$$

where the impulse response function in matrix form becomes:

$$\mathbf{H}(t) = \begin{bmatrix} h(\Delta t) & 0 & \cdots & 0 \\ h(2\Delta t) & h(\Delta t) & \cdots & 0 \\ h(3\Delta t) & h(2\Delta t) & \cdots & 0 \\ \vdots & \vdots & \ddots & \vdots \\ h(n\Delta t) & h((n-1)\Delta t) & \cdots & h(\Delta t) \end{bmatrix} \tag{4.18}$$

Stellenbosch University https://scholar.sun.ac.za

and the internal shaft-line torque ($\mathbf{Q}_{shaft}$) and external ice induced moment ($\mathbf{Q}_{ice}$) respectively are (De Waal, 2017):

$$\mathbf{Q}_{shaft}(t) = \begin{Bmatrix} q_s(\Delta t) \\ q_s(2\Delta t) \\ q_s(3\Delta t) \\ \vdots \\ q_s(n\Delta t) \end{Bmatrix} \tag{4.19}$$

$$\mathbf{Q}_{ice}(t) = \begin{Bmatrix} q_p(\Delta t) - q_p(0) \\ q_p(2\Delta t) - q_p(\Delta t) \\ q_p(3\Delta t) - q_p(2\Delta t) \\ \vdots \\ q_p(n\Delta t) - q_p((n-1)\Delta t) \end{Bmatrix} \tag{4.20}$$

The impulse response matrix, for a given measurement point on the model, is obtained by subjecting the model to a unit step input at the propeller. That is, the externally applied moment becomes:

$$\mathbf{Q}_{ice}(t) = \begin{Bmatrix} q_p(\Delta t) - q_p(0) \\ q_p(2\Delta t) - q_p(\Delta t) \\ q_p(3\Delta t) - q_p(2\Delta t) \\ \vdots \\ q_p(n\Delta t) - q_p((n-1)\Delta t) \end{Bmatrix} = \begin{Bmatrix} 1 \\ 0 \\ 0 \\ \vdots \\ 0 \end{Bmatrix} \tag{4.21}$$

representing a unitary change in external moment at the first time step, and the moment remaining constant for the following time steps.

Substitution of Equation 4.21 into Equation 4.17 allows for the solution of the impulse response matrix for a unit step input:

$$\mathbf{H}(t) = \begin{bmatrix} q_s(\Delta t) & 0 & \cdots & 0 \\ q_s(2\Delta t) & q_s(\Delta t) & \cdots & 0 \\ q_s(3\Delta t) & q_s(2\Delta t) & \cdots & 0 \\ \vdots & \vdots & \ddots & \vdots \\ q_s(n\Delta t) & q_s((n-1)\Delta t) & \cdots & q_s(\Delta t) \end{bmatrix} \tag{4.22}$$

Using this impulse response matrix it is now possible to perform the inverse solution using Equation 4.23.

$$\mathbf{Q}_{ice}(t) = \mathbf{H}^{-1}(t)\mathbf{Q}_{shaft}(t) \tag{4.23}$$

Stellenbosch University https://scholar.sun.ac.za

As commonly occurs in the discretization of inverse problems, the coefficient matrix, in this case the impulse response matrix, becomes highly ill-conditioned (Golub *et al.*, 1999). This problem is ill-conditioned as the impulse response matrix has a high condition number, of the order 10^{20}. The condition number is the ratio between the largest and smallest singular values of the system and represents the stability of the system (Ikonen *et al.*, 2014), with condition numbers higher than 1 indicating instability. This instability leads to the amplification of any noise, or errors, in a measured signal (Jacquelin *et al.*, 2003).

Inverting the ill-conditioned matrix and multiplying with measured data from the shaft-line will thus lead to large errors on the inversely estimated propeller moment. It is therefore necessary to apply regularization to the inverse solution.

4.3.1 Regularization methods

The main difficulty with discrete ill-conditioned problems is that they are effectively underdetermined due to having a number of small singular values in the coefficient matrix (Hansen, 2008). It is therefore necessary to provide extra information about the desired solution to stabilise the problem and find a single solution. This is what is known as regularization (Hansen, 2008).

A number of different regularization methods exist, and these can be either direct or iterative methods. Only direct methods are considered for the solution of this model in order to avoid the extra computations necessary in iterative methods.

The direct regularization methods considered for the inverse solution of the discrete model are:

- Truncated singular value decomposition (TSVD)
- Modified truncated singular value decomposition (MTSVD)
- Truncated generalised singular value decomposition (TGSVD)
- Damped singular value decomposition (DSVD)
- Damped generalised singular value decomposition (DGSVD)
- Tikhonov
- Least squares using either a quadratic constraint or the discrepancy principle

These methods were chosen as their implementations were readily available in literature (Hansen, 2008). This expands on the methods originally used by Ikonen *et al.* (2014) and De Waal (2017), who considered the TSVD, TGSVD, and Tikhonov methods.

Stellenbosch University https://scholar.sun.ac.za

TSVD

The SVD of the impulse response matrix is (Hansen, 2008):

$$\mathbf{H} = \sum_{i=1}^{n} \mathbf{u}_i \sigma_i \mathbf{v}_i^T \tag{4.24}$$

with σ_i being the singular values of $\mathbf{H}$, and $\mathbf{u}_i$ and $\mathbf{v}_i$ the left and right singular vectors of $\mathbf{H}$ respectively.

The TSVD method replaces $\mathbf{H}$ with a rank-deficient coefficient matrix $\mathbf{H}_k$ by truncating the SVD expansion at k (Hansen, 2008)

$$\mathbf{H}_k = \sum_{i=1}^{k} \mathbf{u}_i \sigma_i \mathbf{v}_i^T \ , \ k \leq n \tag{4.25}$$

The method then solves the problem:

$$\min \|\mathbf{Q}_{ice}\|_2 \quad \text{subject to} \quad \min \left\|\mathbf{H}_k \mathbf{Q}_{ice} - \mathbf{Q}_{shaft}\right\|_2 \tag{4.26}$$

which leads to the solution:

$$\mathbf{Q}_{ice} = \sum_{i=1}^{k} \frac{\mathbf{u}_i^T \mathbf{Q}_{shaft}}{\sigma_i} \mathbf{v}_i \tag{4.27}$$

MTSVD

The MTSVD method is similar to the TSVD, but has been modified to make use of a regularization matrix $\mathbf{L}$ that contains assumed information about the smoothness of the solution.

In this case, the problem solved is (Hansen, 2008)

$$\min \|\mathbf{L}\mathbf{Q}_{ice}\|_2 \quad \text{subject to} \quad \min \left\|\mathbf{H}_k \mathbf{Q}_{ice} - \mathbf{Q}_{shaft}\right\|_2 \tag{4.28}$$

which leads to the solution:

$$\mathbf{Q}_{ice} = \sum_{i=1}^{k} \frac{\mathbf{u}_i^T \mathbf{Q}_{shaft}}{\sigma_i} \mathbf{v}_i - \mathbf{V}_k (\mathbf{L}\mathbf{V}_k)^{\dagger} \mathbf{L} \sum_{i=1}^{k} \frac{\mathbf{u}_i^T \mathbf{Q}_{shaft}}{\sigma_i} \mathbf{v}_i \tag{4.29}$$

where † denotes the pseudoinverse and $\mathbf{V}_k = \{\mathbf{v}_{k+1} \ \cdots \ \mathbf{v}_n\}$.

Stellenbosch University https://scholar.sun.ac.za

TGSVD

For the GSVD the system is defined by the matrix pair $\mathbf{H} \in \mathbb{R}^{m\times n}$ and $\mathbf{L} \in \mathbb{R}^{p\times n}$, with $m \geq n \geq p$. The GSVD is then a decomposition of $\mathbf{H}$ and $\mathbf{L}$ of the form (Hansen, 2008):

$$\mathbf{H} = \mathbf{U}\begin{bmatrix}\Sigma & 0 \\ 0 & I_{n-p}\end{bmatrix}\mathbf{X}^{-1} \tag{4.30}$$

$$\mathbf{L} = \mathbf{V}(\mathbf{M}, 0)\mathbf{X}^{-1} \tag{4.31}$$

where the columns of $\mathbf{U} \in \mathbb{R}^{m\times n}$ and $\mathbf{V} \in \mathbb{R}^{p\times p}$ are orthonormal, $\mathbf{X} \in \mathbb{R}^{n\times n}$ is nonsingular, $\Sigma = \mathrm{diag}(\sigma_1, \sigma_2, \cdots, \sigma_p)$, and $\mathbf{M} = \mathrm{diag}(\mu_1, \mu_2, \cdots, \mu_p)$

The TGSVD solution for the problem:

$$\min \left\|\mathbf{L}\mathbf{Q}_{ice}\right\|_2 \quad \text{subject to} \quad \min \left\|\mathbf{H}_k\mathbf{Q}_{ice} - \mathbf{Q}_{shaft}\right\|_2 \tag{4.32}$$

is given by:

$$\mathbf{Q}_{ice} = \sum_{i=p-k+1}^{p} \frac{\mathbf{u}_i^T\mathbf{Q}_{shaft}}{\sigma_i}\mathbf{x}_i + \sum_{i=p+1}^{n}\left(\mathbf{u}_i^T\mathbf{Q}_{shaft}\right)\mathbf{x}_i \tag{4.33}$$

DSVD and DGSVD

The damped SVD and GSVD methods are based on the SVD and GSVD methods respectively (Hansen, 2008). The filter factors for the damped methods differ, and are given by:

$$f_i = \frac{\sigma_i}{\sigma_i + \lambda} \tag{4.34}$$

$$f_i = \frac{\sigma_i}{\sigma_i + \lambda\mu_i} \tag{4.35}$$

for the DSVD and DGSVD respectively. The solutions for the DSVD and DGSVD methods respectively are:

$$\mathbf{Q}_{ice} = \sum_{i=1}^{n} f_i\frac{\mathbf{u}_i^T\mathbf{Q}_{shaft}}{\sigma_i}\mathbf{v}_i \tag{4.36}$$

$$\mathbf{Q}_{ice} = \sum_{i=1}^{p} f_i\frac{\mathbf{u}_i^T\mathbf{Q}_{shaft}}{\sigma_i}\mathbf{x}_i + \sum_{i=p+1}^{n}\left(\mathbf{u}_i^T\mathbf{Q}_{shaft}\right)\mathbf{x}_i \tag{4.37}$$

Stellenbosch University https://scholar.sun.ac.za

Tikhonov

One of the most common and well known methods is Tikhonov regularization (Hansen, 2008). Here, the regularized solution is defined as the minimizer of a weighted combination of the residual norm and solution seminorm:

$$\mathbf{Q}_{ice} = \min \left(\left\| \mathbf{HQ}_{ice} - \mathbf{Q}_{shaft} \right\|_2^2 + \lambda \left\| \mathbf{LQ}_{ice} \right\|_2^2 \right) \tag{4.38}$$

where λ is the regularization parameter.

Least squares methods

The least squares methods work by minimizing either the residual norm or solution seminorm subject to some constraint (Hansen, 2008), leading to two similar methods.

The minimization of the residual norm is subject to a quadratic inequality constraint on the solution seminorm. Hereafter, this method is referred to as least squares with quadratic constraint:

$$\min \left\| \mathbf{HQ}_{ice} - \mathbf{Q}_{shaft} \right\|_2 \quad \text{subject to} \quad \left\| \mathbf{LQ}_{ice} \right\|_2 \leq \lambda_1 \tag{4.39}$$

The minimization of the solution seminorm is subject to a constraint on the residual norm. This method is referred to as least squares with discrepancy principle, based on the method for choosing a regularization parameter.

$$\min \left\| \mathbf{LQ}_{ice} \right\|_2 \quad \text{subject to} \quad \min \left\| \mathbf{HQ}_{ice} - \mathbf{Q}_{shaft} \right\|_2 \leq \lambda_2 \tag{4.40}$$

In these methods λ acts as the regularization parameter.

4.3.2 Regularization matrix

For a number of the regularization methods in Section 4.3.1, the regularization matrix $\mathbf{L}$ is incorporated to provide information about the presumed smoothness of the solution (Ikonen *et al.*, 2014). The matrix $\mathbf{L}$ is usually the identity matrix or a $p \times n$ discrete approximation of the $(n-p)^{th}$ derivative operator (Hansen, 2008).

Due to the solution vector in this problem being defined as changes between times steps, the m^{th} order regularization matrix corresponds to the $(m+1)^{th}$ derivative operator (Ikonen *et al.*, 2014).

Ikonen *et al.* (2014) tested the 0^{th}, 1^{st} and 2^{nd} order regularization matrices, corresponding to the 1^{st}, 2^{nd} and 3^{rd} derivative operators respectively. The 1^{st}

Stellenbosch University https://scholar.sun.ac.za

order regularization matrix was found to be the best for the discrete model (Ikonen *et al.*, 2014).

$$\mathbf{L} = \begin{bmatrix} -1 & 1 & 0 & 0 & \cdots & 0 \\ 0 & -1 & 1 & 0 & \cdots & 0 \\ \vdots & \ddots & \ddots & \ddots & \ddots & \vdots \\ 0 & \cdots & 0 & -1 & 1 & 0 \\ 0 & \cdots & 0 & 0 & -1 & 1 \end{bmatrix} \tag{4.41}$$

4.3.3 Regularization parameter

Each of the regularization methods in Section 4.3.1 requires the selection of some regularization parameter.

For the SVD based methods the parameter is the number of singular values to keep in the calculation, in other words where to truncate the expansion. For the other methods, the parameter λ must be selected.

The L-curve method was chosen for the selection of the regularization parameters (Hansen and O'Leary, 1993). This method plots the solution seminorm against the residual norm, for all valid regularization parameters, forming an L-shaped curve, as depicted in Figure 4.6. The L-curve provides a way to visually determine where both the solution and residual norms are minimized simultaneously. The error on the regularized solution consists of a perturbation error, from the noise on the measured shaft torque, and a regularization error. The regularization parameter corresponding to the corner of the L-curve minimizes both these errors, and results in the optimal regularized solution. The L-curve method has also been successfully applied in the regularization of ill-posed problems in other fields (Lloyd *et al.*, 1997; Xu *et al.*, 2016).

The L-curve method was similarly employed by both Ikonen *et al.* (2014) and De Waal (2017) to determine regularization parameters. However, in both these studies, the parameters were optimised for a specific known moment impulse. This parameter was subsequently used for all cases.

This can lead to errors in the regularization, causing cases to become under- or over-regularized. As an example, Figure 4.7 provides the L-curve determined using the Tikhonov method for a 1.8 second recording made at 05:11:06 on the 17 December 2018. The corner of the L-curve is located where the regularization parameter is 13.0348. The parameters determined by Ikonen *et al.* (2014) and De Waal (2017) were 0.0512 and 0.2457 respectively. It can be seen that both of these parameters are higher up on the L-curve than the optimal parameter for this case. This leads to under-regularization when using the parameters from Ikonen *et al.* (2014) or De Waal (2017) for this case, resulting in larger errors on the solution norm. The algorithm was therefore expanded to automatically select a regularization parameter for each case it was provided with.

Stellenbosch University https://scholar.sun.ac.za

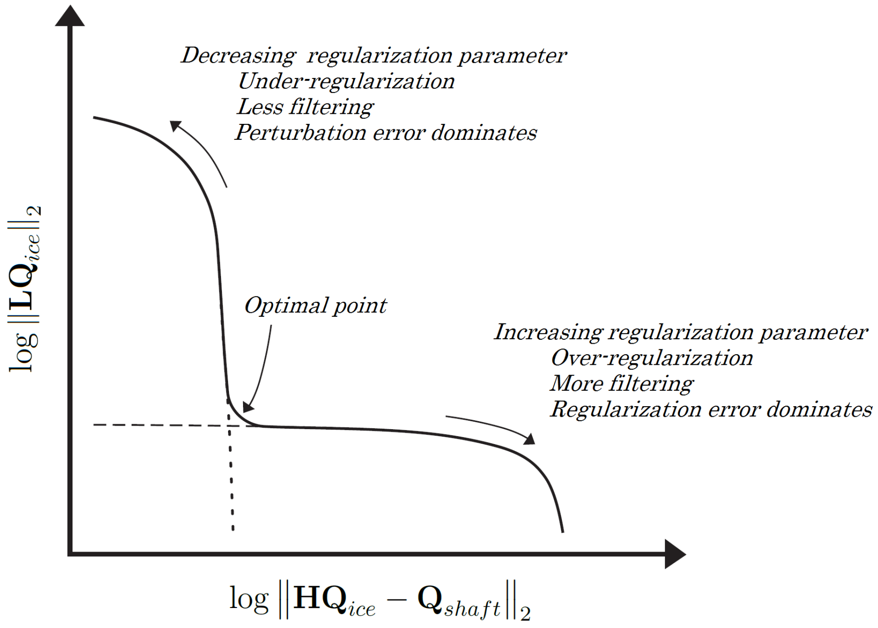

Figure 4.6: Example of an L-curve. Adapted from Hansen (2008)

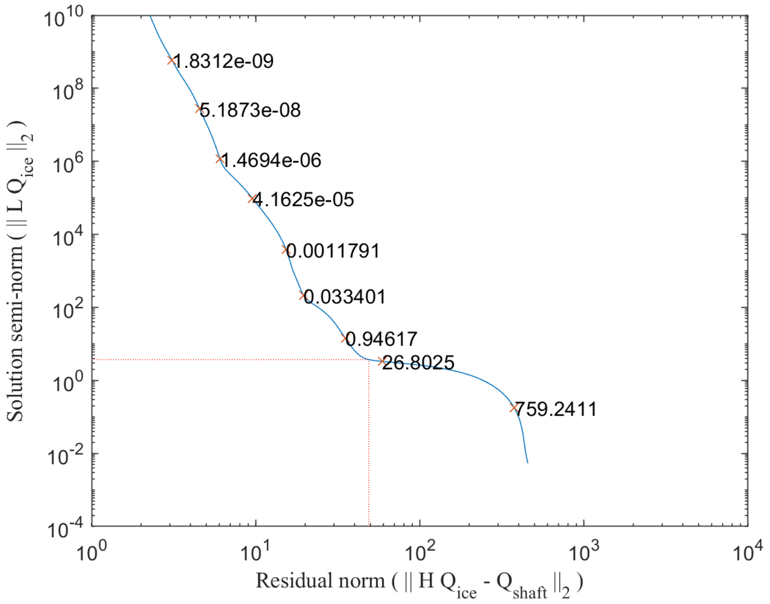

Figure 4.7: Tikhonov L-curve for case at 05:11:06 on the 17 December 2018

For the TSVD, MTSVD, TGSVD, DSVD, DGSVD and Tikhonov methods the regularization parameter was chosen as the corner of the L-curve giving a good compromise between errors on the solution and errors on the residual.

Stellenbosch University https://scholar.sun.ac.za

For the first least squares method the quadratic constraint λ_1 is chosen as the solution semi-norm corresponding to the corner of the L-curve. Similarly, for the second least squares method the parameter λ_2 was selected as the residual norm corresponding to the corner of the L-curve. The algorithm automatically finds the corner of the L-curve on a case by case basis during the indirect propeller load estimation.

Where the regularization parameter is continuous, the L-curve is also continuous. In contrast, regularization methods with discrete parameters result in discrete L-curves. The DSVD, DGSVD, Tikhonov and both least squares methods all produce continuous L-curves, in which case the corner is located by finding the point with maximum curvature through differention of the L-curve. The TSVD, MTSVD, and TGSVD methods produce discrete L-curves. In this case the corner is found using the adaptive pruning algorithm from Hansen *et al.* (2007), which determines a list of candidate corners by pruning points on the discrete L-curve and selecting a best corner from this pruned list.

4.4 Evaluation of the discrete model

The inverse solution has been performed on selected ice-impact cases from the full-scale measurements on the SAA II. Specifically, the various regularization methods were evaluated in order to determine which is most suitable for the current application. In addition, the results from the model when different measurement locations were used as input were investigated.

The data used for the evaluation of the discrete model originates from the 2018/19 Antarctic Relief voyage. During this voyage, torque was measured at two locations on the shaft-line, Q_1 and Q_2, as shown in Figures 3.2 and 4.2. The data was recorded on the morning of 17 December 2018. At the time, the ship was breaking through ice en route to the ice shelf at Penguin Bukta for logistics operations. Fifty ice impact cases were extracted for analysis. The operational parameters and sea ice conditions for each case are presented in Table C.4 in Appendix C. These case studies varied in operational parameters and duration for improved testing of the various regularization methods used by the algorithm.

4.4.1 Evaluation of the regularization methods

The regularization of the inverse solution needed to be robust and efficient. As the regularization parameter was automatically selected, this selection process needed to be reliable. Furthermore, the regularization needed to be efficient to allow the use of the algorithm in real-time analysis.

The internal torques Q_1 and Q_2 that were measured for each case were used as inputs for the algorithm. The computer used to perform the analysis

Stellenbosch University https://scholar.sun.ac.za

had an i7-4720HQ 2.6 GHz processor, 8 GB of RAM, and a 64-bit operating system. The algorithm was solved using MATLAB.

Each of the torques were analysed using the various regularization methods. Failure of a regularization method was based on whether the solution was under- or over-regularized, that is whether or not the algorithm could automatically determine a suitable regularization parameter. The success of each regularization method for the various case studies is provided in Table C.5 in Appendix C.

It can be seen from Figure 4.8 that only two of the eight regularization methods, DGSVD and Tikhnov, had a 100% success rate for the case studies analysed. These methods are followed by the TGSVD and the least squares methods with 85%, TSVD with 51%, MTSVD with 10%, and DSVD with 4%. The success rates reported here reflect the success of the algorithm in automatically locating a suitable regularization parameter for the current application, and thus not under- or over-regularizing the inverse solution. The success rates are not a reflection of the validity of the regularization methods themselves.

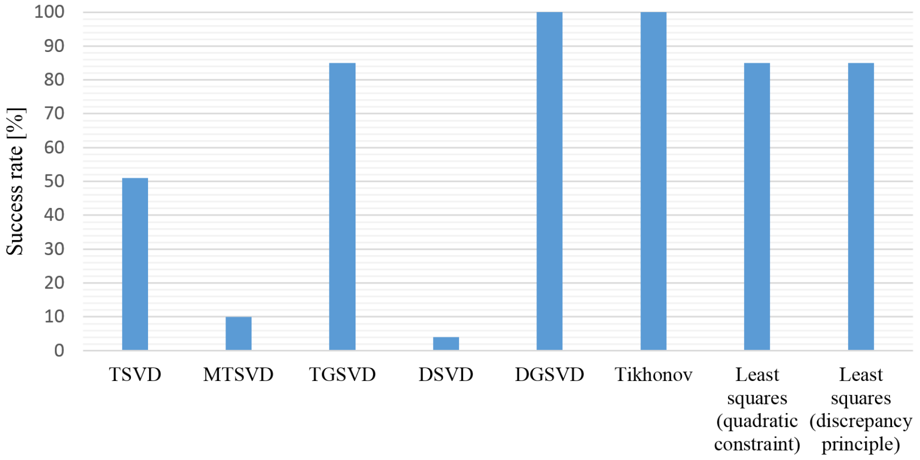

Figure 4.8: Success rates of the different regularization methods

The DGSVD, Tikhonov, and least squares methods achieved high success rates due to the continuous nature of their L-curves. This continuity allowed for easy differentiation of the L-curve during the parameter selection, and thus easy identification of the L-curve corner. The TGSVD method also had a high success rate, and was the only method with a discrete L-curve to achieve this.

The lower success rates of the TSVD and MTSVD methods were related to the discrete nature of their L-curves. Since the L-curve was not continuous, the algorithm could not simply differentiate the curve to determine its curvature, and hence find the corner. This limitation resulted in the parameter selection

Stellenbosch University https://scholar.sun.ac.za

algorithm being more susceptible to finding local or false corners, and returning the incorrect regularization parameter.

The MTSVD in particular suffered from the selection of false corners on the L-curve. Figure 4.9 provides the L-curve used by the algorithm for the internal torque Q_1 of Case 1. It can be seen that the algorithm has selected a false corner (parameter was selected as 4), leading to the results in Figure 4.10(a). These results show a large error when comparing the experimentally measured internal torque to the internal torque obtained using the inversely determined external ice-load, in Figure 4.10(b). By comparison, when a more correct corner was manually chosen (parameter selected as 50) the results were acceptable and comparable to those obtained by the DGSVD and Tikhonov methods, shown in Figure 4.11.

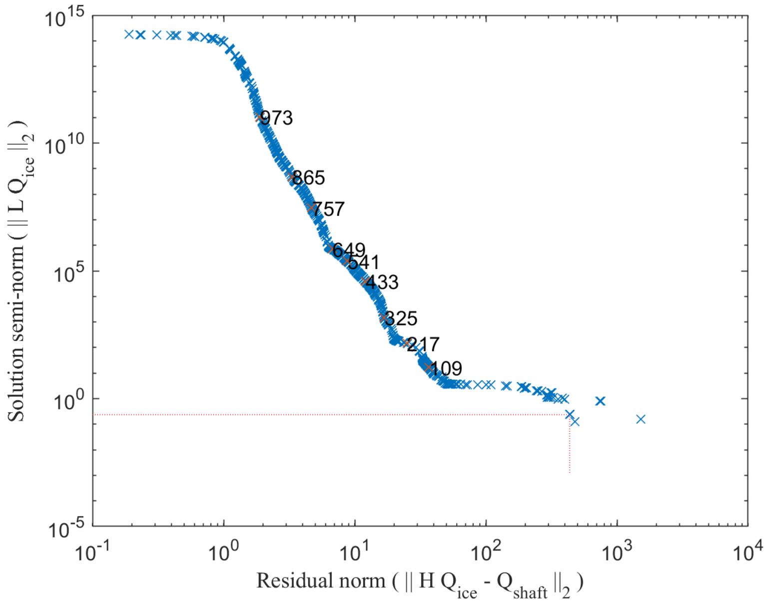

Figure 4.9: MTSVD L-curve for the inverse calculation using internal torque Q_1 of Case 1

Of further note in Figure 4.11 is that the resulting estimation for the propeller moment is similar for each successful regularization method, with the possibility of small differences arising at the peak values. This finding agrees with that observed by Ikonen *et al.* (2014).

The extremely low success rate of the DSVD method was related to the smoothness of its L-curve. Though the curve was continuous and thus easily differentiable, the corner was not clear which resulted in the failure of the algorithm. The lack of distinct corner can be seen for Case 1 in Figure 4.12. The algorithm consistently chose a parameter higher up on the L-curve than

Stellenbosch University https://scholar.sun.ac.za

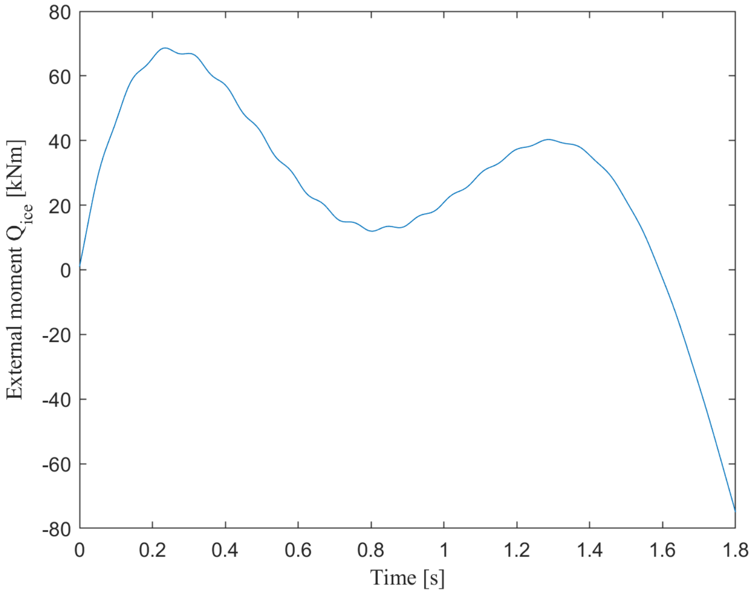

(a) Estimated ice induced propeller moment

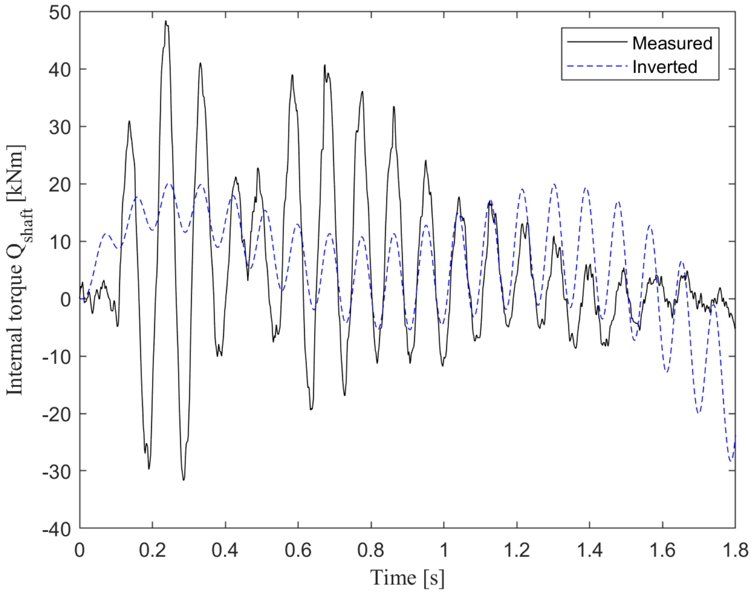

(b) Internal torque Q_1

Figure 4.10: Results using the MTSVD method with incorrect corner at 4 for Case 1

Stellenbosch University https://scholar.sun.ac.za

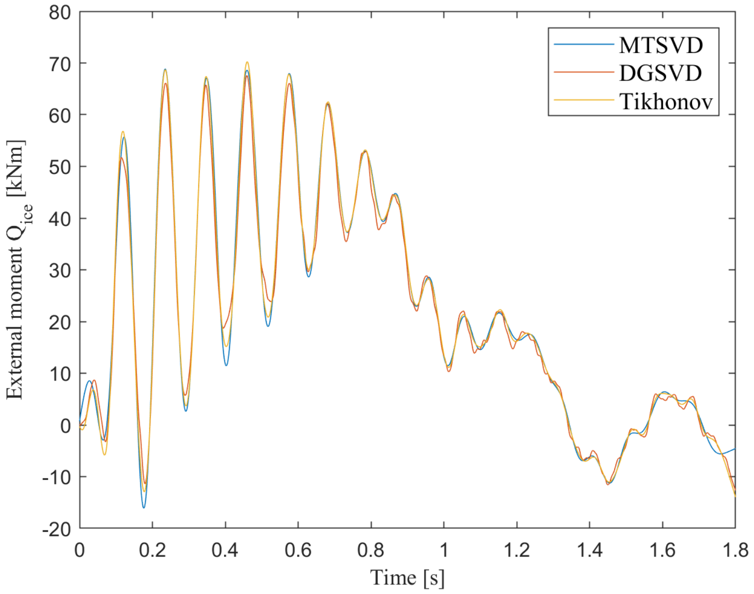

(a) Estimated ice induced propeller moment

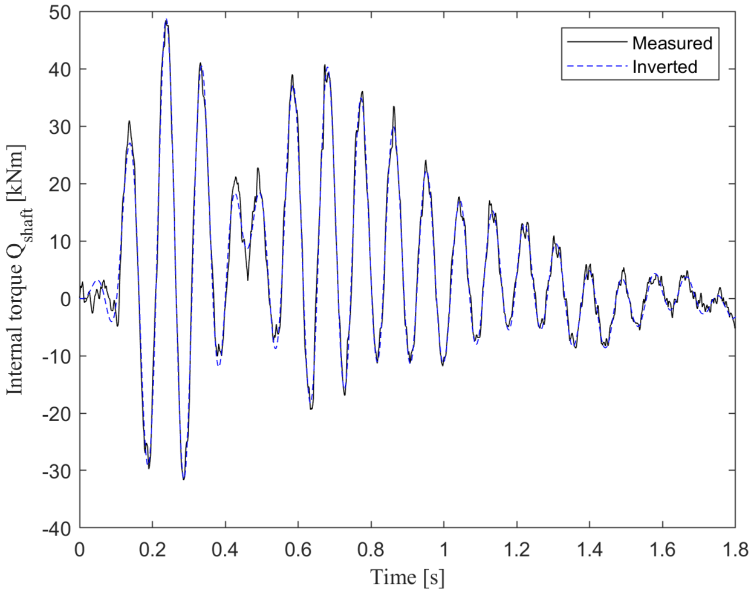

(b) Internal torque Q_1

Figure 4.11: Results using the MTSVD method with correct corner at 50 for Case 1

Stellenbosch University https://scholar.sun.ac.za

the optimum, resulting in insufficient filtering and thus noise on the estimated propeller moment.

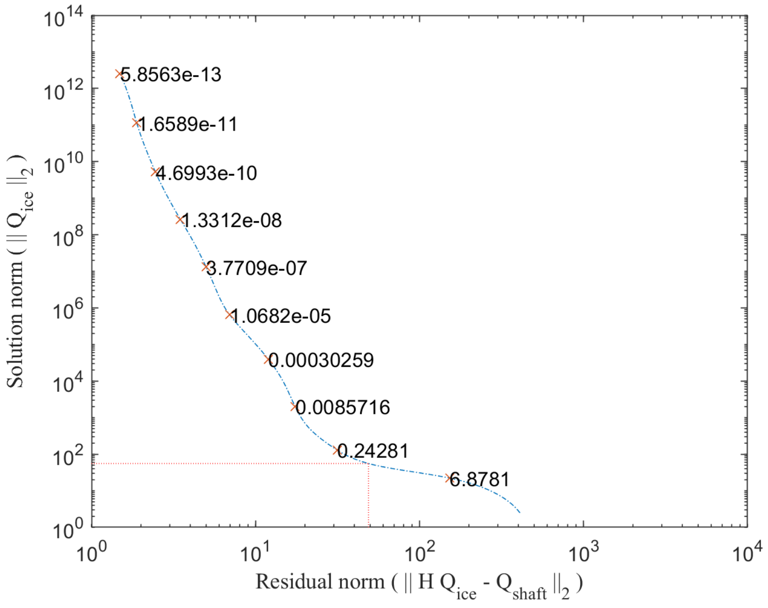

Figure 4.12: DSVD L-curve for the inverse calculation using internal torque Q_1 of Case 1

In addition to testing the robustness of the algorithm for the various regularization methods, the solution times were also recorded to test the efficiency. As only the DGSVD and Tikhonov methods achieved 100% success rates, only these two methods are compared. The solution times for these methods are presented in Table C.6. The presented solution times include the determination of an L-curve and regularization parameter, and the inverse solution itself. The construction of the impulse response function is not included in the presented solution times.

Firstly, it can be seen from the results in Table C.6 that the DGSVD and Tikhonov methods have very similar solution times. One method does not consistently outperform the other. On average, the Tikhonov method is faster by 0.06 seconds. Though that difference is small, it is 6% of the total time of the shortest case presented here and any savings in computational time can be beneficial. However, based on the data presented here, one method does not appear to be significantly more efficient than the other.

Second, both methods failed to solve in less time than the actual duration of the case study. This makes implementing the methods in real-time impossible as the solution will continually take longer than the measurements. However, the slower solution times are a limitation of the hardware used to solve the algorithm, and could be overcome by using a computer with access to more

Stellenbosch University https://scholar.sun.ac.za

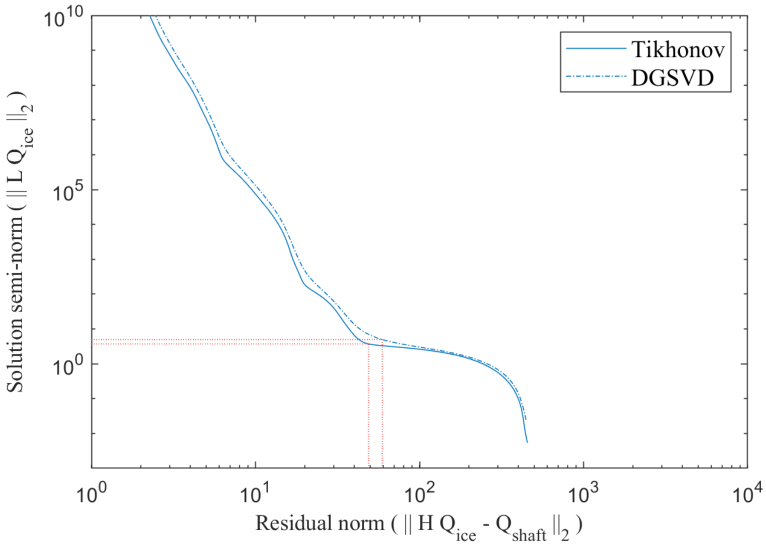

Figure 4.13: Comparison of Tikhonov and DGSVD L-curves for Q_1 of Case 1

RAM and processing power. This means the computational expense of this algorithm leads to more expensive hardware.

Third, there is a difference between the DGSVD and Tikhonov methods in the peaks of the external ice-loading determined by the algorithm, which can be seen in Figure 4.11(a). The Tikhonov method consistently predicts higher peak values. The slightly lower peak values predicted by the DGSVD resulted in a slightly larger error on the internal torque obtained using the inversely determined external ice-load. This is due to the Tikhonov method being able to better minimize the solution norm, leading to better peak estimates, and residual norm, leading to smaller errors on the internal torque. This is highlighted by comparing the L-curves of the two methods, in Figure 4.13, where it can be seen that the Tikhonov residuals are lower. De Waal (2017); De Waal *et al.* (2018*b*) similarly found the Tikhonov method to provide the best estimation of peak values.

The better peak estimates, and the slightly faster average solution time, suggest that the Tikhonov method is the better method for the application of this algorithm.

Finally, it can be seen from the results in Table C.6 that the solution time increases significantly as case duration increases. The solution time is roughly proportional to the square of the case duration. This is highlighted in Figure 4.14. The reason for this increase in solution time is as a result of the way the algorithm makes use of the impulse response function. The impulse response function is calculated as an $n \times n$ square matrix, where n is the number of data points in the given case study. Thus, longer duration cases require larger impulse response functions to solve. Similarly, the $p \times n$ regularization matrix $\mathbf{L}$ also increases in size as duration increases. Therefore

Stellenbosch University https://scholar.sun.ac.za

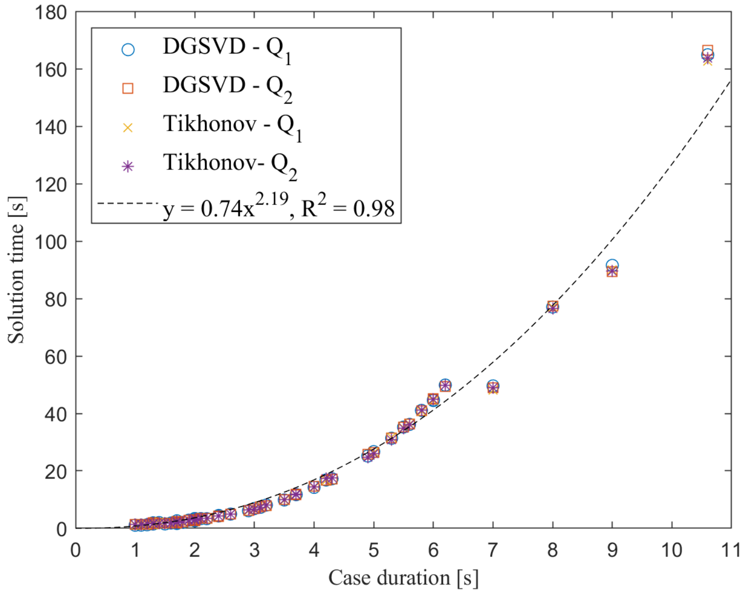

Figure 4.14: Relationship between case study duration and solution time - discrete model

the solution time increases in size roughly proportional to n^2 as case duration increases.

The large increase in solution time for an increase in the duration of the case study has an impact on the use of the algorithm for real-time analysis. It limits the duration of real-time data that can be analysed in a single run of the algorithm. This means that the algorithm will either need to be adapted to handle larger duration cases more efficiently or that real-time data should be supplied to the algorithm in smaller segments.

A final note is that each case provided to the algorithm should always contain the same number of data points. This would allow for a single calculation of the impulse response function, as it only depends on the duration of the input, instead of needing to calculate the function for each input. Only needing to calculate the impulse response function once, instead of once per input, will also have large time savings with regards to the solution of the algorithm.

4.4.2 Comparison between measurement locations for the inverse solution

During the 2018/19 Antarctic voyage, the shaft-line torque was measured at two separate locations, Q_1 and Q_2 in Figures 3.2 and 4.2. This was done in order to investigate whether the inverse model provided similar results irrespective of measurement location.

The similarity of results between different measurement locations indicates

Stellenbosch University https://scholar.sun.ac.za

whether the discrete lumped model is a sufficiently accurate representation of the continuous shaft-line. Only the Tikhonov method was considered, as it was found to be most suitable for the regularization of the inverse problem.

The relative errors and correlation coefficients were calculated for each case using Equations 4.42 and 4.43 respectively (Xu *et al.*, 2016):

$$error = \frac{||Q_{ice2} - Q_{ice1}||_2}{||Q_{ice1}||_2} \tag{4.42}$$

$$correlation = \frac{\sum\limits_{i=1}^{n} \left(Q_{ice1,i} - \overline{Q}_{ice1}\right)\left(Q_{ice2,i} - \overline{Q}_{ice2}\right)}{\sqrt{\sum\limits_{i=1}^{n} \left(Q_{ice1,i} - \overline{Q}_{ice1}\right)^2 \sum\limits_{i=1}^{n} \left(Q_{ice2,i} - \overline{Q}_{ice2}\right)^2}} \tag{4.43}$$

where Q_{ice1} and Q_{ice2} represent the estimated propeller moments from measurements Q_1 and Q_2 respectively.

As the shaft-line is a continuous structure and the cross sectional area is the same at both measurement locations, it is expected that the measured internal torques should be similar. Differences may arise due to measurement errors, sensor placement errors, or differences between the physical system and what was assumed.

To put the errors for the propeller moment estimates in perspective, the same calculations were performed for the measured data. This was done to determine whether any errors in the propeller moment estimates were due to errors in the measurement, or due to problems with the model.

The relative errors for the measured internal torque and estimated propeller moments are presented in Figure 4.15. The correlation coefficients are presented in Figure 4.16. These values were calculated with the hydrodynamic torque removed from both the external propeller moment and the measured internal torque.

It can be seen, from Figures 4.15 and 4.16, that as the errors between the measurements increase, so do the errors between the estimations from the different measurement locations. When the error between measurements is small, and the correlation high, there is good agreement in the estimated propeller moments determined by the model. However, the model amplifies any errors on the measurement significantly. Small increases in measurement error result in much larger errors between the propeller moment estimates.

Stellenbosch University https://scholar.sun.ac.za

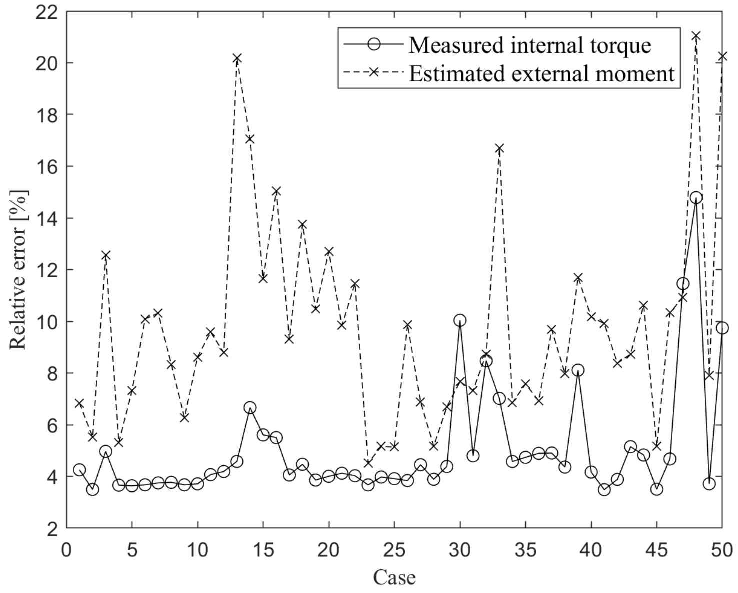

Figure 4.15: Relative errors for the measured internal torques and estimated propeller moments

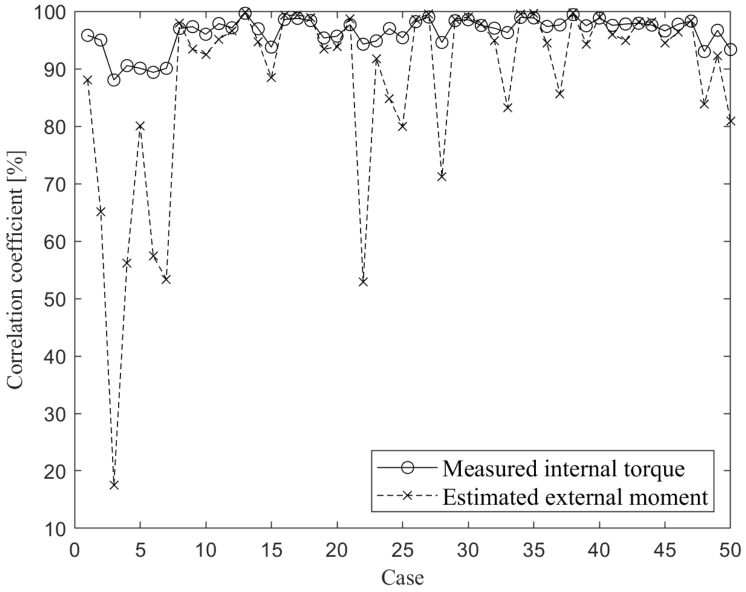

Figure 4.16: Correlation coefficients for the measured internal torques and estimated propeller moments

4.4.3 Comparison to literature

The discrete model was tested in the forward problem using the first IACS case from Rolls-Royce AB (2010*a*). The results from the model differed to those presented by Rolls-Royce AB (2010*a*). This was due to the discrete model assuming a constant motor torque.

Rolls-Royce AB (2010*a*) made use of a model similar to the discrete model to perform a forward solution of an ice-impact simulation for the SAA II. The ice impact is given in Figure 4.17(a), and the motor-shaft torque and motor speed from Rolls-Royce AB (2010*a*) in Figures 4.17(b) and 4.17(c) respectively. This data was extracted using a plot digitizer (Rohatgi, 2020).

The discrete model was provided with the internal torque and velocity results from Rolls-Royce AB (2010*a*) (Figures 4.17(b) and 4.17(c) respectively) as input and the estimated propeller moment was determined. As the discrete model and the model used by Rolls-Royce AB (2010*a*) represent the same propulsion line, the discrete model's parameters were left unchanged. The results provided by Rolls-Royce AB (2010*a*) were for the motor shaft, as such

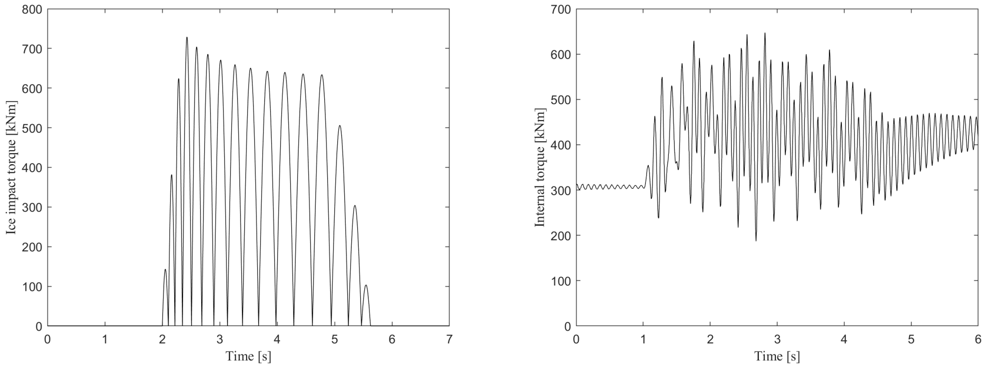

(a) Ice impact (b) Motor shaft internal torque

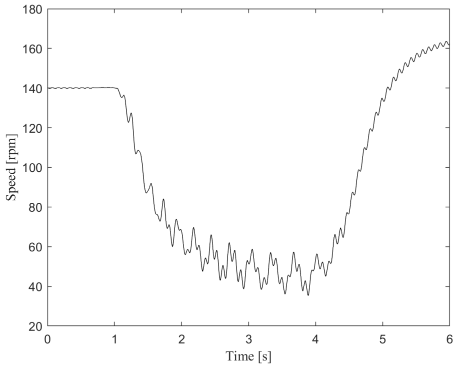

(c) Motor speed

Figure 4.17: Results from Rolls-Royce AB (2010*a*)

Stellenbosch University https://scholar.sun.ac.za

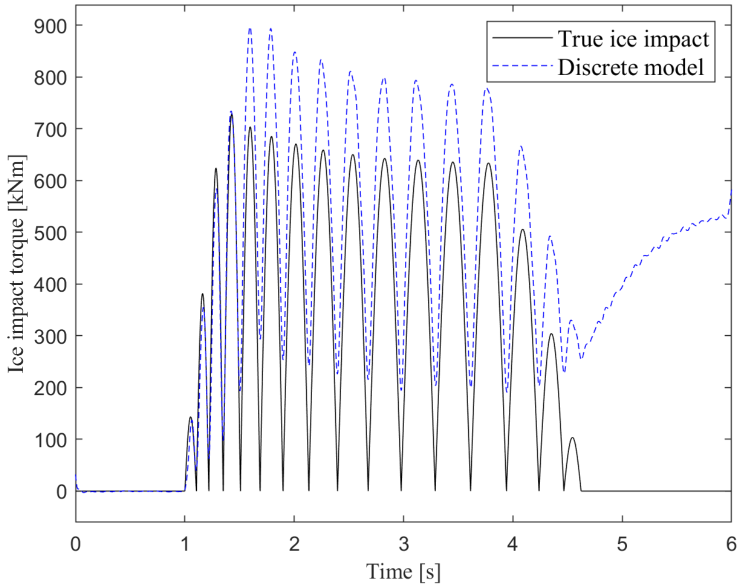

Figure 4.18: Comparison between IACS Case 1 ice impact (Rolls-Royce AB, 2010*a*) and discrete model

the location to the left of the motor inertia was selected for the input to the discrete model. The comparison between the actual ice impact and that determined by the discrete model is provided in Figure 4.18.

The results in Figure 4.18 illustrate a shortcoming in the discrete model, due to the assumptions of constant motor torque and hydrodynamic load. The results from Rolls-Royce AB (2010*a*) in Figure 4.17(c) clearly show an increase in the motor speed from the original steady-state value. This is due to an increase in motor torque. Consequently, the hydrodynamic load would also increase and this is seen in Figure 4.17(b) with the internal torque converging to a higher steady-state value.

As the discrete model cannot account for changes in the motor torque, the increase in the internal torque is attributed solely to the ice induced loading. This results in the offset of the ice impact values determined by the discrete model in Figure 4.18.

Comparing the rotational speeds from Rolls-Royce AB (2010*a*) and the discrete model, Figure 4.19, also shows that the rotational speed determined by the discrete model is incorrect. The increased ice induced loading results in the shaft velocity decreasing, with the shaft eventually spinning in the opposite direction as there is no corresponding motor torque increase to result in the correct shaft speed.

Stellenbosch University https://scholar.sun.ac.za

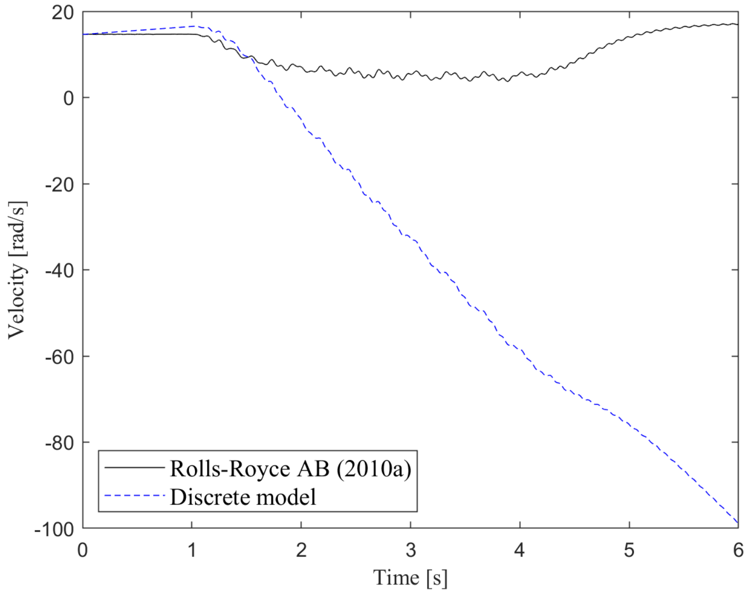

Figure 4.19: Comparison between angular velocity from Rolls-Royce AB (2010*a*) and discrete model

4.5 Limitations of the discrete model

The discrete lumped mass model of the shaft-line suffers from a number of limitations.

The algorithm is computationally expensive. It was not possible to obtain the inverse solution in less time than the actual case duration, with the hardware that was used. This means more computing power is necessary to solve the algorithm faster, leading to increased financial expenses. Using the algorithm to examine longer cases also becomes prohibitively computationally expensive, as the time taken to solve the inverse solution increases roughly proportional to the square of the case duration.

As the shaft-line is a continuous system, it should be possible for the model to make use of measurements conducted at any point along the length of the shaft-line. However, as the model is a discrete representation of the continuous system, errors can be introduced when selecting a measurement location. The errors between propeller moment estimates from different measurement locations increase as the errors between measurement locations increase, as seen in Figure 4.20. Since it is not possible to capture perfect measurements, it would be preferable that the model be robust to the errors between measurement locations. Instead, the model tends to amplify these errors.

The model assumes a constant hydrodynamic torque, which is subtracted from the measured internal torque in order to determine the ice induced propeller moment. The assumption of constant hydrodynamic torque does not

Stellenbosch University https://scholar.sun.ac.za

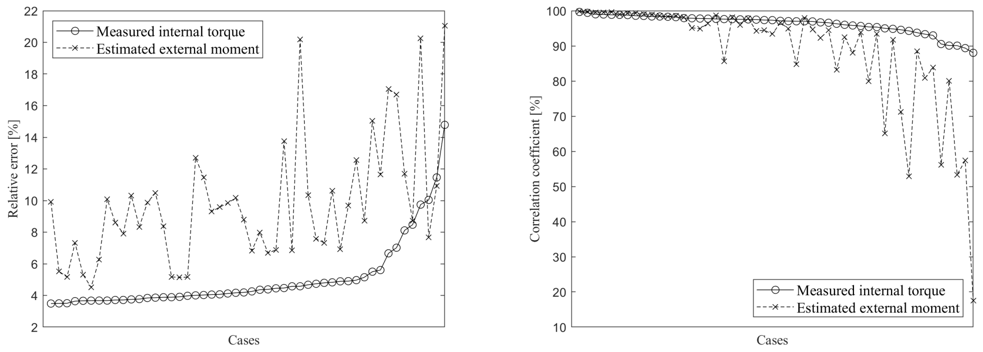

(a) Relative error

(b) Correlation coefficient

Figure 4.20: Relationship between increasing measurement error between locations, and increasing error between propeller moment estimations

hold for all cases as the ship speed, motor power, propeller pitch, and to a lesser extent the motor and shaft speed, are all varied during the navigation of the ship. These changes cause the hydrodynamic torque to fluctuate over time. In addition to this, the hydrodynamic load is not constant during a propeller ice impact. An impact to the propeller results in a moment opposite to the direction of rotation, causing the propeller's rotation to slow. One of the components of the hydrodynamic load is the moment due to water damping, which is dependent on the rotational speed of the propeller. Therefore, as the propeller speed changes during an impact, so does the hydrodynamic load.

The model also assumes the motor torque is constant. In actual operation the motor would compensate for any losses in shaft-line rotational speed due to external moments. In other words, if an ice impact occurred on the propeller, slowing the shaft down, the motor would speed up to compensate. This model of the shaft-line is not able to take this into account.

The errors introduced due to the assumption of constant hydrodynamic loads and motor torques were clearly illustrated in Section 4.4.3.

The model has no ability to determine the actual rotational displacements, velocities, or accelerations. This is due to the model only being defined to calculate the changes in these values. The model thus requires initial conditions, which must either be assumed or retrieved from another measurement.

Relating to the motor torque and shaft-line angular velocity, the model is not able to take into account how the shaft-line speed changes during an ice impact. The internal torque is only a function of the spatial derivative of the angular displacement of the shaft, represented by Equation 4.44, and does not contain information about the angular velocity. The same measured internal torque could thus be obtained using different external moments at different shaft-line angular velocities.

Stellenbosch University https://scholar.sun.ac.za

$$Q(x,t) = GJ\frac{\partial\theta(x,t)}{\partial x} \tag{4.44}$$

Finally, the model assumes a constant propeller pitch for the calculation of the hydrodynamic mass and hydrodynamic damping. However, the propeller pitch varies during operation and navigation. As the ship uses a controllable pitch propeller, the pitch is varied in order to control thrust and therefore speed of the ship. This model does not take this variation of the propeller pitch, and thus variation of the hydrodynamic properties, into account.

4.6 Discussion

Though the discrete model was not developed by this study it was further analysed, in particular with regards the methods used for regularization.

In previously published results (Ikonen *et al.*, 2014; De Waal *et al.*, 2018*b*) the parameters used for the various regularization methods were optimised using a reference linear moment impulse. It was found that using this optimised parameter can lead to errors (over- or under-regularization) in the solution. This is due to the optimised parameter only being valid for the case it was optimised for, and not being the most optimal parameter in general.

Instead, the algorithm was expanded to include automated regularization parameter selection on a case by case basis. This was achieved through the use of the L-curve method, and tested for eight regularization methods. It was found that for the current application, the Tikhonov and DGSVD methods were the most reliable. However, the Tikhonov method achieved lower residuals on the solution norm which lead to better peak estimates.

Despite these improvements, it was found to be limited in its current state. Due to the assumption of a constant motor torque, it produced large errors on the propulsion shaft angular velocity.

The discrete model would need alterations in order to be better able to estimate propeller moments. An improvement could be to treat the model as a multiple-input single-output (MISO) system, instead of a single-input single-output (SISO), the single input being the load at the propeller. This would entail determining the impulse response function of the system as a result of inputs from both the propeller and motor loading. This would also require knowledge of how much of the measured output should be attributed to each input.

It was also found to be prohibitively computationally expensive for larger datasets.

Stellenbosch University https://scholar.sun.ac.za

Chapter 5

Propeller moment estimation using a continuous model of the propulsion shaft

A new model of the propulsion shaft has been developed, which represents the shaft as a continuous system.

This model relies on the concept of modal superposition, which allows the calculation of the angular displacement, velocity, and acceleration at infinite degrees of freedom along the shaft by superimposing its mode shapes. The model is a continuous representation of the propulsion shaft, which differs from the discrete approaches by including the effects of distributed mass.

The propeller loading is estimated indirectly from the torque and angular velocity measurements from the propulsion shaft. This is done by solving a system of equations representing the modal coordinates as functions of time, alongside equations representing the measured torque and velocity as functions of these modal coordinates.

For brevity, this model is henceforth referred to as the continuous model.

Section 5.1 provides the description and mathematical derivation of the continuous model.

The forward solution of the continuous model is described in Section 5.2. The number of modes used in the forward solution is discussed, along with a comparison to the discrete model's forward solution.

Section 5.3 describes the inverse solution of the continuous model. Here, the inverse solution is evaluated using inputs obtained from a forward solution of the discrete model. The number of mode shapes for the inverse solution is discussed.

Section 5.4 focuses on the evaluation of the continuous model. The continuous model is compared to the discrete model in Section 5.4.1, in terms of results from the inverse solution and efficiency. A comparison of the results between the inverse solutions from the two measurement locations on the propulsion shaft is provided in Section 5.4.2. Results from the inverse solution

Stellenbosch University https://scholar.sun.ac.za

are compared to results provided by Rolls-Royce AB (2010*a*) and Polić *et al.* (2019) in Section 5.4.3.

Finally, the limitations of the continuous model and a discussion of the results are provided in Sections 5.5 and 5.6 respectively.

Figure 5.1 provides a breakdown of the research presented in this chapter, and shows where the contributions to literature arise.

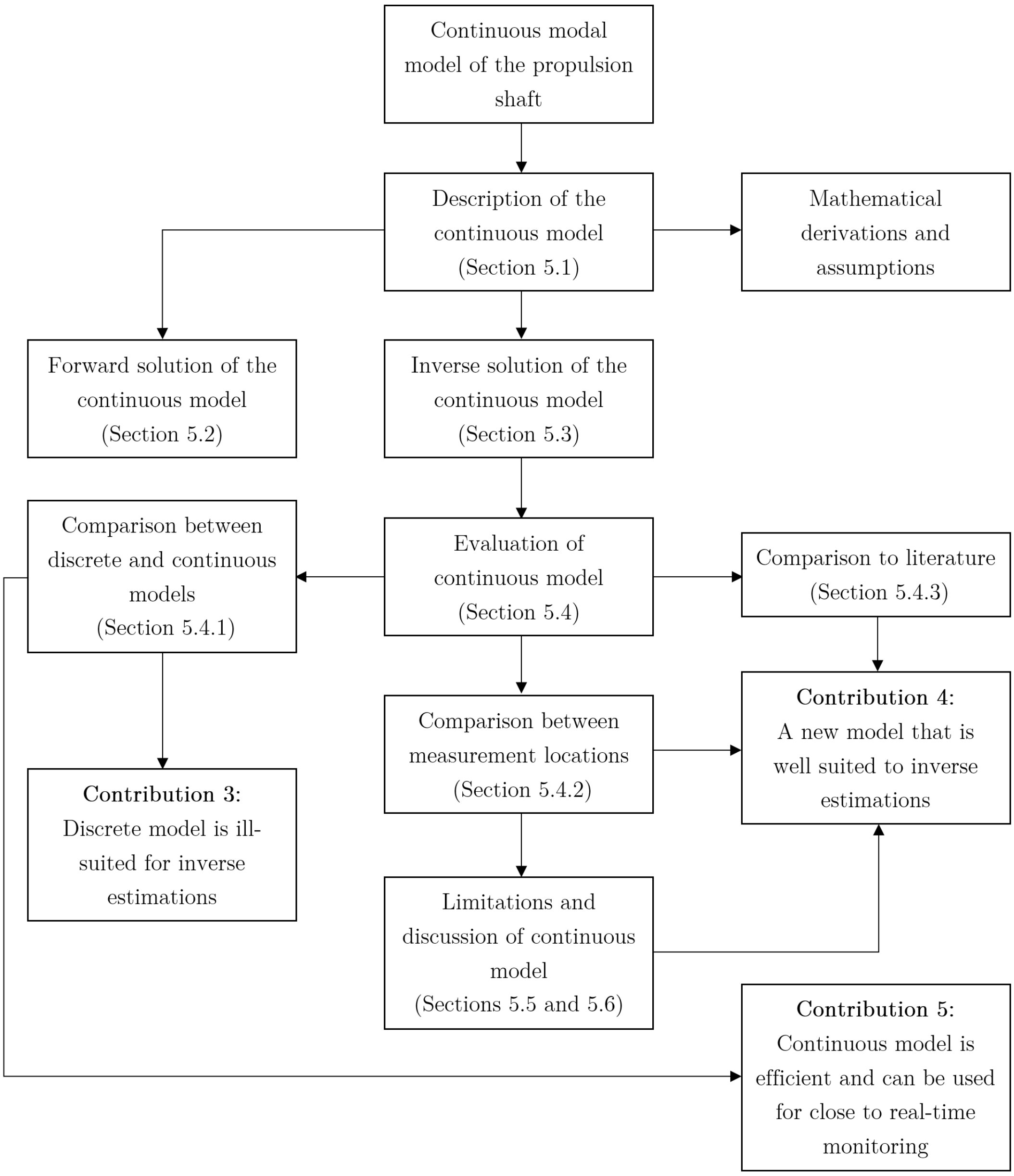

Figure 5.1: Breakdown for Chapter 5 research and contributions

Stellenbosch University https://scholar.sun.ac.za

5.1 Description of the continuous model

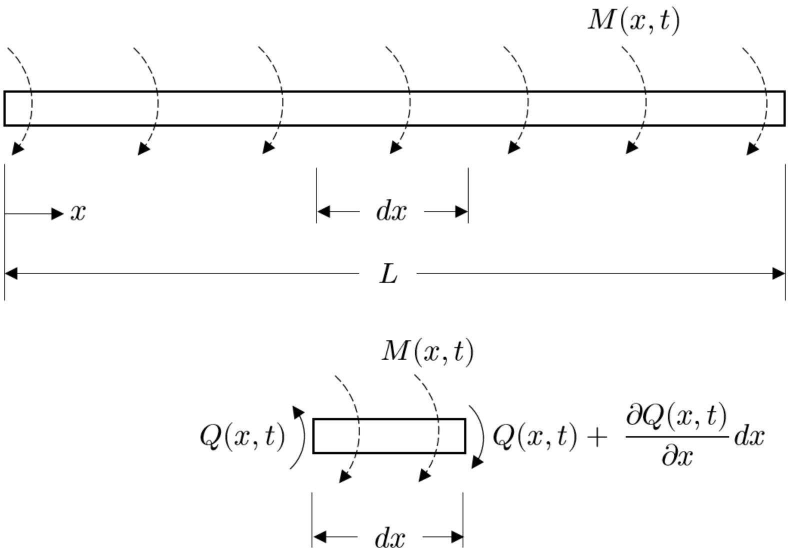

Figure 5.2: Continuous shaft line model for propeller moment estimation

For this model, a single shaft is considered connecting the propeller and motor. The values for the properties of the shaft, used in the model, are provided in Table C.2 in Appendix C.2.

Figure 5.2 shows the model of the propulsion shaft, with a differential element selected at a distance x along the shaft. The moments acting on the differential element are also shown, with $Q(x,t)$ representing the internal propulsion shaft torque and $M(x,t)$ the applied torsional moment. The propeller is located at $x = 0$ while the propulsion motor is situated at $x = L$. The model assumes a constant hollow circular cross section and consistent material properties along the length of the shaft. For the derivation of the model, an unknown distributed moment is initially assumed to act along the length of the shaft. The shaft is considered as having free boundary conditions at either end.

Euler's second law states that the sum of the applied torques on a body is equal to the rate of change of the angular momentum of that body (Inman, 2014). Equation 5.1 describes this dynamic equilibrium for the shaft.

$$\sum_i M_i = J\ddot{\theta} \tag{5.1}$$

where M_i represents the applied torques, J is the mass moment of inertia, and $\ddot{\theta}$ is the second derivative of the angular displacement with respect to time, or angular acceleration.

Stellenbosch University https://scholar.sun.ac.za

Substituting the torques applied to the differential element in Figure 5.2 into Equation 5.1 gives Equation 5.2, describing the dynamic equilibrium of the differential element.

$$-Q(x,t) + M(x,t)dx + \left(Q(x,t) + \frac{\partial Q(x,t)}{\partial x}dx\right) = J_0\frac{\partial^2\theta(x,t)}{\partial t^2}dx \tag{5.2}$$

where J_0 is the mass moment of inertia of the shaft per unit length, $Q(x,t)$ the internal torque at distance x, and $M(x,t)$ the externally applied distributed moment.

Rearranging Equation 5.2 and dividing all terms by dx gives Equation 5.3:

$$J_0\frac{\partial^2\theta(x,t)}{\partial t^2} - \frac{\partial Q(x,t)}{\partial x} = M(x,t) \tag{5.3}$$

From solid mechanics the torque in the shaft at x is related to the torsional deflection at x by (Shames and Pitarresi, 2000):

$$Q(x,t) = GJ\frac{\partial\theta(x,t)}{\partial x} \tag{5.4}$$

with G being the shear modulus and J representing the polar moment of inertia of the cross section.

Substitution of Equation 5.4 into Equation 5.3 yields

$$J_0\frac{\partial^2\theta(x,t)}{\partial t^2} - \frac{\partial}{\partial x}\left(GJ\frac{\partial\theta(x,t)}{\partial x}\right) = M(x,t) \tag{5.5}$$

Assuming a uniform cross section of the shaft, the mass moment of inertia per unit length, J_0, becomes ρJ with ρ the density of the shaft. Furthermore, J can be factored out of the partial derivative with regards to x and Equation 5.5 becomes

$$\rho J\frac{\partial^2\theta(x,t)}{\partial t^2} - GJ\frac{\partial^2\theta(x,t)}{\partial x^2} = M(x,t) \tag{5.6}$$

Modal superposition, see Appendix A, is applied in order to transform the partial differential Equation 5.6 into a set of ordinary differential equations. Separation of variables (Inman, 2014), as discuessed in Section 2.2, is used to obtain a solution for the angular displacement in terms of spatial and temporal solutions. The angular displacement $\theta(x,t)$ can be described as:

$$\theta(x,t) = \sum_{n=0}^{N}\phi_n(x)q_n(t) \tag{5.7}$$

Stellenbosch University https://scholar.sun.ac.za

where N is the number of mode shapes used to describe the deflection of the shaft. The spatial solutions $\phi_n(x)$ are the mode shape values at x, and the temporal solutions $q_n(t)$ are the corresponding modal coordinates as functions of time.

As the shaft has free torsional boundary conditions and is able to rotate around its axis, the mode shapes are described by (Rao, 2007):

$$\phi_n(x) = A_n \cos\left(\frac{n\pi x}{L}\right), n = 0, 1, 2, ..., N \tag{5.8}$$

where the A_n are constant values determined from boundary conditions.

Note that the mode shape for $n = 0$ is a rigid body mode describing the free rotation, and is a constant. This can be seen in Equation 5.8 when substituting $n = 0$, which results in $\phi_0(x) = A_0$.

Substitution of Equation 5.7 into Equation 5.6 yields:

$$\rho J \sum_{n=0}^{N} \phi_n(x)\ddot{q}_n(t) - GJ \sum_{n=0}^{N} \phi_n''(x) q_n(t) = M(x,t) \tag{5.9}$$

where the overdots on $\ddot{q}_n(t)$ and the primes on $\phi''(x)$ represent the second derivatives with respect to t and x respectively.

Differentiating the mode shape with respect to x twice leads to:

$$\phi_n'(x) = \frac{d}{dx}\phi_n(x) = -A_n\left(\frac{n\pi}{L}\right)\sin\left(\frac{n\pi x}{L}\right) \tag{5.10}$$

$$\phi_n''(x) = \frac{d}{dx}\phi_n'(x) = -A_n\left(\frac{n\pi}{L}\right)^2\cos\left(\frac{n\pi x}{L}\right) = -\left(\frac{n\pi}{L}\right)^2\phi_n(x) \tag{5.11}$$

It should also be noted that the A_n values are assumed to be absorbed into the $q_n(t)$ values during solution, and are henceforth assumed equal to one. Substituting the second derivative of the mode shape into Equation 5.9 gives:

$$\rho J \sum_{n=0}^{N} \phi_n(x)\ddot{q}_n(t) + GJ \sum_{n=0}^{N} \left(\frac{n\pi}{L}\right)^2 \phi_n(x) q_n(t) = M(x,t) \tag{5.12}$$

The moment function $M(x,t)$ applied to the shaft consists of a number of loads applied to the ends of the shaft, as seen in Figure 5.3. The propeller, along with the hydrodynamic mass, is modelled as an inertial load while the hydrodynamic damping is modelled as a viscous damping force, both applied to the end of the shaft at $x = 0$. The ice induced loading is applied at the

Stellenbosch University https://scholar.sun.ac.za

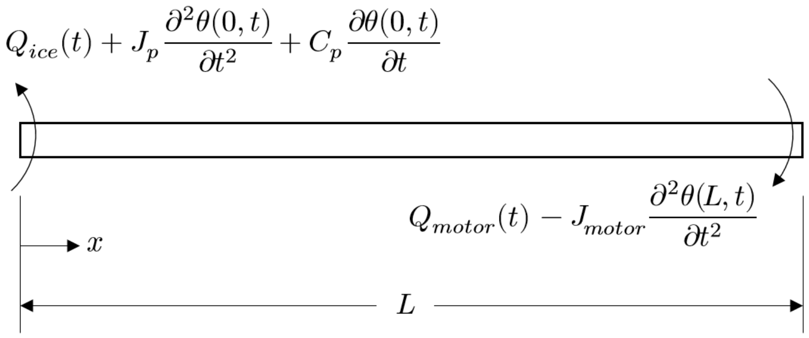

Figure 5.3: Torsional loads applied to propulsion shaft continuous model

propeller at $x = 0$ and the load from the motor is applied at $x = L$. The motor itself is also modelled as an inertial load.

The moment function becomes

$$\begin{aligned} M(x,t) = -\Bigg(& Q_{ice}(t)\delta(x-0) + J_p\frac{\partial^2\theta(0,t)}{\partial t^2}\delta(x-0) \\ &+C_p\frac{\partial\theta(0,t)}{\partial t}\delta(x-0)\Bigg) + Q_{motor}(t)\delta(x-L) - J_{motor}\frac{\partial^2\theta(L,t)}{\partial t^2}\delta(x-L) \end{aligned} \tag{5.13}$$

where δ is the Dirac-delta function which states for some constant value a:

$$\delta(x-a) = \begin{cases} 1 & x = a \\ 0 & x \neq a \end{cases} \tag{5.14}$$

The summation terms in Equation 5.12 are simplified using the orthogonality of the mode shapes (Inman, 2014):

$$\int_0^L \phi_m(x)\phi_n(x)dx = \begin{cases} 0 & n \neq m \\ \frac{L}{2} & n = m \neq 0 \\ L & n = m = 0 \end{cases} \tag{5.15}$$

Also note that

$$\int_0^L \phi_m(x)\delta(x-a)dx = \phi_m(a)\cdot H(L-a) \tag{5.16}$$

where H is the Heaviside step function

Stellenbosch University https://scholar.sun.ac.za

$$H(L-a)=\begin{cases} 0 & L<a \\ 1 & L\geq a \end{cases} \tag{5.17}$$

Substituting Equation 5.13 into Equation 5.12, multiplying through by $\phi_m(x)$ and integrating over the length of the shaft gives

$$\begin{aligned}\rho J\sum_{n=0}^{N}\int_0^L \phi_m(x)\phi_n(x)dx\cdot\ddot{q}_n(t)+GJ\sum_{n=0}^{N}\left(\frac{n\pi}{L}\right)^2\int_0^L \phi_m(x)\phi_n(x)dx\cdot q_n(t)=\\ -Q_{ice}(t)\int_0^L \phi_m(x)\delta(x-0)dx-J_p\frac{\partial^2\theta(0,t)}{\partial t^2}\int_0^L \phi_m(x)\delta(x-0)dx\\ -C_p\frac{\partial\theta(0,t)}{\partial t}\int_0^L \phi_m(x)\delta(x-0)dx+Q_{motor}(t)\int_0^L \phi_m(x)\delta(x-L)dx\\ -J_{motor}\frac{\partial^2\theta(L,t)}{\partial t^2}\int_0^L \phi_m(x)\delta(x-L)dx\end{aligned} \tag{5.18}$$

Substituting the relationships given in Equations 5.15 and 5.16 into Equation 5.18 yields a separate equation for each mode shape n. Equation 5.19 applies to the rigid body mode $n=0$, and Equation 5.20 applies to the flexible modes $n=1,2,...,N$.

$$\begin{aligned}\rho JL\ddot{q}_0(t)=-Q_{ice}(t)\phi_0(0)-J_p\frac{\partial^2\theta(0,t)}{\partial t^2}\phi_0(0)-C_p\frac{\partial\theta(0,t)}{\partial t}\phi_0(0)\\ +Q_{motor}(t)\phi_0(L)-J_{motor}\frac{\partial^2\theta(L,t)}{\partial t^2}\phi_0(L)\end{aligned} \tag{5.19}$$

$$\begin{aligned}\rho J\frac{L}{2}\ddot{q}_n(t)+GJ\frac{(n\pi)^2}{2L}q_n(t)=-Q_{ice}(t)\phi_n(0)-J_p\frac{\partial^2\theta(0,t)}{\partial t^2}\phi_n(0)\\ -C_p\frac{\partial\theta(0,t)}{\partial t}\phi_n(0)+Q_{motor}(t)\phi_n(L)-J_{motor}\frac{\partial^2\theta(L,t)}{\partial t^2}\phi_n(L)\end{aligned} \tag{5.20}$$

Using modal superposition, Equation 5.7, once again for the angular velocity and acceleration terms in Equations 5.19 and 5.20 and then collecting all the q_n terms on the left hand side yields the final equations for each mode shape used in the model, Equation 5.21 for the rigid body mode and Equation 5.22 for the flexible modes.

Stellenbosch University https://scholar.sun.ac.za

$$\rho JL\ddot{q}_0(t) + J_p\phi_0(0)\sum_{i=0}^{N}\phi_i(0)\ddot{q}_i(t) + J_{motor}\phi_0(L)\sum_{i=0}^{N}\phi_i(L)\ddot{q}_i(t) \\ + C_p\phi_0(0)\sum_{i=0}^{N}\phi_i(0)\dot{q}_i(t) = -Q_{ice}(t)\phi_0(0) + Q_{motor}(t)\phi_0(L) \quad (5.21)$$

$$\rho J\frac{L}{2}\ddot{q}_n(t) + J_p\phi_n(0)\sum_{i=0}^{N}\phi_i(0)\ddot{q}_i(t) + J_{motor}\phi_n(L)\sum_{i=0}^{N}\phi_i(L)\ddot{q}_i(t) \\ + C_p\phi_n(0)\sum_{i=0}^{N}\phi_i(0)\dot{q}_i(t) + GJ\frac{(n\pi)^2}{2L}q_n(t) = \\ - Q_{ice}(t)\phi_n(0) + Q_{motor}(t)\phi_n(L) \quad (5.22)$$

In addition, due to mode shape symmetry (Figure 5.4), the value of $q_n(t)$ for an even mode is negligible. This is due to the assumption that the torsionally symmetric shaft has purely asymmetric loads, that is the propeller moment is always opposite in direction to the motor torque. Thus, the contribution from the even modes can be neglected in the calculation (COMSOL, 2018). This assumption was also used in the model by Polić *et al.* (2016).

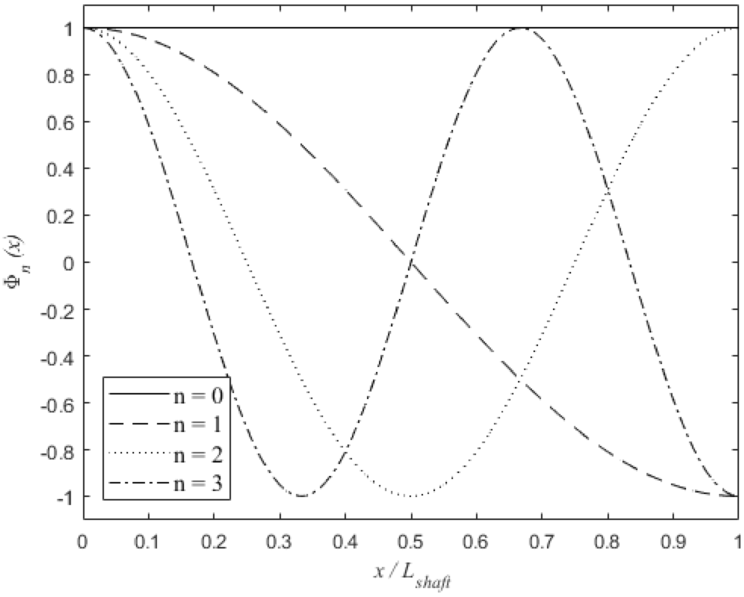

Figure 5.4: Propulsion shaft mode shapes

Stellenbosch University https://scholar.sun.ac.za

In this case, the value for $\phi_n(0) = 1$ and $\phi_n(L) = -1$. Also since the rigid mode is constant, $\phi_0(0) = \phi_0(L) = 1$. This simplifies Equations 5.21 and 5.22 to Equations 5.23 and 5.24 respectively, where the q_n terms for $n > 0$ represent only the uneven modes ($n = 1, 3, 5, \cdots, N-1$).

$$\begin{aligned}(\rho JL + J_p + J_{motor})\ddot{q}_0(t) + (J_p - J_{motor})\sum_{i=1}^{N/2}\ddot{q}_{(2i-1)}(t) + C_p\dot{q}_0(t)\\ + C_p\sum_{i=1}^{N/2}\dot{q}_{(2i-1)}(t) = -Q_{ice}(t) + Q_{motor}(t)\end{aligned} \tag{5.23}$$

$$\begin{aligned}\rho J\frac{L}{2}\ddot{q}_n(t) + (J_p - J_{motor})\ddot{q}_0(t) + (J_p + J_{motor})\sum_{i=1}^{N/2}\ddot{q}_{(2i-1)}(t) + C_p\dot{q}_0(t)\\ + C_p\sum_{i=1}^{N/2}\dot{q}_{(2i-1)}(t) + GJ\frac{(n\pi)^2}{2L}q_n(t) = -Q_{ice}(t) - Q_{motor}(t)\end{aligned} \tag{5.24}$$

Equations 5.23 and 5.24 can then be written in matrix form, which facilitates their solution using a time integration scheme (Appendix B).

$$\mathbf{J}\ddot{\mathbf{q}} + \mathbf{C}\dot{\mathbf{q}} + \mathbf{K}\mathbf{q} = \mathbf{Q} \tag{5.25}$$

where

$$\mathbf{q} = \{q_0\ q_1\ q_3\ q_5\ \cdots\ q_{N-1}\}^T$$

$$\mathbf{J} = \begin{bmatrix} \rho JL + J_p + J_{motor} & J_p - J_{motor} & \cdots & J_p - J_{motor} \\ J_p - J_{motor} & \rho J\frac{L}{2} + J_p + J_{motor} & \cdots & J_p + J_{motor} \\ \vdots & \vdots & \ddots & \vdots \\ J_p - J_{motor} & J_p + J_{motor} & \cdots & \rho J\frac{L}{2} + J_p + J_{motor} \end{bmatrix}$$

$$\mathbf{C} = \begin{bmatrix} C_p & C_p & \cdots & C_p \\ C_p & C_p & \cdots & C_p \\ \vdots & \vdots & \ddots & \vdots \\ C_p & C_p & \cdots & C_p \end{bmatrix}$$

$$\mathbf{K} = \begin{bmatrix} 0 & 0 & 0 & 0 & \cdots & 0 \\ 0 & GJ\frac{(\pi)^2}{2L} & 0 & 0 & \cdots & 0 \\ 0 & 0 & GJ\frac{(3\pi)^2}{2L} & 0 & \cdots & 0 \\ 0 & 0 & 0 & GJ\frac{(5\pi)^2}{2L} & \cdots & 0 \\ \vdots & \vdots & \vdots & \vdots & \ddots & \vdots \\ 0 & 0 & 0 & 0 & \cdots & GJ\frac{((N-1)\pi)^2}{2L} \end{bmatrix}$$

Stellenbosch University https://scholar.sun.ac.za

$$\mathbf{Q} = \begin{Bmatrix} -Q_{ice}(t) + Q_{motor}(t) \\ -Q_{ice}(t) - Q_{motor}(t) \\ \vdots \\ -Q_{ice}(t) - Q_{motor}(t) \end{Bmatrix}$$

This derivation of the model includes only the influence of the propeller and motor inertias. However, there are other inertias that could influence the response of the propulsion shaft such as bearings, couplings, or flanges. These can be taken into account in the same manner as the propeller and motor inertias, by projecting them onto the modal coordinates, and included in the equations of motion. For example, including a bearing with an inertia of J_b situated at some point x_b along the shaft would alter Equations 5.21 and 5.22 as follows:

$$\begin{aligned} \rho J L\ddot{q}_0(t) + J_p\phi_0(0)\sum_{i=0}^{N}\phi_i(0)\ddot{q}_i(t) + J_{motor}\phi_0(L)\sum_{i=0}^{N}\phi_i(L)\ddot{q}_i(t) \\ + J_b\phi_0(x_b)\sum_{i=0}^{N}\phi_i(x_b)\ddot{q}_i(t) + C_p\phi_0(0)\sum_{i=0}^{N}\phi_i(0)\dot{q}_i(t) = \\ - Q_{ice}(t)\phi_0(0) + Q_{motor}(t)\phi_0(L) \end{aligned} \tag{5.26}$$

$$\begin{aligned} \rho J\frac{L}{2}\ddot{q}_n(t) + J_p\phi_n(0)\sum_{i=0}^{N}\phi_i(0)\ddot{q}_i(t) + J_{motor}\phi_n(L)\sum_{i=0}^{N}\phi_i(L)\ddot{q}_i(t) \\ + J_b\phi_n(x_b)\sum_{i=0}^{N}\phi_i(x_b)\ddot{q}_i(t) + C_p\phi_n(0)\sum_{i=0}^{N}\phi_i(0)\dot{q}_i(t) \\ + GJ\frac{(n\pi)^2}{2L}q_n(t) = -Q_{ice}(t)\phi_n(0) + Q_{motor}(t)\phi_n(L) \end{aligned} \tag{5.27}$$

Again, considering mode shape symmetry and the constant rigid mode, $\phi_0(0) = \phi_0(L) = \phi_0(x_b) = \phi_n(0) = 1$ and $\phi_n(L) = -1$. Equations 5.26 and 5.27 can be simplified to:

$$\begin{aligned} (\rho JL+J_p+J_{motor}+J_b)\ddot{q}_0(t)+(J_p-J_{motor})\sum_{i=1}^{N/2}\ddot{q}_{(2i-1)}(t)+J_b\sum_{i=1}^{N/2}\phi_{(2i-1)}(x_b)\ddot{q}_i(t) \\ + C_p\dot{q}_0(t) + C_p\sum_{i=1}^{N/2}\dot{q}_{(2i-1)}(t) = -Q_{ice}(t) + Q_{motor}(t) \end{aligned} \tag{5.28}$$

Stellenbosch University https://scholar.sun.ac.za

$$\begin{aligned}\rho J\frac{L}{2}\ddot{q}_n(t) + (J_p - J_{motor} + J_b\phi_n(x_b))\ddot{q}_0(t) + (J_p + J_{motor})\sum_{i=1}^{N/2}\ddot{q}_{(2i-1)}(t)\\ + J_b\phi_n(x_b)\sum_{i=1}^{N/2}\phi_{(2i-1)}(x_b)\ddot{q}_i(t) + C_p\dot{q}_0(t)\\ + C_p\sum_{i=1}^{N/2}\dot{q}_{(2i-1)}(t) + GJ\frac{(n\pi)^2}{2L}q_n(t) = -Q_{ice}(t) - Q_{motor}(t)\end{aligned} \tag{5.29}$$

The inclusion of these extra inertial terms can be repeated for as many additional inertias as required.

Similarly, any extra damping components, such as that from bearings, could be taken into account in this manner.

The model could also have been derived using the description in Figure 5.5 instead of that in Figure 5.2. In this case, the mode shapes are derived using the propeller and motor inertias as boundary conditions, instead of using the free-free boundary condition modes and projecting the inertias onto them.

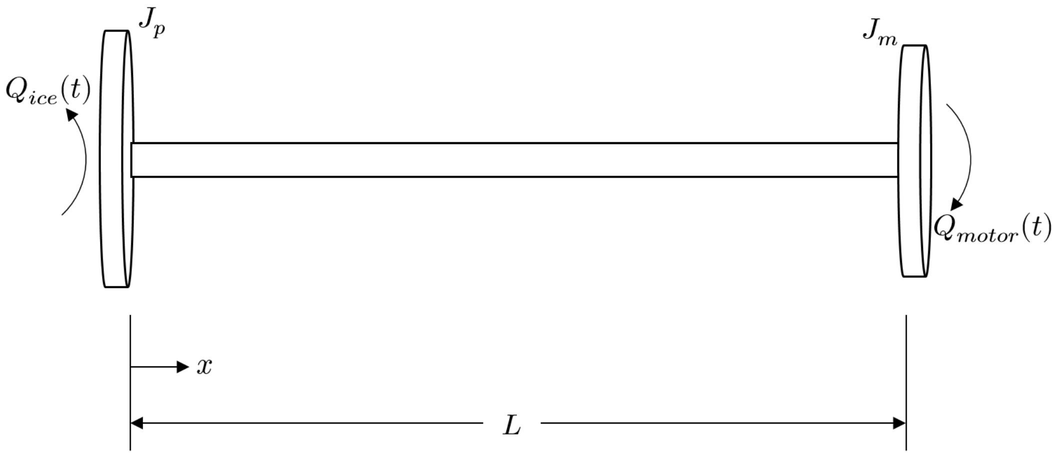

Figure 5.5: Alternate continuous shaft line model for propeller moment estimation

The derivation of the model would have been the same, other than the mode shapes which would be (Rao, 2007):

$$\phi(x) = A_n\left(\cos\left(\frac{\alpha_n x}{L}\right) - \frac{\alpha_n}{\beta_1}\sin\left(\frac{\alpha_n x}{L}\right)\right) \tag{5.30}$$

where

Stellenbosch University https://scholar.sun.ac.za

$$\beta_1 = \frac{\rho J L}{J_p} \tag{5.31}$$

$$\beta_2 = \frac{\rho J L}{J_{motor}} \tag{5.32}$$

$$\tan \alpha = \frac{\alpha \left(\beta_1 + \beta_2\right)}{\alpha^2 - \beta_1 \beta_2} \tag{5.33}$$

This would require that the α value be determined numerically for each mode shape needed for the solution. The reasons for instead selecting the first derivation were:

- it avoids the need for an extra numerical calculation for each mode shape.
- the free-free boundary condition mode shape (Equation 5.8) is easier to integrate, differentiate, and make general computations with.
- the method of projecting inertias onto the modes allows for the easy inclusion of inertias at any distance x along the beam, instead of just at the ends.

5.2 Forward solution of the continuous model

The continuous model was compared to the discrete model to verify whether they achieve similar results in solving a forward problem. For the forward problem the input ice induced loading is known and the internal shaft torque is unknown. The internal torque at a distance x along the shaft can be calculated using

$$Q(x,t) = GJ\frac{\partial \theta(x,t)}{\partial x} = GJ\sum_{n=0}^{N} \phi_n'(x) q_n(t) \tag{5.34}$$

while the displacement, velocity, and acceleration respectively can be determined using

$$\theta(x,t) = \sum_{n=0}^{N} \phi_n(x) q_n(t) \tag{5.35}$$

$$\dot{\theta}(x,t) = \sum_{n=0}^{N} \phi_n(x) \dot{q}_n(t) \tag{5.36}$$

$$\ddot{\theta}(x,t) = \sum_{n=0}^{N} \phi_n(x) \ddot{q}_n(t) \tag{5.37}$$

Stellenbosch University https://scholar.sun.ac.za

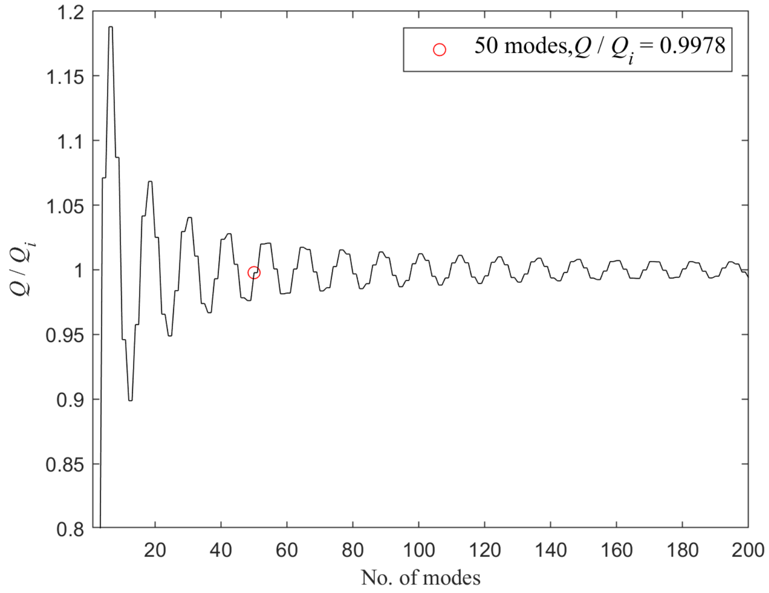

Figure 5.6: Convergence of internal steady-state torque for increasing number of mode shapes in forward problem

The model is evaluated using the IACS Case 1 for 4 bladed propellers during 90° single-blade impact sequence, used by Rolls-Royce in their ice impact simulation of the SAA II shaft line (Rolls-Royce AB, 2010*a*), as shown in Figure 4.4. The case load is applied as the ice induced loading (Q_{ice}) in the model. The motor load is modelled as having a constant value, so as to compare the results with that of the discrete model. The solution is obtained using the JWH-α numerical integration scheme (Appendix B.2). Reasons for the selection of this scheme are expanded on in Section 5.3.

The number of mode shapes selected for the simulation was determined by considering the steady-state response of the model. At steady state, the internal torque of the propulsion shaft at a given location is constant. For the forward solution with constant motor torque, the internal torque at steady state at any location on the propulsion shaft should be equal to the motor torque. Thus the correct value of the internal torque is known. The ratio between the internal torque calculated during the forward solution and the known internal torque was determined for increasing mode shapes, and provided in Figure 5.6. The results in Figure 5.6 were determined using both even and uneven modes.

It can be seen from Figure 5.6 that as the number of modes in the forward solution increases, the error decreases as expected. However it should be noted that the error oscillates, with the oscillation also decreasing as more modes are used. The smallest errors are achieved by selecting a number of modes at which

Stellenbosch University https://scholar.sun.ac.za

the oscillation crosses, or is close to crossing, a value of one for the ratio.

Figure 5.6 also shows that the influence of the even modes is negligible, as assumed in the derivation of the model. This is seen in the near zero change in the ratio from an uneven mode to an even one, appearing as horizontal steps in the figure.

It was decided to include 50 mode shapes in the solution, leading to an error on the steady-state internal torque of 0.22 percent.

The results of the solution for the internal torque from both the continuous and the discrete models are provided for comparison in Figure 5.7. The location chosen for comparison was near to the propeller. This was due to the internal torque in the discrete model varying after each lumped mass, while the internal torque in the continuous model varies along the length of the shaft. Choosing a location near to the propeller mitigates the variation as both the discrete and continuous models have accounted for a similar inertia by this point. The results for the discrete model are taken from the first shaft between J_1 and J_3 in Figure 4.2, while the results for the continuous model were taken from a location 5 m along the shaft from the propeller.

It can be seen from Figure 5.7(a) that the two models achieve similar solutions for the internal torque values. The differences in the torque values arise mainly from the fact that the discrete model only calculates the response for large sections of the shaft, while the continuous model calculates the response at the exact location. It thus becomes difficult to directly compare the results.

Furthermore, from Figure 5.7(b), it can be seen that the models deliver well matching responses from 0 Hz to 68 Hz. Following this, the differences in the results are due to the differences in the natural frequencies of the two models. The natural frequencies of the continuous model account for the frequencies of the shaft, with the propeller and motor inertias added. The discrete model accounts for the inertias of the various components attached to the shaft such as bearings. The continuous model could be expanded to include these attachments by modelling them as inertial loads, as discussed at the end of Section 5.1, at the cost of increased model complexity.

As the first torsional mode is dominant in the forced torsional response of the propulsion shaft (Senjanović *et al.*, 2019), the agreement between the low frequency response of the two models is significant. The continuous model agrees well with the discrete model based on that originally used by Rolls-Royce AB (2010*a*,*b*,*c*) in the design of the propulsion shaft, and since used in its analysis (Ikonen *et al.*, 2014; De Waal, 2017; De Waal *et al.*, 2018*b*).

Stellenbosch University https://scholar.sun.ac.za

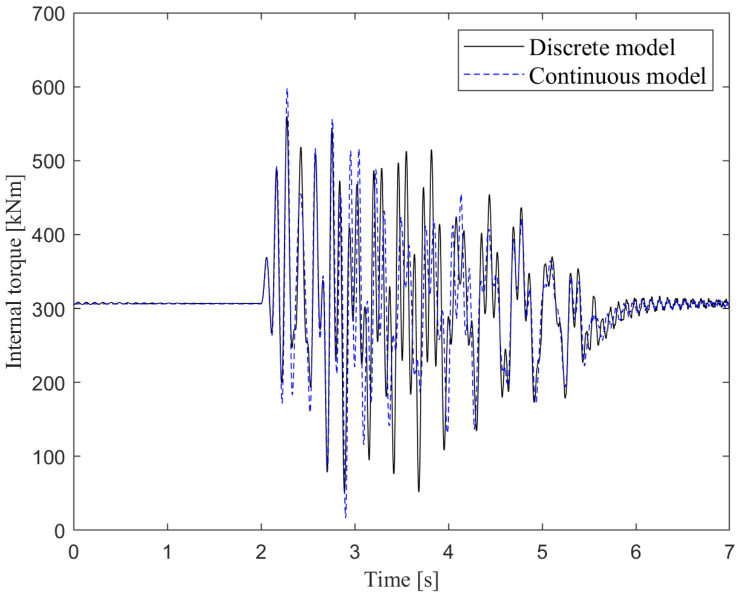

(a) Internal torque

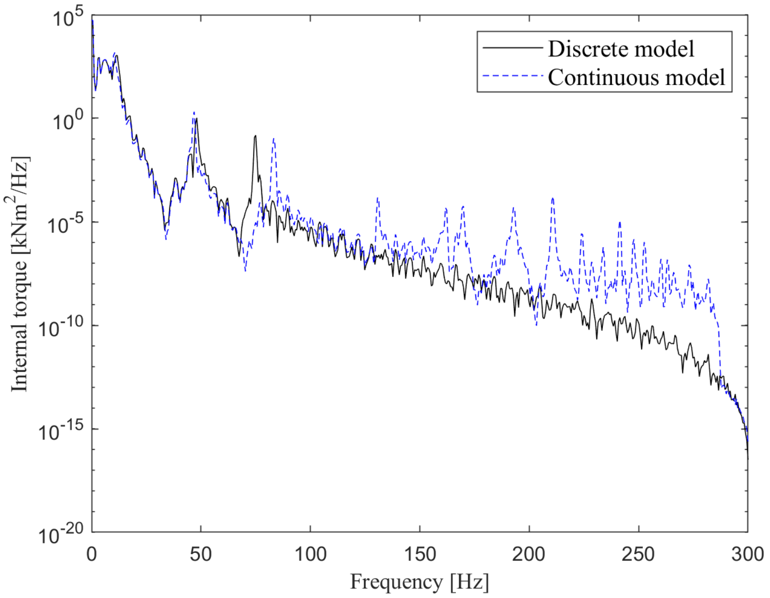

(b) Power spectral density

Figure 5.7: Comparison of discrete and continuous models for forward problem

Stellenbosch University https://scholar.sun.ac.za

5.3 Inverse solution of the continuous model

For the inverse problem the internal torque at a location is known, based on measurements, and the ice induced loading is unknown. The motor torque is treated as an unknown as well, instead of an inertial load. Though the motor torque is known through the CMU, it is measured at a sample rate of 1 Hz which is too low to be used in the calculation. It is therefore modelled as unknown and can be compared with the measured motor torque as a check that the model is solving correctly.

Therefore the inverse solution has $N + 2$ unknowns, namely q_0 to q_{N-1}, Q_{ice}, and Q_{motor}. The model thus needs a further two equations in order to solve for the unknowns directly at each time step. The equations chosen are based on the available measurement data on the shaft line, the internal torque and angular velocity measurements at some location x_a. The equations for the torque and velocity for the inverse model are those used for the forward model (Equations 5.34 and 5.36), except that the values for the torque and velocity are known before, or during, the simulation as opposed to them being solved for after a simulation. The equations are also altered to only consider the rigid and uneven modes in the inverse solution:

$$Q(x_a, t) = GJ\frac{\partial\theta(x_a, t)}{\partial x} = GJ\sum_{n=1}^{N/2}\phi'_{2n-1}(x_a)q_{2n-1}(t) \tag{5.38}$$

$$\dot{\theta}(x_a, t) = \phi_0(x_a)q_0(t) + \sum_{n=1}^{N/2}\phi_{2n-1}(x_a)\dot{q}_{2n-1}(t) \tag{5.39}$$

Equations 5.38 and 5.39 are solved along with the equations for each mode shape; Equation 5.40 for the rigid body mode and Equation 5.41 for the flexible modes.

$$\begin{split}(\rho JL + J_p + J_{motor})\ddot{q}_0(t) + (J_p - J_{motor})\sum_{j=1}^{N/2}\ddot{q}_{(2j-1)}(t) + C_p\dot{q}_0(t)\\ + C_p\sum_{i=1}^{N/2}\dot{q}_{(2i-1)}(t) = -Q_{ice}(t) + Q_{motor}(t)\end{split} \tag{5.40}$$

$$\begin{split}\rho J\frac{L}{2}\ddot{q}_n(t) + (J_p - J_{motor})\ddot{q}_0(t) + (J_p + J_{motor})\sum_{j=1}^{N/2}\ddot{q}_{(2j-1)}(t) + C_p\dot{q}_0(t)\\ + C_p\sum_{i=1}^{N/2}\dot{q}_{(2i-1)}(t) + GJ\frac{(n\pi)^2}{2L}q_n(t) = -Q_{ice}(t) - Q_{motor}(t)\end{split} \tag{5.41}$$

Stellenbosch University https://scholar.sun.ac.za

The matrix formulation follows below. The factors for the unknown loads, Q_{ice} and Q_{motor}, have been collected into the stiffness matrix K for each modal equation. The equation for the measured torque, Equation 5.38, is the second last row of the stiffness matrix K. The equation for the measured angular velocity, Equation 5.39, is the last row of the damping matrix C.

$$\mathbf{J}\ddot{\mathbf{q}} + \mathbf{C}\dot{\mathbf{q}} + \mathbf{K}\mathbf{q} = \mathbf{Q} \tag{5.42}$$

$$\mathbf{q} = \{q_0 \; q_1 \; q_3 \; q_5 \; \cdots \; q_{N-1} \; Q_{ice} \; Q_{motor}\}^T$$

$$\mathbf{J} = \begin{bmatrix} \rho JL + J_p + J_{motor} & J_p - J_{motor} & \cdots & J_p - J_{motor} & 0 & 0 \\ J_p - J_{motor} & \rho J\frac{L}{2} + J_p + J_{motor} & \cdots & J_p + J_{motor} & 0 & 0 \\ \vdots & \vdots & \ddots & \vdots & \vdots & \vdots \\ J_p - J_{motor} & J_p + J_{motor} & \cdots & \rho J\frac{L}{2} + J_p + J_{motor} & 0 & 0 \\ 0 & 0 & \cdots & 0 & 0 & 0 \\ 0 & 0 & \cdots & 0 & 0 & 0 \end{bmatrix}$$

$$\mathbf{C} = \begin{bmatrix} C_p & C_p & C_p & \cdots & C_p & 0 & 0 \\ C_p & C_p & C_p & \cdots & C_p & 0 & 0 \\ \vdots & \vdots & \vdots & \ddots & \vdots & \vdots & \vdots \\ C_p & C_p & C_p & \cdots & C_p & 0 & 0 \\ 0 & 0 & 0 & \cdots & 0 & 0 & 0 \\ \phi_0(x_a) & \phi_1(x_a) & \phi_3(x_a) & \cdots & \phi_{N-1}(x_a) & 0 & 0 \end{bmatrix}$$

$$\mathbf{K} = \begin{bmatrix} 0 & 0 & 0 & \cdots & 0 & 1 & -1 \\ 0 & GJ\frac{(\pi)^2}{2L} & 0 & \cdots & 0 & 1 & 1 \\ 0 & 0 & GJ\frac{(3\pi)^2}{2L} & \cdots & 0 & 1 & 1 \\ \vdots & \vdots & \vdots & \ddots & \vdots & \vdots & \vdots \\ 0 & 0 & 0 & \cdots & GJ\frac{((N-1)\pi)^2}{2L} & 1 & 1 \\ 0 & GJ\phi_1'(x_a) & GJ\phi_3'(x_a) & \cdots & GJ\phi_{N-1}'(x_a) & 0 & 0 \\ 0 & 0 & 0 & \cdots & 0 & 0 & 0 \end{bmatrix}$$

$$\mathbf{Q} = \begin{Bmatrix} 0 \\ 0 \\ \vdots \\ 0 \\ Q(x_0, t) \\ \dot{\theta}(x_0, t) \end{Bmatrix}$$

Stellenbosch University https://scholar.sun.ac.za

This matrix formulation leads to a badly scaled effective stiffness matrix in the implementation of the time integration scheme (Appendix B). This is due to the terms containing J_p, J_{motor}, C_p, and G being orders of magnitude higher than the unitary terms in the stiffness matrix and the last row in the damping matrix. The badly scaled matrix has a high condition number, which could lead to the amplification of noise in the calculation.

As the high condition number is as a result of the bad scaling, the problem is resolved by rescaling the smaller terms in the matrices above. The unitary terms are simply raised to the same order of magnitude as the other terms in the effective stiffness matrix. This then returns calculated values for Q_{ice} and Q_{motor} that need to be scaled up by the same factor. The last rows in the damping matrix and load vector Q, representing Equation 5.39, are also multiplied by a constant value to raise them to the same order of magnitude as the other terms in the effective stiffness matrix. This amounts to column and row scaling as is often employed to increase the accuracy of solutions of linear systems (Heath, 1997).

It should also be noted that any combination of two measured propulsion shaft parameters could be used to provide the extra equations necessary for the indirect propeller load estimation, provided the measured parameter can be represented in terms of the modal coordinates q_n. For example, two torque measurements at different locations could have been used, instead of a torque measurement and an angular velocity measurement.

The use of two different parameters (torque and angular velocity) makes the model more robust. In order to solve the system of equations, two extra equations were needed that were independent of one another to prevent an underdetermined system. If the same type of measurement were used twice, for example two torque measurements at different locations, there is a risk that at some point in the solution's time history these equations become sufficiently equivalent so as to result in a numerically near singular matrix. This could then lead to inaccurate results.

Furthermore, a limitation identified for the discrete model was the lack of angular velocity information. As stated in Section 4.5, a specified internal torque could occur at different propulsion shaft rotational speeds. This is due to the torque measurements not containing information about the control of the propulsion shaft. Thus, it was necessary to include a measurement that provides information about the control such as rotational displacement, velocity, or acceleration, of which the velocity is easily measurable. Adding the angular velocity information therefore improves the accuracy of the model.

The inverse solution of the continuous model was evaluated using results from the forward solution of the discrete model as input, using the IACS case 1 for 4 bladed propellers during 90° single-blade impact sequence as used by Rolls-Royce in their ice impact simulation of the SAA II shaft line (Rolls-Royce AB, 2010*a*).

The results from the forward solution of the discrete model were used as

Stellenbosch University https://scholar.sun.ac.za

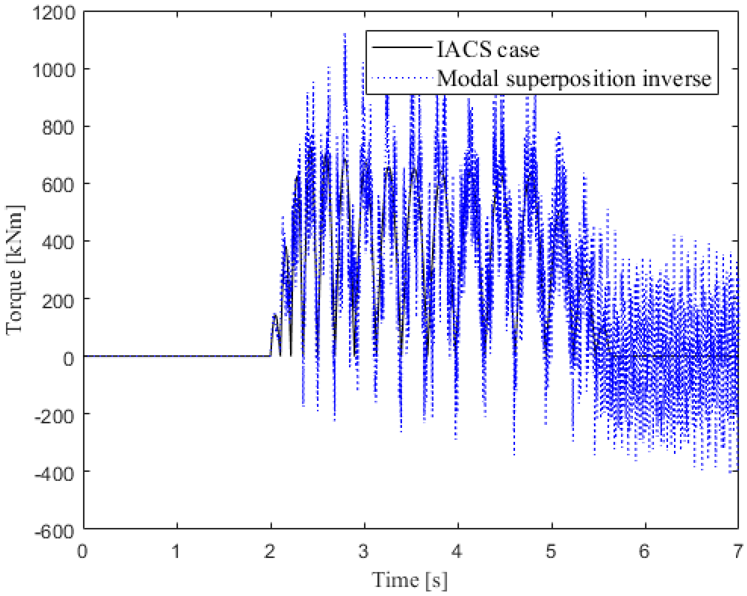

Figure 5.8: Comparison of estimated ice-induced propeller moment and IACS case, using the Newmark-β time integration scheme

input to the inverse problem to avoid inverse crime. The IACS case was used as input to the discrete model, and the internal torque and angular velocity calculated at the first shaft. These results were subsequently used as inputs for the continuous model inverse solution.

Initially, the inverse problem was solved using the Newmark-β time integration scheme as presented by Ikonen *et al.* (2014) and De Waal *et al.* (2018*b*). The estimated propeller moment is presented in Figure 5.8. The estimate is plotted with the input IACS case for comparison. It can be seen that, though the calculated load does somewhat follow the correct trend, it is not a useful estimate due to the high amplitude high frequency noise that is present.

Upon investigation, it was found that the high frequency noise was attributed to the Newmark-β time integration scheme. With the Newmark-β scheme, although second-order accuracy can be achieved, there is no high-frequency numerical damping (Kadapa, 2017). According to Kadapa (2017), a time integration scheme should be able to yield solutions free from non-physical high-frequency oscillations and the Newmark-β is limited in that it can not achieve this. It is also shown that errors can not be reduced simply by reducing the time step.

Kadapa (2017) recommends the use of better methods that possess high-frequency damping. The modified generalised-alpha method based on a first order system, referred to as JWH-α and described in Appendix B.2, was suggested (Kadapa, 2017; Kadapa *et al.*, 2017). This time integration was implemented and the results are presented in Figure 5.9.

Stellenbosch University https://scholar.sun.ac.za

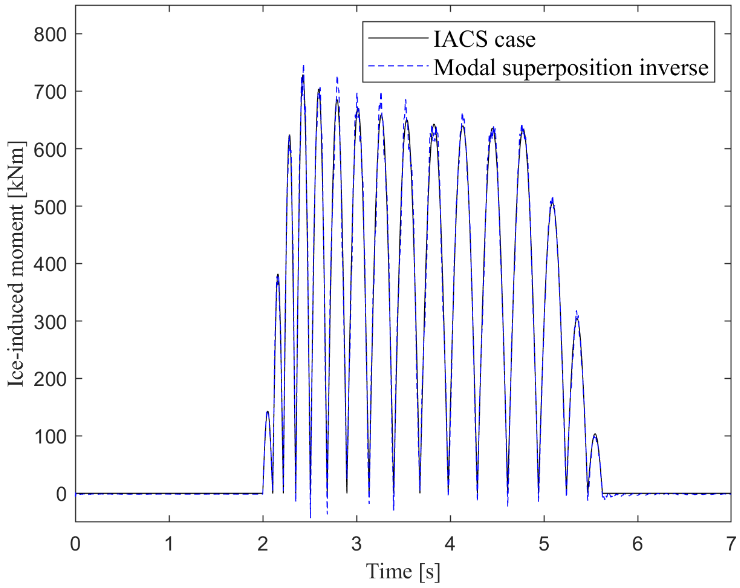

(a) Ice-induced propeller moment

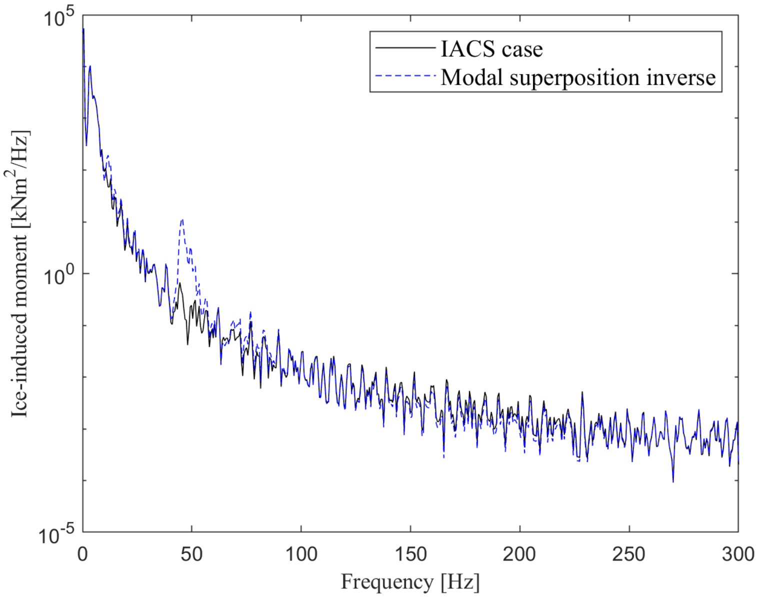

(b) Power spectral density

Figure 5.9: Comparison of estimated ice-induced propeller moment and IACS case, using the JWH-α time integration scheme

Stellenbosch University https://scholar.sun.ac.za

It can be seen in Figure 5.9 that the JWH-α scheme gives significantly better results, with the numerical high-frequency noise eliminated. Differences between the estimated moment and the input case occur, especially at the peaks and troughs. There is also a difference in the frequency content of the two loads around 48 Hz. These differences are due to the differing frequency content of the discrete model which was used to provide the input for the continuous model. Specifically, the difference around 48 Hz comes from the second natural frequency which is present in the forward results produced by the discrete model. Since the continuous model does not use the even modes in the solution, the contribution at this frequency is solved for as part of the external load.

In addition, the differences arise due to the nature of the discrete model used to generate the inputs. The discrete model produces constant torque between inertial elements, while angular velocity varies between these elements. This is contrary to the continuous model, where the torque and angular velocity can vary along the entire length of the shaft. Thus, slightly different results can arise depending on the location chosen along the shaft when performing the inverse calculation. Despite the differences, the estimated ice-induced load agrees well with the input IACS case.

The number of mode shapes selected for the simulation was determined by looking at the steady-state response of the model. The ratio between the internal torque calculated during the inverse solution and the input internal torque for the two different measurement locations is provided in Figure 5.10.

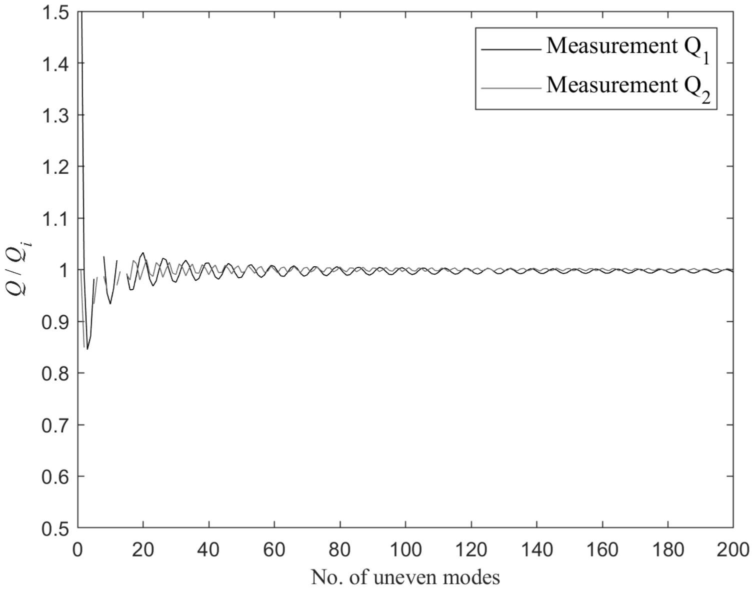

Figure 5.10: Convergence of internal steady-state torque for increasing number of mode shapes in inverse problem

Stellenbosch University https://scholar.sun.ac.za

Figure 5.10 follows a similar pattern to Figure 5.6, with an oscillating error that decreases as the number of modes increase. It is also shown that the number of modes necessary for an accurate calculation is influenced by the measurement location, as the different locations do not converge identically. Finally, it can be seen that there is missing data when using a lower number of modes for each measurement location. This is due to the algorithm failing when too few modes are used for the inverse calculation.

The relative error between the input internal torque and the internal torque calculated during the inverse solution was also determined, to ensure that the error introduced through the filtering of the input data is not significant. The relative error for the IACS case, as well as the first three cases from Table C.7, are presented in Figures 5.11 and 5.12 for locations Q_1 and Q_2 respectively.

As expected, the relative error decreases as more modes are used in the calculation. The relative error also approaches a minimum value, resulting in diminishing returns on accuracy as more modes are used. The errors converge to a value below 2 % for all cases, showing agreement between the input and the results produced by the model.

Based on the data presented in Figures 5.10, 5.11 and 5.12 the number of mode shapes selected for the inverse solution of the continuous model is 51. This results in errors of 0.39 % and 0.43 % for the steady-state internal torque at location Q_1 and Q_2 respectively, and a maximum relative error of 2.05 %.

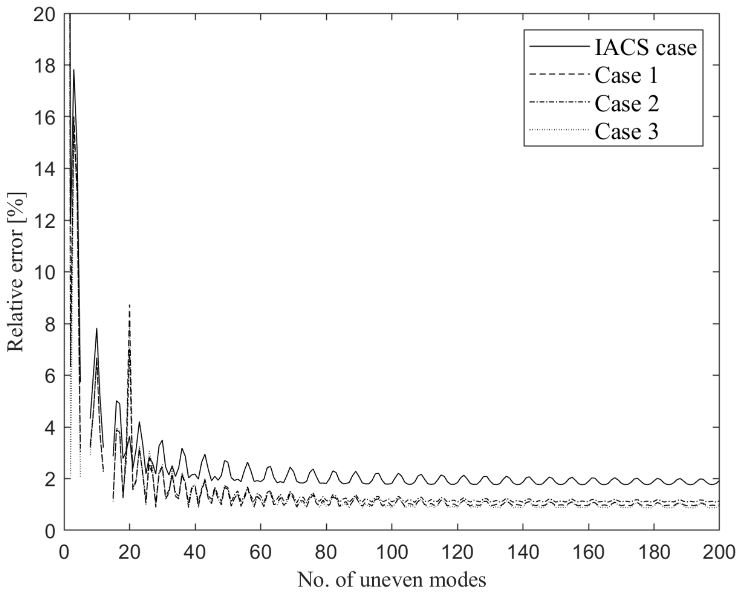

Figure 5.11: Relative error between calculated and measured internal torques at location Q_1

Stellenbosch University https://scholar.sun.ac.za

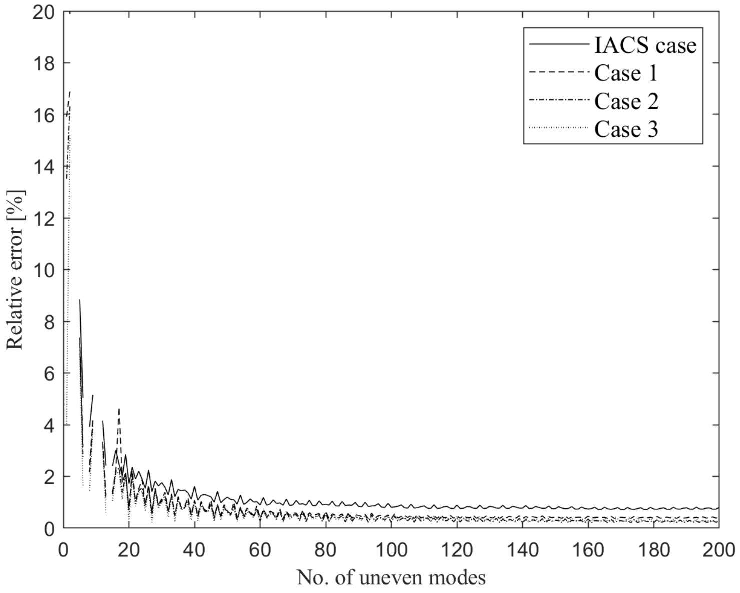

Figure 5.12: Relative error between calculated and measured internal torques at location Q_2

5.4 Evaluation of the continuous model

The continuous model has been evaluated and compared with the discrete model. The differences between propeller moment estimates and the efficiencies of the models were investigated (Section 5.4.1). Furthermore, the differences between inverse results from the continuous model when using different input locations were investigated, and compared to those from the discrete model (Section 5.4.2).

The evaluation of the continuous model, and comparison between the continuous and discrete models, was conducted using ice impacts extracted from the data recorded during the 2019 SCALE Spring Cruise of the SAA II. This voyage took place during October and November of 2019. Ice impacts were identified during ship operations within the marginal ice zone. During this voyage, torque was measured at two locations on the propulsion shaft, Q_1 and Q_2, as shown in Figure 3.2. The propulsion shaft angular velocity was recorded at location Q_1. The data was recorded during the evening of 30 October 2019. Fifty ice impact cases were extracted for analysis. The operational parameters and sea ice conditions for each case are presented in Table C.7 in Appendix C.

Finally, the model was compared to results from literature (Section 5.4.3).

Stellenbosch University https://scholar.sun.ac.za

5.4.1 Comparison between discrete and continuous models

One of the major differences between the two models is the capability of the continuous model to take the angular velocity of the propulsion shaft into account. This allows the continuous model to overcome a number of the discrete model's limitations, such as:

- the assumption of constant motor torque,
- the assumption of constant hydrodynamic torque,
- the assumption of initial conditions,
- and the assumption of constant propeller pitch.

To illustrate the above points, Case 1 from Table C.7 is used. The measured internal torque at location Q_1 is presented in Figure 5.13 for this case. The case consists of a single main ice impact on the propeller, followed by milling.

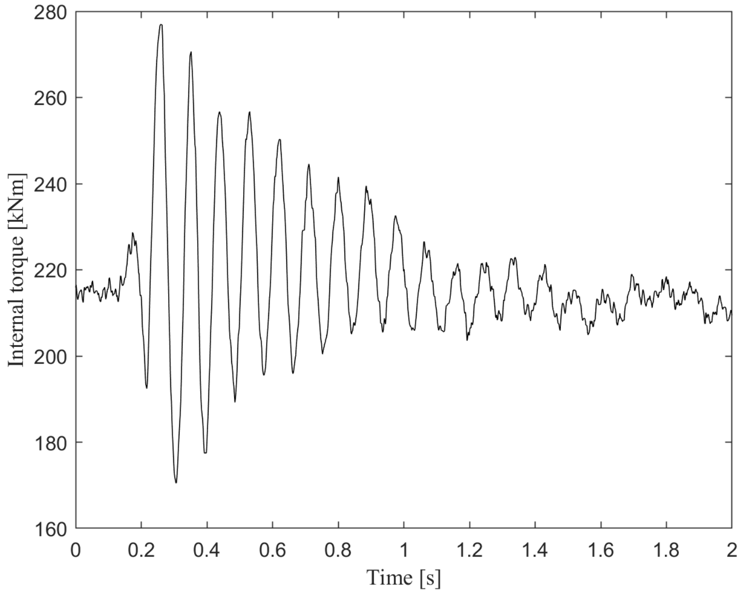

Figure 5.13: Internal propulsion shaft torque Q_1 for Case 1

Firstly, the results from the continuous model, when assuming a constant motor torque, are compared to the discrete model's results. For this comparison, the second extra equation describing the measured velocity is not used for the inverse solution of the continuous model. Instead, an iterative optimisation problem was solved. The difference between the known internal torque

Stellenbosch University https://scholar.sun.ac.za

and the calculated internal torque for some input external load was minimised (Equation 5.43).

$$\text{minimize } f(q_n) = Q(x,t) - GJ\sum_{n=0}^{N} \phi_n'(x)q_n(t) \tag{5.43}$$

The external load that would cause the function $f(q_n)$ in Equation 5.43 to equal zero would lead to the optimal q_n values. Along with the motor torque, the hydrodynamic load was assumed constant which allows for direct comparison between the results from the two different models. Figure 5.14 provides the comparison of the two models' results, using Q_1 as the input measured torque.

It can be seen that there is good agreement between the estimated propeller moments from the two different models, Figures 5.14(a) and 5.14(b). The continuous model appears to have a better peak estimation, and better ability to capture the milling following the initial impact. Both models produce similar propulsion shaft angular velocities, Figure 5.14(c). And when the estimated moments are used to solve a forward problem, the results compare well to the measured input, Figure 5.14(d).

However, the main issue with these results is highlighted when comparing the calculated angular velocity to what was measured. Figure 5.15 provides a comparison between the measured propulsion shaft angular velocity, and that calculated by the models. The initial conditions assumed for the models' results are the initial measured value.

The angular velocities determined by the models initially follow a similar path to the measurement, and contain a similar ripple. After 0.4 seconds, it can be seen that the measured and calculated velocities vary significantly. This is due to the measurement capturing the controlled response of the motor, as it attempts to keep the propulsion shaft spinning at the set rotational speed. Due to this control, the motor torque increases to match the load that caused the propulsion shaft velocity to decrease. This control does not allow the rotational speed to vary as much as the models calculate.

Based on the comparison between the measured and calculated velocities presented in Figure 5.15, the following observations can be made about propeller moment and motor torque:

- The measured velocity drops sooner and to a lower value than the calculated velocities. Thus, the propeller moment shown in Figure 5.14(a) should have a larger initial peak that occurs sooner in time.

- The peaks that occur due to milling, those following the initial peak, should also be larger as the propeller would have a higher velocity when encountering that ice.

Stellenbosch University https://scholar.sun.ac.za

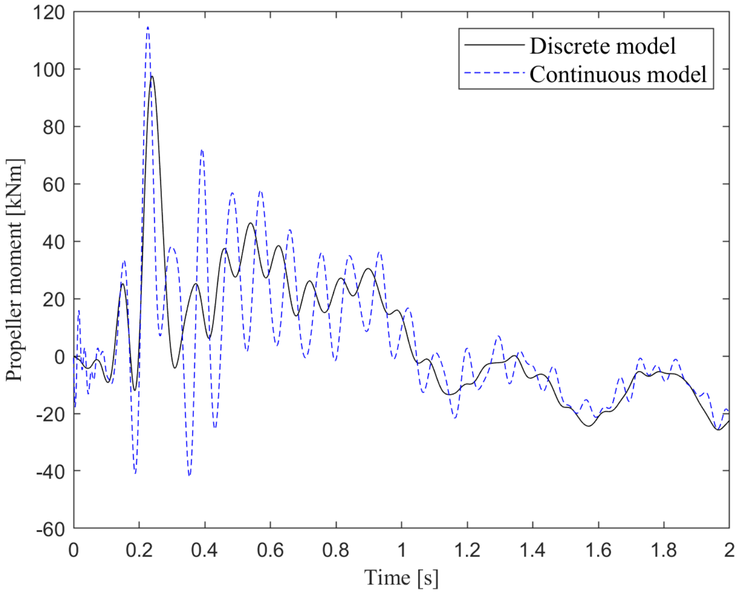

(a) Estimated ice-induced propeller moment

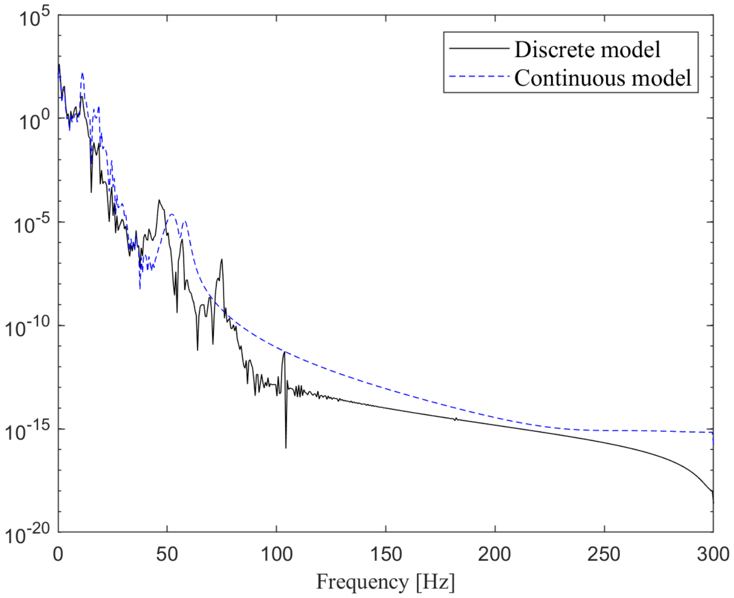

(b) Propeller moment power spectral density

Figure 5.14: Comparison of discrete and continuous models, when not using measured angular velocity, for Case 1

Stellenbosch University https://scholar.sun.ac.za

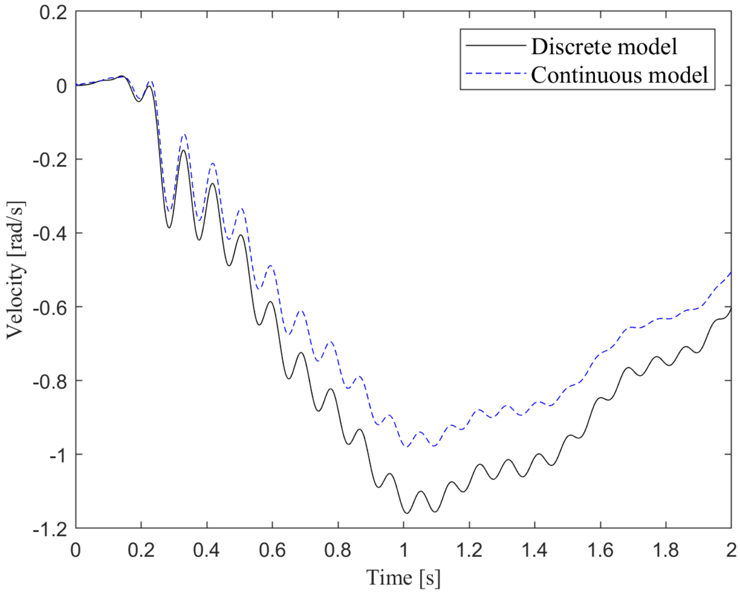

(c) Angular velocity

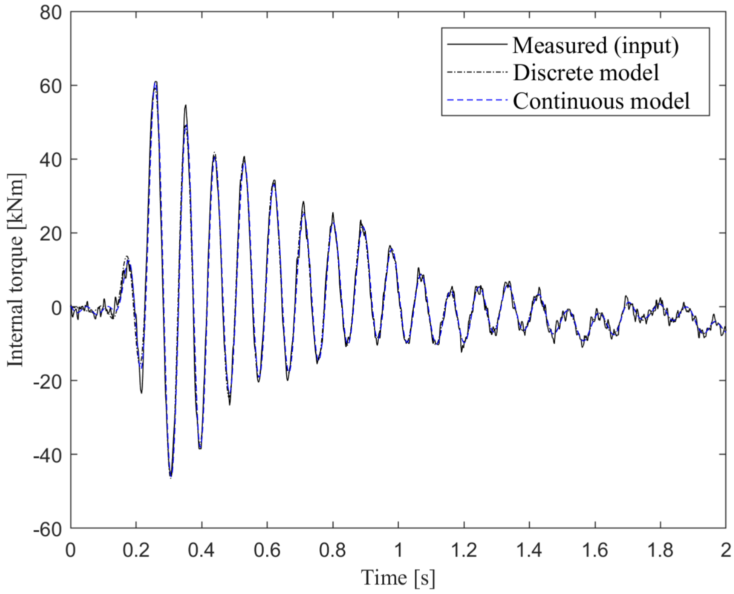

(d) Internal torque Q_1

Figure 5.14: (Continued) Comparison of discrete and continuous models, when not using measured angular velocity, for Case 1

Stellenbosch University https://scholar.sun.ac.za

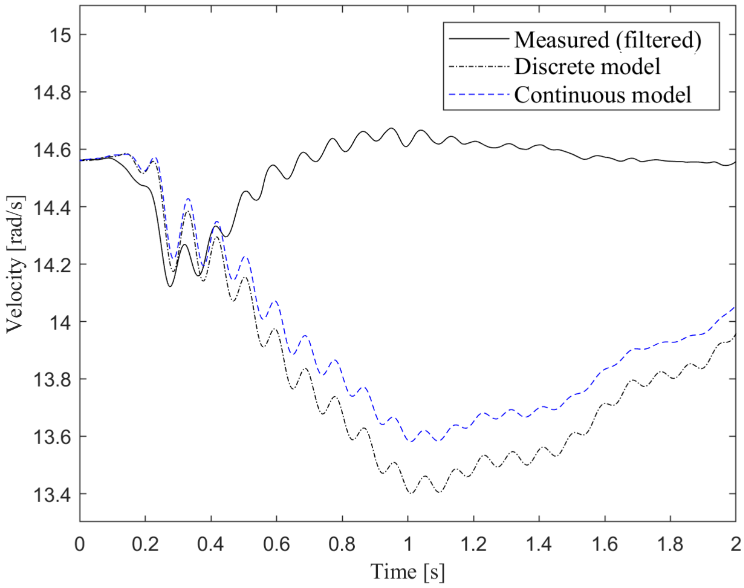

Figure 5.15: Propulsion shaft angular velocity at Q_1 for Case 1

- The motor torque should exhibit an increase to make up for the lost velocity due to the initial impact, and then return to its steady state value. In addition to this trend, the motor torque should exhibit ripples as the motor responds to the milling of the propeller.

Performing the inverse solution for Case 1 using the continuous model, while taking the measured angular velocity into account as in Section 5.3, gives the results in Figure 5.16.

The initial conditions for this solution are obtained by simulating the system at the initial internal torque and angular velocity for 10 seconds and allowing the system to reach equilibrium. The equilibrium values for the internal torque, and angular displacement, velocity, and acceleration are then used as initial values in the inverse solution.

It can be seen that the estimated propeller moment in Figure 5.16(a) differs from that in 5.14(a). The initial peak and milling are larger, as expected from the velocity measurement. The initial peak occurs just before that estimated by the discrete model. Furthermore, the motor torque shows an increase before returning to its steady state value and the ripple in response to the milling is also clearly visible in Figure 5.16(b). Applying these loads in a forward problem gives results that compare well with the measured inputs, Figures 5.16(c) and 5.16(d). These results suggest the inclusion of angular velocity information is crucial in order to get more accurate propeller moment estimates.

It should also be noted that the hydrodynamic load is not assumed constant and is included in the inverse solution. Thus, the propeller moment presented

Stellenbosch University https://scholar.sun.ac.za

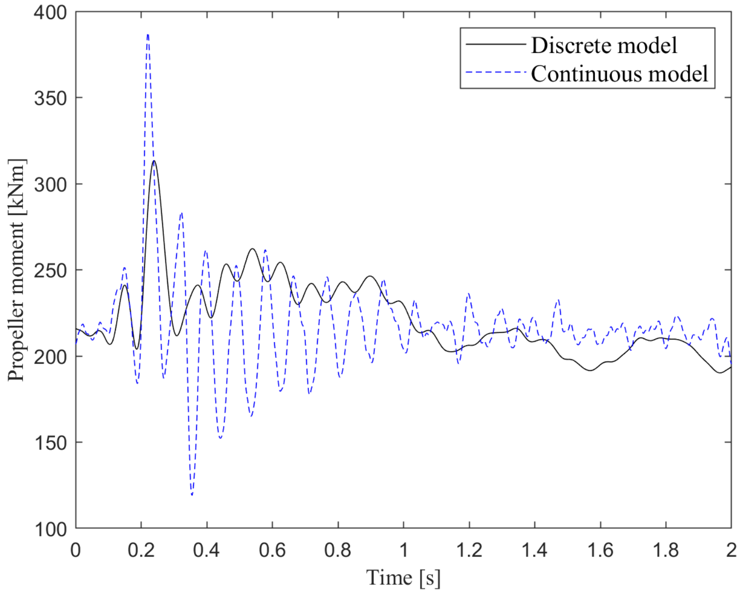

(a) Estimated propeller moment

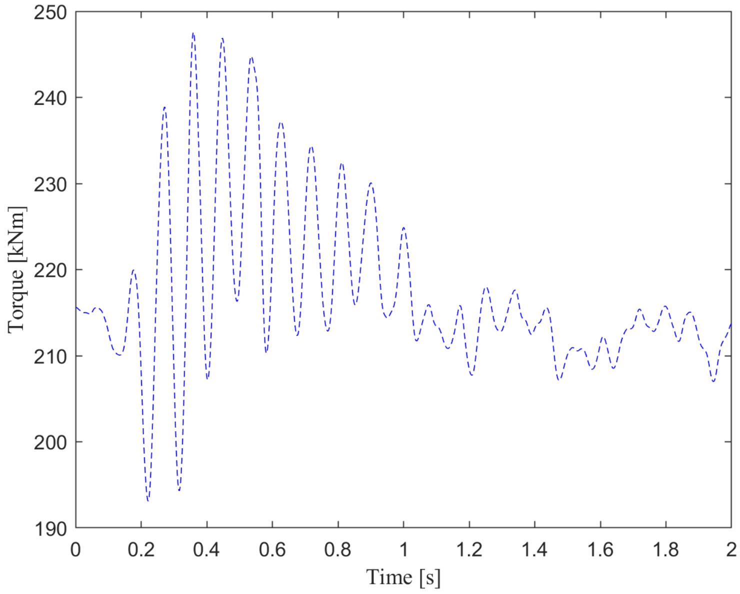

(b) Estimated motor torque

Figure 5.16: Results from continuous model for Case 1

Stellenbosch University https://scholar.sun.ac.za

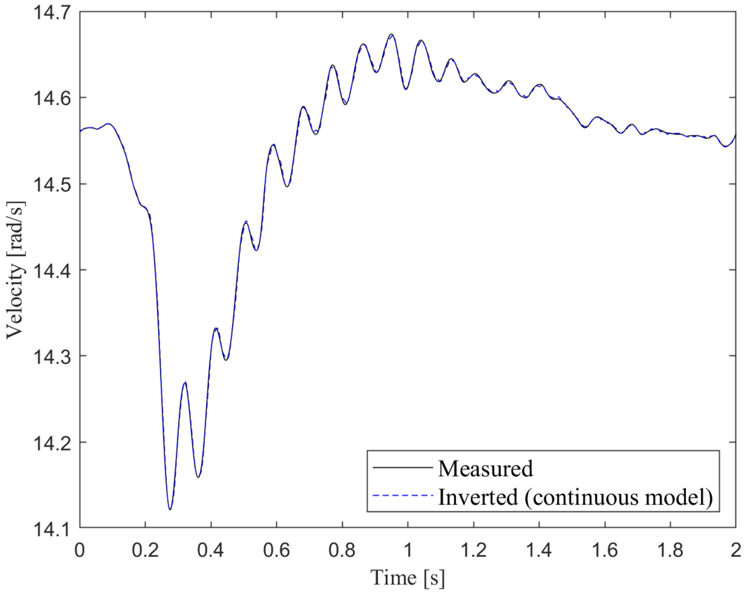

(c) Angular velocity

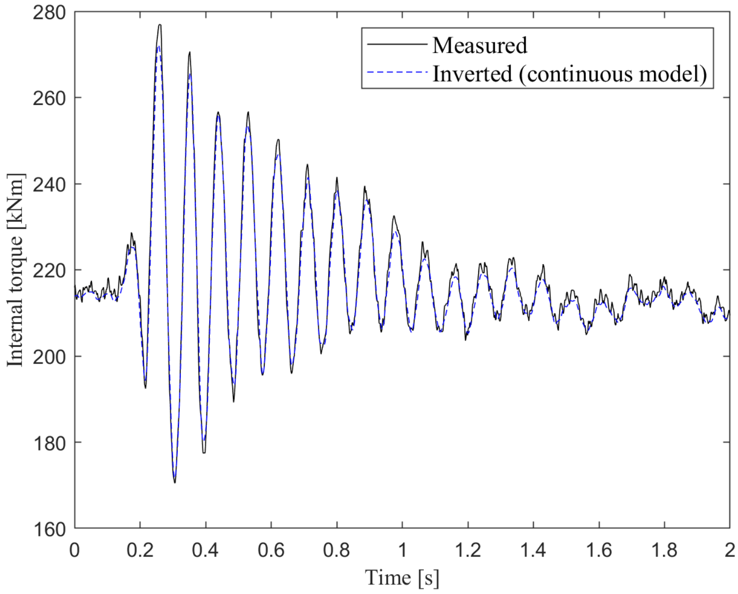

(d) Internal torque Q_1

Figure 5.16: (Continued) Results from continuous model for Case 1

Stellenbosch University https://scholar.sun.ac.za

in Figure 5.16(a) provides the total load acting on the propeller, including both the ice-induced moment and the hydrodynamic load. Any changes in the hydrodynamic load are directly taken into account during the solution by the continuous model. The hydrodynamic load is related to the hydrodynamic mass and damping, and calculated using the propeller pitch as described in Appendix C. The continuous model, like the discrete model, assumes a constant propeller pitch which in turn assumes a constant hydrodynamic mass and damping. As the SAA II makes use of propellers with variable pitch, this leads to an error in the offsets of the propeller ice and hydrodynamic moments when the pitch is different to that assumed when calculating the hydrodynamic mass and damping. However, as the actual hydrodynamic load is accounted for by the measured propulsion shaft torque and angular velocity, the offsets in the propeller ice and hydrodynamic moments cancel one another. The total propeller load, as shown in Figure 5.16(a), thus does not contain this offset error and it can be seen that the hydrodynamic load (215.9 kN in this case) agrees in Figures 5.16(a), 5.16(b), and 5.16(d).

Finally, the continuous and discrete models were compared in terms of their solution times. The cases in Table C.7 were analysed using both the discrete and continuous models, in order to make a comparison. The same computer used to evaluate the discrete model in Section 4.4.1 was used with MATLAB. Only the Tikhonov regularization method was considered in the solution of the discrete model. The solution times, from Table C.8, are presented graphically in Figure 5.17. For the discrete model, the solution times only reflect the time needed to perform the inverse solution. The time taken to set up the impulse response function is not taken into account, as this only need be done once for each measurement location. Similarly, for the continuous model the time taken to set up the necessary matrix equations is not taken into account as these can also be done once. The solution times presented for the continuous model include both the determination of initial values and the inverse solution.

The trend from the discrete model is the same as shown in Figure 4.14 where the solution time is roughly proportional to the square of the case duration. Also of note is that Case 46, with a duration of 18 seconds, was not solved by the discrete model due to insufficient memory.

The continuous model shows a significant improvement in solution time, increasing linearly with an increase in case duration. Furthermore, once the case duration reaches 2 seconds or longer the solution time becomes less than the case duration.

Stellenbosch University https://scholar.sun.ac.za

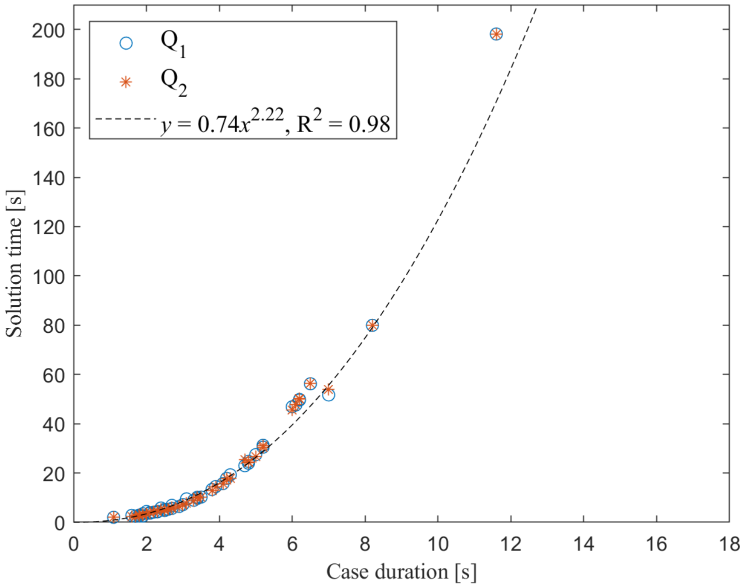

(a) Discrete model

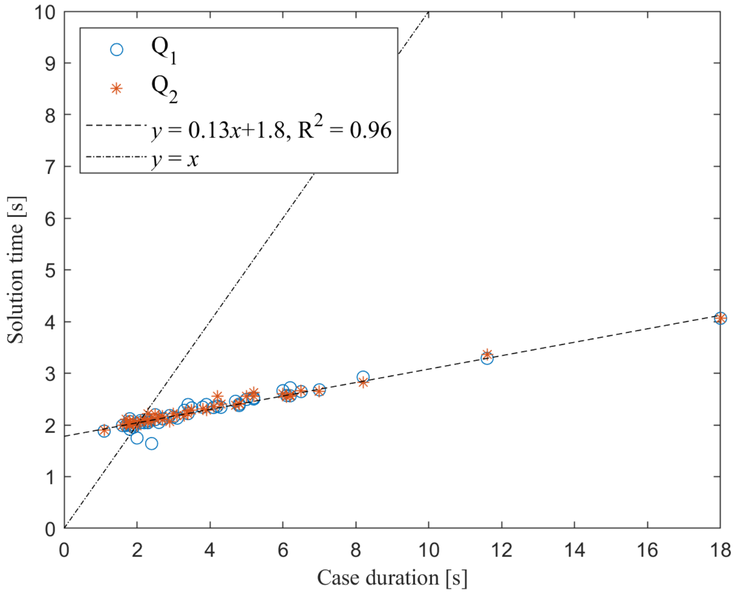

(b) Continuous model

Figure 5.17: Relationship between case study duration and solution time - comparison between discrete and continuous models

Stellenbosch University https://scholar.sun.ac.za

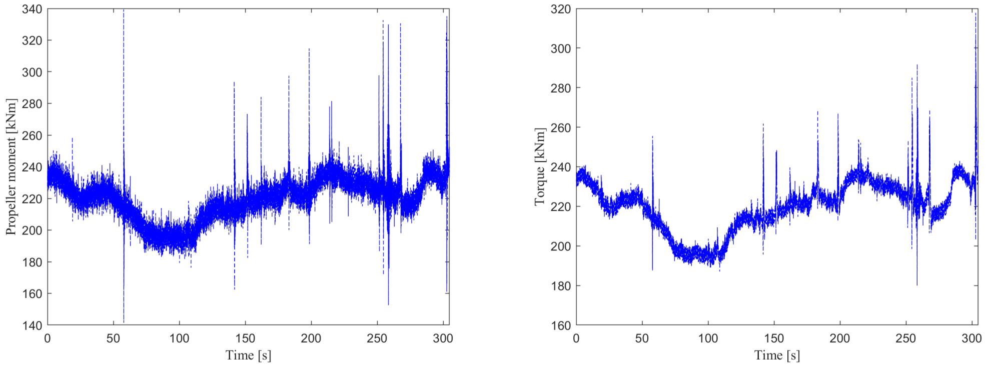

(a) Estimated propeller moment (b) Estimated motor torque

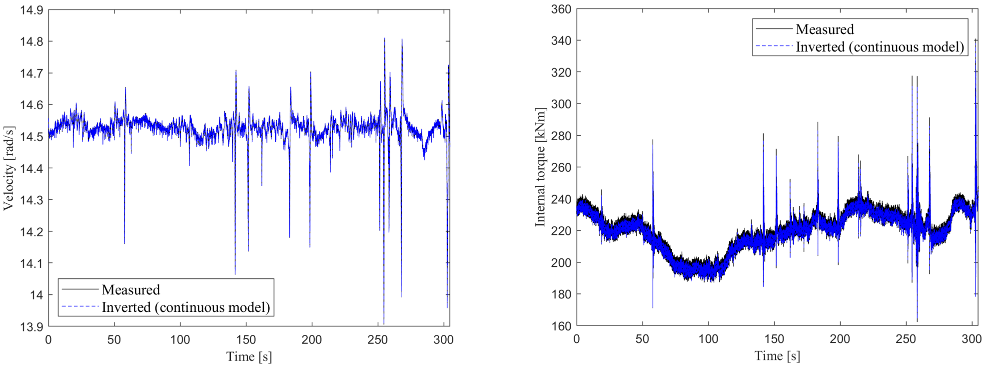

(c) Angular velocity (d) Internal torque Q_1

Figure 5.18: Results from continuous model for 5 minute recording on 30 October 2019 at 20:10:26

Since the measurement system on board the SAA II has been designed to save data every 5 minutes, a 5 minute file recorded at 20:10:26 on 30 October 2019 was supplied as input to the continuous model to determine its solution time. The solution time for the 5 minute file was 30.6 seconds, and the results are given in Figure 5.18.

Adding this point to Figure 5.17(b) gives the relationship shown in Figure 5.19. These solution times allow the continuous model to operate in close to real-time which is another improvement over the discrete model.

Stellenbosch University https://scholar.sun.ac.za

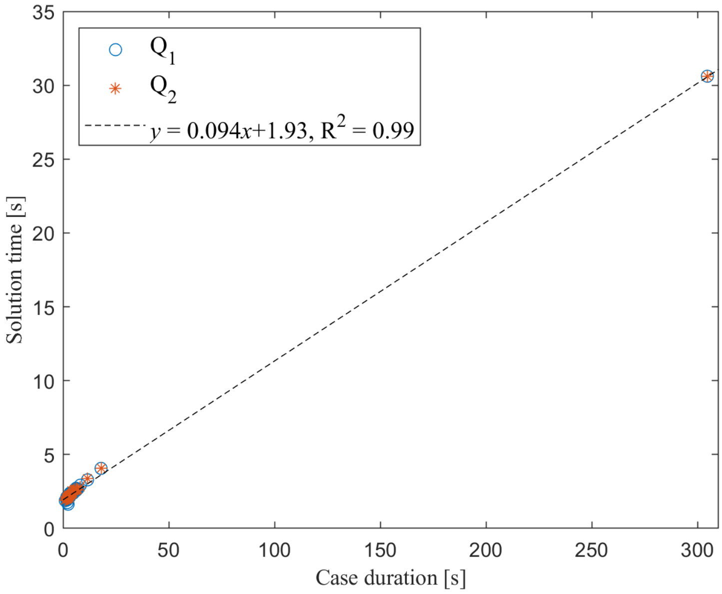

Figure 5.19: Relationship between case study duration and solution time - continuous model

5.4.2 Comparison between measurement locations for the inverse solution

As in the 2018/19 Antarctic voyage, during the 2019 SCALE Spring Cruise the propulsion shaft torque was measured at two separate locations to investigate whether the inverse model provided similar results irrespective of measurement location. These measurement locations were Q_1 and Q_2 in Figures 3.2 and 4.2.

The cases in Table C.7 were analysed using both the discrete and continuous models, in order to make a comparison. It should be noted that only the differences between the two measurement locations' internal torques were taken into account. This is due to the fact that the angular velocity was only measured at a single location.

For each case, the estimated external propeller moment was calculated from each measurement location. The relative errors and correlation coefficients between the external moments were calculated for each case using Equations 4.42 and 4.43. The relative errors and correlation coefficients between the measured torques for each case was also calculated. These are presented in Figures 5.20 and 5.21 respectively.

The first thing to note from Figures 5.20 and 5.21 is that the errors between the measured torques are lower than in Figures 4.15 and 4.16. They are however still amplified by the discrete model in its inverse solution, leading to larger errors between the estimated external moments. By comparison, the errors between the estimated external moments determined by the continuous model are much smaller and close to the errors between the measurements.

Stellenbosch University https://scholar.sun.ac.za

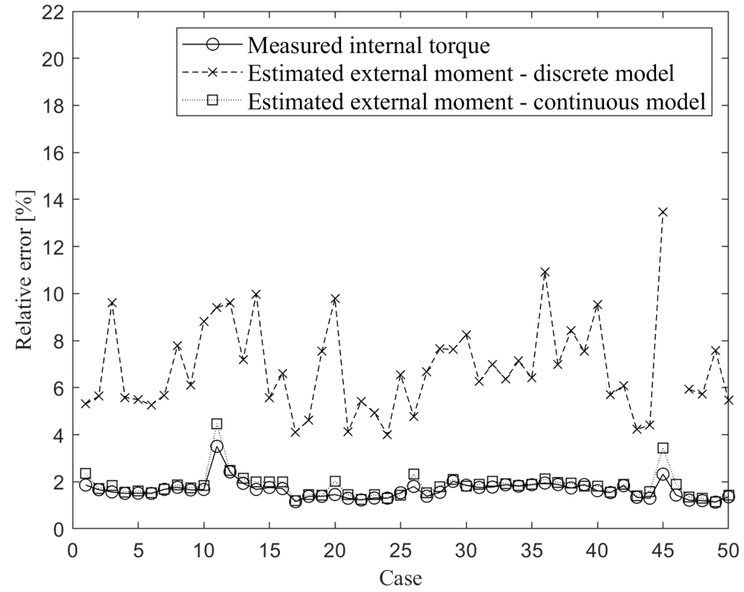

Figure 5.20: Relative errors for the measured internal torques and estimated propeller moments

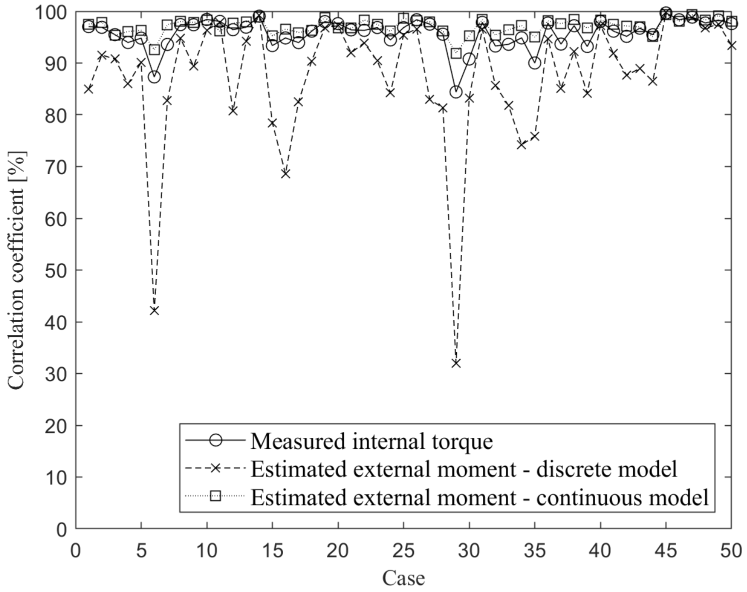

Figure 5.21: Correlation coefficients for the measured internal torques and estimated propeller moments

Stellenbosch University https://scholar.sun.ac.za

This means there is very little amplification of the errors when using the continuous model. As an example, the propeller moments determined for Case 1 from Table C.7 using the continuous model are shown in Figure 5.22 along with the measured internal torques.

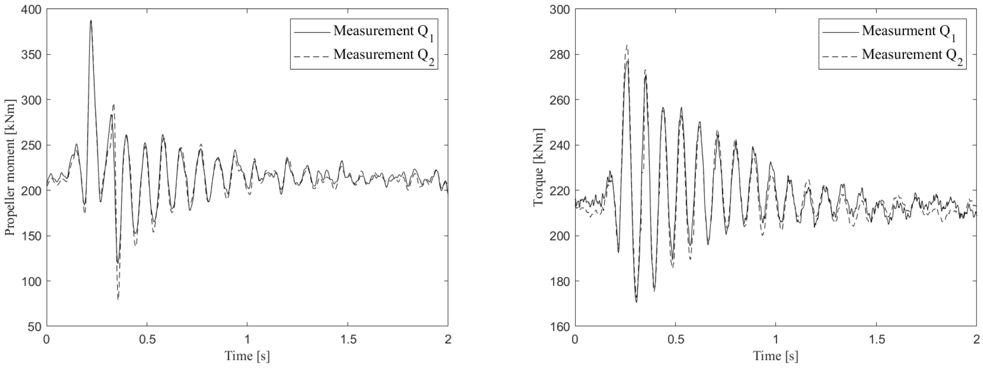

(a) Estimated propeller moment (b) Measured internal torque

Figure 5.22: Comparison between measurement locations for continuous model

The reduction in error suggests that the continuous model is a more accurate representation of the propulsion shaft than the discrete model.

5.4.3 Comparison to literature

The continuous model was evaluated using published data, the first data coming from Rolls-Royce AB (2010*a*) and the second from Polić *et al.* (2016, 2019).

5.4.3.1 Data from ice impact simulation by Rolls-Royce AB (2010*a*)

Both the discrete and continuous models were evaluated in the forward problem using the first IACS case from Rolls-Royce AB (2010*a*). The two models achieved similar results, but their results were different to those presented by Rolls-Royce AB (2010*a*). This was due to the discrete model assuming a constant motor torque, which was also assumed for the forward problem of the continuous model in order to make a comparison.

Rolls-Royce AB (2010*a*) made use of a model similar to the discrete model to perform a forward solution of an ice-impact simulation for the SAA II. The ice impact is given in Figure 5.23(a), and the motor-shaft torque and motor speed from Rolls-Royce AB (2010*a*) in Figures 5.23(b) and 5.23(c) respectively.

The external propeller moment that causes the results in Figures 5.23(b) and 5.23(c) was not provided by Rolls-Royce AB (2010*a*). The external moment was therefore reconstructed using the ice loading from Figure 5.23(a)

Stellenbosch University https://scholar.sun.ac.za

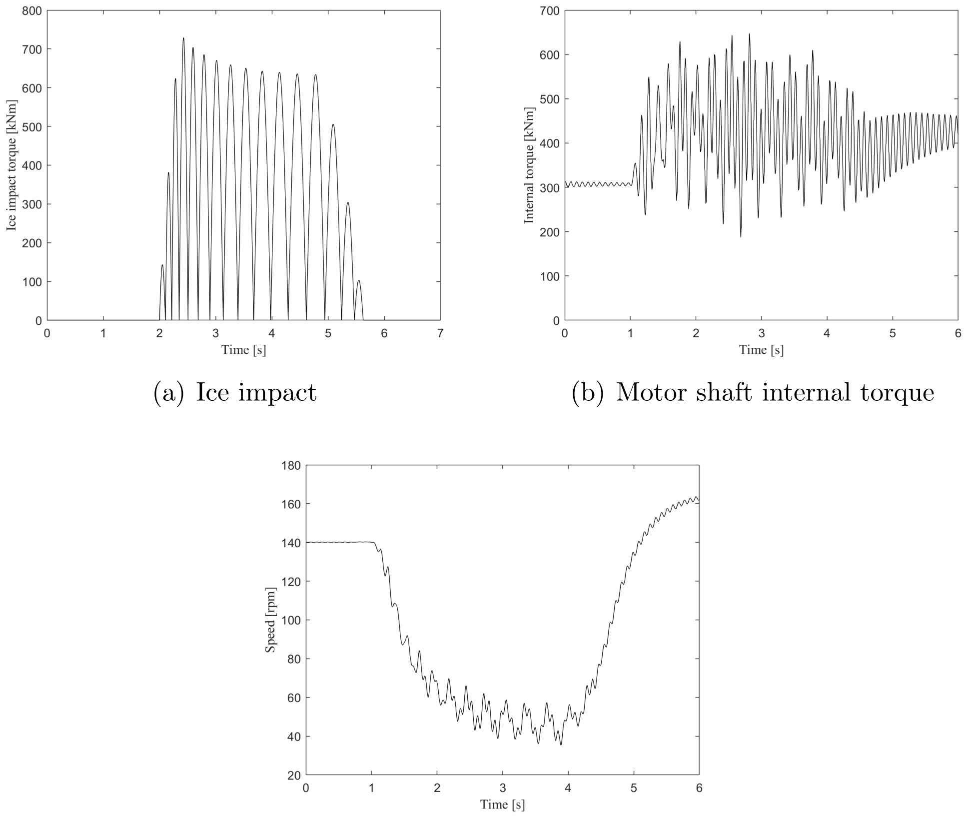

(a) Ice impact (b) Motor shaft internal torque

(c) Motor speed

Figure 5.23: Results from Rolls-Royce AB (2010*a*)

and the hydrodynamic torque. As there was no information about the change in the angular velocity of the propeller over time, the hydrodynamic torque had to be reconstructed using the motor speed provided by Rolls-Royce AB (2010*a*).

The continuous model was provided with the internal torque and velocity results from Rolls-Royce AB (2010*a*) (Figures 5.23(b) and 5.23(c) respectively) as input and the estimated propeller moment was determined. As the continuous model and the model used by Rolls-Royce AB (2010*a*) represent the same propulsion line, the continuous model's parameters were left unchanged. The results provided by Rolls-Royce AB (2010*a*) were for the motor shaft, which the continuous model does not consider. As such, the inputs were applied close to the motor inertia, at $x = 29.4$ m. The comparison between the actual propeller moment and that determined by the continuous model is provided in Figure 5.24.

The propeller moment estimated by the continuous model is similar to the actual propeller moment, with a relative error of 8.02% and a correlation of 98.36%. The errors between the first peak values could be due to the

Stellenbosch University https://scholar.sun.ac.za

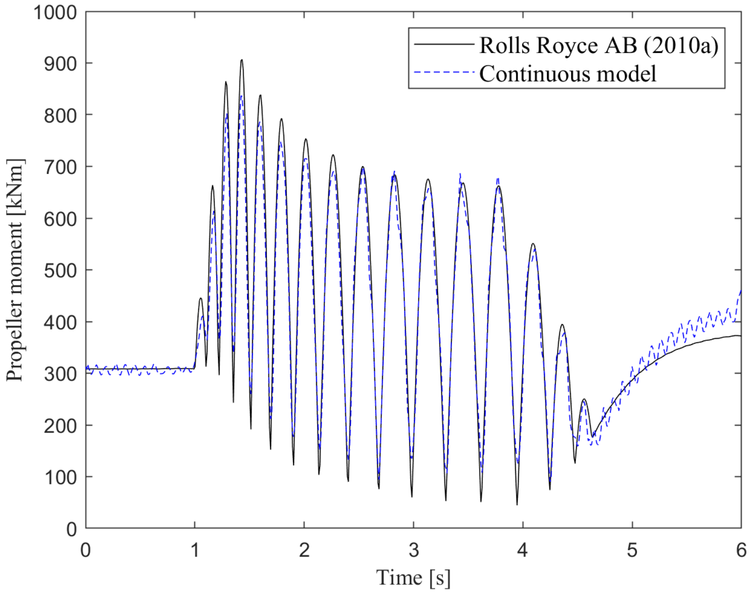

Figure 5.24: Comparison between propeller moments for ice impact simulation (Rolls-Royce AB, 2010*a*) and continuous model

continuous model not accounting for all the inertial components that Rolls-Royce AB (2010*a*) does. Furthermore, errors will arise as the results provided by Rolls-Royce AB (2010*a*) were for the motor shaft, which is not considered by the continuous model, and as such the location for the inputs was on the propulsion shaft close to the motor inertia.

5.4.3.2 Data from Polić *et al.* (2016, 2019)

A model of a shaft line was also developed by Polić *et al.* (2019) to perform inverse propeller moment estimations. The model similarly makes use of modal superposition to develop the equations of motion for each mode shape n:

$$J_n\ddot{q}_n(t) + C_n\dot{q}_n(t) + K_nq_n(t) = -Q_{prop}(t)\phi_n(0) + Q_{motor}(t)\phi_n(L) \tag{5.44}$$

However, Polić *et al.* (2019) assume that the contribution of the inertial terms ($J_n\ddot{q}_n$) in the equation of motion for flexible modes ($n > 0$) is negligible by assuming that the ratio between the frequency of the external moment and the natural frequencies of the shaft are small. Thus, this simplification relies on assuming that the frequency of the external propeller moment is far from resonance.

In contrast to the model developed by Polić *et al.* (2019), the continuous model developed here does not make these assumptions, and instead includes

Stellenbosch University https://scholar.sun.ac.za

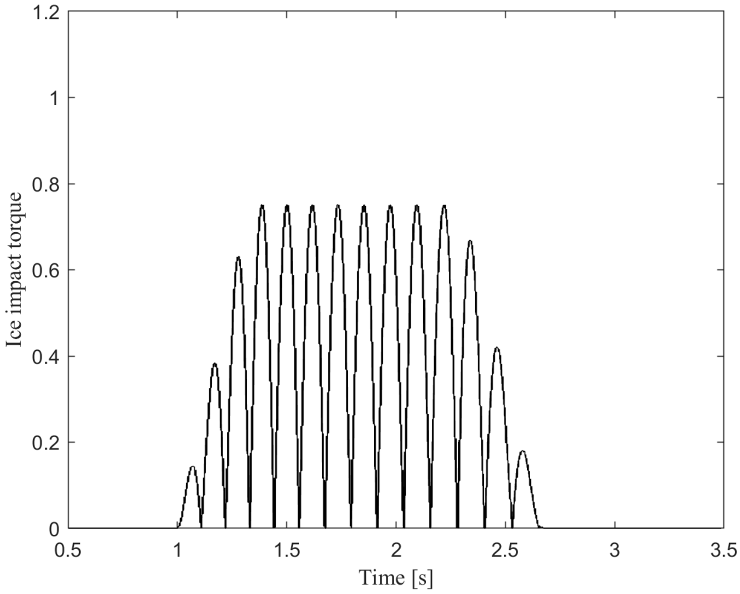

Figure 5.25: Design ice load for propulsion line case 1, adapted from Det Norske Veritas (2016)

the contribution from all modal inertial terms. The propeller damping is also projected onto the modal coordinates and considered by the model.

Polić *et al.* (2016) provide a propulsion system model developed using the bond graph method. This model is independent from the inverse model by Polić *et al.* (2019), and from the continuous model developed here. Data is provided for a propulsion shaft subjected to the ice impact described by the case 1 design ice load for propulsion line torque in Det Norske Veritas (2016), shown in Figure 5.25.

The full propeller moment, including the hydrodynamic load, and the resulting internal torque and propulsion shaft speed from Polić *et al.* (2016, 2019) is presented in Figure 5.26.

In order to test the continuous model against these results, it was necessary to alter the model parameters. Specifically, the propulsion shaft geometry and material properties, and the propeller and motor inertias were changed. The values of these parameters are given in Table C.3 in Appendix C.2. The measurement location was selcted as 11 m from the propeller. Note that the propeller damping was not taken into account during the inverse solution by Polić *et al.* (2019) and is thus considered to be zero for the continuous model. Also the time step of the continuous model was decreased to match the 1 kHz sample rate used by Polić *et al.* (2019).

The propulsion shaft torque and velocity, from Figures 5.26(b) and 5.26(c) respectively, were then used as the input to the continuous model. The inverse solution was performed and the results are compared to the actual propeller

Stellenbosch University https://scholar.sun.ac.za

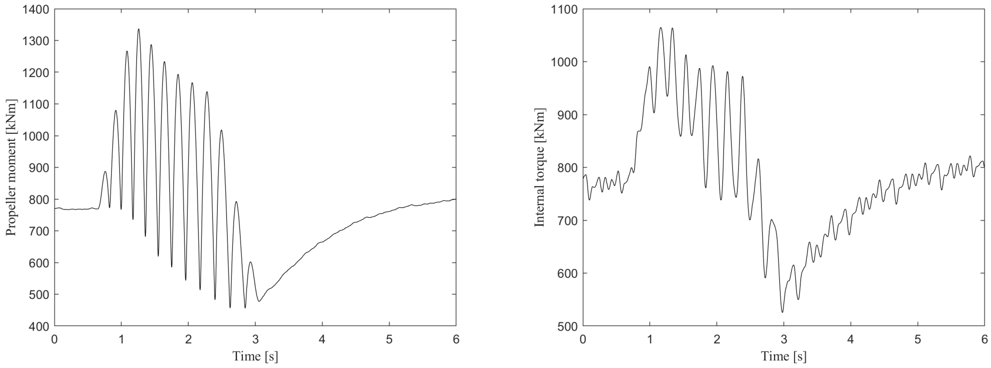

(a) External propeller moment, adapted from Polić *et al.* (2019)

(b) Internal torque, adapted from Polić *et al.* (2016)

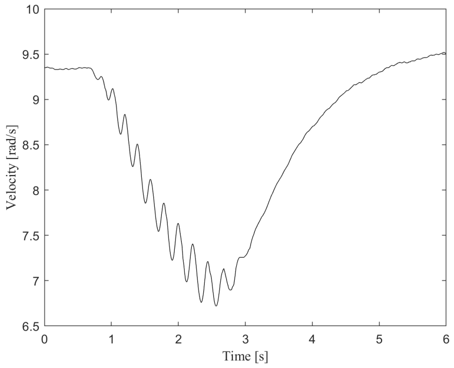

(c) Angular velocity, adapted from Polić *et al.* (2016)

Figure 5.26: Propeller moment and propulsion shaft response from Polić *et al.* (2016, 2019)

moment from Figure 5.26(a) in Figure 5.27(a).

Figure 5.27(a) shows that the continuous model delivers a well matched propeller moment estimate compared to the actual propeller moment. This result further validates the continuous model, as it is able to reproduce an estimated propeller moment from data produced by an independent model. In addition, it shows that the continuous model can be easily adapted to suit another propulsion shaft by altering the material and geometric properties.

In addition to testing the inputs directly, Polić *et al.* (2019) colour the inverse model inputs with noise according to Equation 5.45:

$$\hat{y}(t) = y(t) + u(t)e\bar{y} \tag{5.45}$$

with $y(t)$ the original signal as a function of time, $u(t)$ a signal describing the noise, and e set as a percentage of the mean of the signal $\bar{y}$.

Stellenbosch University https://scholar.sun.ac.za

The noise $u(t)$ was generated from uniformly distributed random numbers with a mean value of zero and a standard deviation of $\sqrt{1/3}$. The noise was then transformed into white ($1/f^0$), pink ($1/f$), and red ($1/f^2$) power spectral densities. White noise has the same power across the frequency range, while pink and red noise have more power in the lower frequency range. The noise signals were set as 1% ($e = 0.01$) of the mean signal values at steady state, as done by Polić *et al.* (2019), with the mean internal torque value equal to 770 kNm and the mean velocity value equal to 9.34 rad/s.

After the noise is added to the inputs, they are filtered using locally waited regression. This is done in the same manner as Polić *et al.* (2019), using the MATLAB *smooth* function with the *loess* setting which makes use of weighted linear least squares and a second degree polynomial for interpolation. The span for the smoothing function was the same as that used by Polić *et al.* (2019) for a signal sampled at 1 kHz, in this case 84.

The estimated propeller moments determined by the continuous model under these conditions are given in Figure 5.27. Contamination with pink noise results in the worst propeller moment estimate, with significant noise in the signal and errors on the peaks. Both white and red noise contamination result in a lower noise level on the estimated propeller moment, with lower peak errors.

The effect of noise on the different input signals, torque and velocity, was also investigated. This was achieved by adding noise to either the input torque or the input velocity. The resultant propeller moment estimates are given in Figure 5.28. The results shows that, for the level of 1% of the mean value, noise on the input velocity results in larger errors than noise on the input torque.

Stellenbosch University https://scholar.sun.ac.za

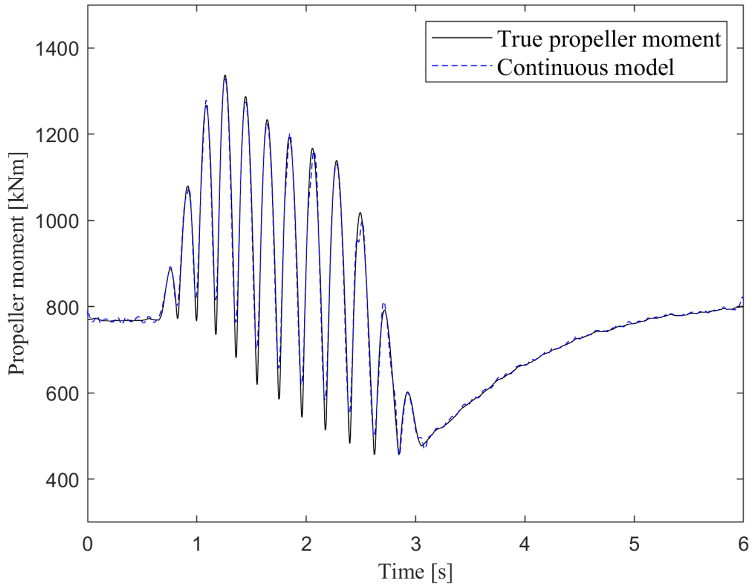

(a) No noise (Relative error - 2.15%, Correlation - 99.58%)

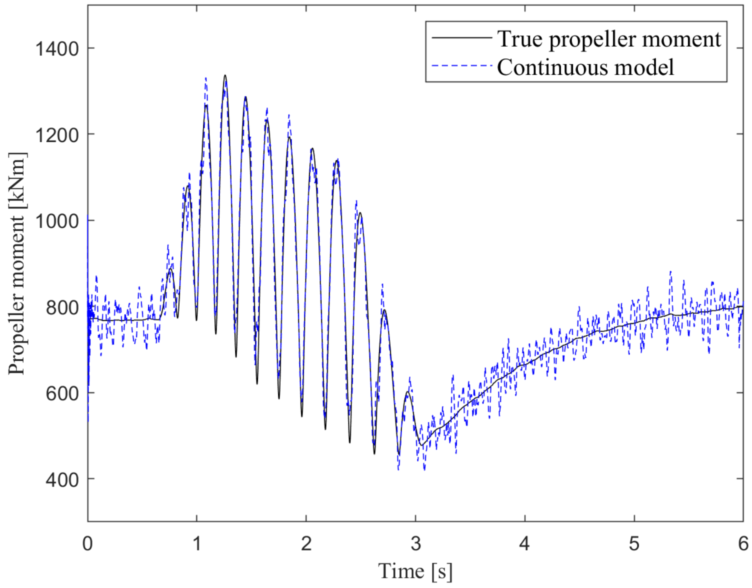

(b) White noise (Relative error - 4.64%, Correlation - 97.95%)

Figure 5.27: Estimated propeller moments from inputs coloured with noise

Stellenbosch University https://scholar.sun.ac.za

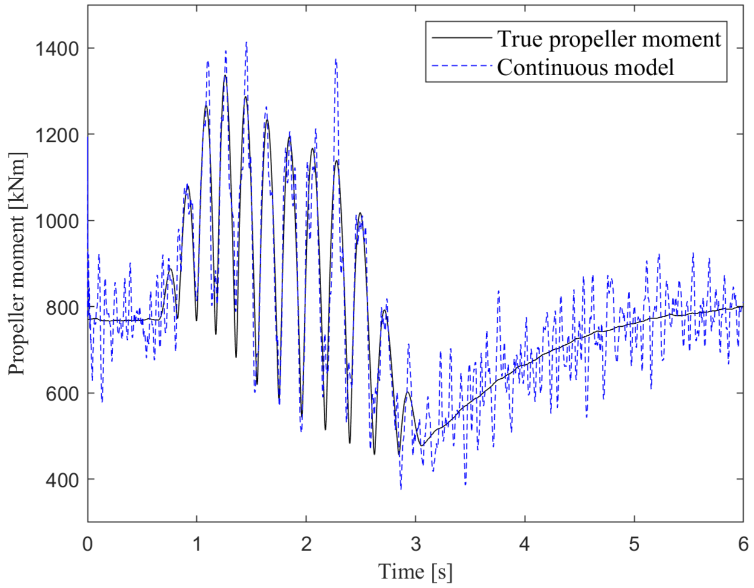

(c) Pink noise (Relative error - 8.96%, Correlation - 92.88%)

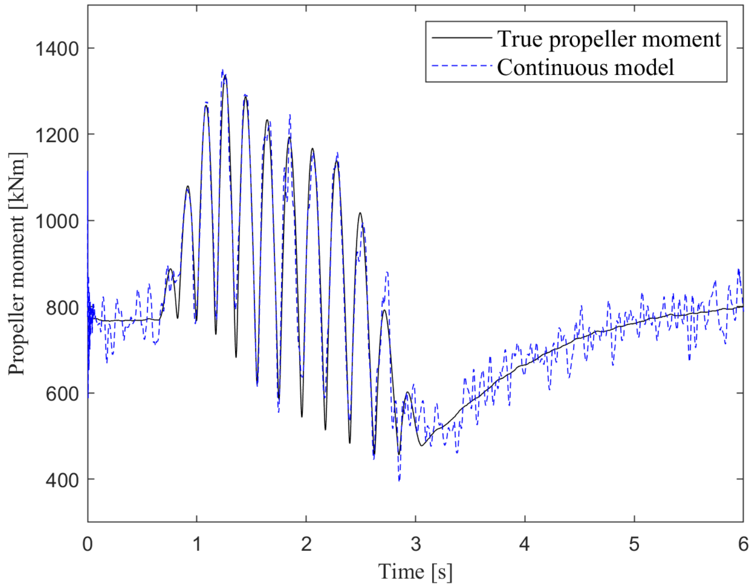

(d) Red noise (Relative error - 5.13%, Correlation - 97.51%)

Figure 5.27: (Continued) Estimated propeller moments from inputs coloured with noise

Stellenbosch University https://scholar.sun.ac.za

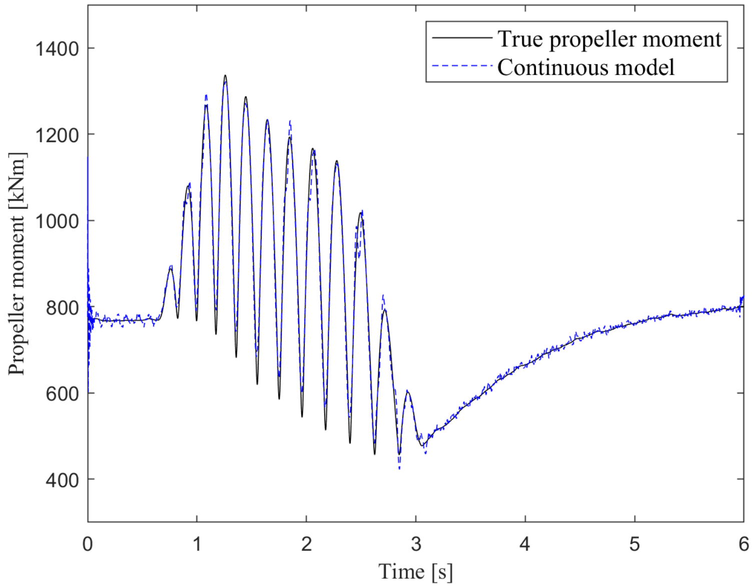

(a) White noise on torque (Relative error - 2.41%, Correlation - 99.45%)

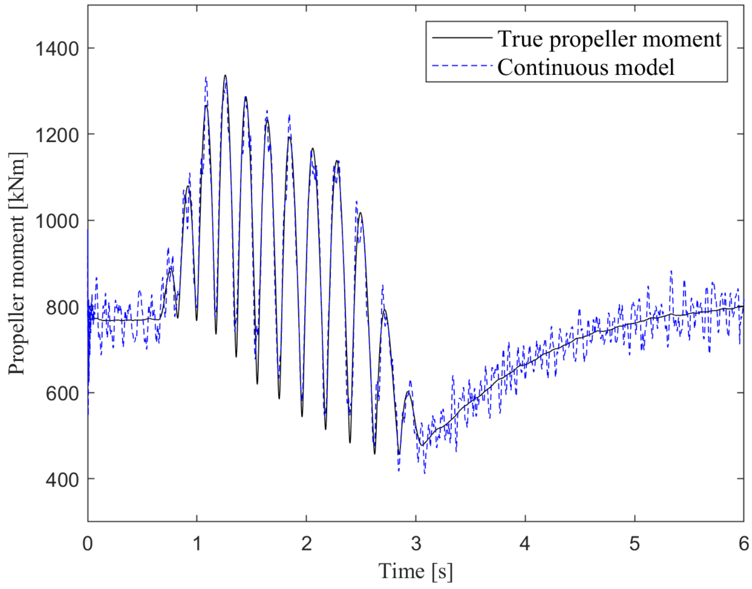

(b) White noise on velocity (Relative error - 4.61%, Correlation - 97.98%)

Figure 5.28: Estimated propeller moments from inputs coloured separately with noise

Stellenbosch University https://scholar.sun.ac.za

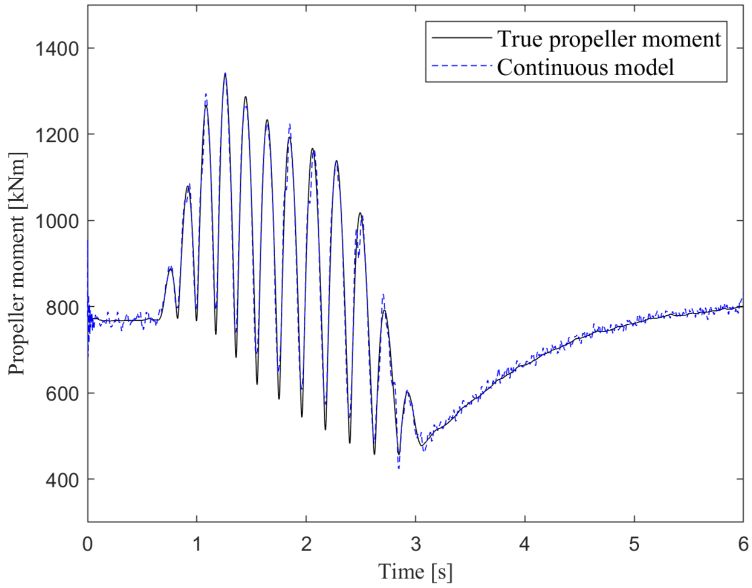

(c) Pink noise on torque (Relative error - 2.39%, Correlation - 99.46%)

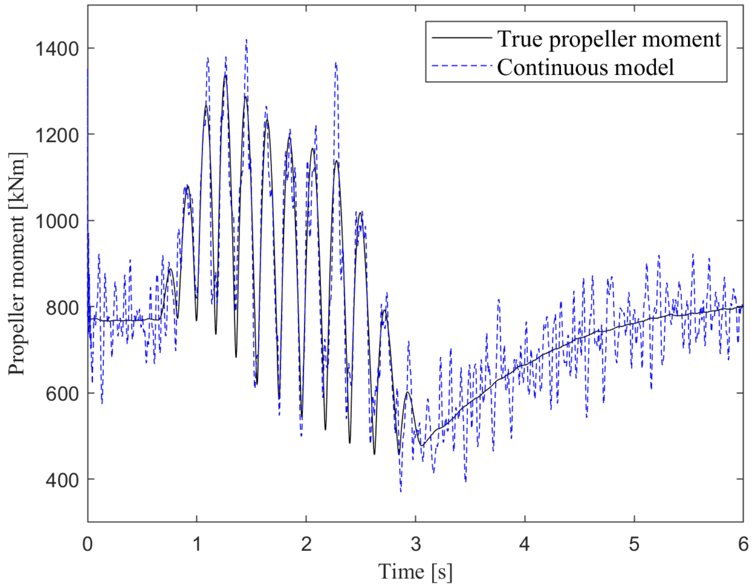

(d) Pink noise on velocity (Relative error - 8.95%, Correlation - 92.93%)

Figure 5.28: (Continued) Estimated propeller moments from inputs coloured separately with noise

Stellenbosch University https://scholar.sun.ac.za

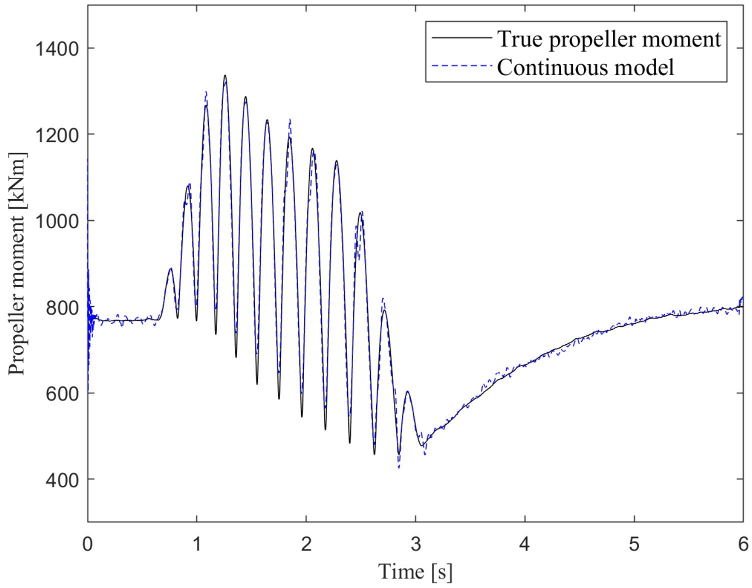

(e) Red noise on torque (Relative error - 2.41%, Correlation - 99.44%)

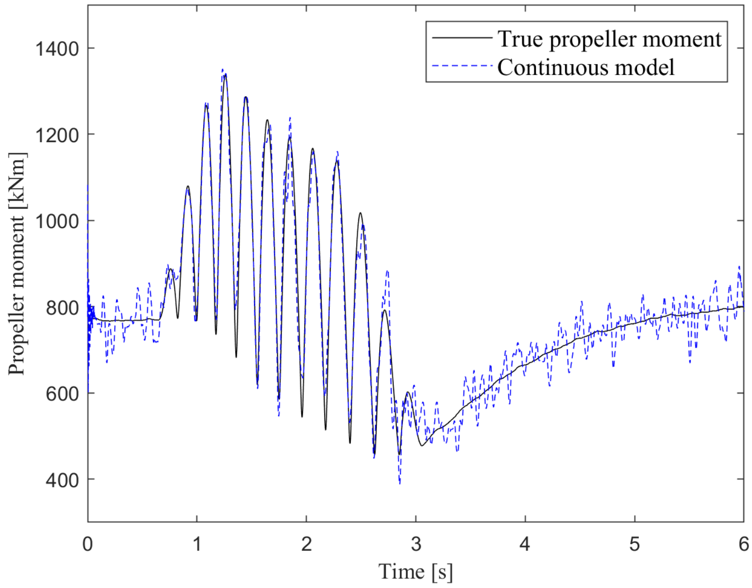

(f) Red noise on velocity (Relative error - 5.09%, Correlation - 97.54%)

Figure 5.28: (Continued) Estimated propeller moments from inputs coloured separately with noise

Stellenbosch University https://scholar.sun.ac.za

5.5 Limitations of the continuous model

The continuous model of the propulsion shaft is able to overcome the limitations of the discrete model. However, it does also suffer from its own limitations.

The model requires two separate inputs in order to perform an inverse calculation. The inputs used for the development of the model were the measured internal torque and the angular velocity, at some point along the shaft. This means that the measurement equipment and installation on board a vessel becomes more costly, as two sensors are required instead of one. Furthermore, a measurement that provides information about the speed control of the shaft is specifically needed.

The model only considers the uneven modes in the inverse solution. With reference to Figure 5.29, it was shown that including the even modes in the forward solution does not give any extra information. This is due to the propeller moment and motor torques being opposite in direction, resulting in the excitation of the even modes being negligible. It was found that due to this interaction, the inclusion of even modes in the inverse solution resulted in instability. If an even mode is excited, then the contribution from that mode will be solved as part of the external propeller moment or motor torque.

Since only the uneven modes are considered, care needs to be taken when selecting measurement locations. This is due to the equations for the measured torque and angular velocity that are added to the matrices for the inverse

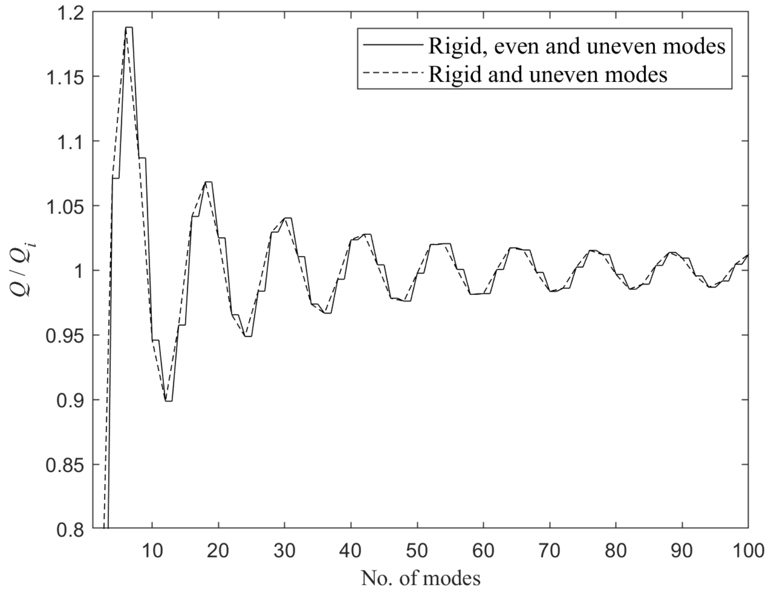

Figure 5.29: Convergence of internal steady-state torque in forward problem - comparison between even and uneven modes

Stellenbosch University https://scholar.sun.ac.za

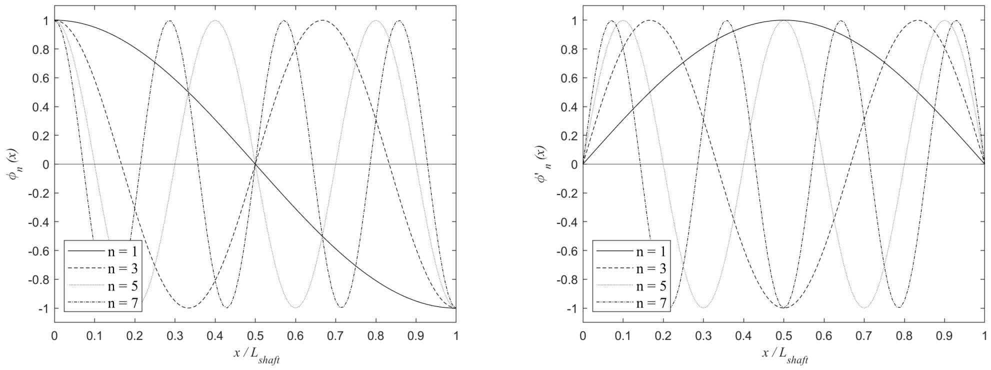

(a) Mode shapes

(b) First derivatives

Figure 5.30: Propulsion shaft uneven mode shapes and first derivatives

solution:

$$Q(x_1,t) = GJ\frac{\partial\theta(x_1,t)}{\partial x} = GJ\sum_{n=0}^{N}\phi'_n(x_1)q_n(t) \tag{5.46}$$

$$\dot{\theta}(x_2,t) = \sum_{n=0}^{N}\phi_n(x_2)\dot{q}_n(t) \tag{5.47}$$

With reference to Figure 5.30, it is possible to choose measurement locations x_1 and x_2 such that the terms $\phi'_n(x_1)$ and/or $\phi_n(x_2)$ for some modes n are equal to zero. This means that those modes do not contribute to the inverse solution. In particular, if x_2 is chosen such that $x_2/L = 1/2$ then all $\phi_n(x_2)$ will be equal to zero, resulting in the inverse problem being underdetermined.

The model assumes that the propulsion line consists of a single shaft between the motor and propeller. This assumption may not be valid in all cases. Specifically in the case of the SAA II, there are two shafts between the motor and propeller. As they are all rigidly coupled, the assumption of a single shaft led to a simpler model.

The model is also sensitive to noise at frequencies near the first torsional natural frequency of the propulsion shaft. This stems from the fact that for the torsional vibration of ship propulsion lines, the first torsional mode is dominant (Senjanović *et al.*, 2019). Introducing low frequency noise has the effect of altering the power of the frequency content of the measured signal at these low frequencies. This causes errors in the model when the frequencies near the first torsional mode are affected. In the case of the SAA II propulsion shaft the first torsional mode is located at roughly 11 Hz and in the altered continuous model used for the comparison of results from Polić *et al.* (2019) the first torsional mode is at roughly 20 Hz. Figure 5.31 highlights where these frequencies are located and how white, pink, and red noise relate to them. It

Stellenbosch University https://scholar.sun.ac.za

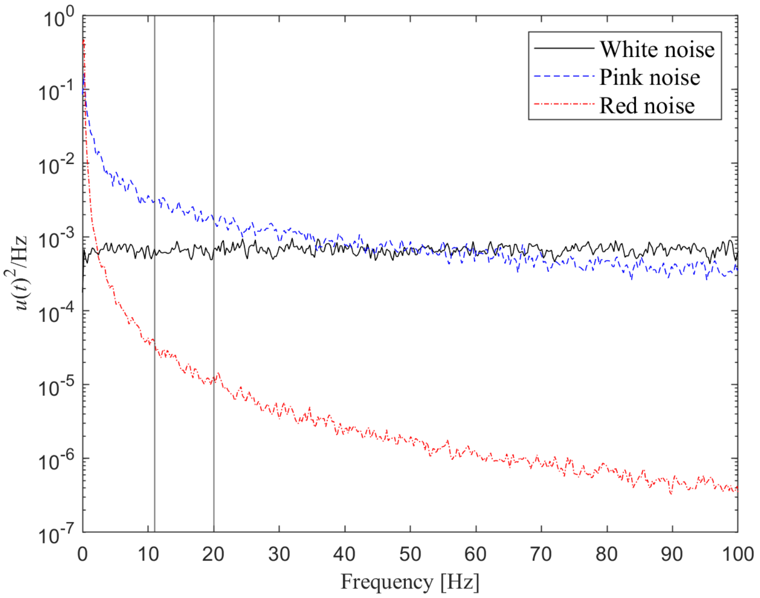

Figure 5.31: Power spectral densities for white, pink, and red noise

can be seen that pink noise, which caused the largest errors in the propeller moment estimates, adds more noise to the signal at the same frequency as the first torsional mode.

Finally, the model is more sensitive to errors on the measured velocity than on the measured torque. This could have been due to the row scaling employed in the inverse solution, discussed in Section 5.3. As the row containing the equation for the measured velocity was scaled up, so was any noise on the measurement. As both the equation and the measured noise were scaled up by the same factor, it was assumed that this would not introduce errors.

Even so, a different scaling was investigated to see if this was leading to the sensitivity to noise on the velocity measurements. The original scaling consisted of column scaling on the last two columns and row scaling on the last row of the $\mathbf{J}$, $\mathbf{C}$, $\mathbf{K}$, and $\mathbf{Q}$ terms of the matrix formulation in Equation 5.42. These columns and rows were multiplied with constant factors to raise them to equivalent magnitudes as the other terms in the combined effective stiffness matrix (see Appendix B).

The alternate scaling consisted of scaling down all columns but the last two, and then rescaling up the last two rows representing the equations for the measured values such that the net scaling applied to these rows was a factor of one. This led to a higher condition number (by a factor of 10^9), but resulted in the measurements being unscaled. Thus, any noise on the measurements were not scaled either.

The newly scaled inverse problem was then provided the noise coloured input data that gave the results in Figures 5.27 and 5.28. Despite the changes,

Stellenbosch University https://scholar.sun.ac.za

and with the higher condition number, the exact same results were achieved. This suggests that the continuous model's sensitivity to noise on the velocity measurement is not as a result of the scaling.

It follows that the inversely estimated propeller moments are more sensitive to the velocity measurements than the torque measurements, and therefore more sensitive to any errors on the velocity measurements.

5.6 Discussion

The continuous model overcomes much of the limitations of the discrete model. The motor torque and hydrodynamic loads are no longer assumed constant and are factored into the inverse solution, while angular velocity measurements are incorporated to provide extra information. This leads to more accurate results.

The model is also efficient. Specifically it can solve longer datasets in less time than it takes to record them, meaning it has the capability for close to real-time analysis.

As the model is derived from the same principle as another model in literature (Polić *et al.*, 2019), it is necessary to discuss the differences between them. Both models make use of modal superposition to transform the partial differential equation that governs the torsional vibration of the propulsion shaft into a set of N ordinary differential equations, with N the number of mode shapes used in the modal superposition.

Polić *et al.* (2019) then assume that for the flexible modes, the inertial terms $J_n\ddot{q}_n$ and damping terms $C_n\dot{q}_n$ are negligible. The assumption that $J_n\ddot{q}_n \approx 0$ follows from the assumption of small frequency ratios, or that the frequencies of the propeller moment and motor torques are less than 20 % of the natural frequency of the shaft. This allows for the set of N ordinary differential equations to be reduced to two equations representing the torques acting at the ends of the shaft (propeller and motor torques) as the only two unknowns.

These two equations rely on two measured parameters, the angular deformation (measured strain) and the derivative of the measured angular velocity.

Once the torque acting at the propeller end of the shaft is obtained, the propeller inertia is considered and the propeller loading determined using another sub-model.

In contrast, the presently introduced continuous model does not assume the inertial terms to be zero. The modal damping terms are assumed to be zero, although the influence of water damping on the propeller is still considered. The influence of the assumption that the modal damping terms are zero should be investigated further.

The model calculates the projection of the propulsion shaft inertia onto the modal coordinates q_n for both the rigid and flexible modes. Similarly, the projection of the propeller and motor inertias and propeller damping onto

Stellenbosch University https://scholar.sun.ac.za

the modal coordinates are included. This means the model is fully defined, without sub-models, and includes the terms for all modal coordinates.

The continuous model likewise makes use of two measured parameters, the angular deformation (measured strain) which is converted to an internal torque and the angular velocity. However, the angular velocity can be included directly into the inverse solution without needing to use its derivative, as the $\dot{q}_n$ terms are available in the model. In comparison to Polić *et al.* (2019), differentiation of the measured angular velocity is not necessary meaning numerical differentiation can be avoided.

The resultant system of equations for the continuous model contains $N+2$ unknowns (N modal coordinates q_n, and the propeller and motor torques) instead of the two unknowns in the Polić *et al.* (2019) model. A generalised-α numerical time integration scheme is employed to solve the system of equations at each time step.

While Polić *et al.* (2019) only include the influence of the propeller inertia, it is possible to include the influence of other inertias with the continuous model. This is in addition to the propeller and motor inertias already considered by the model. This is due to how the inertial components are projected onto the modal coordinates, and is discussed at the end of Section 5.1. Similarly, additional damping effects can be included.

As an example, the estimated propeller moment for the first case from Table C.7 was calculated while including a fictitious bearing located 5 m from the propeller, with an inertia of 300 $\text{kg} \cdot \text{m}^2$. The results are shown in Figure 5.32, with higher peaks on the ice impact due to the extra inertia.

A key assumption in the model by Polić *et al.* (2019) was that the inertial terms $J_n\ddot{q}_n(t)$ were negligible for flexible modes, $n > 0$. This assumption followed from the fact that the transmissibility of force was much smaller than the transmissibility of displacement, for small frequency ratios. Since $J_n >> 0$ it follows that $\ddot{q}_n(t) \approx 0$ for $n > 0$. However, at or near resonance this assumption is no longer valid. As the ice-induced impacts would result in a broadband frequency excitation, they would excite resonances and violate this assumption. Furthermore, ice-induced loading such as milling at frequencies near to a resonant frequency would violate this assumption.

To evaluate this assumption, the $\ddot{q}_n(t)$ values for the results obtained using the data presented in Figure 5.26 from Polić *et al.* (2016, 2019) were investigated. Figure 5.33 provides the first five $\ddot{q}_n(t)$ values. The results show that the rigid mode $\ddot{q}_0(t)$ values are larger than the flexible mode $\ddot{q}_n(t)$ values, as assumed by Polić *et al.* (2019). The flexible mode $\ddot{q}_n(t)$ values reduce closer to zero as n increases. However, the flexible mode $\ddot{q}_n(t)$ are shown to have non-zero values, especially for $\ddot{q}_1(t)$. Since the torsional vibration is dominated by the first torsional mode, it follows that $\ddot{q}_n(t)$ for this mode would have higher values.

In the case of the SAA II, the first torsional natural frequency of the shaft is close to 11 Hz. The MCR rotational speed of the shaft is 140 rpm, which

Stellenbosch University https://scholar.sun.ac.za

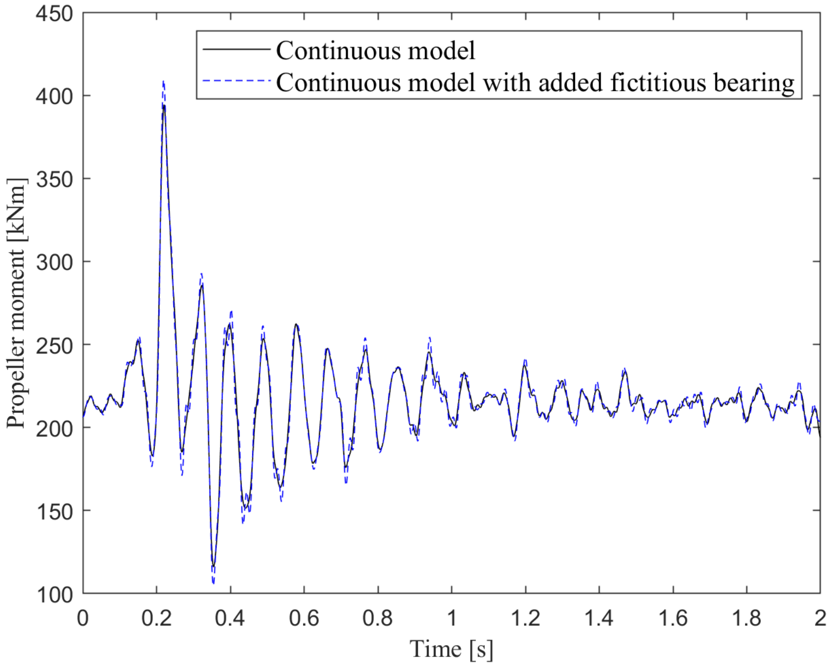

Figure 5.32: Influence of fictitious added inertia on the continuous model

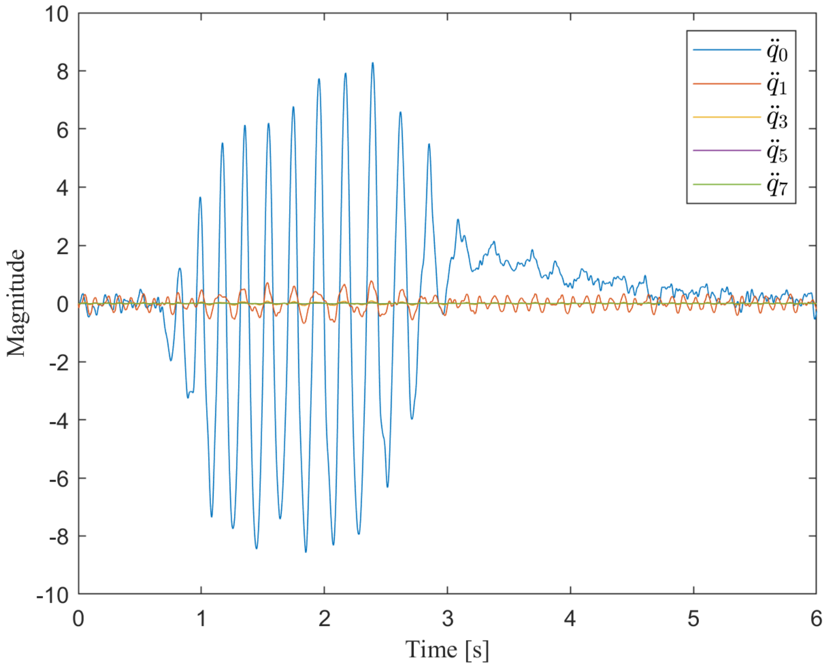

Figure 5.33: Second time derivatives of modal coordinates ($\ddot{q}_n(t)$) from inverse solution, using data from Polić *et al.* (2016, 2019)

Stellenbosch University https://scholar.sun.ac.za

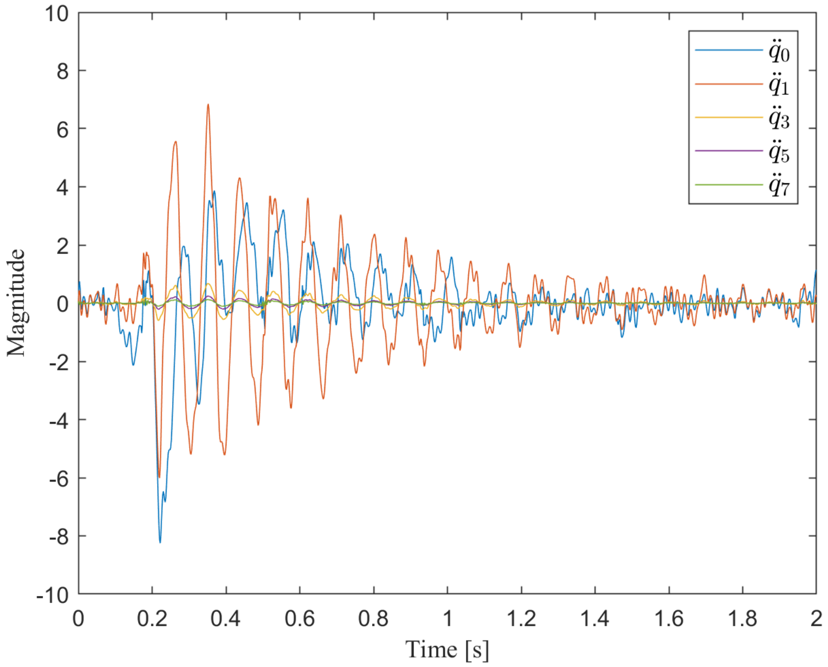

Figure 5.34: Second time derivatives of modal coordinates ($\ddot{q}_n(t)$) from inverse solution, using ice impact Case 1 from Table C.7

is 2.33 Hz. As the propeller has four blades, the blade pass frequency is four times the rotational speed at 9.33 Hz. As such, during milling at MCR speed it could be expected that impacts occur at a rate of 9.33 Hz which is close to a resonant frequency for the shaft. The frequency ratio between this milling and the first torsional natural frequency for the SAA II is 85 % which is significantly larger than the small frequency ratios (< 20 %) assumed by Polić *et al.* (2019).

Case 1 from Table C.7 is used to illustrate this. The average rotational speed for the ice impact in Case 1 is close to the MCR speed at 138.8 rpm and contains milling. The first five $\ddot{q}_n(t)$ values for the solution of Case 1 are presented in Figure 5.34.

The results in Figure 5.34 show that the flexible mode $\ddot{q}_n(t)$ have non-zero values, again especially for $\ddot{q}_1(t)$. In this case the first flexible mode $\ddot{q}_1(t)$ values are significantly larger and comparable to the rigid mode $\ddot{q}_0(t)$ values. This is due to both the dominance of the first torsional mode in the vibration response and the fact that the ice-induced loading from milling occurs at a frequency close to this first torsional mode. Clearly, the assumption that $\ddot{q}_n(t) \approx 0$ for $n > 0$ does not hold for this case. Furthermore, the assumption does not hold in general for the data recorded on the SAA II propulsion shaft as the frequency of the excitations are regularly higher than 20 % of the first torsional natural frequency.

To demonstrate the influence of assuming $\ddot{q}_n(t) \approx 0$ for $n > 0$, the contin-

Stellenbosch University https://scholar.sun.ac.za

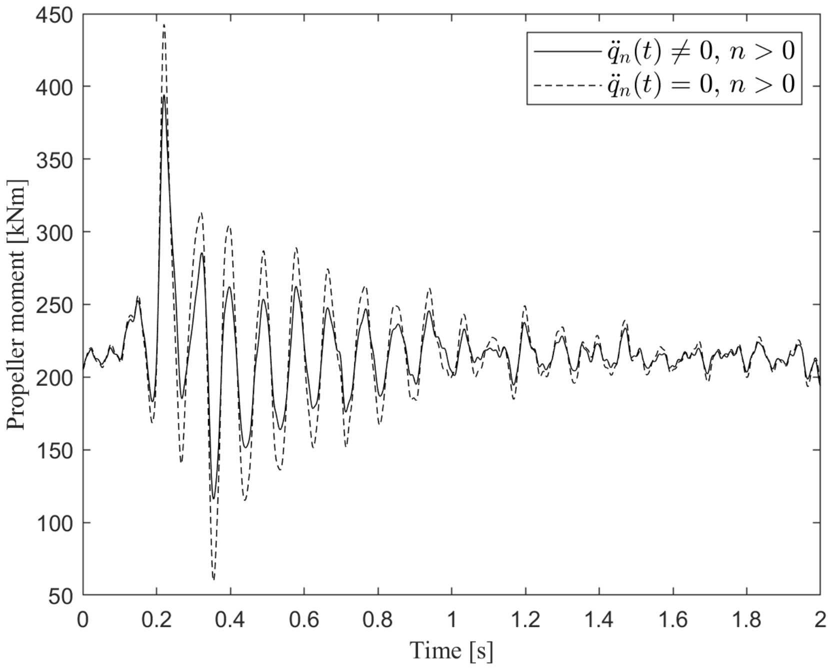

Figure 5.35: Comparison of inverse propeller moments using the continuous model, assuming $\ddot{q}_n(t) = 0$ for $n > 0$

uous model was altered to assume that $\ddot{q}_n(t) = 0$ for $n > 0$, and the inverse solution for Case 1 was performed. The results are compared to the previous inverse solution for Case 1 with $\ddot{q}_n(t) \neq 0$ for $n > 0$. The results show that larger amplitudes are estimated under the assumption. If the previous estimation, produced with $\ddot{q}_n(t) \neq 0$ for $n > 0$, were to be considered accurate then the assumption that $\ddot{q}_n(t) \approx 0$ for $n > 0$ leads to an overestimation in the inverse propeller moment. Again, it is clear that the assumption does not lead to the same results and thus does not hold.

The continuous model thus offers an advantage over the model by Polić *et al.* (2019), due to taking all the $\ddot{q}_n(t)$ into account during the inverse solution. Being able to do so becomes important in the case that the ice-induced propeller moment contains frequencies near to the first natural frequency of the propulsion shaft.

Stellenbosch University https://scholar.sun.ac.za

Chapter 6

Voyage data analysis

Full-scale measured propulsion shaft data from the SAA II was used to illustrate the practical value of the new continuous model. In addition to the analysis of single ice impacts and milling cases the continuous model was applied to efficiently estimate the propeller moments for a full voyage.

Figure 6.1 provides a breakdown of the research presented in this chapter, and shows where the contributions to literature arise.

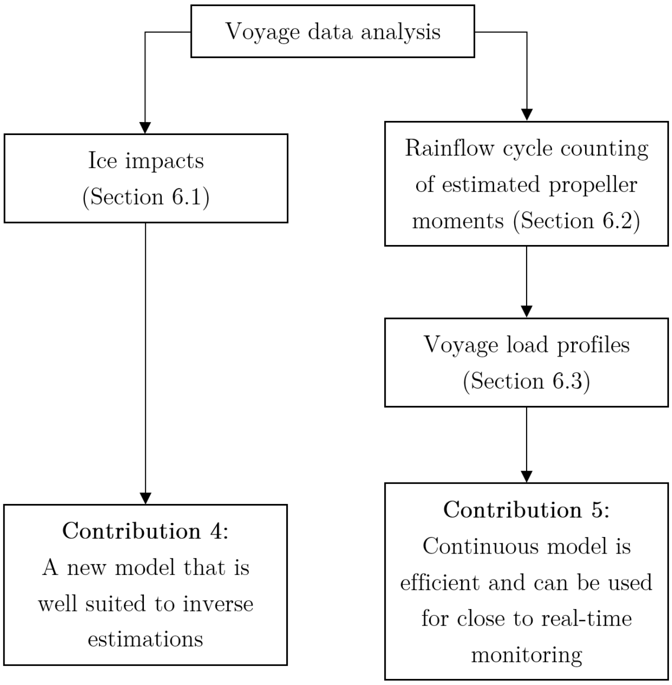

Figure 6.1: Breakdown for Chapter 6 research and contributions

Stellenbosch University https://scholar.sun.ac.za

Data from the 2019 SCALE Spring Cruise was analysed using the new continuous model. This voyage took place from 11 October to 20 November 2019, with the propulsion shaft measurements sampled continuously throughout the voyage. The voyage included operation in both open water and ice. In total, 38 days of measurements were made, with roughly 10 of those spent in ice. Figure 6.2 provides a graphical breakdown of the percentage of measurements in open water and ice.

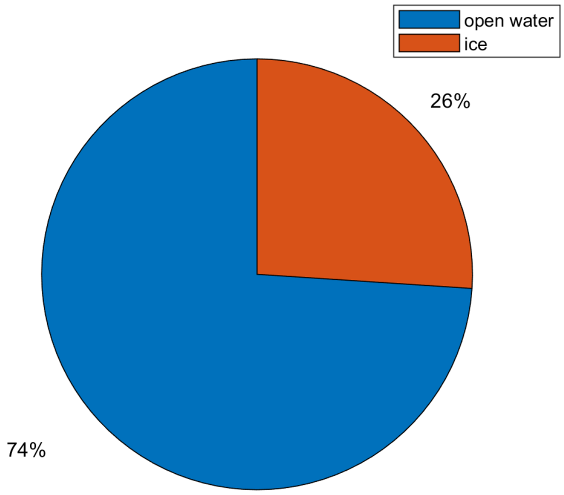

Figure 6.2: Amount of time spent in open water and ice for the 2019 SCALE Spring Cruise

In addition to the results from the analysed cases in Table C.7 (C), discussed in Section 6.1, an analysis of the propeller moment estimates for the entire voyage was conducted, Sections 6.2 and 6.3.

Analysing the propeller moments for a full voyage was not previously practical with the discrete model, due to its prohibitive computational cost. Thus, analyses like this were limited to the measured propulsion shaft torque (De Waal, 2017).

A total of 921 hours of data, at a sample rate of 600 Hz, were analysed for the 2019 SCALE Spring Cruise. The computer used to analyse the full dataset had an i7-8700 4.6 GHz processor, 16 GB of RAM, and a 64-bit operating system. In comparison to the computer used to solve the propeller moment estimates for the ice impacts, which took roughly 30 seconds to solve a 5 minute input file, this computer took roughly 16 seconds to solve the same input file. It took 3 to 4 days to analyse the dataset using the continuous model and estimate the propeller moments for the full voyage.

Stellenbosch University https://scholar.sun.ac.za

6.1 Ice impacts

An overview of the ice impacts from Table C.7, used in the evaluation of the continuous model, is provided Figure 6.3. Only the results for measurement location Q_1 are presented here, as the results from location Q_2 appear similar. The scaling on the y-axes was selected such that all impacts were easily visible.

When comparing internal torque to the ice-induced propeller moments, it was found that the ice impact peaks are consistently larger than the internal torque peaks. Before accepting this as a general statement, further investigation is required as this contrasts with the findings by De Waal (2017). That study found that, in some cases, the internal torque was higher than the external ice loads. The higher internal torques were either attributed to the dynamic response of the shaft amplifying the internal torque, or to possible shortcomings of the model. A possible reason, considering the dynamics, is the reflection of the torsional stress waves which may cause constructive interference.

It is possible that the propeller loads would be higher due to them needing to overcome both the material's resistance to deformation and the inertia of the rotating components. By comparison, in the static case only the material's stiffness or rigidity will be taken into account, meaning the internal torque and propeller moment would be equal.

For the ice impact cases that were analysed, it was rare that the ice-induced propeller moment consisted of a single impact such as for Case 29. More often milling was involved, even when the ice-induced load was dominated by a single impact such as in Cases 1 or 5. Following an ice impact or milling event is a ripple on the propeller moment which is attributed to vibrations imparted by the impacts, the first torsional mode being the dominant response at roughly 11.1 Hz.

The ice impact peaks were found to consistently occur before the internal torque peaks. Again, this was expected as it would take time for the torsional wave generated by the ice impacts to reach the measurement location on the shaft 25 m away.

The speed of the torsional wave can be found through the one-dimensional wave equation (Rao, 2007):

$$c^2 \frac{\partial^2 u(x,t)}{\partial x^2} = \frac{\partial^2 u(x,t)}{\partial t^2} \tag{6.1}$$

where c is the wave speed. Rewriting Equation 5.6, by removing the externally applied moment, gives the one-dimensional wave equation for torsional vibrations of a shaft:

$$\frac{G}{\rho} \frac{\partial^2 \theta(x,t)}{\partial x^2} = \frac{\partial^2 \theta(x,t)}{\partial t^2} \tag{6.2}$$

Stellenbosch University https://scholar.sun.ac.za

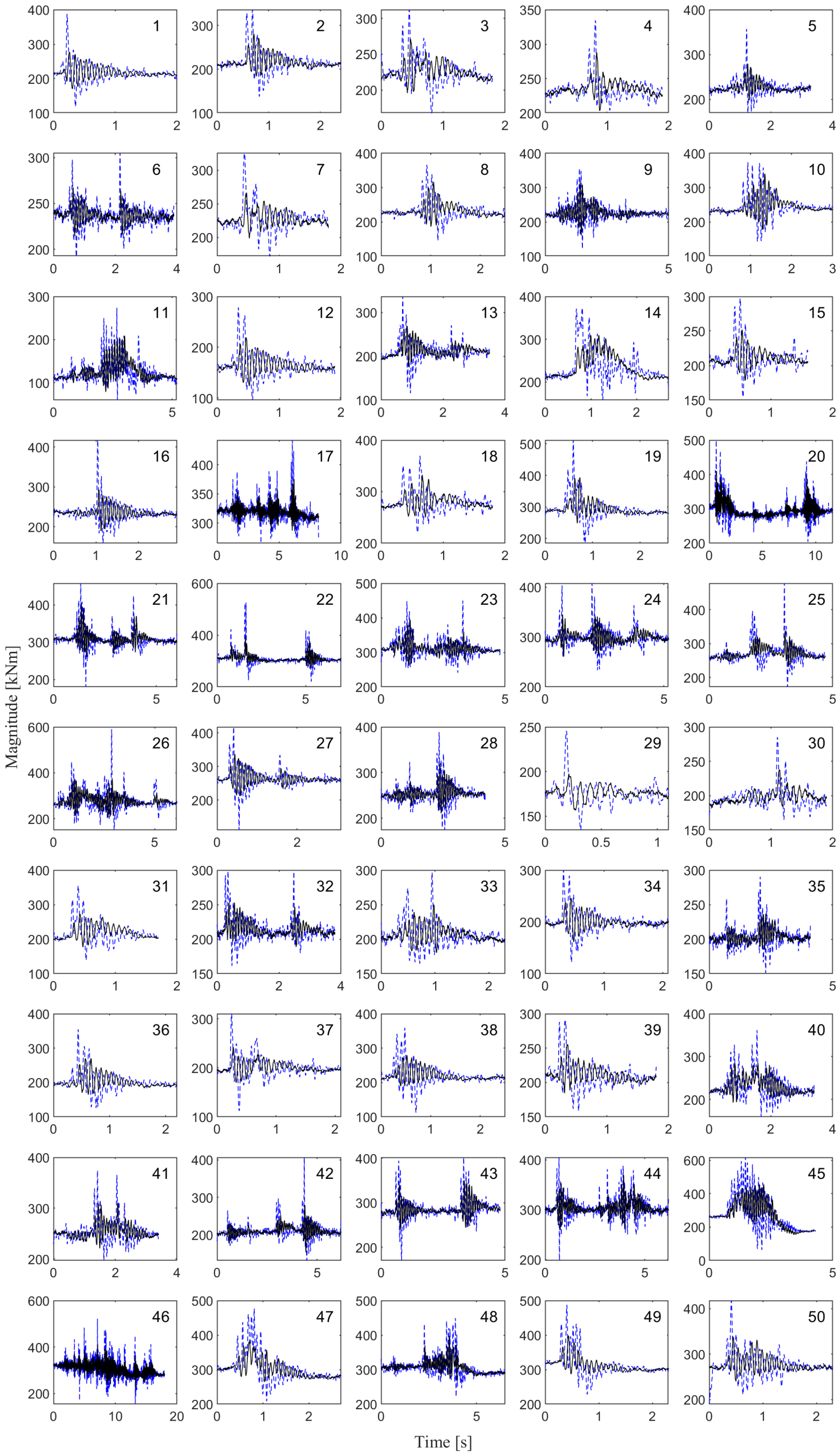

Figure 6.3: Overview of internal torques and corresponding propeller moment estimates. Internal torques are the solid black lines, while the propeller moments are the dashed blue lines

Stellenbosch University https://scholar.sun.ac.za

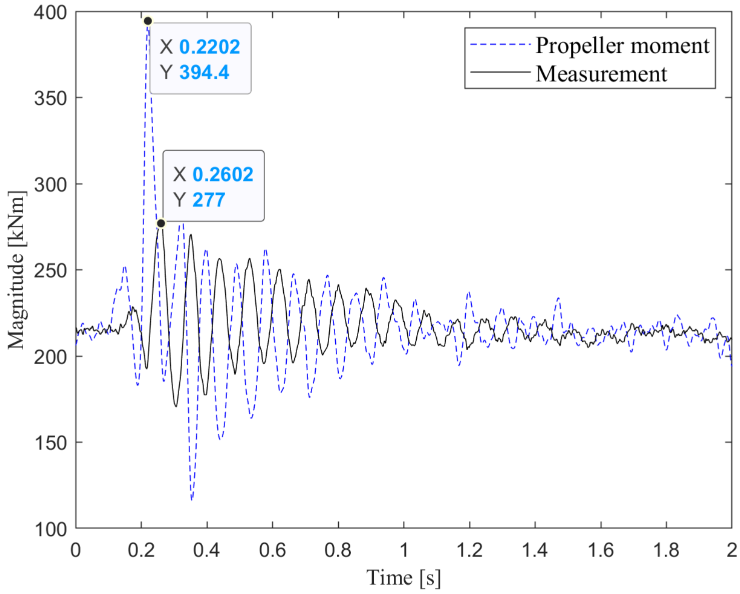

Figure 6.4: Time between ice impact and internal torque peaks for Case 1

where the wave speed is related to the shear modulus and density of the shaft:

$$c = \sqrt{\frac{G}{\rho}} \tag{6.3}$$

From Equation 6.3, the torsional wave speed for the SAA II propulsion shaft was calculated as 3212.2 m/s. As the measurement location is 25 m away from the propeller, it follows that it would take the wave 7.8 milliseconds to travel there.

It was found that this is true for the model in the static case. However, from the impacts estimated in Figure 6.3, the internal torque peaks occurred more than 7.8 milliseconds after the ice impact peaks. This is highlighted in Figure 6.4, showing the internal response 40 milliseconds after the main ice impact peak for the first case.

The same phenomenon was observed with the simulated data from Polić *et al.* (2016). In this case, the wave speed for the shaft was 3131.9 m/s, which leads to a travel time of 3.5 milliseconds to the measurement location, but again the internal torque peaks appeared later. These results suggest that the shaft dynamics or the motor control play a role in the propagation of the torsional waves.

Comparisons were made between the measured internal torque and shaft angular velocity during the impacts. The first case is used as an example for the discussion, but all the cases showed similar results.

Stellenbosch University https://scholar.sun.ac.za

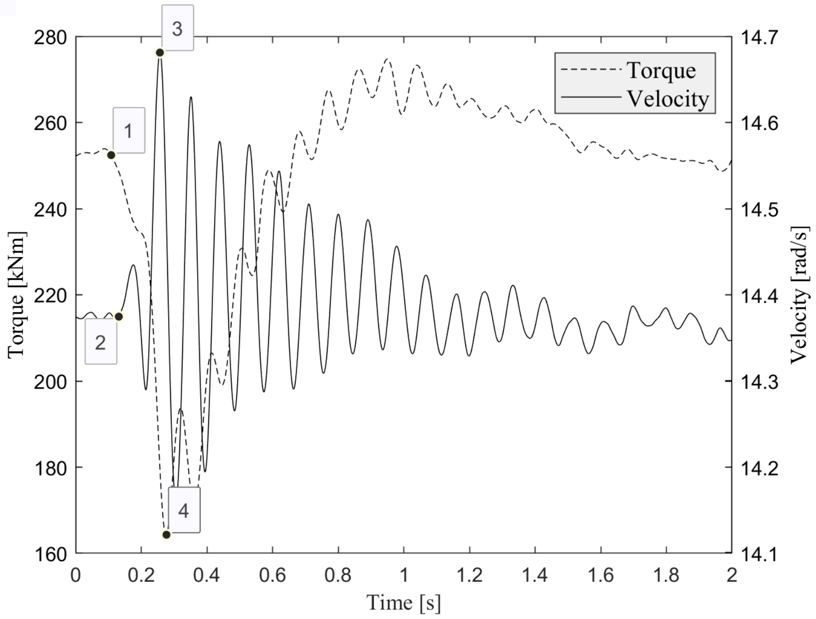

Figure 6.5: Comparison between internal torque and shaft angular velocity

At the onset of ice-propeller interaction,it can be seen that the velocity starts to decrease at 108.4 milliseconds, (Point 1 on Figure 6.5) before the torque in the shaft increases at 131.8 milliseconds (Point 2 on Figure 6.5).

Furthermore, Figure 6.5 shows that the torque peaks do not line up with the drops in velocity, with the change in torque appearing to lead the change in velocity. The torque peak at Point 3 occurs at 256.9 milliseconds while the velocity trough at Point 4 occurs at 275.2 milliseconds (18.3 milliseconds later).

From this data, the response of the shaft to an ice impact can be summarised as follows:

1. When an ice impact occurs, the angular velocity of the shaft begins decreasing, before any stresses or torques are induced on the shaft (Point 1 on Figure 6.5).
2. The torque on the shaft begins increasing after the velocity has decreased (Point 2 on Figure 6.5), and increases up to a maximum point.
3. The shaft velocity continues to decrease for a short time after the maximum torque is reached, resulting in a delay between the maximum torque and minimum velocity (Points 3 and 4 on Figure 6.5).
4. During milling after the initial impact, the torque peaks continue to lead the velocity troughs.
5. This same process occurs for any subsequent impacts.

Stellenbosch University https://scholar.sun.ac.za

The fact that the angular velocity slows before the internal torque suggests that part of the ice induced propeller moment is absorbed by components other than the propulsion shaft, with the load transferring to the shaft later. For example, the propeller blades themselves could bend in response to a load. This load on the propeller blade would still result in a reduction of angular velocity, but not in twisting of the propulsion shaft. This is another example of why the measurement of the shaft angular speed is important for the inverse model as it helps to capture load effects that may not be present in the shear deformation of the shaft.

The possibility that the load is partially absorbed by components before being transferred to the propulsion shaft provides another reason for the difference in wave speeds, as discussed with regards to Figure 6.4. Since the load is transferred to the shaft some time after the impact occurs, this time would be added to the time taken for the wave to travel from the propeller to the measurement location.

In addition to this response, the control response can be seen to command an increase in velocity to compensate for the losses caused by the impact. This leads to an overshoot as the milling reduces, with the velocity eventually settling at its pre-impact value. This increase in velocity leads to higher milling loads on the propeller, as the blades make contact with the ice while they are accelerating. The faster the control system responds to the loss in speed, the higher the induced milling loads could be. Understanding how the motor control leads to increased milling loads can help in the design of the control, and can be used to reduce the magnitude of milling loads.

6.2 Rainflow cycle counting of estimated propeller moment

Rainflow cycle counting was performed on the estimated propeller moments for the voyage. This was done to provide an overview of the loads experienced by the propeller over the course of the voyage. The cycle counting was performed using an algorithm written by Nieslony (2020), which was developed according to the ASTM E1049-85 (2017) standard.

An example of the cycle counting for a portion of the external propeller moment for Case 1 from Table C.7 is presented in Figure 6.6. Figure 6.6(a) identifies the maxima and minima in the signal, and Figure 6.6(b) shows the cycles extracted from the signal

Cycle counting was performed separately for open water navigation and ice navigation. A histogram presenting the extracted peak values from the cycle counting results for the open water and ice navigation is given in Figure 6.7. The bin size for the histogram is 1 kNm.

From Figure 6.7, it can be seen that significantly more cycles were experi-

Stellenbosch University https://scholar.sun.ac.za

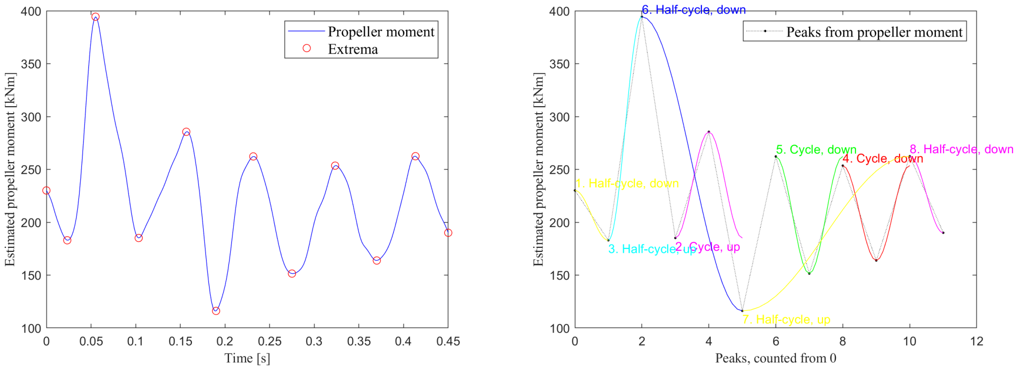

(a) External propeller moment extrema

(b) Extracted cycles

Figure 6.6: Rainflow cycle counting example

enced during open water navigation, since more time is spent in open water. As such, the scaling on the y-axes of Figures 6.7(a) and 6.7(b) are not matched, so that it is easier to see and compare the data presented in Figure 6.7(b).

The majority of peaks during open water navigation occur around 200 kNm. This corresponds to the relatively constant torque used during open water navigation. The increase in peaks below 100 kNm is attributed to when the ship is stationary, as found by De Waal (2017).

During ice navigation the spread of the propeller peaks increases significantly. More peaks occur above 200 kNm, due to the ice impacts on the propeller causing higher peak values. The number of peaks around 200 kNm is reduced, with more peaks between 70 to 200 kNm. This is due to changes in the propeller pitch and reductions in propulsion shaft rotational speed during ice navigation. This results in more varied torque on the propulsion line, as opposed to the relatively constant torque during open water navigation.

The full overview of the cycle counting for the voyage is presented in Figure 6.8. This provides a useful tool for investigating the propeller loads experienced during a voyage. The mean operating conditions for the propeller are clearly visible, with the higher amplitudes occurring during propeller-ice interaction.

These loads can be used in conjunction with a high fidelity propulsion line model, such as a finite element model, to perform stress and fatigue analysis.

Stellenbosch University https://scholar.sun.ac.za

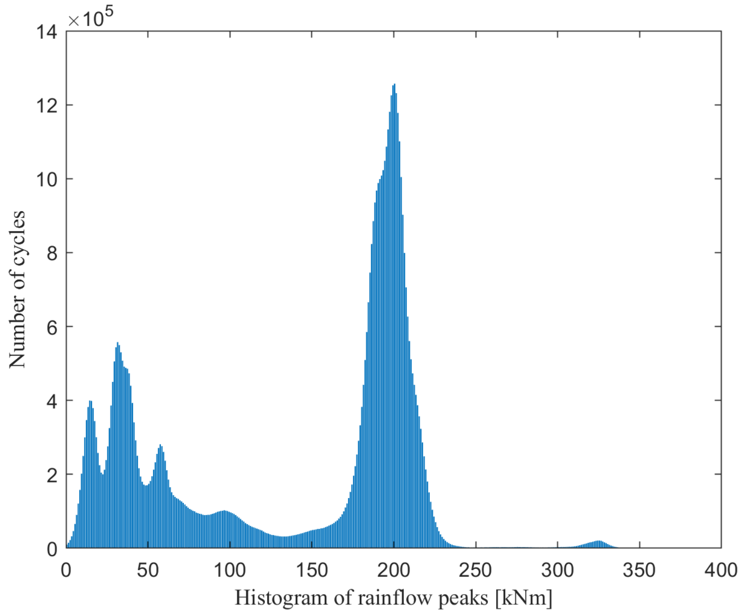

(a) Open water

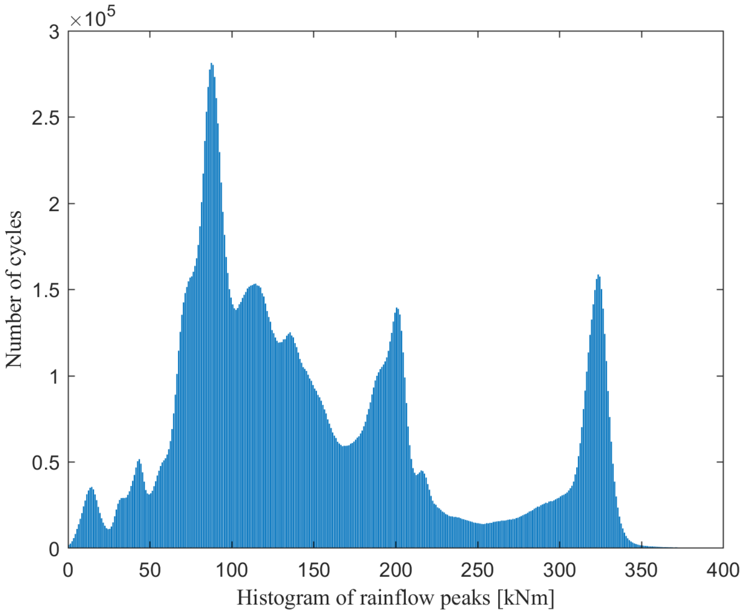

(b) Ice

Figure 6.7: Comparison of propeller moment peaks from rainflow cycle counting for open water and ice navigation

Stellenbosch University https://scholar.sun.ac.za

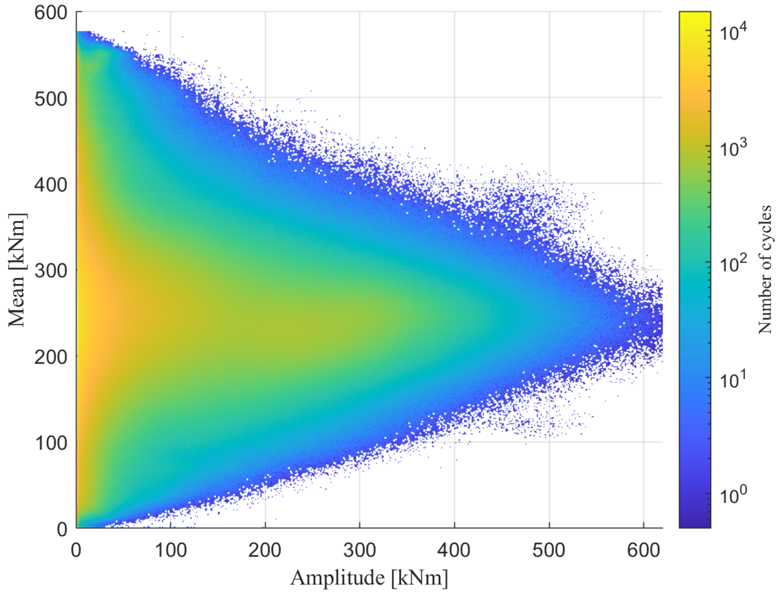

Figure 6.8: Cycle counting for 2019 SCALE Spring Cruise propeller moments

6.3 Voyage load profiles

The cycle counts of the estimated propeller loads were used to construct load profiles for the voyage, presented in Figure 6.9. The load response factor K_a was determined by dividing the peak values by the rated torque Q_{MCR}. This is usually used for vessels exposed to varying loads to determine safe loading for propulsion line components, such as the propeller (De Waal, 2017). The amplitudes are divided by the maximum amplitude, and presented as a percentage.

As found by Myklebost and Dahler (2003) and De Waal (2017), the data in Figures 6.9(a) and 6.9(b) exhibit a change of slope. This is attributed to the distribution above the slope change resulting from ice impacts on the propeller, and the distribution below the slope change resulting from motor excitations. Thus, to focus on the results from ice related loads, only the distribution above the change in slope should be considered. These are presented in Figures 6.9(c) and 6.9(d)

Load profiles such as these can be used for the design or analysis of propulsion systems, to ensure they are capable of withstanding the expected loads for a given voyage. They can also be used to monitor the propulsion line components, by cumulatively tracking load profiles experienced over the system's life cycle.

These load profiles are also useful in the comparison of different voyages or vessels' loading conditions. De Waal (2017) attempted to make comparisons between the loads experienced by the SAA II and the Polarstern propulsion

Stellenbosch University https://scholar.sun.ac.za

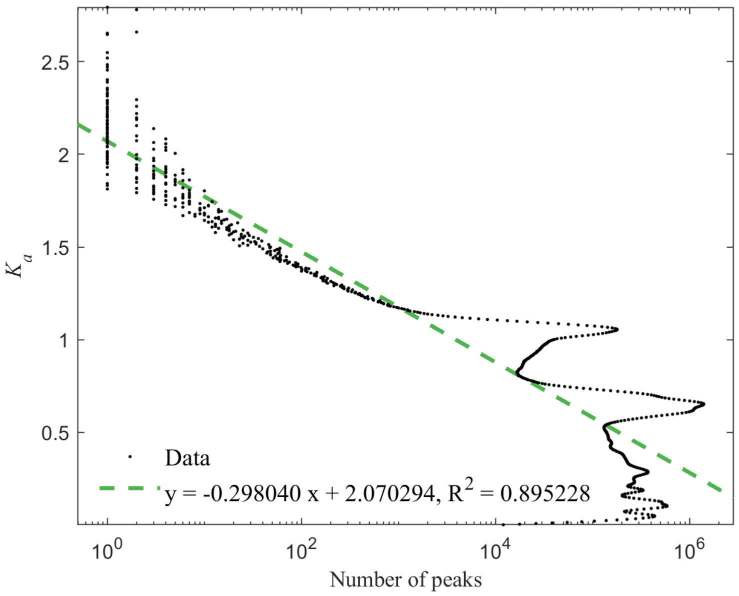

(a) Peak

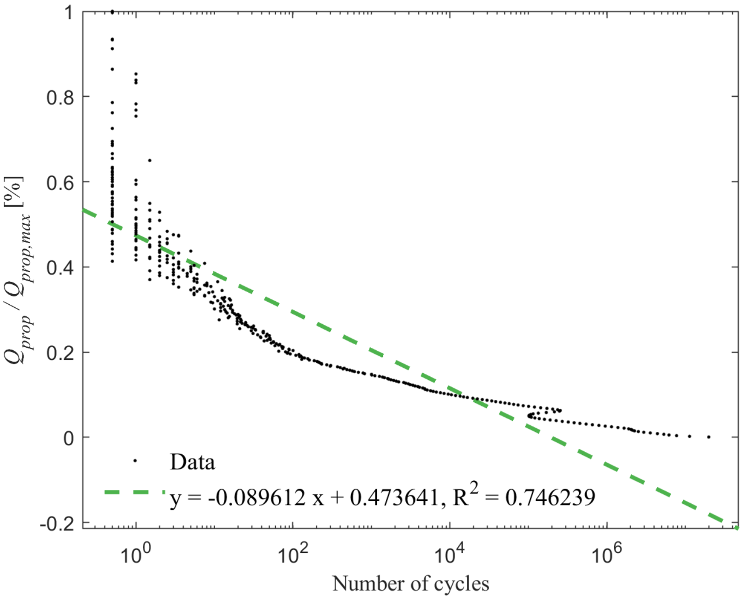

(b) Amplitude

Figure 6.9: Load profiles for 2019 SCALE Spring Cruise estimated propeller moment

Stellenbosch University https://scholar.sun.ac.za

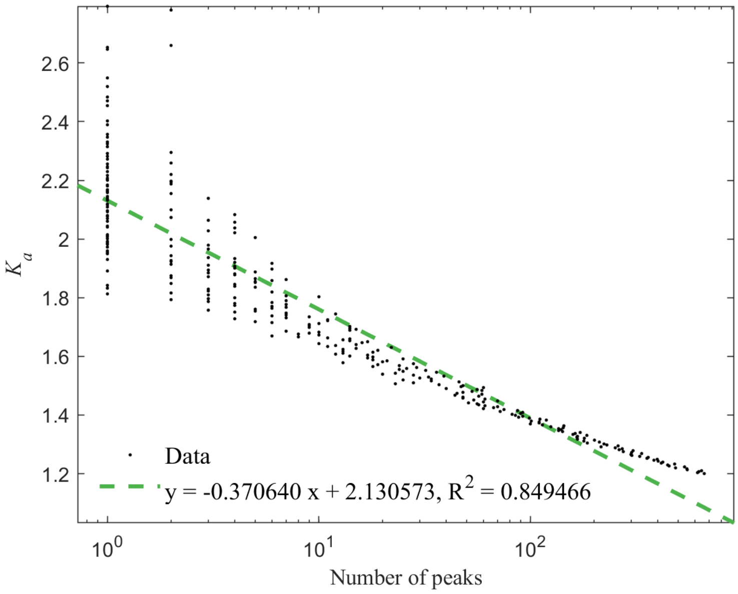

(c) Peak - ice related

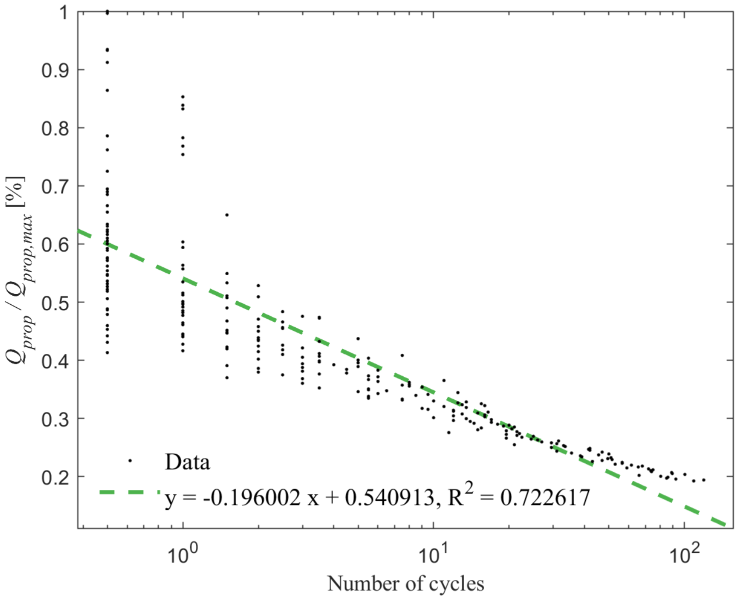

(d) Amplitude - ice related

Figure 6.9: (Continued) Load profiles for for 2019 SCALE Spring Cruise estimated propeller moment

Stellenbosch University https://scholar.sun.ac.za

lines through torque measurements conducted on their propulsion shafts. This was done to compare the typical loads a vessel might experience in the Antarctic to those experienced in the Arctic. However, it was difficult to make a fair comparison as:

- the vessels' propulsion lines have different shaft geometries, meaning that for the same external propeller moment they would each experience a different torque in the propulsion shaft,
- and torque fluctuates along the length of the propulsion shaft, so selection of measurement locations can result in differences.

De Waal (2017) suggested that the propulsion shaft loads should be converted to propeller loads for a fair comparison to be made between the ice induced propeller moments. This is now readily achievable with the continuous model. Load profiles can be built for a variety of ships under a variety of operational conditions. These profiles can be used:

- to compare the propeller loading experienced by different vessels,
- to predict the loading a particular vessels propulsion line may experience under certain conditions, using estimated propeller moments,
- in the design of vessels propulsion lines,
- and in the design of standards for use in the design of vessels.

The propeller loading can also be monitored in close to real time throughout a voyage. This is due to the algorithm being able to analyse large sections of data efficiently. Cycle counting, loading profiles, and maximum conditions could all be monitored.

Stellenbosch University https://scholar.sun.ac.za

Chapter 7

Conclusions and recommendations

The aim of this research was to investigate the estimation of propeller moments of ice going vessels. Furthermore, the research set out to add novel contributions to the literature currently available.

A literature review analysing the state of the art inverse propeller moment estimation techniques was conducted. Areas where the literature on inverse models for propeller moment estimation could be contributed to were noted. These included:

- the assessment of the discrete model by Ikonen *et al.* (2014) and De Waal *et al.* (2018*b*), in which the following areas were noted:
    - the selection of a particular regularization method,
    - the selection of regularization parameter,
    - the difference between input locations,
    - and the assessment of assumptions made for these models.
- the development of new inverse models based on modal superposition that do not require regularization, in which the following areas were noted:
    - there was opportunity to develop a model that could account for modal inertia and the inertias of propulsion shaft components other than the propeller,
    - since only one of these models were available in literature, another model could assist in validation,
    - and the use of full-scale measured data in the evaluation of the model.
- the comparison of these new continuous inverse models to the previous discrete inverse models

Stellenbosch University https://scholar.sun.ac.za

7.1 Conclusions

Full scale measurements were performed on the SAA II to provide the necessary propulsion shaft torque data for the development and assessment of the inverse models. Based on the recommendations of De Waal (2017), the work done by Polić *et al.* (2019), and the development of the continuous model, the measurement system was upgraded to include a higher frequency measurement of the rotational speed of the propulsion shaft.

The full-scale measurements were used in the evaluation of the inverse models. Furthermore, they provide additional data to the literature that can be used in the future development of inverse models or in the design process of ice-going vessels.

The discrete lumped mass model used by De Waal *et al.* (2018*b*) was investigated. Automated selection of the regularization parameters was developed and implemented on a case by case basis. A number of regularization methods were evaluated and the Tikhonov method selected as the preferred one due to it being the most robust and efficient. The model was evaluated using data from literature as well as full scale measurements. It was found to introduce errors on the propeller moment estimates due to assumptions made in the derivation of the model. It was also found to be prohibitively computationally expensive for large datasets. Based on the evaluation of the model and its assumptions, it is suggested that it is unsuitable for inverse estimations of propeller moments.

A new inverse model for propeller moment estimates was developed. This model is based on the modal superposition of a continuous shaft, and does not require regularization to perform the inverse solution. The continuous model was evaluated through comparisons to the previous discrete model using the full-scale measurements conducted on board the SAA II, and was found to be a significant improvement over the discrete model. Specifically, it was more accurate and significantly more efficient.

The continuous model was compared to the state of the art in literature (Polić *et al.*, 2019), and the differences discussed. It was found that the continuous model is advantageous, as it accounts for the modal inertia terms in the solution. This allows its use when the frequencies of the propeller moments are close to the natural frequencies of the shaft. The model by (Polić *et al.*, 2019) assumed this was not the case, but it was shown through full-scale measurements that this can and does occur in practice.

The continuous model now provides an efficient method for analysing longer sections of data, and can be employed to relatively quickly analyse the external propeller moments for a full voyage. There is also potential for close to real-time analysis of measurements. This can be used in the operational monitoring of shaft-line systems or in the development of digital services such as propulsion shaft digital twins.

Stellenbosch University https://scholar.sun.ac.za

7.2 Recommendations

Based on the research presented, the following recommendations are made:

1. The discrete model, in its current state, is not recommended for use in the inverse estimation of propeller moments. It needs to be altered in order to take the shaft angular velocity and a varying motor torque into account. A possible line of enquiry is to determine the impulse response function while treating the system as MISO, with both the ice-induced loading and the motor torque inputs contributing to the output internal shaft torque.

2. The continuous model should be expanded to consider more than a single shaft between the motor and propeller, to make it more universally applicable.

3. For the inverse models, some information about the control response to external ice loads is necessary. This can come from measurements of the propulsion shaft rotational speed.

4. Scale model testing should be performed, in which both the propeller moment and shaft torque and velocity are measured. This can be used as another form of validation for the continuous model.

5. The axial propeller loads could be estimated using a similar approach to the propeller moment estimation. This would entail the development and evaluation of a continuous model of the propulsion shaft using axial modes instead of torsional ones (see Appendix D).

6. A high fidelity numerical model, such as an FE Model, of the propulsion line system should be built. This model could be used to investigate whether the estimated propeller moments indeed cause the results measured on the shaft during operation. It can also be used to investigate the critical locations on the shaft and the wave propagation through the shaft.

7. If possible, simultaneous measurements of the propeller load through measurements on the blade could be used as a validation tool for the continuous model. Since simultaneous measurement of propeller loads may be difficult, higher sample rate measurements of the motor torque can be used as a validation tool by comparing these measurements to the motor torque estimated by the continuous model in the inverse solution.

Stellenbosch University https://scholar.sun.ac.za

Appendices

Stellenbosch University https://scholar.sun.ac.za

Appendix A

Modal superposition

Modal superposition is a technique that can be used in the analysis of linear structures. With this technique, the dynamic response of a structure can be approximated by a superposition of a number of its mode shapes (eigenmodes).

Assuming the standard form for the equations of motion for a structure

$$\mathbf{M\ddot{u}} + \mathbf{C\dot{u}} + \mathbf{Ku} = \mathbf{f}(t) \tag{A.1}$$

where $\mathbf{M}$ is the mass matrix, $\mathbf{C}$ the damping matrix, and $\mathbf{K}$ the stiffness matrix. The vector $\mathbf{u}$ represents the degrees of freedom of the system. The vector $\mathbf{f}$ represents the loads applied to the system, as a function of time. In the case of N degrees of freedom, the $\mathbf{M}$, $\mathbf{C}$, and $\mathbf{K}$ matrices will all be of size $N \times N$.

It is generally assumed that the matrices are real and symmetric and that $\mathbf{K}$ is positive definite. However, it is possible to perform modal superposition in the case of unsymmetric matrices (COMSOL, 2018). The principles that apply to the symmetric case also apply to the unsymmetric case, although the theory becomes more complicated (COMSOL, 2018).

In order to perform modal superposition, one first needs to compute the natural frequencies (eigenfrequencies) and corresponding mode shapes (eigenmodes). This is done by solving the eigenvalue problem

$$\left(-\omega^2\mathbf{M} + \mathbf{K}\right)\mathbf{u} = 0, \{x\} \neq 0 \tag{A.2}$$

A number n of the natural frequencies ω_i and corresponding mode shapes $\mathbf{u_i}$ are calculated, with $i = 1, 2, ..., n$. The number of mode shapes is chosen such that $n < N$.

The computed mode shapes are orthogonal with respect to the $\mathbf{M}$, and $\mathbf{K}$ matrices (Rao, 2007). This means that

$$\mathbf{u_i}^T\mathbf{M}\mathbf{u_j} = 0, i \neq j \tag{A.3}$$

$$\mathbf{u_i}^T\mathbf{K}\mathbf{u_j} = 0, i \neq j \tag{A.4}$$

Stellenbosch University https://scholar.sun.ac.za

The mode shapes can be placed into a $N \times n$ matrix $\mathbf{U}$, with each column containing a mode shape. The orthogonality relationships above can then be written as

$$\mathbf{U}^T\mathbf{M}\mathbf{U} = \begin{bmatrix} m_1 & 0 & 0 & \cdots & 0 \\ 0 & m_2 & 0 & \cdots & 0 \\ 0 & 0 & m_3 & \cdots & 0 \\ \vdots & \vdots & \vdots & \ddots & \vdots \\ 0 & 0 & 0 & \cdots & m_n \end{bmatrix} = \boldsymbol{\mu} \tag{A.5}$$

$$\mathbf{U}^T\mathbf{K}\mathbf{U} = \begin{bmatrix} m_1\omega_1^2 & 0 & 0 & \cdots & 0 \\ 0 & m_2\omega_2^2 & 0 & \cdots & 0 \\ 0 & 0 & m_3\omega_3^2 & \cdots & 0 \\ \vdots & \vdots & \vdots & \ddots & \vdots \\ 0 & 0 & 0 & \cdots & m_n\omega_n^2 \end{bmatrix} = \boldsymbol{\Omega} \tag{A.6}$$

where the m_i are referred to as the modal masses, whose values depend on the normalization of the mode shapes (Rao, 2007).

The response of the system is then calculated as a linear summation of the mode shapes

$$u(t) \approx \sum_{i=1}^{n} \mathbf{u_i} q_i(t) \tag{A.7}$$

where q_i represents the modal amplitudes. If all mode shapes were to be used in the calculation, the result would be exact. When fewer modes are selected, the modal superposition can be seen as a projection of the displacements onto the subspace spanned by the chosen mode shapes (COMSOL, 2018).

The modal superposition expression in matrix form is

$$\mathbf{u} = \mathbf{U}\mathbf{q} \tag{A.8}$$

with $\mathbf{q}$ a column vector containing the modal amplitudes. Substituting Equation A.8 into Equation A.1 and left multiplying by $\mathbf{U}^T$ gives

$$\mathbf{U}^T\mathbf{M}\mathbf{U}\ddot{\mathbf{q}} + \mathbf{U}^T\mathbf{C}\mathbf{U}\dot{\mathbf{q}} + \mathbf{U}^T\mathbf{K}\mathbf{U}\mathbf{q} = \mathbf{U}^T\mathbf{f}(t) \tag{A.9}$$

Using the orthogonality relationships, Equation A.9 becomes

$$\boldsymbol{\mu}\ddot{\mathbf{q}} + \mathbf{U}^T\mathbf{C}\mathbf{U}\dot{\mathbf{q}} + \boldsymbol{\Omega}\mathbf{q} = \mathbf{r}(t) \tag{A.10}$$

If one then assumes the modal damping matrix as diagonal (e.g. using Modal damping, Rayleigh Damping or Caughey damping) the system of equations becomes uncoupled, with a separate equation to solve for each modal amplitude

Stellenbosch University https://scholar.sun.ac.za

$$\ddot{q}_i(t) + 2\zeta_i\omega_i\dot{q}_i(t) + \omega_i^2 q_i(t) = \frac{r_i(t)}{m_i}, i = 1, 2, \cdots, n \tag{A.11}$$

The modal load $\mathbf{r}(t)$ is a projection of the external loads onto the selected mode shapes (COMSOL, 2018). If the projection of the load onto a certain mode is negligible, then that mode can be ignored in the modal superposition. For example, this happens when a symmetric structure is loaded symmetrically which allows the exclusion of the asymmetric mode shapes (COMSOL, 2018). Also of note is that since only a subset of the total mode shapes of the structure is used in the analysis, a portion of the original load is lost during projection to modal coordinates.

It is also necessary, in order to obtain satisfactory stress results, to use more mode shapes than what is necessary to obtain good displacement results (COMSOL, 2018).

Limitations are also outlined by Besselink *et al.* (2013) as:

- The selected mode shapes do not span the complete space
- mode shape computation for large systems can be expensive and time consuming
- the number of mode shapes necessary for computation is not easily known
- the selected mode shapes may be orthogonal to the loading and will therefore have negligible contribution to the solution

However, methods do exist to allow for the consideration of the truncated portion of the applied loading such as static correction, modal acceleration and modal truncation augmentation (Dickens *et al.*, 1997), (Besselink *et al.*, 2013), (COMSOL, 2018).

Stellenbosch University https://scholar.sun.ac.za

Appendix B

Numerical time integration schemes

Numerical time integration of dynamic equations is one of the most common approaches to the solution of structural dynamic responses (Wilson, 2002). There are several time integration schemes for the solution of structural dynamic problems. These methods may be either explicit or implicit. Explicit schemes express responses in terms of previously determined displacement, velocity, and acceleration values (Dukkipati, 2010). Implicit schemes combine difference equations with equations of motion and calculate displacements directly by solving these equations (Dukkipati, 2010).

Generally, implicit schemes have better stability than explicit ones (Kadapa *et al.*, 2017). Implicit schemes also allow for large time steps, requiring shorter solution times and less computational effort. However large time steps may lead to unwanted numerical dissipation in the low frequency range (Kadapa *et al.*, 2017). A competitive integration scheme for structural dynamic problems should possess the following properties (Kadapa *et al.*, 2017):

1. Unconditional stability when used in the solution of linear problems.
2. Only one set of implicit equations should be solved at each time step.
3. Must be second-order accurate.
4. Must have controllable algorithmic dissipation in the higher modes or frequency range.
5. Must be self-starting.
6. The scheme should not suffer from overshoot behaviour.

There has been significant research conducted in the development of implicit schemes that satisfy some or all of the properties listed above. These include the following methods (Kadapa *et al.*, 2017):

Stellenbosch University https://scholar.sun.ac.za

- Newmark-β (Newmark, 1959)
- Wilson-θ (Wilson *et al.*, 1973)
- HHT-α (Hilbur *et al.*, 1977)
- Collocation scheme (Hilbur and Hughes, 1978)
- WBZ-α (Wood *et al.*, 1981)
- HP-θ (Hoff and Pahl, 1988)
- CH-α (Chung and Hulbert, 1993)
- G-α (KaiPing, 2008)

The Newmark-β method is elaborated on in Section B.1, as this is the method used to solve the lumped mass models developed by Ikonen *et al.* (2014) and De Waal (2017). Section B.2 elaborates on a first-order generalised-α scheme, first proposed by Jansen *et al.* (1999) for the solution of the Navier-Stokes equations, and suggested for use in structural dynamic problems by Kadapa *et al.* (2017). Kadapa *et al.* (2017) refer to this scheme as JWH-α. Lavrenčič and Brank (2020) compare various generalised-α schemes and show that the JWH-α method has the best dissipative properties. This JWH-α scheme is used in the solution of the modal model.

B.1 Newmark-β method

This numerical integration scheme was first presented by Newmark (1959). It has since been a popular solution method for structural dynamics and has been improved and modified by a number of researchers (Wilson, 2002). This method can be used to solve dynamic equations of the form

$$\mathbf{M}\ddot{\mathbf{u}} + \mathbf{C}\dot{\mathbf{u}} + \mathbf{K}\mathbf{u} = \mathbf{f} \tag{B.1}$$

Through direct Taylor series expansion, the following two equations can be derived

$$\mathbf{u}_{n+1} = \mathbf{u}_n + \Delta t\dot{\mathbf{u}}_n + \frac{\Delta t^2}{2}\ddot{\mathbf{u}}_n + \frac{\Delta t^3}{6}\dddot{\mathbf{u}}_n + ... \tag{B.2}$$

$$\dot{\mathbf{u}}_{n+1} = \dot{\mathbf{u}}_n + \Delta t\ddot{\mathbf{u}}_n + \frac{\Delta t^2}{2}\dddot{\mathbf{u}}_n + ... \tag{B.3}$$

Newmark (1959) provides truncated versions of Equations B.2 and B.3 of the following form

Stellenbosch University https://scholar.sun.ac.za

$$\mathbf{u}_{n+1} = \mathbf{u}_n + \Delta t \dot{\mathbf{u}}_n + \frac{\Delta t^2}{2} \ddot{\mathbf{u}}_n + \beta \dddot{\mathbf{u}}_n \tag{B.4}$$

$$\dot{\mathbf{u}}_{n+1} = \dot{\mathbf{u}}_n + \Delta t \ddot{\mathbf{u}}_n + \gamma \dddot{\mathbf{u}}_n \tag{B.5}$$

where γ and β are truncation constants he introduced.

Furthermore, if the acceleration is assumed as linear across the time step then

$$\dddot{\mathbf{u}}_{n+1} = \frac{\ddot{\mathbf{u}}_{n+1} - \ddot{\mathbf{u}}_n}{\Delta t} \tag{B.6}$$

Substituting Equation B.6 into Equations B.4 and B.5 results in Newmark's equations in their standard form

$$\mathbf{u}_{n+1} = \mathbf{u}_n + \left(\frac{1}{2} - \beta\right) \Delta t^2 \ddot{\mathbf{u}}_n + \beta \Delta t^2 \ddot{\mathbf{u}}_{n+1} \tag{B.7}$$

$$\dot{\mathbf{u}}_{n+1} = \dot{\mathbf{u}}_n + (1 - \gamma) \Delta t \ddot{\mathbf{u}}_n + \gamma \Delta t \ddot{\mathbf{u}}_{n+1} \tag{B.8}$$

Equations B.7 and B.8 are then solved by performing an iteration at each time step.

Wilson (1962) reformulated Equations B.7 and B.8 to remove the need for iteration. He proposed rewriting the equations as

$$\ddot{\mathbf{u}}_{n+1} = b_1 (\mathbf{u}_{n+1} - \mathbf{u}_n) + b_2 \dot{\mathbf{u}}_n + b_3 \ddot{\mathbf{u}}_n \tag{B.9}$$

$$\dot{\mathbf{u}}_{n+1} = b_4 (\mathbf{u}_{n+1} - \mathbf{u}_n) + b_5 \dot{\mathbf{u}}_n + b_6 \ddot{\mathbf{u}}_n \tag{B.10}$$

where

$$b_1 = \frac{1}{\beta \Delta t^2}$$

$$b_2 = \frac{1}{\beta \Delta t}$$

$$b_3 = \beta - \frac{1}{2}$$

$$b_4 = \gamma \Delta t b_1$$

$$b_5 = 1 + \gamma \Delta t b_2$$

$$b_6 = \Delta t (1 + \gamma b_3 - \gamma)$$

Stellenbosch University https://scholar.sun.ac.za

Equation B.1 can be rewritten, through substitution of Equations B.9 and B.10, in terms of the unknown solution vector for the current time step, Equation B.11. This equation can then be solved directly at each time step.

$$\bar{\mathbf{K}}\mathbf{u}_{n+1} = \bar{\mathbf{f}} \tag{B.11}$$

where the effective stiffness matrix ($\bar{\mathbf{K}}$) and effective force vector ($\bar{\mathbf{f}}$) are given by

$$\bar{\mathbf{K}} = \mathbf{K} + b_1\mathbf{M} + b_4\mathbf{C} \tag{B.12}$$

$$\bar{\mathbf{f}} = \mathbf{f}_{n+1} + \mathbf{M}\cdot(b_1\mathbf{u}_n - b_2\dot{\mathbf{u}}_n - b_3\ddot{\mathbf{u}}_n) + \mathbf{C}\cdot(b_4\mathbf{u}_n - b_5\dot{\mathbf{u}}_n - b_6\ddot{\mathbf{u}}_n) \tag{B.13}$$

Once $\mathbf{u}_{n+1}$ is solved for then $\ddot{\mathbf{u}}_{n+1}$ and $\dot{\mathbf{u}}_{n+1}$ can be solved using Equations B.9 and B.10 respectively.

Wilson (2002) shows that this method is unconditionally stable if

$$\frac{1}{2} \leq \gamma \leq 2\beta$$

however errors occur if γ is larger than $\frac{1}{2}$.

This leads to a few variations in the method, depending on the selection of parameters. The most commonly used methods are summarised in Table B.1 below (Wilson, 2002).

Table B.1: Summary of Newmark-β methods (adapted from Wilson (2002))

Method	γ	β	Accuracy
Central difference	$\frac{1}{2}$	0	Excellent for small time steps, Unstable for large time steps
Linear acceleration	$\frac{1}{2}$	$\frac{1}{6}$	Very good for small time steps, Unstable for large time steps
Average acceleration	$\frac{1}{2}$	$\frac{1}{4}$	Good for small time steps, Unconditionally stable, No energy dissipation

B.2 JWH-α method

This numerical integration scheme was first presented by Jansen *et al.* (1999) for the solution of filtered Navier-Stokes equations within the context of a stabilised finite element method. It has since been applied in the analysis of incompressible nonlinear elastodynamics (Rossi *et al.*, 2016) and incompressible solid dynamics of viscoelastic materials (Zeng *et al.*, 2017).

Stellenbosch University https://scholar.sun.ac.za

The method was recommended for use in structural dynamics problems by Kadapa *et al.* (2017), where it was tested against other time integration methods. It was shown that this method has improved numerical dissipation and dispersion properties when compared to other methods, and that it does not suffer from overshoot. Kadapa *et al.* (2017) refer to this method as JWH-α, named for the original authors Jansen, K., Whiting, C., and Hulbert, G. (Jansen *et al.*, 1999).

The JWH-α method can be used to solve dynamic equations of the form

$$\mathbf{M}\ddot{\mathbf{u}} + \mathbf{C}\dot{\mathbf{u}} + \mathbf{K}\mathbf{u} = \mathbf{f} \tag{B.14}$$

by converting the second-order differential equation into a set of first-order equations. This is done by introducing an auxiliary variable $\mathbf{v} = \dot{\mathbf{u}}$. The first-order system equivalent to Equation B.14 in matrix form is

$$\begin{bmatrix} \mathbf{M} & 0 \\ 0 & \mathbf{M} \end{bmatrix} \begin{Bmatrix} \dot{\mathbf{u}} \\ \dot{\mathbf{v}} \end{Bmatrix} + \begin{bmatrix} 0 & -\mathbf{M} \\ \mathbf{K} & \mathbf{C} \end{bmatrix} \begin{Bmatrix} \mathbf{u} \\ \mathbf{v} \end{Bmatrix} = \begin{Bmatrix} 0 \\ \mathbf{f} \end{Bmatrix} \tag{B.15}$$

Applying the JWH-α scheme to Equation B.15 results in the following system

$$\begin{bmatrix} \mathbf{M} & 0 \\ 0 & \mathbf{M} \end{bmatrix} \begin{Bmatrix} \dot{\mathbf{u}}_{n+\alpha_m} \\ \dot{\mathbf{v}}_{n+\alpha_m} \end{Bmatrix} + \begin{bmatrix} 0 & -\mathbf{M} \\ \mathbf{K} & \mathbf{C} \end{bmatrix} \begin{Bmatrix} \mathbf{u}_{n+\alpha_f} \\ \mathbf{v}_{n+\alpha_f} \end{Bmatrix} = \begin{Bmatrix} 0 \\ \mathbf{f}_{n+\alpha_f} \end{Bmatrix} \tag{B.16}$$

$$\dot{\mathbf{u}}_{n+\alpha_m} = \alpha_m \dot{\mathbf{u}}_{n+1} + (1-\alpha_m)\dot{\mathbf{u}}_n \tag{B.17}$$

$$\dot{\mathbf{v}}_{n+\alpha_m} = \alpha_m \dot{\mathbf{v}}_{n+1} + (1-\alpha_m)\dot{\mathbf{v}}_n \tag{B.18}$$

$$\mathbf{u}_{n+\alpha_f} = \alpha_f \mathbf{u}_{n+1} + (1-\alpha_f)\mathbf{u}_n \tag{B.19}$$

$$\mathbf{v}_{n+\alpha_f} = \alpha_f \mathbf{v}_{n+1} + (1-\alpha_f)\mathbf{v}_n \tag{B.20}$$

$$\mathbf{f}_{n+\alpha_f} = \alpha_f \mathbf{f}_{n+1} + (1-\alpha_f)\mathbf{f}_n \tag{B.21}$$

$$\dot{\mathbf{u}}_{n+1} = \frac{1}{\gamma\Delta t}(\mathbf{u}_{n+1} - \mathbf{u}_n) + \frac{\gamma - 1}{\gamma}\dot{\mathbf{u}}_n \tag{B.22}$$

$$\dot{\mathbf{v}}_{n+1} = \frac{1}{\gamma\Delta t}(\mathbf{v}_{n+1} - \mathbf{v}_n) + \frac{\gamma - 1}{\gamma}\dot{\mathbf{v}}_n \tag{B.23}$$

where γ, α_m, and α_f are the constants of the integration scheme.

Using Equations B.17-B.23, the system in Equation B.16 could then be solved for $\{\mathbf{u}_{n+1}\ \mathbf{v}_{n+1}\}^T$. However this requires solving a matrix system twice

Stellenbosch University https://scholar.sun.ac.za

as large as the original. Kadapa *et al.* (2017) show that the system in Equation B.16 can be rewritten so that the system to be solved is the same size as the original. This is done by noting that the first equation in the system can be simplified to

$$\dot{\mathbf{u}}_{n+\alpha_m} = \mathbf{v}_{n+\alpha_f} \tag{B.24}$$

which, using Equations B.17 and B.20, can be rewritten as

$$\mathbf{v}_{n+1} = \frac{\alpha_m}{\alpha_f}\dot{\mathbf{u}}_{n+1} + \frac{1-\alpha_m}{\alpha_f}\dot{\mathbf{u}}_n + \frac{\alpha_f - 1}{\alpha_f}\mathbf{v}_n \tag{B.25}$$

Then, using Equations B.22, B.23, and B.25, $\mathbf{v}_{n+1}$ and $\dot{\mathbf{v}}_{n+1}$ can be written as

$$\mathbf{v}_{n+1} = \frac{\alpha_m}{\alpha_f \gamma \Delta t}\left(\mathbf{u}_{n+1} + \mathbf{u}_n\right)\frac{\gamma - \alpha_m}{\gamma \alpha_f}\dot{\mathbf{u}}_n + \frac{\alpha_f - 1}{\alpha_f}\mathbf{v}_n \tag{B.26}$$

$$\dot{\mathbf{v}}_{n+1} = \frac{\alpha_m}{\alpha_f \gamma^2 \Delta t^2}\left(\mathbf{u}_{n+1} + \mathbf{u}_n\right) + \frac{\gamma - \alpha_m}{\alpha_f \gamma^2 \Delta t}\dot{\mathbf{u}}_n - \frac{1}{\alpha_f \gamma \Delta t}\mathbf{v}_n + \frac{\gamma - 1}{\gamma}\dot{\mathbf{v}}_n \tag{B.27}$$

And finally, using Equations B.18-B.20,B.26, and B.27, the second equation of the system in Equation B.16

$$\mathbf{M}\dot{\mathbf{v}}_{n+\alpha_m} + \mathbf{C}\mathbf{v}_{n+\alpha_f} + \mathbf{K}\mathbf{u}_{n+\alpha_f} = \mathbf{f}_{n+\alpha_f} \tag{B.28}$$

can be solved for $\mathbf{u}_{n+1}$ from

$$\bar{\mathbf{K}}\mathbf{u}_{n+1} = \bar{\mathbf{f}} \tag{B.29}$$

where the effective stiffness matrix ($\bar{\mathbf{K}}$) and effective force vector ($\bar{\mathbf{f}}$) are given by

$$\bar{\mathbf{K}} = \frac{\alpha_m^2}{\alpha_f \gamma^2 \Delta t^2}\mathbf{M} + \frac{\alpha_m}{\gamma \Delta t}\mathbf{C} + \alpha_f \mathbf{K} \tag{B.30}$$

$$\begin{aligned}\bar{\mathbf{f}} = \mathbf{f}_{n+\alpha_f} &- (1-\alpha_m)\mathbf{M}\dot{\mathbf{v}}_n - (1-\alpha_f)\mathbf{C}\mathbf{v}_n - (1-\alpha_f)\mathbf{K}\mathbf{u}_n \\ &+ \alpha_f \mathbf{C}\left(\frac{\alpha_m}{\alpha_f \gamma \Delta t}\mathbf{u}_n - \frac{\gamma - \alpha_m}{\gamma \alpha_f}\dot{\mathbf{u}}_n - \frac{\alpha_f - 1}{\alpha_f}\mathbf{v}_n\right) \\ &+ \alpha_m \mathbf{M}\left(\frac{\alpha_m}{\alpha_f \gamma^2 \Delta t^2}\mathbf{u}_n - \frac{\gamma - \alpha_m}{\alpha_f \gamma^2 \Delta t}\dot{\mathbf{u}}_n + \frac{1}{\alpha_f \gamma \Delta t}\mathbf{v}_n - \frac{\gamma - 1}{\gamma}\dot{\mathbf{v}}_n\right)\end{aligned} \tag{B.31}$$

Once $\mathbf{u}_{n+1}$ is solved for then $\dot{\mathbf{u}}_{n+1}$, $\mathbf{v}_{n+1}$, and $\dot{\mathbf{v}}_{n+1}$ are solved using Equations B.22, B.26, and B.27 respectively.

Stellenbosch University https://scholar.sun.ac.za

The only additional cost in solving the second-order differential equation (Equation B.14) as a system of first-order differential equations (Equation B.15) is the memory required to store the additional variable $\mathbf{v}_n$, and the scalar-vector calculations to determine $\mathbf{v}_{n+1}$ (Kadapa *et al.*, 2017).

In order for the method to be second order accurate, Jansen *et al.* (1999) find that

$$\gamma = \frac{1}{2} + \alpha_m - \alpha_f \tag{B.32}$$

Therefore the method relies only on the selection of α_m and α_f. Jansen *et al.* (1999) also show that the stability of the method requires

$$\frac{1}{2} \leq \alpha_f \leq \alpha_m \tag{B.33}$$

Jansen *et al.* (1999) then express α_m and α_f in terms of a single constant, the spectral radius for an infinite time step ($0 \leq \rho_\infty \leq 1$)

$$\alpha_m = \frac{1}{2}\left(\frac{3 - \rho_\infty}{1 + \rho_\infty}\right) \tag{B.34}$$

$$\alpha_f = \frac{1}{1 + \rho_\infty} \tag{B.35}$$

This allows for the method to rely on a single tunable parameter, giving strict control over high frequency damping. If ρ_∞ is chosen as zero, the method will eliminate the highest frequency in one step. If ρ_∞ is chosen as one, the highest frequency in the solution is preserved.

Stellenbosch University https://scholar.sun.ac.za

Appendix C

Specifications and data for the shaft-line models

C.1 Discrete lumped mass model parameters

The parameters for the discrete lumped mass model are presented in Table C.1. The inertia value for the propeller includes both the propeller inertia and the inertia of entrained water, or hydrodynamic mass. Both the hydrodynamic mass and the hydrodynamic damping values were determined by Rolls-Royce AB (2010*b*) using the method developed by Schwanecke (1963). This method is also described in detail by Bertram (2012). It uses an unsteady lifting line method to compute the hydrodynamic mass and damping matrices for propellers vibrating as rigid bodies with six degrees of freedom. The hydrodynamic mass and damping values are approximated as functions of the water density, the expanded area ratio (EAR), the propeller pitch (P), the number of propeller blades (Z), the propeller blade diamter (D), and the propeller angular frequency (ω).

The propeller in this model only considers the rotational degree of freedom about the x-axis, or along the length of the shaft. The corresponding moment of inertia for the hydrodynamic mass is calculated using Equation C.1. The hydrodynamic damping is determined using Equation C.2.

$$J = 0.052\rho D^5 \left(\frac{P}{D}\right)^2 \frac{EAR^2}{\pi Z} \tag{C.1}$$

$$C = 0.017\rho\omega D^5 \left(\frac{P}{D}\right)^2 \frac{EAR}{\pi} \tag{C.2}$$

Stellenbosch University https://scholar.sun.ac.za

Table C.1: Properties of the lumped mass model (Rolls-Royce AB, 2010*a*,*b*)

Component	Symbol	Value
Propeller	J_1	1.347×10^4 kg · m^2
Mid propeller shaft	J_3	5.590×10^2 kg · m^2
Sleeve coupling	J_5	5.120×10^2 kg · m^2
Oil distribution box flange	J_7	4.870×10^2 kg · m^2
Thrust shaft collar	J_9	1.410×10^2 kg · m^2
Motor flange	J_{11}	1.740×10^2 kg · m^2
Propulsion motor	J_{13}	4.415×10^3 kg · m^2
Hydrodynamic damping	c_1	1.136×10^5 Nm · s/rad
Steel shaft	c_{2-12}	0
Steel shaft	k_2	5.880×10^7 Nm/rad
Steel shaft	k_4	5.950×10^7 Nm/rad
Steel shaft	k_6	1.120×10^8 Nm/rad
Steel shaft	k_8	6.930×10^8 Nm/rad
Steel shaft	k_{10}	5.090×10^8 Nm/rad
Steel shaft	k_{12}	1.430×10^8 Nm/rad

C.2 Continuous modal superposition model parameters

The parameters for the continuous modal superposition model are presented in Table C.2.

The inertia value for the propeller includes both the propeller inertia and the inertia of entrained water, or hydrodynamic mass. Both the hydrodynamic mass and the hydrodynamic damping values were determined by Rolls-Royce AB (2010*b*) using the method developed by Schwanecke (1963), as described in Section C.1.

Table C.2: Properties of the modal superposition model

Parameter	Symbol	Value
Propeller inertia	J_p	1.347×10^4 kg · m^2
Motor inertia	J_{motor}	4.415×10^3 kg · m^2
Hydrodynamic damping	C_p	1.136×10^5 Nm · s/rad
Shear modulus	G	81 GPa
Density	ρ	7850 kg/m^3
Shaft-line length	L	29.5 m
Inner shaft diameter	d_i	0.175 m
Outer shaft diameter	d_o	0.5 m

The parameters for the continuous modal superposition model when used with the data published by Polić *et al.* (2016, 2019) are presented in Table C.3.

Stellenbosch University https://scholar.sun.ac.za

Table C.3: Parameters for the model used by Polić *et al.* (2016, 2019)

Parameter	Symbol	Value
Propeller inerita	J_p	4.60×10^4 kg $\cdot$ m^2
Motor inertia	J_{motor}	5.25×10^3 kg $\cdot$ m^2
Hydrodynamic damping	C_p	0 Nm $\cdot$ s/rad
Shear modulus	G	77 GPa
Density	ρ	7850 kg/m^3
propulsion shaft length	L	12 m
Inner shaft diameter	d_i	0.2 m
Outer shaft diameter	d_o	0.6 m

C.3 Data for the evaluation of the discrete lumped mass model

The following tables provide data that was used in the evaluation of the discrete lumped mass model of the S.A. Agulhas II shaft-line. Fifty cases of ice impacts were extracted from data recorded on the morning of 17 December 2018. At this time, the ship was breaking through ice en route to the ice shelf at Penguin Bukta for logistics operations.

The operational parameters of the S.A. Agulhas II for the cases used to evaluate the discrete model are presented in Table C.4.

The successes of the different regularization methods are presented in Table C.5. A method was said to be successful if the regularization parameter could be successfully automatically determined by the algorithm, and the optimal inverse solution thus obtained.

Table C.6 provides a comparison of the solution times for the two methods that achieved 100% success rates, the DGSVD and Tikhonov methods.

Stellenbosch University https://scholar.sun.ac.za

Table C.4: Ship operational parameters for cases used in the evaluation of the discrete model, from the 17 December 2018

Case	Time	Case duration [sec]	Ship speed [knots]	Hydrodynamic torque [kNm]	Motor speed [rpm]	Motor power [kW]	Propeller pitch [%]	Average ice concentration [%]	Average ice thickness [cm]	Average floe size [m]
1	05:11:06	1.8	2.4	263.07	139	3180	71	81	36	255
2	06:54:43	2.0	2.4	323.95	136	4725	81	59	48	478
3	07:18:12	1.0	2.7	219.14	140	3610	72	38	70	48
4	07:19:27	4.9	2.1	321.13	139	4320	78	38	70	48
5	07:19:33	1.0	2.0	321.89	138	4100	80	38	70	48
6	07:20:02	1.3	1.9	315.26	138	4320	81	95	66	323
7	07:22:18	1.1	2.1	294.17	139	3920	74	95	66	323
8	07:23:09	1.6	1.9	323.58	139	2970	68	95	66	323
9	07:23:12	2.0	1.9	306.69	136	3600	78	95	66	323
10	07:24:36	1.7	1.7	316.70	139	4165	81	95	66	323
11	07:24:40	2.2	1.9	317.26	139	4450	81	95	66	323
12	07:25:31	5.0	2.0	274.29	140	3800	74	95	66	323
13	07:25:36	8.0	2.0	295.52	140	3750	74	95	66	323
14	07:25:44	6.0	1.9	143.02	139	3775	74	95	66	323
15	07:28:45	5.8	1.7	179.60	139	2150	59	95	66	323
16	07:28:51	10.6	1.8	173.61	139	2500	61	95	66	323
17	07:54:25	2.0	1.6	318.05	136	4600	81	95	60	998
18	07:55:27	4.2	1.2	262.15	139	3620	70	95	60	998
19	07:58:17	1.7	1.3	316.79	135	4520	81	95	60	998
20	07:58:20	3.7	1.4	305.69	136	4450	81	95	60	998

Stellenbosch University https://scholar.sun.ac.za

Table C.4 continued from previous page

Case	Time	Case duration [sec]	Ship speed [knots]	Hydrodynamic torque [kNm]	Motor speed [rpm]	Motor power [kW]	Propeller pitch [%]	Average ice concentration [%]	Average ice thickness [cm]	Average floe size [m]
21	07:58:27	6.0	1.6	315.83	138	4400	81	95	60	998
22	07:59:24	1.2	2.6	309.30	139	4275	81	95	60	998
23	08:00:43	6.0	1.6	316.16	114	2750	81	95	48	276
24	08:12:04	1.5	2.1	308.48	139	4775	81	95	48	132
25	08:12:30	1.3	2.5	303.49	139	4225	81	95	48	132
26	08:13:00	2.9	2.5	322.23	139	4175	81	95	48	132
27	08:13:16	5.5	2.1	326.06	139	4575	81	95	48	132
28	08:14:42	1.9	1.6	327.09	138	4580	81	95	48	132
29	08:16:37	3.1	0.6	218.80	139	1600	-40	95	48	132
30	08:18:53	3.7	0.2	60.41	139	1460	-41	95	48	132
31	08:29:19	2.0	0.8	243.04	139	1060	-31	95	50	1250
32	08:29:44	2.4	0.4	92.83	139	3525	-75	95	50	1250
33	08:37:56	2.0	2.9	152.37	140	3850	81	95	72	204
34	08:38:47	6.2	3.4	264.77	137	2900	72	95	72	204
35	08:39:10	9.0	2.9	326.11	138	3500	75	95	72	204
36	08:42:17	3.0	0.3	189.89	140	2300	-52	95	76	3500
37	08:42:42	1.4	0.5	193.78	139	2580	-68	95	76	3500
38	08:42:46	4.0	0.5	193.70	139	3100	-69	95	76	3500
39	08:42:55	4.3	0.6	110.26	139	2900	-68	95	76	3500
40	08:43:28	2.6	0.5	242.20	136	1600	-50	95	76	3500
41	08:47:01	3.2	0.1	303.32	129	1400	-50	95	76	3500
42	08:47:30	2.4	0.4	304.92	136	4450	-89	95	76	3500

Stellenbosch University https://scholar.sun.ac.za

Table C.4 continued from previous page

Case	Time	Case duration [sec]	Ship speed [knots]	Hydrodynamic torque [kNm]	Motor speed [rpm]	Motor power [kW]	Propeller pitch [%]	Average ice concentration [%]	Average ice thickness [cm]	Average floe size [m]
43	08:48:25	5.6	0.6	194.49	139	4250	-82	95	76	3500
44	08:48:38	2.0	0.7	240.16	140	1000	-25	95	76	3500
45	08:48:56	3.5	0.4	289.63	138	3250	-67	95	76	3500
46	08:54:56	1.7	0.6	258.55	137	3025	-78	95	72	3500
47	08:59:37	7.0	1.1	49.92	139	1000	-25	95	72	3500
48	08:59:46	2.0	1.1	55.00	139	700	0	95	72	3500
49	09:00:22	5.3	0.4	321.02	139	940	-2	95	70	3500
50	09:12:28	2.1	0.6	62.74	138	2235	-64	95	70	3500

Stellenbosch University https://scholar.sun.ac.za

Table C.5: Success of the various regularization methods

	Regularisation method															
	TSVD		MTSVD		TGSVD		DSVD		DGSVD		Tikhonov		Least squares (quadratic constraint)		Least squares (discrepancy principle)	
Case	Q1	Q2	Q1	Q2	Q1	Q2	Q1	Q2	Q1	Q2	Q1	Q2	Q1	Q2	Q1	Q2
1		✓			✓	✓	✓	✓	✓	✓	✓	✓	✓	✓	✓	✓
2	✓	✓			✓	✓			✓	✓	✓	✓	✓	✓	✓	✓
3	✓	✓			✓	✓			✓	✓	✓	✓	✓	✓	✓	✓
4	✓	✓				✓			✓	✓	✓	✓	✓	✓	✓	✓
5	✓	✓			✓	✓			✓	✓	✓	✓	✓	✓	✓	✓
6	✓	✓	✓	✓	✓	✓			✓	✓	✓	✓	✓	✓	✓	✓
7	✓	✓	✓	✓	✓	✓			✓	✓	✓	✓	✓	✓	✓	✓
8		✓			✓	✓			✓	✓	✓	✓	✓	✓	✓	✓
9	✓	✓			✓	✓			✓	✓	✓	✓	✓		✓	
10	✓	✓			✓	✓			✓	✓	✓	✓	✓	✓	✓	✓
11		✓	✓	✓	✓	✓			✓	✓	✓	✓	✓	✓	✓	✓
12					✓	✓			✓	✓	✓	✓	✓		✓	
13									✓	✓	✓	✓				
14					✓	✓			✓	✓	✓	✓	✓		✓	
15	✓	✓		✓	✓	✓			✓	✓	✓	✓	✓	✓	✓	✓
16	✓	✓				✓			✓	✓	✓	✓				
17	✓	✓			✓	✓	✓	✓	✓	✓	✓	✓	✓	✓	✓	✓
18					✓	✓			✓	✓	✓	✓	✓		✓	
19		✓			✓	✓			✓	✓	✓	✓	✓	✓	✓	✓
20		✓			✓	✓			✓	✓	✓	✓	✓		✓	
21					✓	✓			✓	✓	✓	✓	✓		✓	

Stellenbosch University https://scholar.sun.ac.za

Table C.5 continued from previous page

	Regularisation method															
	TSVD		MTSVD		TGSVD		DSVD		DGSVD		Tikhonov		Least squares (quadratic constraint)		Least squares (discrepancy principle)	
Case	Q1	Q2	Q1	Q2	Q1	Q2	Q1	Q2	Q1	Q2	Q1	Q2	Q1	Q2	Q1	Q2
22	✓	✓			✓	✓			✓	✓	✓	✓	✓	✓	✓	✓
23	✓	✓			✓	✓			✓	✓	✓	✓	✓		✓	
24	✓	✓	✓		✓	✓			✓	✓	✓	✓	✓	✓	✓	✓
25	✓	✓			✓	✓			✓	✓	✓	✓	✓		✓	
26		✓			✓	✓			✓	✓	✓	✓	✓		✓	
27					✓	✓			✓	✓	✓	✓	✓	✓	✓	✓
28	✓	✓			✓	✓			✓	✓	✓	✓	✓	✓	✓	✓
29	✓				✓	✓			✓	✓	✓	✓	✓	✓	✓	✓
30									✓	✓	✓	✓	✓	✓	✓	✓
31		✓		✓	✓	✓			✓	✓	✓	✓	✓	✓	✓	✓
32					✓	✓			✓	✓	✓	✓	✓	✓	✓	✓
33	✓	✓	✓		✓	✓			✓	✓	✓	✓	✓	✓	✓	✓
34					✓	✓			✓	✓	✓	✓	✓	✓	✓	✓
35									✓	✓	✓	✓	✓	✓	✓	✓
36	✓	✓			✓	✓			✓	✓	✓	✓	✓	✓	✓	✓
37	✓				✓	✓			✓	✓	✓	✓	✓	✓	✓	✓
38									✓	✓	✓	✓	✓		✓	
39	✓	✓			✓				✓	✓	✓	✓	✓	✓	✓	✓
40					✓				✓	✓	✓	✓	✓	✓	✓	✓
41					✓	✓			✓	✓	✓	✓	✓	✓	✓	✓
42					✓	✓			✓	✓	✓	✓	✓	✓	✓	✓

Stellenbosch University https://scholar.sun.ac.za

Table C.5 continued from previous page

	Regularisation method															
	TSVD		MTSVD		TGSVD		DSVD		DGSVD		Tikhonov		Least squares (quadratic constraint)		Least squares (discrepancy principle)	
Case	Q1	Q2	Q1	Q2	Q1	Q2	Q1	Q2	Q1	Q2	Q1	Q2	Q1	Q2	Q1	Q2
43					✓	✓			✓	✓	✓	✓	✓	✓	✓	✓
44		✓			✓	✓			✓	✓	✓	✓	✓	✓	✓	✓
45		✓			✓	✓			✓	✓	✓	✓	✓	✓	✓	✓
46		✓			✓	✓			✓	✓	✓	✓	✓	✓	✓	✓
47									✓	✓	✓	✓	✓		✓	
48					✓	✓			✓	✓	✓	✓	✓	✓	✓	✓
49	✓				✓				✓	✓	✓	✓	✓	✓	✓	✓
50					✓	✓			✓	✓	✓	✓	✓	✓	✓	✓

Stellenbosch University https://scholar.sun.ac.za

Table C.6: Solution times for the DGSVD and Tikhonov regularization methods

Case	Case duration [sec]	Solution time [sec]			
		DGSVD		Tikhonov	
		Q_1	Q_2	Q_1	Q_2
1	1.8	2.07	2.17	2.00	2.21
2	2.0	2.62	2.84	2.89	2.86
3	1.0	1.08	1.45	1.13	1.31
4	4.9	25.19	25.75	24.67	24.76
5	1.0	1.09	1.30	1.09	1.30
6	1.3	1.50	1.52	1.55	1.62
7	1.1	1.11	1.34	1.08	1.38
8	1.6	1.86	1.87	1.85	1.85
9	2.0	2.83	2.83	2.94	2.80
10	1.7	2.00	2.00	2.16	2.08
11	2.2	3.37	3.37	3.36	3.45
12	5.0	26.70	26.43	26.38	26.04
13	8.0	77.05	77.36	77.04	76.50
14	6.0	44.51	45.14	44.99	44.87
15	5.8	41.06	40.97	40.79	41.10
16	10.6	164.85	166.35	162.60	163.58
17	2.0	2.68	2.57	2.86	2.96
18	4.2	16.82	16.68	16.68	17.44
19	1.7	1.70	1.76	1.77	1.90
20	3.7	11.77	11.80	11.75	11.80
21	6.0	44.70	44.89	44.97	44.87
22	1.2	1.26	1.44	1.29	1.52
23	6.0	44.50	44.87	44.63	45.02
24	1.5	1.55	1.72	1.49	1.84
25	1.3	1.93	1.99	1.25	1.69
26	2.9	6.13	6.16	6.17	6.48
27	5.5	35.25	35.17	35.12	34.92
28	1.9	2.87	2.86	2.82	2.83
29	3.1	7.32	7.44	7.43	7.34
30	3.7	11.72	11.74	11.71	11.77
31	2.0	3.03	3.01	2.99	3.06
32	2.4	4.49	4.24	4.23	4.22
33	2.0	3.02	3.02	3.01	3.09
34	6.2	49.88	49.42	49.81	49.81
35	9.0	91.53	89.42	89.99	89.55
36	3.0	6.89	6.78	6.89	6.65
37	1.4	2.00	1.85	2.17	1.83
38	4.0	14.26	14.71	14.26	14.34

Stellenbosch University https://scholar.sun.ac.za

Table C.6 continued from previous page

Case	Case duration [sec]	Solution time [sec]			
		DGSVD		Tikhonov	
		Q_1	Q_2	Q_1	Q_2
39	4.3	17.26	17.14	17.58	17.51
40	2.6	4.97	4.91	4.95	4.98
41	3.2	8.10	7.87	7.95	8.02
42	2.4	4.30	4.08	4.33	4.38
43	5.6	36.18	36.26	36.25	36.12
44	2.0	2.96	3.03	3.16	2.96
45	3.5	9.89	9.98	9.84	9.96
46	1.7	2.62	2.45	2.52	2.49
47	7.0	49.58	49.02	48.09	48.85
48	2.0	3.43	3.01	3.09	3.23
49	5.3	31.37	31.49	31.76	30.92
50	2.1	3.39	3.44	3.39	3.41

C.4 Data for the comparison of the discrete and continuous models

The following tables provide data that was used in the evaluation of the discrete and continuous models of the S.A. Agulhas II shaft-line. Fifty cases of ice impacts were extracted from data recorded during the 2019 SCALE Spring Cruise on the evening of 30 October 2019. Ice impacts were identified during operations within the marginal ice zone.

The operational parameters of the S.A. Agulhas II for the cases used to compare the models are presented in Table C.7.

Table C.8 provides a comparison of the solution times for the two models.

Stellenbosch University https://scholar.sun.ac.za

Table C.7: Ship operational parameters for cases used in the comparison of the discrete and continuous models

Case	Time	Case duration [sec]	Ship speed [knots]	Hydrodynamic torque [kNm]	Motor speed [rpm]	Motor power [kW]	Propeller pitch [%]	Average ice concentration [%]	Average ice thickness [cm]	Average floe size [m]
1	20:06:20	2.0	5.1	215.95	140	3096	76	84	30	17
2	20:07:43	2.4	4.7	211.69	139	1978	60	84	30	17
3	20:07:53	1.8	4.8	213.66	139	2313	62	84	30	17
4	20:08:25	1.9	4.6	229.36	140	2273	62	84	30	17
5	20:08:40	3.3	4.3	218.88	137	3054	68	84	30	17
6	20:08:56	3.9	4.1	238.78	140	3015	69	84	30	17
7	20:09:33	1.8	4.7	226.56	140	2745	67	84	30	17
8	20:09:36	2.5	4.7	226.32	140	2625	68	84	30	17
9	20:09:39	5.0	4.8	221.05	140	2564	68	84	30	17
10	20:10:24	3.0	4.7	227.54	139	3341	74	95	25	43
11	20:10:33	5.2	4.8	111.64	140	3280	74	95	25	43
12	20:12:01	1.9	6.6	155.10	140	1736	62	95	25	43
13	20:12:15	3.5	6.6	193.76	140	805	49	95	25	43
14	20:12:26	2.7	6.4	208.47	140	864	49	95	25	43
15	20:25:45	1.6	6.8	204.56	140	3201	82	63	30	60
16	20:28:56	2.9	4.5	240.91	140	794	0	63	30	60
17	20:35:58	8.2	5.5	321.17	140	4065	83	89	40	20
18	20:37:22	1.8	4.3	271.24	139	4542	83	89	40	20
19	20:38:54	2.6	4.7	283.35	140	4086	83	89	40	20
20	20:40:18	11.6	5.5	311.70	140	3952	83	95	42	25
21	20:42:52	6.0	5.7	308.20	140	3901	82	95	42	25

Stellenbosch University https://scholar.sun.ac.za

Table C.7 continued from previous page

Case	Time	Case duration [sec]	Ship speed [knots]	Hydrodynamic torque [kNm]	Motor speed [rpm]	Motor power [kW]	Propeller pitch [%]	Average ice concentration [%]	Average ice thickness [cm]	Average floe size [m]
22	20:48:50	7.0	4.8	313.61	140	3972	82	95	42	25
23	20:49:02	4.8	5.0	308.94	140	3755	82	95	42	25
24	20:51:41	5.2	5.9	291.40	140	3632	83	83	32	25
25	20:53:42	4.7	5.9	257.80	139	3687	83	83	32	25
26	20:54:17	6.1	6.1	259.90	140	3497	83	83	32	25
27	20:54:48	3.1	5.9	263.29	139	4052	83	83	32	25
28	21:01:12	4.2	6.7	244.35	140	2632	73	95	16	10
29	21:04:49	1.1	5.7	176.93	140	3068	74	95	16	10
30	21:05:36	1.9	5.6	188.22	140	2918	73	95	16	10
31	21:08:14	1.7	6.0	201.38	140	2679	73	95	16	10
32	21:09:41	3.8	6.1	209.00	140	2692	73	95	16	10
33	21:10:14	2.3	6.0	200.07	140	2710	73	95	16	10
34	21:10:54	2.1	5.8	198.27	139	2903	73	95	16	10
35	21:11:02	4.1	5.8	202.72	140	2787	73	95	16	10
36	21:16:55	2.2	6.0	189.79	140	2478	73	95	16	10
37	21:20:45	2.1	5.7	193.89	139	2905	74	67	14	21
38	21:22:16	2.5	5.6	209.25	140	2793	73	67	14	21
39	21:25:47	1.8	5.5	212.83	140	3486	77	67	14	21
40	21:28:48	3.4	6.0	214.47	139	2956	76	67	14	21
41	21:31:00	3.4	6.4	250.82	139	2957	76	89	40	20
42	21:34:41	6.2	4.0	202.82	138	4404	84	89	40	20
43	21:35:57	4.8	4.8	278.51	140	4262	84	89	40	20

Stellenbosch University https://scholar.sun.ac.za

Table C.7 continued from previous page

Case	Time	Case duration [sec]	Ship speed [knots]	Hydrodynamic torque [kNm]	Motor speed [rpm]	Motor power [kW]	Propeller pitch [%]	Average ice concentration [%]	Average ice thickness [cm]	Average floe size [m]
44	21:36:29	6.2	5.3	302.08	140	4287	83	89	40	20
45	21:37:21	4.3	5.5	264.69	139	4295	84	89	40	20
46	21:41:55	18.0	0.5	322.23	140	2469	50	95	42	25
47	21:42:21	2.7	0.5	298.71	140	2479	50	95	42	25
48	21:42:33	6.5	0.6	302.62	140	2374	50	95	42	25
49	21:42:55	2.3	0.7	321.28	140	2460	50	95	42	25
50	21:49:30	2.3	1.6	272.39	140	3662	65	95	42	25

Stellenbosch University https://scholar.sun.ac.za

Table C.8: Solution times for the discrete and continuous models

Case	Case duration [sec]	Solution time [sec]			
		Discrete		Continuous	
		Q_1	Q_2	Q_1	Q_2
1	2.0	4.37	3.35	1.75	1.98
2	2.4	5.79	5.22	1.64	2.07
3	1.8	2.61	2.81	2.12	2.07
4	1.9	2.61	2.72	1.96	2.02
5	3.3	8.94	8.70	2.28	2.18
6	3.9	14.50	14.49	2.39	2.29
7	1.8	2.72	2.60	1.99	2.03
8	2.5	4.77	4.89	2.20	2.21
9	5.0	27.46	26.77	2.49	2.56
10	3.0	7.16	7.08	2.15	2.21
11	5.2	30.48	30.36	2.50	2.56
12	1.9	2.52	2.83	2.00	2.07
13	3.5	10.22	10.20	2.33	2.29
14	2.7	5.64	5.58	2.12	2.17
15	1.6	2.81	2.28	1.99	2.00
16	2.9	6.42	6.49	2.18	2.06
17	8.2	79.93	79.96	2.93	2.82
18	1.8	2.51	2.75	1.92	1.99
19	2.6	5.28	5.20	2.05	2.14
20	11.6	199.32	198.14	3.29	3.36
21	6.0	46.87	45.47	2.66	2.60
22	7.0	51.68	53.86	2.68	2.65
23	4.8	24.72	24.31	2.40	2.41
24	5.2	31.25	31.02	2.52	2.62
25	4.7	22.96	25.31	2.46	2.38
26	6.1	47.62	47.85	2.57	2.54
27	3.1	9.49	7.85	2.13	2.18
28	4.2	17.83	17.75	2.36	2.56
29	1.1	2.02	2.01	1.88	1.90
30	1.9	3.48	3.35	1.95	2.01
31	1.7	2.44	2.44	1.99	2.11
32	3.8	13.31	12.88	2.34	2.31
33	2.3	4.24	4.47	2.08	2.21
34	2.1	3.95	4.02	2.09	2.07
35	4.1	15.72	15.57	2.34	2.35
36	2.2	4.13	4.18	2.04	2.09
37	2.1	3.72	3.81	2.05	2.09
38	2.5	5.26	5.06	2.10	2.12

Stellenbosch University https://scholar.sun.ac.za

Table C.8 continued from previous page

Case	Case duration [sec]	Solution time [sec]			
		Discrete		Continuous	
		Q_1	Q_2	Q_1	Q_2
39	1.8	2.90	2.98	2.06	2.01
40	3.4	10.18	9.92	2.39	2.27
41	3.4	9.71	10.11	2.22	2.22
42	6.2	49.60	50.31	2.56	2.55
43	4.8	23.96	24.36	2.37	2.40
44	6.2	49.84	50.04	2.72	2.58
45	4.3	19.27	17.90	2.34	2.40
46	18.0			4.06	4.07
47	2.7	6.86	6.01	2.12	2.10
48	6.5	56.21	56.42	2.65	2.66
49	2.3	4.41	4.34	2.04	2.10
50	2.3	4.31	4.31	2.05	2.06

Stellenbosch University https://scholar.sun.ac.za

Appendix D

Propeller axial load estimation using a continuous model of the propulsion shaft

Though the axial propeller loads are not part of the scope of this study, it is worth showing how the continuous modal superposition model can be used in their estimation for future research opportunities.

For the model, a single shaft is considered between the propeller and thrust bearing. Since the thrust bearing is meant to absorb axial loads, this end is assumed to be a fixed support. Figure D.1 shows the model of the propulsion shaft with a differential element selected at a distance x along the shaft. The forces acting on the differential element are also shown, with $F(x,t)$ representing the internal propulsion shaft axial load and $F_d(x,t)$ the applied axial load. The propeller is located at $x = 0$ while the thrust bearing is situated at $x = L$. The model assumes a constant hollow circular cross section and consistent material properties along the length of the shaft. For the derivation of the model, an unknown distributed axial load is initially assumed to be applied along the length of the shaft.

Newton's second law states that the sum of the applied forces on a body is equal to the rate of change of the momentum of that body (Inman, 2014). Equation D.1 describes this dynamic equilibrium for the shaft.

$$\sum_i F_i = M\ddot{u} \tag{D.1}$$

where F_i represents the applied forces, M is the mass, and $\ddot{u}$ is the second derivative of the displacement in the x direction with respect to time.

Substituting the forces applied to the differential element in Figure D.1 into Equation D.1 gives Equation D.2, describing the dynamic equilibrium of the differential element.

Stellenbosch University https://scholar.sun.ac.za

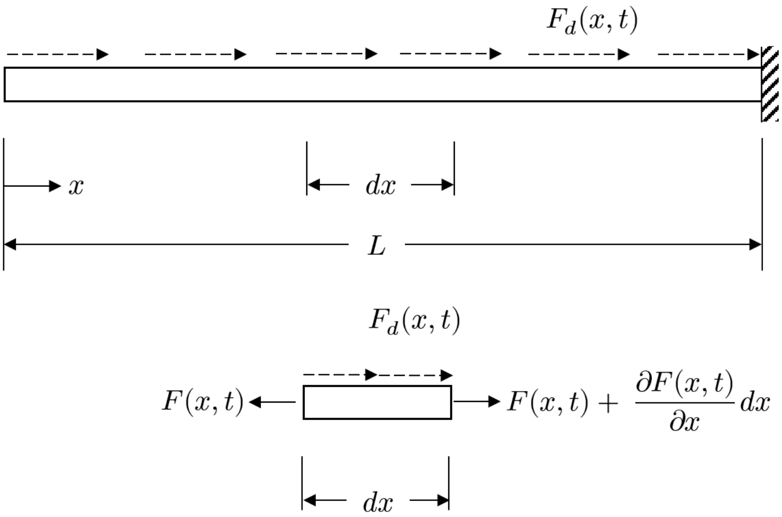

Figure D.1: Continuous shaft line model for propeller axial load estimation

$$-F(x,t) + F_d(x,t)dx + \left(F(x,t) + \frac{\partial F(x,t)}{\partial x}dx\right) = \rho A(x)\frac{\partial^2 u(x,t)}{\partial t^2}dx \quad \text{(D.2)}$$

where $A(x)$ is the cross sectional area of the shaft, ρ is the density, $F(x,t)$ the internal axial load at distance x, and $F_d(x,t)$ the externally applied distributed axial load.

Rearranging Equation D.2 and dividing all terms by dx gives Equation D.3:

$$\rho A(x)\frac{\partial^2 u(x,t)}{\partial t^2} - \frac{\partial}{\partial x}\left(F(x,t)\right) = F_d(x,t) \quad \text{(D.3)}$$

The axial load in the shaft at x is related to the axial deflection at x by:

$$F(x,t) = EA(x)\frac{\partial u(x,t)}{\partial x} \quad \text{(D.4)}$$

with E the elastic modulus.

Substitution of Equation D.4 into Equation D.3 yields:

$$\rho A(x)\frac{\partial^2 u(x,t)}{\partial t^2} - \frac{\partial}{\partial x}\left(EA(x)\frac{\partial u(x,t)}{\partial x}\right) = F_d(x,t) \quad \text{(D.5)}$$

Assuming a uniform cross section of the shaft, the area becomes constant and can factored out of the partial derivative with regards to x and Equation D.5 becomes:

Stellenbosch University https://scholar.sun.ac.za

$$\rho A \frac{\partial^2 u(x,t)}{\partial t^2} - EA \frac{\partial^2 u(x,t)}{\partial x^2} = F_d(x,t) \tag{D.6}$$

Modal superposition is applied in order to transform the partial differential Equation D.6 into a set of ordinary differential equations. The axial deflection $u(x,t)$ can be described as:

$$u(x,t) = \sum_{n=1}^{N} \phi_n(x) q_n(t) \tag{D.7}$$

where N is the number of mode shapes used to describe the deflection of the shaft, $\phi_n(x)$ are the mode shape values at x, and $q_n(t)$ are the corresponding modal coordinates as functions of time. The mode shapes are described by (Inman, 2014):

$$\phi_n(x) = B_n \sin\left(\frac{(2n-1)\pi(L-x)}{2L}\right), n = 1, 2, ..., N \tag{D.8}$$

where the B_n are constant values determined from initial conditions.

Substitution of Equation D.7 into Equation D.6 yields:

$$\rho A \sum_{n=0}^{N} \phi_n(x)\ddot{q}_n(t) - EA \sum_{n=0}^{N} \phi_n''(x) q_n(t) = F_d(x,t) \tag{D.9}$$

where the overdots on $\ddot{q}_n(t)$ and the primes on $\phi''(x)$ represent the second derivatives with respect to t and x respectively.

Differentiating the mode shape with respect to x twice leads to:

$$\phi_n'(x) = -B_n \left(\frac{(2n-1)\pi}{2L}\right) \cos\left(\frac{(2n-1)\pi(L-x)}{2L}\right) \tag{D.10}$$

$$\begin{aligned}\phi_n''(x) = -B_n \left(\frac{(2n-1)\pi}{2L}\right)^2 \sin\left(\frac{(2n-1)\pi(L-x)}{2L}\right) \\ = -\left(\frac{(2n-1)\pi}{2L}\right)^2 \phi_n(x)\end{aligned} \tag{D.11}$$

Substituting the second derivative of the mode shape into Equation D.9 gives:

$$\rho A \sum_{n=0}^{N} \phi_n(x)\ddot{q}_n(t) + EA \sum_{n=0}^{N} \left(\frac{(2n-1)\pi}{2L}\right)^2 \phi_n(x) q_n(t) = F_d(x,t) \tag{D.12}$$

Stellenbosch University https://scholar.sun.ac.za

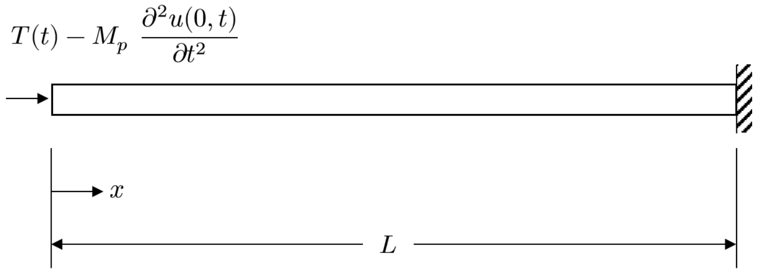

Figure D.2: Axial loads applied to propulsion shaft continuous model

The distributed axial load $F_d(x,t)$ applied to the shaft consists of a number of loads applied to the ends of the shaft, as seen in Figure D.2. The propeller is modelled as an inertial load and the axial loading is applied at the propeller at $x = 0$.

The axial load $F_d(x,t)$ becomes:

$$F_d(x,t) = T(t)\delta(x-0) - M_p \frac{\partial^2 u(0,t)}{\partial t^2}\delta(x-0) \tag{D.13}$$

where δ is the Dirac-delta function which states for some constant value a:

$$\delta(x-a) = \begin{cases} 1 & x = a \\ 0 & x \neq a \end{cases} \tag{D.14}$$

In order to remove the summations from Equation D.12, the orthogonality of the mode shapes is used (Inman, 2014). This means that

$$\int_0^L \phi_m(x)\phi_n(x)dx = \begin{cases} 0 & n \neq m \\ \frac{L}{2} & n = m \end{cases} \tag{D.15}$$

Also note that

$$\int_0^L \phi_m(x)\delta(x-a)dx = \phi_m(a) \cdot H(L-a) \tag{D.16}$$

where H is the Heaviside step function

Stellenbosch University https://scholar.sun.ac.za

$$H(L-a)=\begin{cases} 0 & L<a \\ 1 & L\geq a \end{cases} \tag{D.17}$$

Substituting Equation D.13 into Equation D.12, multiplying through by $\phi_m(x)$ and integrating over the length of the shaft gives

$$\begin{aligned} &\rho A\sum_{n=0}^{N}\int_0^L \phi_m(x)\phi_n(x)dx\cdot\ddot{q}_n(t) \\ &\qquad + EA\sum_{n=0}^{N}\left(\frac{(2n-1)\pi}{2L}\right)^2\int_0^L \phi_m(x)\phi_n(x)dx\cdot q_n(t) = \\ &T(t)\int_0^L \phi_m(x)\delta(x-0)dx - M_p\frac{\partial^2 u(0,t)}{\partial t^2}\int_0^L \phi_m(x)\delta(x-0)dx \end{aligned} \tag{D.18}$$

Substituting the relationships given in Equations D.15 and D.16 into Equation D.18 yields a separate equation for each mode shape n.

$$\rho A\frac{L}{2}\ddot{q}_n(t) + EA\frac{\pi^2(2n-1)^2}{8L}q_n(t) = T(t)\phi_n(0) - M_p\frac{\partial^2 u(0,t)}{\partial t^2}\phi_n(0) \tag{D.19}$$

Using modal superposition, Equation D.7, once again for the deflection term in Equation D.19 yields the final equations for each mode shape used in the model:

$$\begin{aligned} &\rho A\frac{L}{2}\ddot{q}_n(t) + M_p\phi_n(0)\sum_{i=1}^{N}\phi_i(x)\ddot{q}_i(t) \\ &\qquad + EA\frac{\pi^2(2n-1)^2}{8L}q_n(t) - T(t)\phi_n(0) = 0 \end{aligned} \tag{D.20}$$

For the inverse problem there are N equations, one for each mode shape, and $N+1$ unknowns, the q_n terms and the propeller thrust load $T(t)$. Therefore, one extra equation is necessary and this comes from a thrust measurement taken on the shaft at $x = x_a$:

$$F(x_a,t) = EA\frac{\partial u(x_a,t)}{\partial x} = EA\sum_{n=1}^{N}\phi_n'(x_a)q_n(t) \tag{D.21}$$

Stellenbosch University https://scholar.sun.ac.za

Equations D.20 and D.21 can then be written in matrix form, which facilitates their solution using a time integration scheme.

$$\mathbf{M}\ddot{\mathbf{q}} + \mathbf{C}\dot{\mathbf{q}} + \mathbf{K}\mathbf{q} = \mathbf{F} \tag{D.22}$$

where

$$\mathbf{q} = \{q_1 \ q_2 \ q_3 \ \cdots \ q_N \ T\}^T$$

$$\mathbf{J} = \begin{bmatrix} \rho A\frac{L}{2} + M_p\phi_1(0)\phi_1(0) & M_p\phi_1(0)\phi_2(0) & \cdots & M_p\phi_1(0)\phi_N(0) & 0 \\ M_p\phi_2(0)\phi_1(0) & \rho A\frac{L}{2} + M_p\phi_2(0)\phi_2(0) & \cdots & M_p\phi_2(0)\phi_N(0) & 0 \\ \vdots & \vdots & \ddots & \vdots & \vdots \\ M_p\phi_N(0)\phi_1(0) & M_p\phi_N(0)\phi_2(0) & \cdots & \rho A\frac{L}{2} + M_p\phi_N(0)\phi_N(0) & 0 \\ 0 & 0 & \cdots & 0 & 0 \end{bmatrix}$$

$$\mathbf{C} = \begin{bmatrix} 0 & 0 & \cdots & 0 \\ 0 & 0 & \cdots & 0 \\ \vdots & \vdots & \ddots & \vdots \\ 0 & 0 & \cdots & 0 \end{bmatrix}$$

$$\mathbf{K} = \begin{bmatrix} GJ\frac{(\pi)^2}{8L} & 0 & \cdots & 0 & -\phi_1(0) \\ 0 & GJ\frac{(3\pi)^2}{8L} & \cdots & 0 & -\phi_2(0) \\ \vdots & \vdots & \ddots & \vdots & \vdots \\ 0 & 0 & \cdots & GJ\frac{((2N-1)\pi)^2}{8L} & -\phi_N(0) \\ EA\phi_1'(x_a) & EA\phi_2'(x_a) & \cdots & EA\phi_N'(x_a) & 0 \end{bmatrix}$$

$$\mathbf{F} = \begin{Bmatrix} 0 \\ 0 \\ \vdots \\ 0 \\ F(x_a, t) \end{Bmatrix}$$

This model has been used along with measured data. Figure D.3 shows results for an ice impact measured on the 30 October 2019 at 20:06:20. These results show that the model is capable of estimating propeller axial loads from propulsion shaft measurements. However, further evaluation of the model is necessary.

Stellenbosch University https://scholar.sun.ac.za

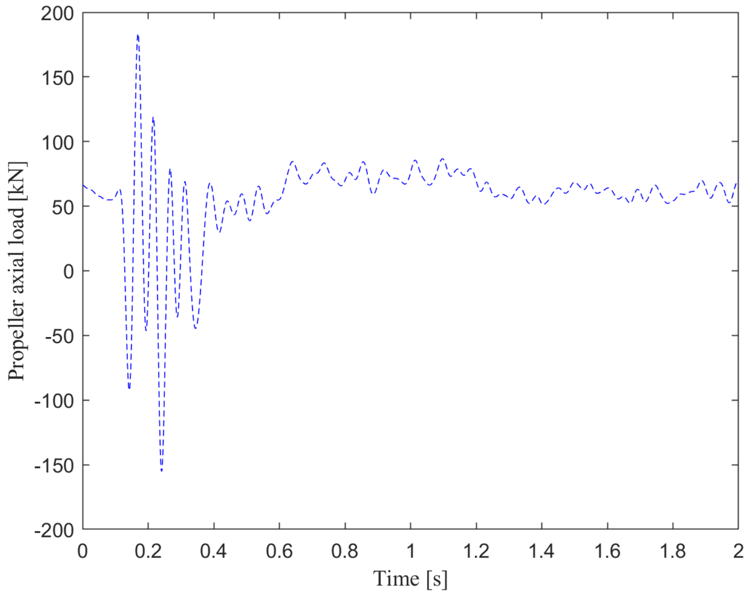

(a) Estimated propeller axial load

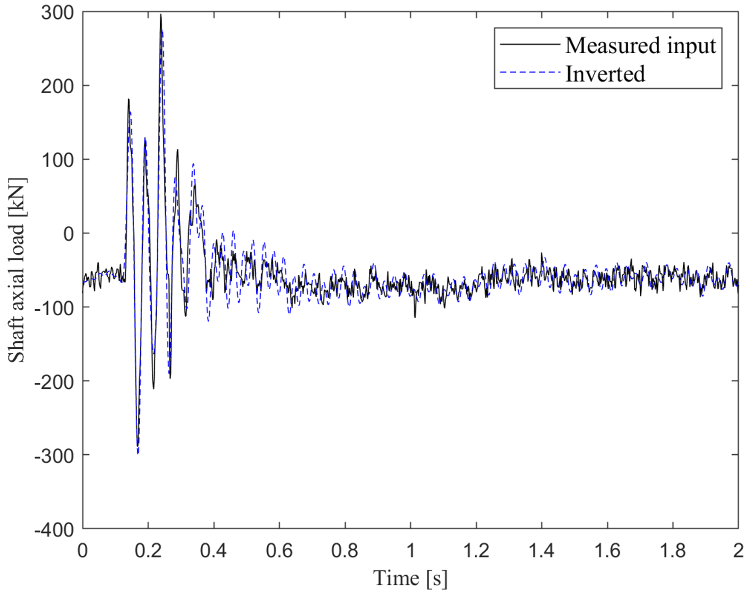

(b) Measured shaft axial load

Figure D.3: Results from continuous model for inverse estimation of axial propeller loads

Stellenbosch University https://scholar.sun.ac.za

References

Al-Bedoor, B., Aedwesi, S. and Al-Nassar, Y. (2006). Blades condition monitoring using shaft torsional vibration signals. *Journal of Quality in Maintenence Engneering*, vol. 12, no. 3, pp. 275–293.

American Bureau of Shipping (2006). Guidance notes on ship vibration.

Araujo, L.S., Mendes, M.C., de Almeida L H, Dutra, M.S. and Cardoso, D. (2013). Failure of a concentric pipe for a controllable pitch propeller system. *Journal of Failure Analysis and Prevention*, vol. 14, no. 1, pp. 55–60.

ASTM E1049-85 (2017). *Standard Practices for Cycle Counting in Fatigue Analysis.* West Conshohocken: ASTM International.

Barro, R.D. and Lee, D.C. (2011). Excitation response of polar class vessel propulsion shafting system. *Transactions of the Korean Society for Noise and Vibration Engineering*, vol. 21, no. 12, pp. 1166–1176.

Batrak, Y.A., Serdjuchenko, A.M. and Tarasenko, A.I. (2014 May). Calculation of torsional vibration responses in propulsion shafting system caused by ice impacts. In: *Torsional Vibration Symposium*. Salzburg, Austria.

Bekker, A., Suominen, M., Kujala, P., De Waal, R.J.O. and Soal, K.I. (2019). From data to insight for a polar supply and research vessel. *Ship Technology Research*, vol. 66, no. 1, pp. 57–73.
Available at: `https://doi.org/10.1080/09377255.2018.1464241`

Bertram, V. (2012). *Practical Ship Hydrodynamics.* 2nd edn. Oxford: Butterworth-Heinemann.

Besselink, B., Tabak, U., Lutowska, A., Van De Wouw, N., Nijmeijer, H., Rixen, D.J., Hochstenbach, M.E. and Schilders, W.H. (2013). A comparison of model reduction techniques from structural dynamics, numerical mathematics and systems and control. *Journal of Sound and Vibration*, vol. 332, no. 19, pp. 4403–4422. ISSN 0022460X.
Available at: `http://dx.doi.org/10.1016/j.jsv.2013.03.025`

Brewer, G.A. (1972). Operating stresses on the SS Michigan propeller. *Experimental Mechanics*, vol. 12, no. 3, pp. 159–168.

Stellenbosch University https://scholar.sun.ac.za

Browne, R.P., Revill, C.R., Ritch, A.R. and Keinonen, A.J. (1998). Propeller design load model. *Transport Canada Publication - TP 13243E, Institute for Marine Dynamics, National Research Council Canada.*

Casciani-Wood, J. (2015). An introduction to propeller cavitation. `http://www.iims.org.uk/introduction-propeller-cavitation/`. Accessed: 21 July 2017.

Chung, J. and Hulbert, G.M. (1993). A time integration algorithm for structural dynamics with improved numerical dissipation: the generalized-alpha method. *Journal of Applied Mechanics*, vol. 60, pp. 371–375.

COMSOL (2018). Mode superposition. `https://www.comsol.com/multiphysics/mode-superposition`. Accessed: 06 February 2020.

Dashnaw, F.J. and Reed, F.E. (1971). Propeller strain measurements and vibration measurements on the SS Michigan. *Marine Technology Society Journal*, vol. 8, no. 4, pp. 486–509.

De Waal, R.J.O. (2017). *An investigation of shaft line torsional vibration during ice impacts on PSRVs*. Master's thesis, Stellenbosch University, South Africa.

De Waal, R.J.O., Bekker, A. and Heyns, P.S. (2018*a*). Data for indirect load case estimation of ice-induced moments from shaft line torque measurments. *Data in Brief*, vol. 19, pp. 1222–1236.

De Waal, R.J.O., Bekker, A. and Heyns, P.S. (2018*b*). Indirect load case estimation of ice-induced moments from shaft line torque measurments. *Cold Regions Science and Technology*, vol. 151, pp. 237–248.

Det Norske Veritas (2011). Ice strengthening of propulsion machinery. *Classification Notes*, vol. 1, no. 51.

Det Norske Veritas (2016). Ships for navigation in ice. *Rules for Classification of Ships*, vol. 5, no. 1.

Diamond, D.H., Heyns, P.S. and Oberholster, A.J. (2016). Online shaft encoder geometry compensation for arbitrary shaft speed profiles using Bayesian regression. *Mechanical Systems and Signal Processing*, vol. 81, pp. 402–418. ISSN 10961216.

Dickens, J.M., Nakagawa, J.M. and Wittbrodt, M.J. (1997). A critique of mode acceleration and modal truncation augmentation methods for modal response analysis. *Computers and Structures*, vol. 62, no. 6, pp. 985–998. ISSN 00457949.

Doyle, J.F. (1987). Experimentally determining the contact force during the transverse impact of an orthotropic plate. *Journal of Sound and Vibration*, vol. 118, no. 3, pp. 441–448.

Dukkipati, R.V. (2010). *MATLAB: An introduction with applications*. New Delhi: New Age International Publishers.

Stellenbosch University https://scholar.sun.ac.za

Fan, Y.C., Ju, M.S. and Tsuei, Y.G. (1994). Experimental study on vibration of a rotating blade. *Transactions of the ASME Journal of Engineering for Gas Turbines and Power*, vol. 116, pp. 672–677.

Figliola, R.S. and Beasley, D.E. (2011). *Theory and Design for Mechanical Measurements.* 5th edn. Asia: John Wiley and Sons, Inc.

Finnish Maritime Administration and Swedish Maritime Administration (2006). Guidelines for the application of the Finnish - Swedish Ice Class Rules.

Garcia, D. (2010). Robust smoothing of gridded data in one and higher dimensions with missing values. *Computational Statistics and Data Analysis*, vol. 54, no. 4, pp. 1167–78. ISSN 01679473.

Garcia, D. (2020). smoothn. *MATLAB Central File Exchange.* Available at: `https://www.mathworks.com/matlabcentral/fileexchange/25634-smoothn`

Germanishcer Lloyd (2007). Rules for classification and construction. *Part 6 Offshore Technology, Chapter 5 Machinery Installations, Section 7 Torsional Vibrations.*

Golub, G.H., Hansen, P.C. and O'Leary, D.P. (1999). Tikhonov regularization and total least squares. *Siam Journal on Matrix Analysis and Applications*, vol. 21, no. 1, pp. 185–194.

Hansen, P.C. (2008). *Regularization Tools: A Matlab Package for Analysis and Solution of Discrete Ill-Posed Problems.* Lyngby: Technical University of Denmark.

Hansen, P.C., Jensen, T.K. and Rodriguez, G. (2007). An adaptive pruning algorithm for the discrete L-curve criterion. *Computational and Applied Mathematics*, vol. 198, pp. 483–492.

Hansen, P.C. and O'Leary, D.P. (1993). The use of the L-curve in the regularization of discrete ill-posed problems. *Journal of Scientific Computing*, vol. 14, no. 6, pp. 1487–1503.

He, Q. and Du, D. (2010). Modeling and calculation analysis of torsional vibration for turbine generator shafts. *Journal of Information and Computational Science*, vol. 10, no. 3, pp. 2174–2182.

Heath, M.T. (1997). *Scientific Computing: An Introductory Survey.* Urbana-Champaign: University of Illinois.

Hibbeler, R.C. (2011). *Mechanics of Materials.* 8th edn. Singapore: Pearson Prentice Hall.

Hilbur, H.M. and Hughes, T.J.R. (1978). Collocation, dissipation and overshoot for time integration schemes in structural dynamics. *Earthquake Engineering and Structural Dynamics*, vol. 6.

Stellenbosch University https://scholar.sun.ac.za

Hilbur, H.M., Hughes, T.J.R. and Taylor, R.L. (1977). Improved numerical dissipation for time integration algorithms in structural dynamics. *Earthquake Engineering and Structural Dyanmics*, vol. 5.

Hoff, C. and Pahl, P.J. (1988). Development of an implicit method with numerical dissipation from generalized single-step algorithm for structural dynamics. *Computer Methods in Applied Mechanics and Engineering*, vol. 67, pp. 367–385.

Hoffmann, K. (2001). Applying the Wheatstone Bridge Circuit. *HBM W1569-1.0 en, HBM, Darmstadt, Germany.*

Huisman, T.J., Bos, R.W., Hagesteijn, G., Brouwer, J. and de Koning Gans, H.J. (2014 June). Interaction between warm model ice and a propeller. In: *Proceedings of the ASME 2014 33rd International Conference on Ocean, Offshore and Arctic Engineering OMAE2014*. San Francisco, California, USA.

Ikonen, T., Peltokorpi, O. and Karhunen, J. (2014). Inverse ice-induced moment determination on the propeller of an ice-going vessel. *Cold Regions Science and Technology*, vol. 112, pp. 1–13.

Inman, D.J. (2014). *Engineering Vibration*. 4th edn. Harlow: Pearson Education Limited.

International Association of Classification Societies (2016). Requirements concerning polar class.

Jacquelin, E., Bennani, A. and Hamelin, P. (2003). Force reconstruction: Analysis and regularization of a deconvolution problem. *Journal of Sound and Vibration*, pp. 81–107.

Jansen, K., Whiting, C. and Hulbert, G. (1999). A generalized-a method for integrating the filtered Navier-Stokes equations with a stabilized finite element method. *Computer Methods in Applied Mechanics and Engineering*, vol. 190, no. 3-4, pp. 305–320.

Jussila, M. and Koskinen, P. (1989*a*). Ice loads on cp-propeller blade and propulsions shaft of small ferry and their statistical distributions during winter -87. In: *Proceedings of the 8thInternational Conference on Offshore Mechanics and Arctic Engineering*.

Jussila, M. and Koskinen, P. (1989*b*). Ice loads on propeller blade of small car ferry. In: *Proceedings of the 10th International Conference on Port and Ocean Engineering under Arctic Conditions*. Luleaa, Sweden.

Kadapa, C. (2017). Newmark-beta method -disadvantages. `https://ckadapa.wordpress.com/2017/06/23/newmark-beta-method-disadvantages/`. Accessed: 1 June 2020.

Kadapa, C., Dettmer, W.G. and Perić, D. (2017). On the advantages of using the first-order generalised-alpha scheme for structural dynamic problems. *Computers and Structures*, vol. 193, pp. 226–238. ISSN 00457949.

Stellenbosch University https://scholar.sun.ac.za

KaiPing, Y. (2008). A new family of generalized-alpha time integration algorithms without overshoot for structural dynamics. *Earthquake Engineering and Structural Dyanmics*, vol. 37.

Kaufman, P. and Kershisnik, M. (1984). Case history - a high speed turbine wheel. *Mechanical Engineering*, pp. 38–45.

Korean Register (2015). Guidance for ship navigation in ice. http://www.krs.co.kr/KRRules/KRRules2015/KRRulesE.html. Accessed: 21 July 2017.

Kujala, P., Kulovesi, J., Lehtiranta, J. and Suominen, M. (2014). Full-scale measurements on board S.A. Agulhas II in the Antarctic waters 2013-2014. *Technical Report, Aalto University.*

Kushwaha, V. (2012). *Analysis of torsional vibration characteristics for multi-rotor and gear-branched systems using finite element method.* Ph.D. thesis, National Institute of Technology.

Lavrenčič, M. and Brank, B. (2020). Comparison of numerically dissipative schemes for structural dynamics: generalized-alpha versus energy-decaying methods. *Thin-walled Structures*, vol. 157.

Lloyd, J.J., Taylor, C.J., Lawson, R.S. and Shields, R.A. (1997). The use of the L-curve method in the inversion of diffusion battery data. *Journal of Aerosol Science*, vol. 28, no. 7, pp. 1251–1264. ISSN 00218502.

LORD MicroStrain sensing systems (2016). LORD prroduct datasheet: V-Link LXRS.

Martelli, M., Figari, M., Altosole, M. and Vignolo, S. (2013). Controllable pitch propeller actuating mechanism, modelling and simulation. *Proceedings of the Institution of Mechanical Engineers, Part M: Journal of Engineering for the Maritime Environment*, vol. 228, no. 1, pp. 29–43.

Mashadi, B. and Crolla, D. (2012). *Appendix: An Introduction to Bond Graph Modelling*, pp. 511–528. John Wiley & Sons, Ltd. ISBN 9781119958376. Available at: https://onlinelibrary.wiley.com/doi/abs/10.1002/9781119958376.app1

Morozov, V.A. (1984). *Methods for Solving Incorrectly Posed Problems.* New York: Springer-Verlag.

Myklebost, M.R. and Dahler, G. (2003). Agulhas II data analysis of torsional shaft responses from operation in Arctic waters - Technical Summary Report. *Det Norske Veritas AS.*

Newmark, N.M. (1959). A method of computation for structural dynamics. *ASCE Journal of the Engineering Mechanics Division*, vol. 85.

Stellenbosch University https://scholar.sun.ac.za

Nieslony, A. (2020). Rainflow counting algorithm. `https://www.mathworks.com/matlabcentral/fileexchange/3026-rainflow-counting-algorithm`. Accessed: 1 June 2020.

Paynter, H.M. (1998). *Analysis and Design of Engineering Systems*. Cambridge: MIT Press.

PCB Piezotronics (2009). ICP Accelerometer Model 333B32 Specifications. `http://www.pcb.com/contentstore/docs/PCB_Corporate/Vibration/Products/Specsheets/333B32_G.pdf`. Accessed: 03 January 2019.

PCB Piezotronics (2015). ICP Impact Hammer Model 086D20 Specifications. `http://www.pcb.com/contentstore/docs/PCB_Corporate/Vibration/Products/Specsheets/086D20_H.pdf`. Accessed: 03 January 2019.

PCB Piezotronics (2017). Mechanical Impedance Sensor Model 288D01 Specifications. `http://www.pcb.com/contentstore/docs/PCB_Corporate/Vibration/Products/Specsheets/288D01_J.pdf`. Accessed: 03 January 2019.

Peltokorpi, O., Bekker, A., Kulovesi, J., M, S., Kujala, P. and Karhumen, J. (2014 June). Full-scale measurements on a polar supply and research vessel during manouver tests in an ice field in the baltic sea. In: *Proceedings of the ASME 2014 33rd International Conference on Ocean, Offshore and Arctic Engineering OMAE2014*. San Francisco, California, USA.

Persson, S. (2015). Ice impact simulation for propulsion machinery. *MTZ Industrial*, vol. 5, no. 1, pp. 34–41.

Polić, D., Æsøy, V. and Ehlers, S. (2016). Transient simulation of the propulsion machinery system operating in ice - Modeling approach. *Ocean Engineering*, vol. 124, pp. 437–449. ISSN 00298018.

Polić, D., Ehlers, S. and Æsøy, V. (2017). Propeller torque load and propeller shaft torque response correlation during ice-propeller interaction. *Journal of Marine Science and Application*, vol. 16.

Polić, D., Ehlers, S. and Æsøy, V. (2019). Inverse modeling approach for transformation of propeller shaft angular deformation and velocity to propeller torque load. *Marine Structures*, vol. 67. ISSN 09518339.
Available at: `https://doi.org/10.1016/j.marstruc.2019.04.002`

Polić, D., Ehlers, S., Æsøy, V. and Pedersen, E. (2014 June). Shaft response as a propulsion machinery design load. In: *Proceedings of the ASME 2014 33rd International Conference on Ocean, Offshore and Arctic Engineering OMAE2014*. San Francisco, California, USA.

Rao, S.S. (2007). *Vibration of Continuous Systems*. Hoboken: John Wiley & Sons, Inc.

Rohatgi, A. (2020). Webplotdigitizer: Version 4.3.
Available at: `https://automeris.io/WebPlotDigitizer`

Stellenbosch University https://scholar.sun.ac.za

Rolls-Royce AB (2010*a*). Ice impact simulation - polar research vessel. *RRAB STX Research Vessel RES 05B40400 20100414*.

Rolls-Royce AB (2010*b*). Torsional vibration analysis of propulsion shaftline. *STX Rauma NB 1369 Report No. 2010-0451*.

Rolls-Royce AB (2010*c*). Whirling calculation. *Report SA1090*.

Rossi, S., Abboud, N. and Scovazzi, G. (2016). Implicit finite incompressible elastodynamics with linear finite elements: a stabilized method in rate form. *Computer Methods in Applied Mechanics and Engineering*, vol. 311, pp. 208–249.

Scalzo, A.J., Allen, J.M. and Antos, R.J. (1986). Analysis and solution of a non-synchronous vibration problem in the last row turbine blade of a large industrial turbine. *Transactions of the ASME Journal of Engineering for Gas Turbines and Power*, vol. 108, pp. 591–598.

Schwanecke, H. (1963). Gedanken zur Frage der hydrodynamisch erregten Schwingungen des Propellers und der Wellenleitung. *Versuchsanstalt fur Wasserbau und Schiffbau, Berlin, Sonderdruck aus Jahrbuch der Schiffbautechnischen Gesellschaft*, vol. 57, pp. 252–280.

Senjanović, I., Hadžić, N., Murawski, L., Vladimir, N., Alujević, N. and Cho, D.S. (2019). Analytical procedures for torsional vibration analysis of ship power transmission system. *Engineering Structures*, vol. 178, no. May 2018, pp. 227–244. ISSN 18737323.
Available at: https://doi.org/10.1016/j.engstruct.2018.10.035

Shames, I.H. and Pitarresi, J.M. (2000). *Introduction to Solid Mechanics*. 3rd edn. New Delhi: Prentice Hall.

Siemens PLM Software (2014). LMS Test.Lab, Powering testing productivity. http://www.dta.com.tr/pdf/brosur/siemens_lms/Siemens-PLM-LMS-Test-Lab_brosur.pdf. Accessed: 03 January 2019.

Srinivasan, A.V. and Cuts, D.G. (1995). Laser vibrometery measurements of rotating blade vibrations. *Transactions of the ASME Journal of Engineering for Gas Turbines and Power*, vol. 117, pp. 484–488.

STX Finland Oy (2012*a*). Polar supply and research vessel general arrangement.

STX Finland Oy (2012*b*). Polar supply and research vessel shaft line arrangement.

Sun, Y.Q. and Dhanasekar, M. (2002). A dynamic model for the vertical interaction of the rail track and wagon system. *International Journal of Solids and Structures*, vol. 39, pp. 1337–1359.

Tang, B. and Brennan, M.J. (2013). On the influence of the mode-shapes of a marine propulsion shafting system on the prediction of torsional stresses. *Journal of Marine Science and Technology*, vol. 21, no. 2, pp. 209–214.

Stellenbosch University https://scholar.sun.ac.za

Valeri, C. (2015). Constant speed propellers part 2: The mechanics of a constant speed propeller. `http://expertaviator.com/videos/`. Accessed: 21 July 2017.

Wahba, G. (1990). *Spline Models for Observational Data*. Philadelphia: CBMS-NSF Regional Conference Series in Applied Mathematics, Vol. 59, SIAM.

Walker, D.L.N. (1996). *The influence of blockage and cavitation on the hydrodynamic performance of ice class propellers in blocked flow*. Ph.D. thesis, Memorial University of Newfoundland.

Williams, F.M. and Spencer, D. (1992). Full scale trials in level ice with Canadian R-class icebreaker. *Transactions - Society of Naval Architects and Marine Engineers*.

Wilson, E.L. (1962). Dynamic response by step-by-step matrix analysis. In: *Proceedings of the Symposium on the Use of Computers in Civil Engineering*. Labortorio Nacional de Engenharia Civil. Lisbon, Portugal.

Wilson, E.L. (2002). *Three-dimensional Static and Dynamic Analysis of Structures*. 3rd edn. Berkeley: Computers and Structures, Inc.

Wilson, E.L., Farhoomand, I. and Bathe, K.J. (1973). Nonlinear dynamic analysis of complex structures. *Earthquake Engineering and Structural Dynamics*, vol. 1.

Wood, W.L., Bossak, M. and Zienkiwicz, O.C. (1981). An alpha modification of Newmark's method. *International Journal for Numerical Methods in Engineering*, vol. 15.

Xu, Y., Pei, Y. and Dong, F. (2016). An extended L-curve method for choosing a regularization parameter in electrical resistance tomography. *Measurement Science and Technology*, vol. 27, no. 11. ISSN 13616501.

Zeng, X., Scovazzi, G., Abboud, N., Colomes, O. and Rossi, S. (2017). A dynamic variational multiscale method for viscoelasticity using linear tetrahedral elements. *International Journal for Numerical Methods in Engineering*, vol. 112.

Zhai, W., Cai, C.B., Wang, Q.C., Lu, Z.W. and Wu, X.S. (2001). Dynamic effects of vehicles on tracks in the case of raising train speeds. *Proceedings of the Institution of Mechanical Engineers, Part F: Journal of Rail and Rapid Transit*, vol. 215, no. March, pp. 125 – 135.